

Synthesis and Catalytic Structure Activity Relations of Hydrophobic Zeolites with Isolated Framework Metals that act as Water Tolerant Lewis Acids

by

William Robert Gunther

B.S., University of Illinois at Urbana-Champaign (2010)

M.S., Massachusetts Institute of Technology (2012)

Submitted to the Department of Chemical Engineering
In Partial Fulfillment of the Requirements for the Degree of

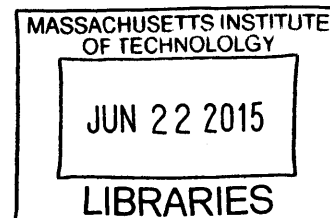
Doctor of Philosophy

at the

MASSACHUSETTS INSTITUTE OF TECHNOLOGY

June 2015

ARCHIVES



© 2015 Massachusetts Institute of Technology. All rights reserved.

Signature redacted

Signature of Author.....

Department of Chemical Engineering

April 16, 2015

Signature redacted

Certified by.....

Yuriy Román-Leshkov

Assistant Professor of Chemical Engineering

Thesis Supervisor

Signature redacted

Accepted by.....

Richard D. Braatz

Edward R. Gilliland Professor of Chemical Engineering

Chairman, Committee for Graduate Students

Synthesis and Catalytic Structure Activity Relations of Hydrophobic Zeolites with Isolated Framework Metals that act as Water Tolerant Lewis Acids

by

William Robert Gunther

Submitted to the Department of Chemical Engineering
on April 16, 2015 in Partial Fulfillment of the
Requirements for the Degree of Doctor of Philosophy in
Chemical Engineering

Abstract

Catalysis provides a technology-based method to efficiently convert raw materials to useful products. Zeolite catalysis enables high product selectivity and is widely used due to the high activity, thermal stability, and well-defined crystalline pore structure of zeolites. Moreover, incorporation of metals into the framework of hydrophobic zeolites results in water-tolerant Lewis acids. This thesis discusses the synthesis, characterization, and structure-activity relations of metal-substituted Beta zeolites in the conversion of oxygenates. Chapter 2 discusses the application of dynamic nuclear polarization (DNP) NMR to characterize natural-abundance Sn-Beta. An indirect use of proton spin diffusion resulted in a 50-fold signal increase and the ability to observe natural-abundance ^{119}Sn -Beta in <24 h. Since DNP NMR only enables efficient detection of spin-1/2 nuclei, a secondary method of adsorbing pyridine on framework metal sites in zeolites permits further characterization of quadrupolar nuclei. Chapter 3 examines how pyridine chemical shift can resolve framework and extraframework metal sites as well as provide a measure of Lewis acidity. Additionally, solid-state NMR offers the ability to quantify the concentrations of these sites. Promoter addition to the active sites of zeolites can further provide cooperative catalysis and tuning of product distribution. Chapter 4 describes the borate-promoted Sn-Beta zeolite-catalyzed conversion of aldoses via an unusual 1,2 carbon shift mechanism. The addition of a borate promoter to Sn-Beta resulted in a complete shift towards near-equilibrium epimerization product distribution. Chapter 5 further examines the catalytic consequences of varying key reaction parameters such as the borate to sugar ratio, pH, and reaction time. This full factorial experimental design showed that epimerization dominates under neutral conditions and is still active at substoichiometric borate to sugar ratio. This observation suggests that borate is acting pseudo-catalytically potentially through interaction with the Sn site. These findings motivated a detailed mechanistic study, as discussed in Chapter 6. Solid-state NMR proximity measurements in conjunction with directed removal of substrate functionality led to a proposed Bilik-type reaction mechanism involving borate. This body of work contributes to a molecular-level understanding of Lewis acid sites in hydrophobic zeolites. Furthermore, the ability to tailor Lewis acid sites through promoter incorporation can enable novel catalytic reactions.

Thesis Supervisor: Yuriy Román-Leshkov
Title: Assistant Professor of Chemical Engineering

Acknowledgements

The work presented in this thesis would not have been possible without the help and encouragement of many people. I would first like to thank my advisor Prof. Yuriy Román-Leshkov for his constant support and guidance throughout my time at MIT. He challenged me to work on many different and exciting projects that helped me to grow as a researcher and engineer. He has provided advice and mentorship throughout my time here and his tireless efforts have prepared me well for my career after graduate school. I am especially grateful for his genuine commitment to the success and well-being of his students, which made graduate school much less daunting than it could have been. I would also like to thank all members of the Román lab for their helpful suggestions on my research. During my time in the lab, I always felt at home and shared many wonderful memories and laughs with my fellow lab mates.

I particularly wish to thank the members of my thesis committee—Prof. Bill Green, Prof. Kristala Prather, and Prof. Gregory Stephanopoulos—for their thoughtful comments and expert advice on my projects. Their guidance helped direct me towards the many exciting questions within catalysis that I have had a chance to pursue.

Through my various projects, I have had the opportunity to work with many brilliant and generous collaborators, and in particular Dr. Vladimir Michaelis. I have been most fortunate to receive his expert mentorship and he taught me much of what I now know of solid-state NMR. There were times when I had to run ssNMR experiments past midnight, but Vlad was always available through email or phone to guide me successfully through setting up and processing my samples. Vlad not only provided technical guidance, but he was also an example of someone who worked incredibly hard and cared about those around him. Without a doubt, I would not be at this point if not for his support and friendship.

There are many others whose support has helped me during these years: Mark Keibler for his friendship since I first came to MIT; Fr. Richard Clancy and my friends at the MIT Tech Catholic Community for the camaraderie and fun times outside of lab; and Sue and John Seelander and their kids for being by my side when my parents passed away. For those who have touched my life in any way since I started my journey at MIT, I am truly grateful for all you have done.

This thesis is dedicated to the loving memory of my parents, Leslie and Kathleen. My parents were always there for me, especially when I was faced with unfamiliar circumstances. This work would not have been possible without the deep foundation provided by them. Ever since I was a little boy, they supported my budding scientific interests and even bought me model rocket kits to build and launch. In the summers, we took our popup camper everywhere and traveled all across the US. These memories I will forever cherish. My mother and father also provided excellent examples of how to approach life. Their positive outlook, care for others, dedication to family and desire to do a good job have set a high bar. Shortly after I was born, my mother decided to stay home and take care of me. We spent many hours at the local Morton Arboretum and I remember the times we gardened together in our backyard. My father and I were members of the YMCA Indian Guides and later Boy Scouts and we enjoyed going fishing together. These experiences were shining examples of my father's leadership and generous spirit. I am deeply grateful for my parents' unending support as I pursued my Ph.D. Their love and affection have constantly motivated me throughout this thesis. They have always encouraged me to strive for more and try my best. Although you may not be physically present, I know you will be watching as I complete another journey in my life. I miss and love you both so much.

Finally, I would like to thank my girlfriend Truc and her family who helped me through the loss of my parents. Truc has gone to great lengths and endured stress and anxiety so that I could realize my dreams. I admire her strength, selfless dedication and work ethic. Without you, this would have been a much lonelier and less enjoyable path. I look forward to continuing on this journey together.

Table of Contents

1	Introduction	14
1.1	Oxygenates as an alternative feedstock	14
1.2	Lewis acids as catalysts	15
1.3	Zeolite Catalysis.....	16
1.4	Hydrophobic Zeolites as Water-Tolerant Lewis Acids.....	17
1.5	Zeolite Modification and Cooperative Catalysis.....	18
1.6	Methods to Characterize Active Sites within Zeolites.....	19
1.7	Focus of this Dissertation	20
2	Dynamic nuclear polarization NMR enables the analysis of Sn-Beta zeolite prepared with natural abundance ^{119}Sn precursors	22
2.1	Abstract.....	22
2.2	Introduction	22
2.3	Results and Discussion	24
3	Interrogating Lewis acid character of metal sites in Beta zeolites with ^{15}N pyridine MAS NMR	30
3.1	Abstract.....	30
3.2	Introduction	30
3.3	Experimental Section	32
3.4	Results and Discussion	36
3.5	Conclusion.....	49
4	Sn-Beta zeolites with borate salts catalyse the epimerization of carbohydrates via an intramolecular carbon shift.....	51
4.1	Abstract.....	51
4.2	Introduction	51
4.3	Results.....	54
4.4	Discussion.....	62
4.5	Methods.....	64
5	Catalytic consequences of borate complexation and pH on the epimerization of L-arabinose to L-ribose in water catalyzed by Sn-Beta zeolite with borate salts	68
5.1	Abstract.....	68
5.2	Introduction	68
5.3	Experimental.....	71
5.4	Results and discussion.....	75
5.5	Conclusion.....	87
6	Mechanistic implications of a novel tin borate nanostructure on the epimerization of glucose with Sn-Beta zeolite.....	88
6.1	Abstract.....	88
6.2	Introduction	88
6.3	Results.....	91
6.4	Conclusion.....	101
7	Concluding Remarks and Future Directions.....	103
7.1	Future work.....	105
7.2	Limitations of this work.....	108
7.3	Future perspective	108
8	References	111
9	Supporting information.....	123

9.1	Dynamic Nuclear Polarization NMR Enables the Analysis of Sn-Beta Zeolite Prepared with Natural Abundance ¹¹⁹ Sn Precursors	123
9.2	Interrogating Lewis acid character of metal sites in Beta zeolites with ¹⁵ N pyridine MAS NMR	132
9.3	Sn-Beta zeolites with borate salts catalyse the epimerization of carbohydrates via an intramolecular carbon shift	143
9.4	Catalytic consequences of borate complexation and pH on the epimerization of L-arabinose to L-ribose in water catalyzed by Sn-Beta zeolite with borate salts	162
9.5	Mechanistic implications of a novel Sn-O-B-O-Si nanostructure on the epimerization of glucose with Sn-Beta zeolite	177

List of Figures

Figure 1. Hyperpolarization of Sn-Beta Zeolite Using Dynamic Nuclear Polarization.....	24
Figure 2. DNP-enhanced ^{119}Sn spectra of dehydrated (a) and hydrated (b) enriched ^{119}Sn -Beta zeolite. Spectra were acquired at 100 K for 3.8 h. ^{119}Sn MAS NMR spectrum of ^{119}Sn enriched dehydrated Sn-Beta zeolite (c) was acquired at 300 K for 58 h. * denotes spinning sidebands.	25
Figure 3. DNP-enhanced ^{119}Sn spectra of hydrated (a) and dehydrated (b) natural abundance Sn-Beta zeolite. Spectra were acquired at 100 K for 18 and 21 h, respectively. ^{119}Sn MAS NMR spectrum of natural abundant dehydrated Sn-Beta zeolite was acquired at 300 K for 246 h. * denotes spinning sidebands.....	29
Figure 4. Rotation of CSA components into the pyridine radial δ_r , tangential δ_t , and perpendicular δ_l reference frame. The pyridine δ_t decreases upon binding to a proton or Lewis acid site, causing it to change from δ_{11} to δ_{22} in NMR nomenclature ($\delta_{33} \leq \delta_{22} \leq \delta_{11}$).....	37
Figure 5. ^{15}N CP MAS NMR of pyridine adsorbed on metal-substituted zeolites. Spinning sidebands appear outside the field of view. Dashed lines correspond to spectra of hydrated samples. H-Al-Beta-F had a Si/Al=50, H-Al-Beta-OH had a Si/Al=19 and all other materials had Si/Metal \approx 100.	39
Figure 6. Experimental Mulliken electronegativity vs. pyridine ^{15}N MAS NMR chemical shift. The chemical shift shown is un-weighted average of the chemical shifts associated with open and closed sites. The dashed line and grey envelope show a regression with standard errors.	43
Figure 7. Distortion and dissociation energetics associated with pyridine adsorption calculated with DFT.	46
Figure 8. Quantification of adsorbed pyridine using ^{15}N MAS NMR. The dotted line represents a parity line. The Y-error bars are based on the signal-to-noise of each spectra; each experimental data point was analyzed in triplicate and the error bars represent two times the sample standard deviation. X-error bars represent the range of errors (ca. 10%) typically obtained during elemental analysis, including zeolite dissolution and ICP characterization.	49
Figure 9. Representative glucose conversion pathways using biological catalysts. Enzymes comprise isomerases, oxidoreductases and epimerases.	52
Figure 10. ^{13}C NMR spectra of reactants and products for epimerization and isomerization reactions. ...	57
Figure 11. ^{13}C and ^{11}B solid-state MAS NMR spectra for glucose adsorbed on Sn-Beta.	61
Figure 12. Schematic representation of the isomerization and epimerization of L-arabinose. The D form is the mirror image of the L form.	69
Figure 13. Schematic representation of borate species in solution and borate–sugar complexes.	75
Figure 14. Factorial design for the conversion of a 5 wt% arabinose solution at 343 K using Sn-Beta and a borate co-catalyst. Reactions were performed at a 100:1 sugar–metal molar ratio with a 5 wt% arabinose feed at 343 K in a stirred batch reactor, using Sn-Beta with a Si/Sn of 96.	78
Figure 15. Contour plots as a function of borate to sugar ratio and pH at 60 minutes for: (a) arabinose conversion, (b) ratio of ribose to ribulose selectivities (i.e., instantaneous selectivity of ribose), (c) ribose selectivity, (d) ribulose selectivity, (e) ribose yield, (f) ribulose yield. The response surface lies the within experimental error of all experimental points which are labeled with dots on the plot. Reactions were	

performed at a 100:1 sugar–metal molar ratio with a 5 wt% arabinose feed at 343 K in a stirred batch reactor, using Sn-Beta with a Si/Sn of 96.	81
Figure 16. Raman spectra for 5 wt% arabinose solutions with borate obtained at 298 K.	83
Figure 17. Madon-Boudart diffusion test at 343 K. Experiments were performed with 20 mg of Sn-Beta and a sufficient volume of 5 wt% arabinose to achieve a 2000 sugar–metal ratio in a stirred batch reactor.	85
Figure 18. Reaction order plot for initial rates at 343 K and 1000:1 sugar–metal with a 5 wt% arabinose 1:1 borate–arabinose solution at pH 7.21 in a stirred batch reactor. The catalyst used was Sn-Beta with a Si/Sn of 98.	85
Figure 19. Arrhenius plot for first order epimerization and isomerization reactions with 1000:1 sugar–metal. Epimerization reactions were performed with a 5 wt% arabinose 1:1 borate–arabinose feed at pH 7.21 in a stirred batch reactor using Sn-Beta with a Si/Sn of 98. Isomerization was performed unbuffered with 5 wt% arabinose.	86
Figure 20. Epimerization mechanism with retention of stereochemistry at C-3.	92
Figure 21. Competitive kinetic isotope study.	94
Figure 22. DFT based hypothetical structure of glucose-borate-tin complex featuring Sn-O-B-O-Si nanostructure and proximity measurements used to 'triangulate' the structure.	97
Figure 23. Carbon observed boron dephased distance measurements using singly labeled ¹³ C glucose 4:1 sodium tetraborate.	98
Figure 24. Boron observed carbon dephased distance measurements.	99
Figure 25. ¹³ C{ ¹¹⁹ Sn} REDOR ssNMR curves show that C-1, C-2 and C-3 are closest to the Sn site and that glucose adsorption is stronger with borate.	99
Figure 26. ¹³ C- ¹³ C RFDR ssNMR shows that C-1 and C-5 may be close together, which is consistent with the pyranose form of glucose.	100
Figure 27. ¹¹⁹ Sn NMR of borate adsorbed on Sn-Beta showing the appearance of two new resonances at -437 and -456 ppm.	100
Figure S1. Scanning electron microscopy image of enriched Sn-Beta illustrating crystal dimensions over which polarization must diffuse. Note the crystal size may be much smaller than the aggregates.	123
Figure S2. Scanning electron microscopy (SEM) images of natural abundance Sn-Beta showing zeolite crystal dimensions.	124
Figure S3. Powder X-ray diffraction patterns of Sn-Beta zeolites.	124
Figure S4. ¹¹⁹ Sn MAS NMR spectra (8.4 T) of ¹¹⁹ Sn-enriched Sn-Beta obtained without DNP (i.e., no microwaves and a sample temperature of 300 K) showing the zeolite remains dehydrated and the solvent/radical combination does not interfere with the Sn site (green) or it does interfere with the Sn site (red). All spectra shown were acquired using a 4 mm ZrO ₂ rotor (80 ul fill volume); experimental times varied between 48 and 96 hours.	126
Figure S5. ¹³ C DNP NMR data acquired at 212 MHz / 140 GHz on a glucose Sn-Beta zeolite with borate salt using 8 W of microwave power at 85 K. (a) ¹³ C{ ¹ H} microwave on and off spectrum using 10 mM TOTAPOL and DMSO/D ₂ O/H ₂ O glassing/cryoprotecting agent, (b) ¹³ C- ¹³ C Proton-Driven Spin Diffusion (PDS) correlation experiment acquired using 5 (rust) and 40 (green) ms of mixing and (c) enhancement results using 10 mM of bTbk or TOTAPOL in various glassing agents.	127

Figure S6. 3-D structural representations and dimensions of the biradicals used in this study. The atoms are colored in the following manner: blue for nitrogen, red for oxygen, yellow for sulfur, grey for carbon, and white for hydrogen.	128
Figure S7. Powder X-Ray diffraction patterns for calcined catalysts	134
Figure S8. Powder X-Ray diffraction patterns for heat treated Sn-Beta catalyst	135
Figure S9. Diffuse reflectance ultraviolet spectra.....	136
Figure S10. ¹¹⁹ Sn MAS NMR of heat treated SnBeta catalysts	136
Figure S11. Calculated ΔN vs. pyridine ¹⁵ N chemical shift shows a linear trend. The dashed line is placed as a guide for the reader.	137
Figure S12. ¹⁵ N metal---pyridine bound spectra at $\omega_r/2\pi = 5$ kHz shows chemical shifts assigned to framework metal sites (high frequency 260-280 ppm) and Brønsted protons (low frequency ~210 ppm).	138
Figure S13. Structures of active site models with adsorbed pyridine.....	140
Figure S14. Calculated NMR parameters and Mulliken charge on the pyridine	141
Figure S15. Solution NMR spectra for D-glucose with a 4:1 sugar:SB molar ratio in H ₂ O. a) ¹³ C NMR of D-(1- ¹³ C)glucose, b) ¹³ C NMR of D-glucose, c) ¹¹ B NMR, d) ¹ H NMR.....	143
Figure S16. Solution NMR spectra for D-fructose with a 4:1 sugar:SB molar ratio in H ₂ O. a) ¹³ C NMR of D-(2- ¹³ C)fructose, b) ¹³ C NMR of D-fructose, c) ¹¹ B NMR, d) ¹ H NMR	144
Figure S17. Solution NMR spectra for D-mannose with a 4:1 sugar:SB molar ratio in H ₂ O. a) ¹³ C NMR of D-(2- ¹³ C)mannose, b) ¹³ C NMR of D-mannose, c) ¹¹ B NMR, d) ¹ H NMR	145
Figure S18. Solution NMR spectra for D-xylose with a 4:1 sugar:SB molar ratio in H ₂ O. a) ¹³ C NMR of D-(1- ¹³ C)xylose, b) ¹³ C NMR of D-xylose, c) ¹¹ B NMR, d) ¹ H NMR	146
Figure S19. Solution NMR spectra for D-xylulose with a 4:1 sugar:SB molar ratio in H ₂ O. a) ¹³ C NMR of D-xylose, b) ¹¹ B NMR, and c) ¹ H NMR.....	147
Figure S20. Solution NMR spectra for D-lyxose with a 4:1 sugar:SB molar ratio in H ₂ O. a) ¹³ C NMR of D-lyxose, b) ¹¹ B NMR, and c) ¹ H NMR.....	148
Figure S21. Solution NMR spectra for D-arabinose with a 4:1 sugar:SB molar ratio in H ₂ O. a) ¹³ C NMR of D-arabinose, b) ¹¹ B NMR, and c) ¹ H NMR	149
Figure S22. Solution NMR spectra for D-ribulose with a 4:1 sugar:SB molar ratio in H ₂ O. a) ¹³ C NMR of D-ribulose, b) ¹¹ B NMR, and c) ¹ H NMR.....	150
Figure S23. Solution NMR spectra for D-ribose with a 4:1 sugar:SB molar ratio in H ₂ O. a) ¹³ C NMR of D-ribose, b) ¹¹ B NMR, and c) ¹ H NMR.....	151
Figure S24. HPLC chromatograph of a 5 wt% D-(1- ¹³ C)glucose solution with a 4:1 glucose:SB molar ratio, reacted at 358 K for 60 min. The peaks correspond to a) glucose, b) mannose, c) fructose, and d) internal standard. The dotted line around peak b represents the fraction collected by fractionation and analyzed by ¹ H and ¹³ C NMR (see Figure S32).	152
Figure S25. Solution NMR spectra of the product fraction obtained by HPLC from a 5 wt% D-(1- ¹³ C)glucose solution with a 4:1 glucose:SB molar ratio, reacted at 358K for 60 min (see dotted line in Figure S31). a) ¹³ C NMR and b) ¹ H NMR.....	153
Figure S26. XPS spectra for Sn 3d and C 1s. a) calcined Sn-Beta; b) Sn-Beta with adsorbed glucose; c) Sn-Beta with adsorbed potassium borate; and d) Sn-Beta with adsorbed glucose and potassium borate. Potassium borate instead of sodium borate was used in these measurements to avoid obfuscation of the	

Sn 3d signal by the sodium $KL_{23}L_{23}$ Auger signal. The Sn 3d signals for calcined Sn-Beta were located at 487.2 eV and 495.6 eV, which is consistent with tetrahedral coordination of Sn in the framework. The presence of glucose lowered the binding energy by ~ 0.3 eV, while the presence of either borate or a glucose/borate mixture decreased the binding energy by ~ 0.9 eV. The observed downward shift in binding energy signifies a change in the electronic environment of the Sn surface sites that has been attributed to adsorbed species or a possible structural modification.¹³⁷ For these samples, the C 1s signal is at a higher binding energy than the adventitious carbon signal. These data suggest the presence of the glucose-borate complex on the surface of the catalyst..... 154

Figure S27. Powder X-ray diffraction pattern of Sn-Beta. 155

Figure S28. UV-Vis diffuse reflectance of Sn-Beta. 155

Figure S29. SEM image of Sn-Beta zeolite. 156

Figure S30. Powder X-ray diffraction pattern of Ti-Beta. 156

Figure S31. Powder X-ray diffraction patterns of Sn-MFI. 156

Figure S32. UV-Vis diffuse reflectance of Sn-MFI. 157

Figure S33. Powder X-ray diffraction pattern of Sn-MCM-41..... 157

Figure S34. Isomerization and epimerization equilibrium calculated based on Tewari⁹⁹ 162

Figure S35. XRD of Sn-Beta 162

Figure S36. Diffuse-reflectance ultraviolet spectra of Sn-Beta 163

Figure S37. ^{119}Sn NMR of Sn-Beta 163

Figure S38. Ribose HPLC fraction used for polarimetry 164

Figure S39. Sugar borate complexation 165

Figure S40. Factorial design for isomerization of arabinose to ribulose. Reactions were performed at a 100:1 sugar:metal molar ratio with a 5 wt% arabinose feed at 343 K in a stirred batch reactor using Sn-Beta with a Si/Sn of 96..... 167

Figure S41. Contour plots as a function of borate to sugar ratio and sodium to borate ratio at 60 minutes for: a) arabinose conversion, b) ratio of ribose to ribulose selectivities (i.e., instantaneous selectivity of ribose), c) ribose selectivity, d) ribulose selectivity, e) ribose yield, f) ribulose yield. The response surface passes within experimental error of all experimental points which are labeled with dots on the plot. Reactions were performed at a 100:1 sugar:metal molar ratio with a 5 wt% arabinose feed at 343 K in a stirred batch reactor, using Sn-Beta with a Si/Sn of 96. 168

Figure S42. pH dependence on sodium to borate ratio measured at 298 K..... 169

Figure S43. ^{11}B NMR performed on 5 wt% arabinose solutions with borate at 298 K..... 170

Figure S44. Madon-Boudart test at 343 K Experiments were performed with 20 mg of catalyst and a sufficient volume of 5 wt% arabinose to achieve 2000 sugar:metal in a stirred batch reactor. 172

Figure S45. Reaction order plot for initial rates at 343 K and 1000:1 sugar:metal Reactions were performed with a 5 wt% arabinose feed in a stirred batch reactor using Sn-Beta with a Si/Sn of 98..... 173

Figure S46. Arrhenius plot for first order epimerization reaction with 1000:1 sugar:metal. Epimerization reactions were performed with a 5 wt% arabinose 1:1 borate:sugar feed at pH 7.21 in a stirred batch reactor using Sn-Beta with a Si/Sn of 98. Isomerization was performed unbuffered with 5 wt% arabinose. 174

Figure S47. ^{13}C NMR of L- $^{13}\text{C}_1$]arabinose with 5:1 sugar:borate at pH 7.09 in D_2O 174

Figure S48. ^{13}C NMR of L- $^{13}\text{C}_1$ Arabinose with 5:1 sugar:borate at pH 7.09 in D_2O after reaction with 100:1 sugar:Sn-Beta at 343 K for 60 minutes.	175
Figure S49. Arrhenius plot for first order isomerization reaction Reactions were performed at a 1000:1 sugar:metal molar ratio with a 5 wt% arabinose feed at 343 K in a stirred batch reactor using Sn-Beta with a Si/Sn of 98.	176
Figure S50. $[2-^{13}\text{C};2-^2\text{H}]$ glucose ^{13}C spectra	178
Figure S51. $[2-^{13}\text{C};2-^2\text{H}]$ glucose ^1H spectra	179
Figure S52. $[2-^{13}\text{C};2-^2\text{H}]$ glucose 4:1 sodium tetraborate with 100:1 Si-Beta at 85°C for 2 h glucose fraction ^{13}C spectra	179
Figure S53. $[2-^{13}\text{C};2-^2\text{H}]$ glucose 4:1 sodium tetraborate with 100:1 Si-Beta at 85°C for 2 h glucose fraction ^1H spectra	180
Figure S54. $[2-^{13}\text{C};2-^2\text{H}]$ glucose 4:1 sodium tetraborate with 100:1 Sn-Beta at 85°C for 2 h glucose fraction ^{13}C spectra	180
Figure S55. $[2-^{13}\text{C};2-^2\text{H}]$ glucose 4:1 sodium tetraborate with 100:1 Sn-Beta at 85°C for 2 h glucose fraction ^1H spectra	181
Figure S56. $[2-^{13}\text{C};2-^2\text{H}]$ glucose 4:1 sodium tetraborate with 100:1 Sn-Beta at 85°C for 2 h mannose fraction ^{13}C spectra	181
Figure S57. $[2-^{13}\text{C};2-^2\text{H}]$ glucose 4:1 sodium tetraborate with 100:1 Sn-Beta at 85°C for 2 h mannose fraction ^1H spectra	182
Figure S58. $[1-^{13}\text{C}]$ erythrose ^{13}C spectra	182
Figure S59. $[1-^{13}\text{C}]$ erythrose with 100:1 Sn-Beta at 50°C for 2 h ^{13}C spectra	183
Figure S60. $[1-^{13}\text{C}]$ erythrose 4:1 sodium tetraborate ^{13}C spectra	183
Figure S61. $[1-^{13}\text{C}]$ erythrose 4:1 sodium tetraborate with 100:1 Sn-Beta at 50°C for 2 h ^{13}C spectra	184
Figure S62. 3-deoxy-D-glucose 4:1 sodium tetraborate with 100:1 Sn-Beta at 85°C for 2 h mannose fraction HSQC spectra	184
Figure S63. 3-deoxy-D-glucose 4:1 sodium tetraborate with 100:1 Sn-Beta at 85°C for 2 h mannose fraction gCOSY spectra	185
Figure S64. 4-deoxy-D-glucose 4:1 sodium tetraborate with 100:1 Sn-Beta at 85°C for 2 h mannose fraction HSQC spectra	185
Figure S65. 4-deoxy-D-glucose 4:1 sodium tetraborate with 100:1 Sn-Beta at 85°C for 2 h mannose fraction gCOSY spectra	186

List of Tables

Table 1. The most important processes involving zeolites as catalysts ⁹	16
Table 2. Experimentally Determined Enhancements (ϵ) and Build-Up Times (T_B) for Hydrated, Isotopically-Enriched ^{119}Sn -Beta Samples Analyzed with 10 mM Nitroxide-Based Biradical Polarizing Agents (20 mM electrons in TCE)	26
Table 3. Enhancements and Build-Up Times of Dehydrated and Hydrated Sn-Beta Zeolites with 10 mM bCTbK in TCE	27
Table 4. Experimental values for ionization potential (I), electron affinity (A), Mulliken electronegativity and hardness taken from literature. ⁶²	42
Table 5. Calculated pyridine-metal (M-N) bond distances, metal-oxygen (M-O, M=O) bond distances, bond dissociation (D_0) and relaxation ($\Delta E_{M\text{ relax}}$) energies. B3LYP/Def2-TZVPD	45
Table 6. Results for the isomerization/epimerization of sugars.	55
Table 7. Results for the isomerization/epimerization of sugars.	59
Table 8. Full factorial design involving pH, borate to sugar ratio and reaction time as reaction variables for the epimerization of arabinose to ribose.....	77
Table 9. Control experiments for arabinose conversion in the presence of borates but in the absence of Sn-Beta. Reactions were performed with a 5 wt% arabinose feed at 343 K in a stirred batch reactor. ...	79
Table 10. Optical rotation measurement used to assess stereospecificity.	87
Table 11. Results from competitive kinetic isotope study using aldonitrile pentapropionate derivatives and GC-MS.	95
Table S1. Metal content calculated from ICP measurements and pore volumes of Sn-Beta samples. ...	125
Table S2. NMR parameters for the metal-beta zeolites	132
Table S3. Probe molecule adsorption frequencies on zeolites using IR spectroscopy	133
Table S4. Probe molecule adsorption frequencies on zeolites using IR spectroscopy	133
Table S5. Probe molecule adsorption frequencies on zeolites using IR spectroscopy	133
Table S6. Metal content in each solid material	135
Table S7. Surface area measurements	136
Table S8. Chemical shift anisotropy parameters for three samples shown above with span Ω and skew κ . The Sn-Beta samples appeared to contain two distinct sites 1 and 2.	139
Table S9. Time study for the epimerization of glucose with SB.....	158
Table S10. Time study for the epimerization of xylose with SB. Reactions were performed at 358 K with a 5 wt% sugar feed, using the corresponding amount of catalyst to maintain a 100:1 sugar:metal molar ratio.	158
Table S11. Time study for the epimerization of arabinose with SB.	158
Table S12. ^{11}B chemical shifts of borate esters taken from Bekkum et al. ⁷⁸ The values have been adjusted to the standard ^{11}B chemical reference.....	159
Table S13. ^{13}C chemical shifts of sugars. Note: ^1H NMR assignments can be found in the respective references.....	159
Table S14. Metal content in each solid material.	160
Table S15. Feed solutions for full factorial design involving pH, borate to sugar ratio and reaction time as reaction variables for the epimerization of arabinose to ribose.	166

Table S16. Summary of ^{11}B NMR chemical shifts.....	171
Table S17. Arrhenius kinetic data for epimerization and isomerization. Epimerization reactions were performed with a 5 wt% arabinose 1:1 borate:sugar feed at pH 7.21 in a stirred batch reactor using Sn-Beta with a Si/Sn of 98. Isomerization was performed unbuffered with 5 wt% arabinose.....	173
Table S18. Epimerization of L-arabinose with 1000:1 sugar:metal, performed with a 5 wt% arabinose 1:1 borate:arabinose feed at pH 7.21 in a stirred batch reactor using Sn-Beta with a Si/Sn of 98.	175
Table S19. Literature ^{13}C chemical shifts referenced to 0.5% DSS in D_2O under MAS.....	177

1 Introduction

The global economy depends on an uninterrupted supply of fuels and chemicals to manufacture medicines, fertilizers, pesticides, synthetic rubber, dyes, paint, lubricants, asphalt and many other needed products. Production of these chemicals often involves the oxidation of hydrocarbons to provide reactive functional groups. However, these processes are energy-intensive due to the high temperatures and pressures required to activate C-H bonds and also come at the cost of a partial loss of the energy content of the molecules. Catalysis provides a technology-based method to improve energy efficiency. For instance, the catalytic cracking of naphtha to olefin can generate energy savings of 10-20% compared to conventional steam cracking and titanium-substituted zeolite (TS-1) catalysts can convert propylene to propylene oxide using hydrogen peroxide with an energy reduction of 10-12%. These relatively small improvements when applied on a large scale can greatly reduce the use of energy in chemical processing. This is particularly significant given that the chemical industry is the largest industrial energy user, accounting for ~10% of final energy demand, and ninety percent of chemical processes use catalysts.¹

1.1 Oxygenates as an alternative feedstock

Oxygenates, molecules containing a high-oxygen content, have a lower energy density than pure hydrocarbons and provide a large scale renewable source of fixed carbon, which the U.S. Department of Energy estimates at 1.3 billion dry tons per year in the U.S.² These reserves have a defined cost structure and can serve as a buffer to swings in the petroleum markets. Through reduction, oxygenates can be converted to many petroleum-derived chemicals such as olefins and aromatics. This is important given the recent collapse of natural gas prices, which has led to the use of ethane as opposed to naphtha in steam crackers, resulting in almost preferential production of ethylene over propylene and aromatics.³ Other oxygenate products can serve as blending components to improve the performance and emissions of internal combustion engines.

Many oxygenates require deconstruction to enable a wide range of catalysis. Deconstruction of oxygenates can occur through a number of processes that result in carbonyl-containing compounds, such as aldoses, ketoses, and furfural derivatives from carbohydrate acid hydrolysis and carboxylic acids, aldehydes and ketones from biomass pyrolysis. The oxygen atoms present as carbonyl groups provide sites for extending the carbon backbone at low temperatures. Additionally, these reactive oxygen sites may be removed through dehydration and hydrogenation reactions to provide a final product. A major

challenge of this process is that the oxygen content leads to high boiling points and poor thermal stability, necessitating low temperature and liquid phase processing which represents a large departure from traditional thermal catalysis.⁴ Many of the early conversion processes rely on enzymatic catalysis and, more recently, a number of inorganic catalytic processes have been developed.² Compared to enzymes, inorganic catalysts can function over a wider range of reactant purities, temperatures and pH, which allows for cost effective process intensification. One class of catalysts that selectively activates carbonyl groups is the Lewis acids.

1.2 Lewis acids as catalysts

Lewis acid catalysis plays a critical role in organic synthesis and oxygenate conversion, particularly in reactions that require activation of carbonyl functionality. Lewis acids are broadly defined as electron pair acceptors, whereas Brønsted acids are molecules that can donate protons.⁵ Unlike Brønsted acids, Lewis acids are not susceptible to ion exchange, which is especially useful for processing oxygenated feedstock containing ionic impurities. In particular, Lewis acids bind to the carbonyl oxygen and withdraw electron density, thus making the carbonyl carbon more electrophilic and susceptible to attack by nucleophiles. Effective catalysis generally involves strong Lewis acid-Lewis base complexation while avoiding product inhibition.⁶ This is achieved through the interaction between the lowest unoccupied molecular orbital (LUMO) of the Lewis acid and the highest occupied molecular orbital (HOMO) of the Lewis base. As an extension of this concept and to explain deviations from electronegativity, Pearson⁷ later introduced the concept of hard and soft acid and bases (HSAB). Hard acids have a high charge density while soft acids have a small charge density and are very polarizable. According to the HSAB theory, hard acids prefer to bind hard bases and soft acids tend to bind soft bases.

Of the many common Lewis acids, the homogeneous catalyst AlCl_3 in particular can catalyze numerous industrial reactions,⁸ but there are limitations with this catalyst. Oftentimes, homogeneous catalysts are used stoichiometrically and dissociation of the product complex can destroy the Lewis acid. Solid acids can facilitate catalyst recovery because these heterogeneous catalysts are easy to separate from gas or liquid phase reactions. Additionally, reactions involving AlCl_3 must be performed under strictly anhydrous conditions since coordinated water leads to decreased catalytic activity and irreversible active site degradation due to unwanted side-formation of oxides.

1.3 Zeolite Catalysis

One important class of heterogeneous catalysis involves zeolites, which are nanoporous crystalline materials comprised of silicon and oxygen and are characterized by their high surface area and thermal stability. In order to add catalytic functionality, Lewis acid metal sites can be incorporated within the pores of zeolites. Two typical zeolite frameworks are the 12-membered ring Beta zeolite and the 10-membered ring MFI zeolite. In particular, Beta zeolites have a 3D intersecting pore structure with large 0.65-nm pores that facilitate small molecule transport to internal catalytic sites within the large surface area. An organic structure-directing agent (SDA) is oftentimes used to direct the formation of a particular zeolite framework. In general, it is difficult to make extra-large pore zeolites containing rings with more than 12 members. Ordered mesoporous silicas such as MCM-41 can have larger pores but are amorphous. Table 1 shows several important processes that utilize zeolite catalysts.

Table 1. The most important processes involving zeolites as catalysts⁹

Structural type (zeolite or zeotype)	Catalytic process
FAU (Y)	Fluid catalytic cracking, hydrocracking, aromatic alkylation and transalkylation, olefin/paraffin alkylation, NO _x reduction, acylation
BEA (Beta)	Benzene alkylation, acylation, Baeyer-Villiger reaction
MOR (Mordenite)	Light alkanes hydroisomerization, dewaxing (cracking), aromatic alkylation and transalkylation, olefin oligomerization
LTL (KL)	Alkane aromatization
MTW (ZSM-12)	Aromatic alkylation
MFI (ZSM-5, TS-1, Silicalite)	Fluid catalytic cracking, dewaxing (cracking), MTG/MTO gasoline/olefins, olefin cracking and oligomerization, benzene alkylation, xylene isomerization, toluene disproportionation and alkylation, aromatization, NO _x reduction, ammoxidation, Beckmann rearrangement
MWW (MCM-22)	Benzene alkylation
FER (Ferrierite)	<i>n</i> -Butene skeletal isomerization
TON (Theta-1, ZSM-22)	Dewaxing (long chain alkane hydroisomerisation), olefin skeletal isomerization
AEL (SAPO-11)	Dewaxing (long chain alkane hydroisomerization)
ERI (Erionite)	Selectoforming
CHA (SAPO-34)	MTO

Zeolite catalysis allows for exquisite shape and product selectivity due to the pores within, which can also minimize subsequent energy-intensive separation tasks. For example, zeolites can break the equilibrium product distribution such as in the selective production of *p*-xylene, which is used to make terephthalic acid for polyester fiber manufacturing.¹⁰ This is enabled by the precise pore size of a specific

catalyst that allows for selective diffusion and thus separation from a mixture of other xylenes. Furthermore, the confined geometry of zeolites can prevent the formation of large transition states and their associated reactions.

1.4 Hydrophobic Zeolites as Water-Tolerant Lewis Acids

Lewis acids are involved in many important C-C bond forming and hydride transfer reactions and typically require anhydrous conditions to prevent adsorption of water. Pure silica zeolites containing isolated metal atoms (e.g. tin, zirconium, and titanium) have recently emerged as a new class of water-tolerant Lewis acid catalysts.¹¹ These materials are salt-tolerant and very stable with greater than 10,000 turnovers per metal center, no leaching and activities comparable to enzymes.¹² The hydrophobic pores of these molecular sieves exclude bulk water similar to certain pockets within enzymes and the metal atoms function analogously to enzyme cofactors. In 2001, Corma et al. showed that Sn-substituted Beta zeolite synthesized under fluoride media was catalytically active in the Baeyer-Villiger oxidation of cyclic ketones under hydrated conditions.^{11c} Then in 2010, Moliner et al. showed that the same catalyst could convert glucose into fructose in the presence of bulk water through an intramolecular Meerwein-Ponndorf-Verley reaction.^{12b} The activity and selectivity of Sn-Beta approaches those of enzymes due in part to the uniform active sites. In these catalysts, Sn is bonded to electronegative silicon atoms and can act as a Lewis acid through the displacement or expansion to pentacoordinate or hexacoordinate structures.⁴ For catalysts containing transition metals, the highly dispersed tetrahedrally coordinated metal centers can accept electron pairs through empty d orbitals and expand their coordination shells.⁴ Finally, the addition of fluoride as a mineralizer in Sn-Beta zeolite production accounts for their defect-free structures, which leads to hydrophobicity and water tolerance. That is, bulk water cannot enter the hydrophobic pores, though gaseous water molecules can still diffuse through without drastically affecting the catalytic potential of the Lewis acid site due to the lack of hydrogen bonding interactions.

Historically, zeolite catalysis has been done in the gas phase at high temperatures, but the different design criteria for oxygenate-containing reactions requires working at low temperatures in the liquid phase.² Water-tolerant Lewis acids provide a solution for such large-scale reactions, while also avoiding waste associated with the use of homogeneous catalysts. Lewis acids catalyze many industrially relevant reactions and the ability to perform Lewis acid catalysis heterogeneously and in the presence of water holds great potential.

1.5 Zeolite Modification and Cooperative Catalysis

Zeolites may be modified by the incorporation of promoters—chemical components that enhance the reactivity of the active site—to enable cooperative catalysis and to tune the product distribution. For example, incorporation of a phosphorous promoter to ZSM-5 can select for olefins over aromatics in fluid catalytic cracking, toluene alkylation and methanol to hydrocarbon conversion and can improve hydrothermal stability.¹³ Cooperative catalysis involves two reactive sites in close proximity. In terms of Sn-Beta, the key to its unique catalytic activity is the ability to hydrolyze one of the four metal-O-Si bonds of the framework that are normally intact to form an open site with dual Lewis acid/base character. This dual character is a result of electron density from an incoming Lewis base being distributed over four Sn-O anti-bonding orbitals, giving the neighboring oxygen atoms basic character and these catalysts their unique activity. In contrast, most Lewis acids absorb electron density into the metal atom itself.

One way to modify the properties of the Sn active site in the hydrophobic zeolite is through the incorporation of a sodium tetraborate promoter. Borate is known to interact with cis-diols such as those present in sugar molecules to shift equilibrium distribution. Similar to sulfated zirconia, borate can also interact with catalysts to form borated zirconia, titania and stannia. Additionally, borate can interact with silica surfaces such as SBA-15.¹⁴ Given that boron has a single-bond radius of 0.85 Å compared to 1.16 Å for Si, borate may fit in the Sn-Beta open site in a manner analogous to complexation with cis-diols.¹⁵ As such, borate can promote stronger complexation by enabling reactants to bind to multiple sites (chelation) and alter the geometry of reactant adsorption, potentially leading to different reaction pathways. These promoter-incorporated materials in general may function as biomimetic catalysts due to the multiple sites present in close proximity. Promoter addition may also impose strains on bonds and therefore promote reactivity.

The ability of boron to expand its coordination shell from trivalent to tetravalent allows it to temporarily form and break bonds to the reactant and catalyst active site. Boron has three valence electrons ($2s^2 2p^1$) which can form a trigonal planar sp^2 hybrid, such as $B(OH)_3$. This structure is stabilized by electron donation from the filled oxygen p_z orbitals to the unfilled $2p_z$ orbital on the boron through the π -bonding framework. However, in this structure, boron is electron deficient (6 shared electrons, unsatisfied octet) and therefore acts as a Lewis acid. Addition of an electron donor to this structure leads to a negatively charged tetrahedral anion with sp^3 hybridization. Borate is known to catalyze Aldol reactions through

tight 6-membered transition states and can also undergo addition with itself to form rigid structures that potentially facilitate more complex reactions.¹⁶

In the borate-promoted Sn-Beta catalyst, boron, silicon and Sn are positioned at the metal-nonmetal boundary and are known to be active in C-C bond forming reactions, which are important in catalysis. They also have increasing electronegativity in the order Sn<Si<B, suggesting that the incorporation of borate may improve the Lewis acidity of the metal active site. Thus, these elements are natural choices for a catalyst and promoter pair.¹⁷ Since the first use of borate-promoted Sn-Beta, a number of other studies have shown the promotional effects of exchanging ions into Sn-Beta zeolites.¹⁸

1.6 Methods to Characterize Active Sites within Zeolites

Within the crystalline framework of the zeolite, atomically dispersed metal sites are tetrahedrally coordinated under dehydrated conditions, but adopt a pseudo-octahedral geometry upon the adsorption of two water molecules. By contrast, extraframework metal oxide species form an octahedral geometry and display very different catalytic activity.¹⁹ Due to their location within the zeolite pores, these materials are not amenable to surface characterization spectroscopic techniques. Consequently, solid-state nuclear magnetic resonance (ssNMR) of samples enriched with ¹¹⁹Sn isotopes are the only reliable methods to verify framework incorporation. In the literature, framework incorporation has mostly been inferred from indirect reactivity data or from qualitative infrared (IR) or diffuse reflectance ultraviolet (DR-UV) spectra. These spectroscopic methods provide additional insight into the nature of active sites and have been used to obtain the site densities needed to calculate turnover frequencies. However, many of these methods are difficult to implement reliably.²⁰ For instance, diffuse reflectance ultraviolet spectroscopy (DRUV)^{19, 21}, x-ray diffraction^{19, 22}, ¹¹⁹Sn Mossbauer spectroscopy^{21b}, x-ray photoelectron spectroscopy (XPS)^{21a}, Raman spectroscopy²¹, and synchrotron based techniques²² provide only qualitative or semi-quantitative measurements.

In solution-state NMR, Brownian motion averages out the orientation effects on local chemical environments, which does not occur in the solid state. In ssNMR, magic angle spinning (MAS) mimics the molecular motion in liquids and averages out the dipolar interaction. Additionally, excitation of ¹H followed by cross polarization (CP) magnetization transfer to ¹³C or other heavy atoms can improve the signal and provide information on chemical structure, though the intensities are not quantitative.

Rotational-echo double-resonance (REDOR) NMR is a ssNMR-based technique that measures the proximity of isolated spin pairs, typically up to 6 Å. In its most basic sense, REDOR involves siphoning off spin polarization on the observed nucleus into the dephased nucleus and measuring the decreased intensity of the observed nucleus. In REDOR, synchronizing a pulse sequence with rotor rotation can selectively reintroduce the dipolar interaction between nuclei under MAS. This allows for the transfer of spin polarization from the observed nuclei to neighboring atoms and the resultant dipolar interaction is inversely proportional to the cube of the distance between the nuclei. For isolated spin pairs, it is possible to fit accurate distances that can be used to infer the structure of an active site complex such as glucose-borate-Sn.

1.7 Focus of this Dissertation

This project seeks to understand the synthesis and properties of isolated Lewis acid sites inside water-tolerant hydrophobic zeolites for tailoring reactivity in heterogeneous catalysis. The production of these advanced catalytic materials with molecular control over the placement of single and multicomponent active sites allows for highly selective chemical transformations. The broad objectives of this thesis are three-fold. We sought to synthesize water-tolerant hydrophobic zeolites and to apply solid-state NMR for characterizing the nature of the Lewis acid sites. Having developed methods to characterize framework incorporation and Lewis acidity, we aimed to modify the catalytic properties of these zeolites and enable cooperative catalysis through the incorporation of promoters.

A major focus of this research has been to distinguish framework and extraframework metal sites within zeolites using ssNMR-based methods. To address the low intrinsic sensitivity of NMR, a dynamic nuclear polarization NMR (DNP NMR) method enabling natural abundance ^{119}Sn spectra of Sn-Beta zeolites was developed. Since some metals are not amenable to NMR characterization, a second method using the indirect probe molecule ^{15}N pyridine was developed that allows quantification of the strength and concentration of acid sites within zeolites. Pyridine ^{15}N NMR was applied to many metal-substituted zeolites, including Sn-Beta.

The next three chapters are motivated by the second goal - to devise catalytic strategies to understand the mechanistic and kinetic behavior of Lewis acid centers and exploit the benefits of cooperative catalysis by rational design of catalytic pairs. The particular system studied was the borate-promoted Sn-Beta catalyzed epimerization of aldoses. It was discovered early on that the addition of a borate

promoter shifted a reaction from a hydride transfer to an unusual 1,2 C-C carbon shift. This was found using isotopic labeling experiments and NMR. As a follow up, I conducted a parametric screen of key reaction parameters, which suggested the importance of a pH-dependent glucose-borate-Sn complex. The study also focused on intrinsic kinetics in the context of L-arabinose to L-ribose. Since then, I have conducted a detailed study of the reaction mechanism. Experiments confirmed the Sn-borate catalytic pair forms a stable nanostructure that may have applications in other reactions. Solid-state NMR proved to be the method of choice for determining the structure of the active site complex.

Concluding remarks and future directions are addressed in Chapter 7. This project involved synthesis of numerous substituted zeolites and detailed catalyst characterization. This work also required the synthesis of metal-substituted zeolites and led to the first ever synthesis of Hf-Beta using hydrothermal methods.

2 Dynamic nuclear polarization NMR enables the analysis of Sn-Beta zeolite prepared with natural abundance ^{119}Sn precursors¹

2.1 Abstract

The catalytic activity of tin-containing zeolites, such as Sn-Beta, is critically dependent on the successful incorporation of the tin metal center into the zeolite framework. However, synchrotron-based techniques or solid-state nuclear magnetic resonance (ssNMR) of samples enriched with ^{119}Sn isotopes are the only reliable methods to verify framework incorporation. This work demonstrates, for the first time, the use of dynamic nuclear polarization (DNP) NMR for characterizing zeolites containing ~2 wt % of natural abundance Sn without the need for ^{119}Sn isotopic enrichment. The biradicals TOTAPOL, bTbK, bCTbK, and SPIROPOL functioned effectively as polarizing sources, and the solvent enabled proper transfer of spin polarization from the radical's unpaired electrons to the target nuclei. Using bCTbK led to an enhancement (ϵ) of 75, allowing the characterization of natural-abundance ^{119}Sn -Beta with excellent signal-to-noise ratios in <24 h. Without DNP, no ^{119}Sn resonances were detected after 10 days of continuous analysis.

2.2 Introduction

Pure-silica zeolites containing a small amount of tetravalent heteroatoms with open coordination sites (e.g., Sn, Zr, or Ti) have emerged as highly active, water-tolerant solid Lewis acids for many important reactions.⁴ Tin-containing zeolites have been shown to promote the intermolecular Meerwein–Ponndorf–Verley (MPV) reaction between alcohols and ketones as well as the Baeyer–Villiger oxidation of cyclic ketones.^{11c, 23} Sn-Beta transforms hexoses, pentoses, and trioses through intramolecular hydride and carbon-atom shifts in both organic and aqueous media.^{12b, 24}

The catalytic activity and water tolerance of Sn-Beta critically depend on three factors: the successful incorporation of the metal center into the zeolite framework, the presence of a defect-free pore structure that promotes a hydrophobic environment, and the hydrolysis of one Sn–O–Si bond to form an “open site” with a neighboring silanol group. These site requirements are essential to catalyze many

¹ This chapter is adapted from Gunther, W. R.; Michaelis, V. K.; Caporini, M. A.; Griffin, R. G.; Román-Leshkov, Y., Dynamic nuclear polarization NMR enables the analysis of Sn-Beta zeolite prepared with natural abundance ^{119}Sn precursors. *J. Am. Chem. Soc.* **2014**, *136*, 6219-6222.

industrially relevant reactions.^{19, 25} Synthesizing the zeolite in fluoride media affords defect-free pores and minimizes extra framework species but also limits the maximum amount of heteroatom incorporation and slows down crystallization when compared to other methods.^{23a}

For this reason, Sn-Beta is usually synthesized with Si/Sn ratios >100 (i.e., <1.9 wt % Sn) and crystallization times >20 days. Recently, other methods, including solid-state ion exchange, seeding, and grafting, have emerged as faster synthesis routes, but framework incorporation has been inferred mostly from indirect reactivity data or from qualitative infrared (IR) or diffuse reflectance ultraviolet (DR-UV) spectra.²⁶

Although framework Sn incorporation can be quantitatively verified with ¹¹⁹Sn (I = 1/2, natural abundance = 8.6%) magic angle spinning (MAS) NMR, the coupled effects of low natural abundance of the ¹¹⁹Sn isotope, low intrinsic NMR sensitivity, and low Sn loadings in the sample make NMR analysis impractical without ¹¹⁹Sn isotopic enrichment.²⁷ Unfortunately, the high cost of isotopic enrichment drastically hinders high-throughput screening, routine analysis, or analysis of low-yield syntheses with NMR. DNP addresses these challenges by transferring the larger polarization of electron spins, such as those found in stable exogenous radical compounds, to nuclear spins through irradiation with high-frequency microwaves. The target nuclei then become dynamically polarized, and their NMR signals are enhanced by orders of magnitude. DNP has been a valuable tool for studying local and medium range structure in challenging biological and inorganic materials,²⁸ including SnO₂ nanoparticles,²⁹ by drastically reducing acquisition times.

Here, we demonstrate DNP NMR characterization of zeolites containing ~2 wt % of natural abundance ¹¹⁹Sn. Our approach, using indirect polarization, is exemplified in Figure 1. First, high-power microwaves irradiate the sample treated with an exogenous biradical and a glassing agent (i.e., 1,1,2,2-tetrachloroethane, [TCE]). Next, the electron polarization is transferred from the radical to the protons in the solvent through electron–nuclear dipolar couplings. Freezing the sample at cryogenic temperatures (100 K) allows for ¹H–¹H spin diffusion to occur efficiently and enables the relay of polarization to the solvent molecules present inside the zeolite pores. Lastly, by using appropriate contact times (ranging from 1 to 8 ms), ¹H polarization can be effectively transferred to the Sn sites using a cross-polarization (CP) step. Enhancements of $\epsilon > 35$ ($\epsilon^\dagger > 100$, accounting for the gain in Boltzmann levels when acquiring the data at 100 vs 300 K) are achieved with nitroxide-based biradicals,

thus enabling the characterization of nonenriched Sn-Beta zeolites with superb signal-to-noise ratios (S/N) in <24 h.

2.3 Results and Discussion

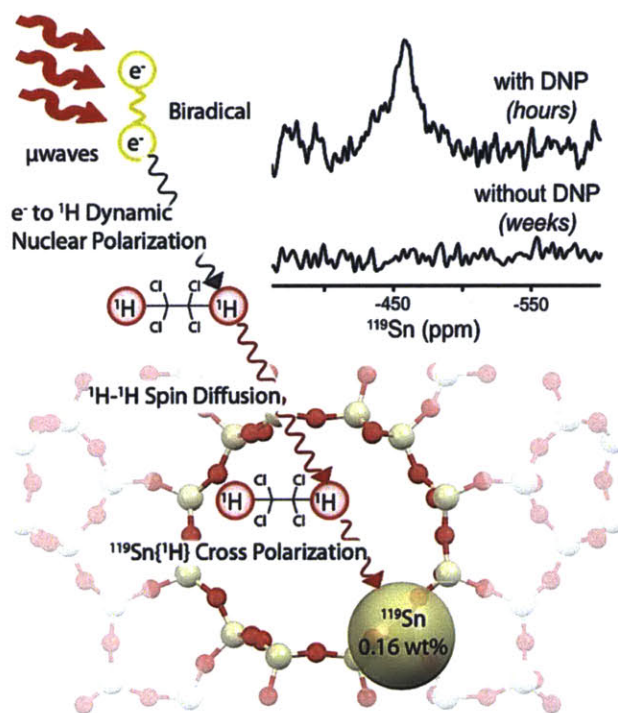


Figure 1. Hyperpolarization of Sn-Beta Zeolite Using Dynamic Nuclear Polarization

The DNP method was first optimized using enriched ^{119}Sn -Beta samples (Si/Sn = 102, 82% ^{119}Sn enrichment). Figure 2 shows the ^{119}Sn DNP NMR resonances for a hydrated and dehydrated ^{119}Sn -Beta calcined sample using bis-cyclohexyl-TEMPO-bisketal (bCTbK) as the radical and TCE as the solvent. In agreement with literature reports, dehydrated Sn-Beta (Figure 2a) features resonances corresponding to tetrahedrally coordinated framework Sn sites in the closed (-443 ppm) and open (-420 ppm) configurations.^{11c, 30} Under hydrated conditions the Sn site complexes with two water molecules leading to a pseudo-octahedral geometry and corresponding resonances centered at -700 ppm (Figure 2b). The ^1H detected enhancements were 36 and 52 for the dehydrated and hydrated ^{119}Sn -Beta materials. These enhancements led to spectra with high S/N ratios in <2 h using 25 μL of sample. For comparison, a typical MAS NMR experiment without DNP requires 58 h of acquisition time at 300 K and using 80 μL of sample to obtain comparable S/N ratios (see Figure 2c).

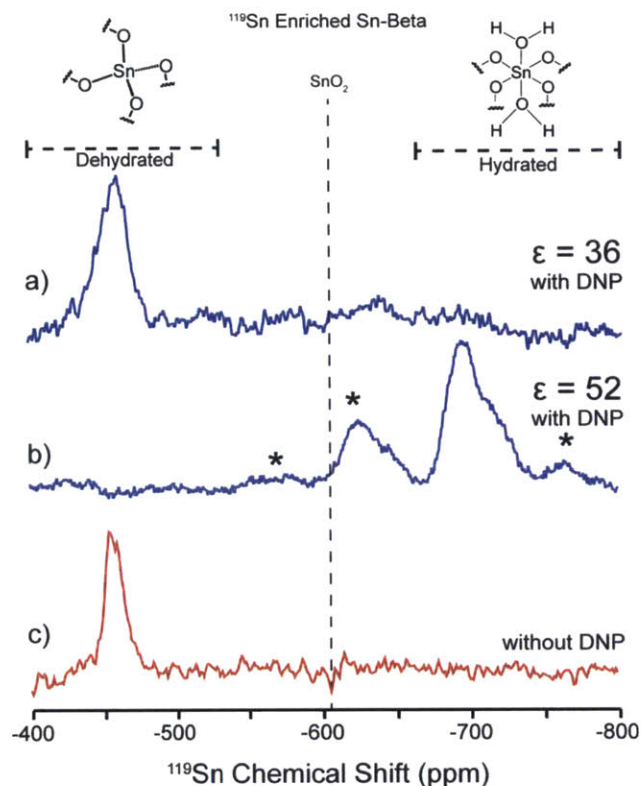


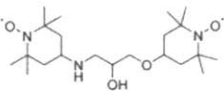
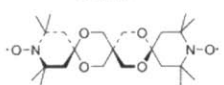
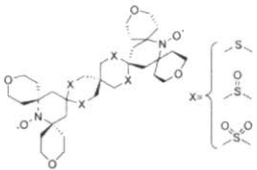

Figure 2. DNP-enhanced ^{119}Sn spectra of dehydrated (a) and hydrated (b) enriched ^{119}Sn -Beta zeolite. Spectra were acquired at 100 K for 3.8 h. ^{119}Sn MAS NMR spectrum of ^{119}Sn enriched dehydrated Sn-Beta zeolite (c) was acquired at 300 K for 58 h. * denotes spinning sidebands.

The strong Lewis acid sites in Sn-Beta readily coordinate with functional groups containing lone pairs of electrons. To determine and minimize potential undesirable interactions of the radical with the Lewis acid center, four biradical polarizing agents with varying kinetic diameters were impregnated on the Sn-Beta sample (Table 2).

The corresponding ^{119}Sn MAS NMR spectra showed that the radicals 1-(TEMPO-4-oxy)-3-(TEMPO-4-amino)propan-2-ol (TOTAPOL) and bis-TEMPO-bis-ketal (bTbK) entered the zeolite pores and complexed with the Sn sites, leading to multiple resonances in the range of -600 to -800 ppm. Conversely, the radicals bis-TEMPO-bis-thioketal-tetra-tetrahydropyran (SPIROPOL) and bCTbK did not affect the resonances of the dehydrated Sn site (Figure S4). We hypothesize that SPIROPOL and bCTbK are too bulky (Table 2) to enter the pores of zeolite Beta (ring pores of $7.7 \times 6.6 \text{ \AA}$ and $5.6 \times 5.6 \text{ \AA}$) and thereby rely exclusively on the protons in the solvent to transfer polarization to internal sites. Note that even

after prolonged exposure (>48 h, 298 K) of both bCTbK and SPIROPOL with the zeolite, no adsorption on the Sn site was detected.

Table 2. Experimentally Determined Enhancements (ϵ) and Build-Up Times (T_B) for Hydrated, Isotopically-Enriched ^{119}Sn -Beta Samples Analyzed with 10 mM Nitroxide-Based Biradical Polarizing Agents (20 mM electrons in TCE)

Polarizing Agent	ϵ	T_B (s)
TOTAPOL ¹⁴ 	9 (1)	3.55
bTbK ¹⁵ 	25 (3)	2.90
SPIROPOL ¹⁶ * 	32 (3)	4.77
bCTbK ¹⁷ 	52 (3)	3.4

*The NMR magnetic field was swept ~ 50 kHz to the left-edge of the maximum SPIROPOL enhancement.³¹

Although both small radicals interacted with the Sn site, they still provided a gain in sensitivity. As shown in Table 2, enhancements of 9 and 25, were observed for TOTAPOL and bTbK, respectively. The sterically hindered SPIROPOL and bCTbK proved to be optimal polarizing agents, offering consistent enhancements >30 at 100 K in TCE. Ultimately, bCTbK was chosen for subsequent studies because it generated slightly better enhancements and shorter build-up times, allowing for faster recycling during acquisition. Note that bCTbK ^1H enhancements range from 28 to 75 depending on the sample (see Table 3), which we attribute to the glass-forming behavior of the solvent.

Table 3. Enhancements and Build-Up Times of Dehydrated and Hydrated Sn-Beta Zeolites with 10 mM bCTbK in TCE

Sn site	T_B (sec)	ϵ	$\epsilon \dagger$
dehydrated (^{119}Sn - enriched)	2.7	36	108
hydrated (^{119}Sn enriched)	3.4	52	156
dehydrated/hydrated (^{119}Sn - enriched)	3.2	36	108
dehydrated (^{119}Sn natural abundance)	5.5	75	225
hydrated (^{119}Sn natural abundance)	4.2	28	84

Although control experiments in the absence of radical showed that the TCE solvent does not interfere with the dehydrated Sn signal, neat TCE is not an ideal glass-forming medium as is the case for glycerol/water or DMSO/water mixtures. For this reason, TCE is typically doped with a small percentage of another solvent (e.g., methanol or ethanol) to assist in the glass-forming process.³² Although the use of TCE dopants or glycerol/water or DMSO/water mixtures was avoided in this study to prevent interaction with the Sn site, appropriate glass formation at low temperatures is a critical parameter to enhance transfer polarization processes.³³ For instance, drastically different enhancements for ^{13}C DNP NMR spectra of glucose bound to Sn-Beta were obtained when performing DNP with 10 mM TOTAPOL dissolved in either TCE, DMSO/water or glycerol/water (Figure S5). TCE generated an enhancement of 3, whereas DMSO/water and glycerol/water generated enhancements of 70 and 100, respectively. Further studies are currently underway to better understand solvent-radical-zeolite interactions.

The use of ^1H - ^1H spin diffusion to polarize crystalline materials in an organic medium was first demonstrated by van der Wel et al. for amyloidgenic peptide cores (dimension, $\sim 0.2 \times 0.2 \times 1 \mu\text{m}$).³⁴ Similar approaches have been used in other chemical systems, including amorphous silica frameworks, wherein the large abundance of intrinsic protons within the matrix governs the ^1H nuclear spin-diffusion across the sample.³⁵ In contrast, dehydrated Sn-Beta zeolite crystals (dimensions, $\sim 0.45 \times 7 \times 7 \mu\text{m}$ based on Figure S) are severely proton deficient, thus limiting intrinsic ^1H spin-diffusion.

Indeed, a polarization gradient can evoke differences in the polarization transfer between the solvent and the crystalline solid system. These effects are mainly dependent on the width of the smallest dimension of the crystal, the nuclear T_1 , and the nuclear spin diffusion.³⁴ The extremely long contact times required during analysis (i.e., 6–8 ms) indicate that a considerable distance exists between the Sn site and the nearest proton. Since the radical is confined to the external surface of the zeolite, the solvent provides the sole medium for ^1H spin diffusion and is therefore responsible for the observed

DNP enhancements.³⁶ The physical barrier between the internal Sn sites and the radical minimizes paramagnetic broadening, while the protonated solvent allows for effective ^1H - ^{119}Sn dipolar couplings for polarization transfer. Importantly, since the ^1H - ^{119}Sn CP transfer efficiency depends on the local proton density, collected spectra can only provide qualitative estimates of Sn resonance intensities.

Tin features a significant shell of electron density, making its inherent chemical shift very sensitive to the local environment. Resolution is very sensitive to the degree of crystallinity, site dynamics, and surrounding environment. Cryogenic temperatures and the TCE solvent impart additional broadening, as evidenced by the spectra of the hydrated samples wherein the isotropic chemical shift is heterogeneously broadened. The spinning side bands result from a larger chemical shift anisotropy generated by the bound water molecules. Thus, although cross-polarization of ^1H to ^{119}Sn is more efficient in the hydrated state, broader isotropic resonance and larger chemical shift anisotropy (CSA) are observed when compared to the dehydrated state due to complex interaction of the TCE solvent and pseudo-octahedral Sn geometry.

Optimized DNP conditions were implemented on the analysis of natural abundance Sn-Beta samples. Figure 3 shows ^{119}Sn resonances for a natural abundance sample (Si/Sn = 89) in both hydrated and dehydrated states. Both spectra were acquired in <24 h using a rotor with a 25 μL fill volume. The natural abundance hydrated and dehydrated Sn-Beta DNP enhancements were 28 and 75, respectively (Figure 3a,b). In stark contrast, a regular MAS NMR experiment performed on the dehydrated sample using a rotor with a 80 μL fill volume showed no evidence of ^{119}Sn resonances after 246 h of continuous analysis (see Figure 3c). These data demonstrate that DNP enables the analysis of Sn-Beta zeolite without ^{119}Sn isotopic enrichment. Table 3 summarizes the enhancements obtained with 10 mM bCTbK in TCE for different Sn-Beta samples. Water molecules increase the proximity of protons to the Sn site, thereby improving CP efficiency. As a result, the effective contact times for ^{119}Sn CP varied drastically between the dehydrated ($\tau_c = 6\text{--}8$ ms) and hydrated ($\tau_c = 2\text{--}3$ ms) sites.^{26d}

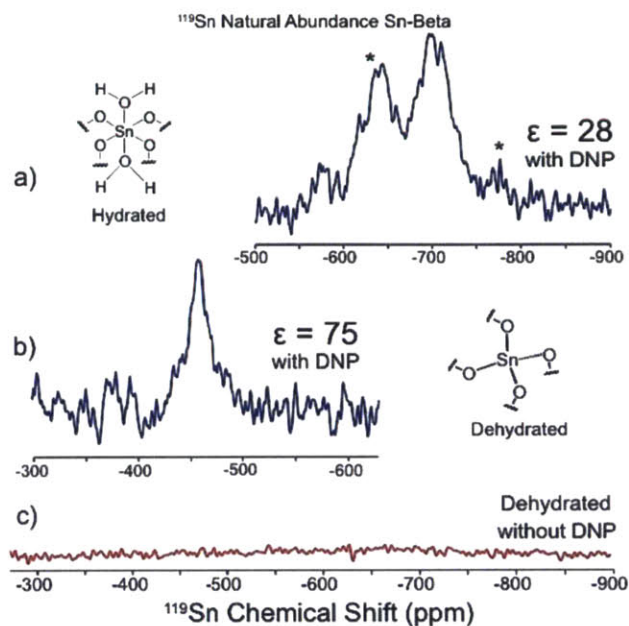


Figure 3. DNP-enhanced ^{119}Sn spectra of hydrated (a) and dehydrated (b) natural abundance Sn-Beta zeolite. Spectra were acquired at 100 K for 18 and 21 h, respectively. ^{119}Sn MAS NMR spectrum of natural abundant dehydrated Sn-Beta zeolite was acquired at 300 K for 246 h. * denotes spinning sidebands.

In conclusion, indirect DNP of ^{119}Sn allows the observation of NMR signals from natural abundance Sn atoms in microporous materials without the need for isotopic enrichment. This technique reduces acquisition times more than ~ 2 orders of magnitude, allowing for a difficult analysis to be completed in a matter of hours. The framework incorporation of Sn in porous materials can be readily studied using appropriate radical/solvent combinations; specifically, we show that the radicals bCTbK or SPIROPOL generate extraordinary gains in sensitivity without interacting directly with intrapore Sn sites. Optimizing methods to resolve local environments of the tetrahedral sites is one of our current objectives. With the development of high-frequency, high-power microwave sources and advances in cryogenic MAS probes,³⁷ DNP NMR has emerged as the method of choice for chemical structure determination in extremely challenging systems.

3 Interrogating Lewis acid character of metal sites in Beta zeolites with ^{15}N pyridine MAS NMR

3.1 Abstract

Pyridine was adsorbed on framework metal sites in Beta zeolites and analyzed with magic-angle spinning nuclear magnetic resonance (MAS NMR). The ^{15}N chemical shift of adsorbed pyridine scales with the acid character of both Lewis (Ti, Hf, Zr, Nb, Ta and Sn) and Brønsted (B, Ga, and Al) acidic heteroatoms. The ^{15}N chemical shift showed a linear correlation with Mulliken electronegativity of the metal center in the order $\text{Ti} < \text{Hf} < \text{Zr} < \text{Nb} < \text{Ta} < \text{Sn} < \text{H}^+$. Theoretical calculations using density functional theory (DFT) showed a strong correlation between experimental ^{15}N chemical shift and the calculated metal-nitrogen bond dissociation energy, revealing the importance of active site reorganization when determining adsorption strength. The relationships found between ^{15}N pyridine chemical shift and intrinsic chemical descriptors of metal framework sites complement adsorption equilibrium data and provide a robust method to characterize, and ultimately optimize, metal-reactant binding and activation for Lewis acid zeolites. Using ^{15}N MAS NMR direct detection protocols for the Lewis acid-base adducts allowed the differentiation and quantification of framework metal sites in the presence of extraframework oxides, including highly quadrupolar nuclei.

3.2 Introduction

Pure-silica zeolites containing framework metal centers with open coordination sites have emerged as highly active, water tolerant solid Lewis acids. For example, framework metal centers, such as Ti, Hf, Zr, Nb, Ta and Sn, have shown remarkable activity for the inter- and intra-molecular Meerwein–Ponndorf–Verley (MPV) reduction of aldehydes and ketones,^{20, 38} the etherification of alcohols,^{20, 39} and the Baeyer–Villiger oxidation of ketones to lactones.⁴⁰ Sn-Beta has also been shown to promote various C-C coupling reactions.⁴¹ The nature of the metal center and the degree of framework incorporation drastically influence reactivity. For example, Bermejo-Deval and co-workers showed that octahedral extraframework SnO_2 and pseudo-tetrahedral framework Sn sites can catalyze the same reaction through completely different reaction pathways.¹⁹

Distinguishing framework and extraframework sites within the confines of a zeolite pore is critical for assessing catalyst performance. Though reactivity studies provide the most direct measure of

framework incorporation, catalysts often have a complex mixture of sites leading to an apparent overall activity. For example, in the isomerization of glucose to fructose with Sn-Beta, various authors have attributed the observed decrease in turnover frequency with increasing metal loading to the presence of framework Sn sites with different activities or the formation of condensed SnO_x species.^{21b, 26b} Spectroscopic methods provide additional insight into the nature of active sites and have been used to obtain the site densities needed to calculate turnover frequencies. However, many of these methods are difficult to implement reliably or routinely.²⁰ For instance, diffuse reflectance ultraviolet spectroscopy (DRUV)^{19, 21}, x-ray diffraction^{19, 22}, ¹¹⁹Sn Mossbauer spectroscopy^{21b}, x-ray photoelectron spectroscopy (XPS)^{21a}, Raman spectroscopy²¹, and synchrotron-based techniques²² provide only qualitative or semi-quantitative measurements. Magic-angle spinning nuclear magnetic resonance (MAS NMR) can quantify the ratio of extraframework to framework metal sites, but is limited to NMR-active nuclei. For instance, analysis of tin in Sn-Beta is accessible with NMR but requires expensive ¹¹⁹Sn isotopic labeling.^{20, 30} Roman-Leshkov *et al.* and Hermans *et al.* have recently shown that hyperpolarization techniques based on dynamic nuclear polarization (DNP) MAS NMR can be implemented to characterize non-enriched Sn-Beta samples, but specialized NMR equipment is required.^{21b, 42} Other metals of interest, including Ti, Zr and Hf, suffer from extreme challenges in NMR sensitivity that stem from low natural abundance, large quadrupolar moment and/or low gyromagnetic ratios (as shown in Table S2).⁴³

The adsorption of probe molecules has been an effective technique to interrogate acid sites in zeolites. Infrared (IR) spectroscopy using pyridine to titrate solid acid sites has been utilized to distinguish Lewis and Brønsted acid sites and provide quantitation with molar extinction coefficients.⁴⁴ IR spectra of pyridine adsorption on zeolites has been used to determine acid strength of several heteroatoms based on differences in vibrational frequencies.^{21a} The frequencies for pyridine adsorbed on different Lewis acid sites (*i.e.*, Ti, Zr, Nb, Ta, Sn, Ga and Al-Beta) appears in a very narrow range from 1445-1454 cm⁻¹ as shown in Table S3.^{21a, 45} Gorte *et al.* showed that careful dosing of acetonitrile onto a dehydrated Sn-Beta sample gives rise to vibrational signatures of the resulting adducts that differentiate framework from extraframework sites with adequate resolution.⁴⁶ As shown in Table S4, limited data exists on the full range of Lewis acidic metals. Corma *et al.* performed a number of cyclohexanone adsorption experiments that cover a wider range (shown in Table S5), but the resonance widths at half maximum of ~25 cm⁻¹ do not provide a high degree of resolution. We note that IR has limitations when analyzing samples in the presence of water or other solvents due to unwanted adsorption frequencies that can interfere with quantitative analysis.

NMR measures the electron shielding around a targeted nucleus, which can be used as a highly sensitive method to study changes that arise from the effects in local electron density and overall electronegativity induced by neighboring atoms. Consequently, the chemical shift of an acid-base adduct can be used to assess Lewis acid character by directly probing the local chemical environment of acid-base interactions, to understand bond activation at a specific site without bulk effects due to non-specific adsorption, and to infer optimal reactant binding strengths both under hydrated and dehydrated environments.⁴⁷ NMR has been used to characterize acidity of Lewis acid catalysts, for instance, by studying the interaction of trimethylphosphine (TMP), trimethylphosphine oxide (TMPO) and acetone with the active sites.⁴⁸ Similarly, ¹⁵N MAS NMR of adsorbed pyridine has been used to distinguish multiple acid sites on γ -alumina with high resolution. Although pyridine ¹⁵N MAS NMR has been used to probe the acidity of certain zeolites, the full range of Lewis acid metal-substituted zeolites has not been investigated with this method.⁴⁹

Here, we assess the acid character of Beta zeolites with Lewis (Ti, Hf, Zr, Nb, Ta and Sn) and Brønsted (B, Ga, and Al) acid centers by investigating the adsorption of pyridine with ¹⁵N MAS NMR. We rationalize that the interaction of pyridine with the metal site leads to a change in chemical shift of the ¹⁵N nucleus that can be correlated to fundamental measures of Lewis acidity, such as bond dissociation energies and Mulliken electronegativities. We show that the method is broadly applicable to investigate metal centers in zeolites under hydrated and dehydrated conditions. Using direct detection protocols, we show that quantitative measurements can be performed on the pyridine-metal adducts, thereby yielding the ability to differentiate and quantify the number of framework metal centers even for NMR-inactive nuclei.

3.3 Experimental Section

Detailed methods and protocols can be found in the supporting information.

Catalyst synthesis

Beta zeolites were synthesized based on the procedure reported by Corma *et al.*^{11c} using the following precursors: hafnium(IV) chloride, zirconium(IV) oxychloride octahydrate, tin(II) chloride dihydrate, titanium(IV) isopropoxide, tantalum(V) ethoxide, and niobium(V) ethoxide. Tin(II), which oxidizes to tin(IV) in water, was used in place of SnCl₄·5H₂O and resulted in Sn-Beta consistently free of

extraframework SnO₂.⁵⁰ Briefly, Hf-Beta was synthesized as follows: aqueous tetraethylammonium hydroxide [27.158 g; Sigma–Aldrich, 35 wt% (TEAOH)] and tetraethylorthosilicate (23.968 g; Sigma–Aldrich, 99 wt%) were added to a Teflon [polytetrafluoroethylene (PTFE)] dish, which was magnetically stirred at 250 rpm and room temperature for 90 min. Additional deionized water (15 mL) was added, and the dish was cooled in an ice bath. Then, hafnium(IV) chloride (0.3747 g; Sigma–Aldrich, 98 wt%) dissolved in ethanol (2 mL) was added drop wise while stirring. The solution was left uncovered on the stir plate for 10 h to reach a total mass of 33.147 g after evaporation of ethanol and some of the water. Next, aqueous hydrofluoric acid (2.620 g; Sigma–Aldrich, 48 wt%) was added drop wise using a plastic syringe, and the mixture was homogenized using a PTFE spatula, resulting in a thick gel. Si-Beta (0.364 g) was seeded into the mixture. The preparation of Si-Beta is analogous to Sn-Beta but without seeding or metal addition. The weight of the resulting sol–gel was evaporated under light heating to 33.956 g over ca. 2 h, resulting in a final molar composition of 1 SiO₂/0.01 HfCl₄/0.56 TEAOH/0.56 HF/7.5 H₂O. The thick paste was transferred to a PTFE-lined stainless steel autoclave (45 mL) and heated to 413 K for 20 days under static conditions. Mixing the contents weekly can accelerate crystallization. The solids were recovered by filtration, washed with ultrapure deionized H₂O, and dried at 373 K. The zeolites were calcined under flowing dry air by heating to 853 K with a 1 K min⁻¹ ramp (with 1 h isothermal steps at 423 and 623 K) and kept at that temperature for 10 h. After calcination, the overall inorganic oxide yield was 80–90%.

Sn-MCM-41 and Sn-MFI were synthesized according to previously published protocols.⁵¹ SnO₂/Si-Beta was prepared by incipient wetness impregnation of Si-Beta with an aqueous tin(IV) chloride solution, followed by drying at 383 K and calcination in air flow at 533 K. Mixed framework/extraframework ¹¹⁹Sn-Beta was made by calcination of the as-prepared material in a box furnace at 1173 K for 10 h with a 1 K min⁻¹ ramp and 1-hour stops at 423 and 623 K. The furnace was connected to a fume hood vent and filled with 100 mL/min of dry air. Analogous experiments showed negligible SnO₂ formation up to 1073 K and heating to 1273 K lead to pore blockages.

Catalyst characterization

Inductively coupled plasma atomic emission spectroscopy (ICP-AES) was recorded on an Optima 2000 DV spectrometer (PerkinElmer Inc.). Samples were dissolved in a few drops of 35% HF before dilution into 2.5% HNO₃. Powder x-ray diffraction (PXRD) patterns were collected using a Bruker D8 diffractometer using a CuK α radiation source between 5 and 45° 2 θ , in 0.02° steps with a step time of 30

s. Ultra-violet/visible (UV/Vis) analysis was performed using a Varian Cary 5000 UV/Vis near-infrared spectrometer equipped with a Praying Mantis diffuse reflectance accessory. The spectra were collected at 190–450 nm and referenced to BaSO₄. N₂ adsorption–desorption isotherms were measured on a Quantachrome Autosorb iQ apparatus at liquid-nitrogen temperature (77 K). All samples were degassed under vacuum prior to use (623 K, 12 h). Micropore volumes were analyzed by the t-plot method.

Pyridine adsorption

Sample preparation consisted of weighing 100 mg of the catalyst, sealing in a 5 mL microwave vial and connecting to a Schlenk line. The air within the sample was purged out by alternating three times between vacuum and Ar, followed by heating the sample to 150°C for 2 h under dynamic vacuum. Samples were pre-dried before pyridine adsorption to promote uniformity among the sites and prevent competitive adsorption. The sample vial was refilled with Ar and removed from the Schlenk line. Next, ¹⁵N-labeled pyridine adsorption was performed by flowing pyridine saturated Ar over the sample. Specifically, the vial containing the dried zeolite sample was connected with a cannula to another purged and septum-sealed vial containing ¹⁵N pyridine under Ar flow (~ 30 mL/min). A needle was inserted into the vial containing the zeolite to avoid pressure build-up. For weakly binding oxide samples, such as SnO₂-Beta and ZrO₂-Beta, as well as Si-Beta, the temperature was reduced from 150 to 100°C. After 30 min, the sample vial was isolated, reconnected to the Schlenk line and placed under vacuum for 1 hr to remove physisorbed pyridine. Afterwards, the sample was transferred into a glovebox where it was opened and packed into an o-ring sealed ZrO₂ NMR rotor. For experiments probing hydrated sites, the zeolite sample was exposed to ambient moisture after dosing with pyridine.

For quantitative runs, 10 mg of 98% ¹⁵N-labeled glycine (Cambridge Isotope Laboratories, Andover, MA) as an internal standard was weighed into a septum-sealed vial, dried at room temperature under vacuum and ground together with the catalyst using a glass stir rod before being packed into a rotor. For all pyridine quantitation experiments, zeolites were calcined under dry air before dosing to remove any contamination and avoid the creation of open sites from the hydrolysis of one of the Sn-O-Si bonds.

Nuclear magnetic resonance

MAS NMR experiments were performed on custom-designed spectrometers (courtesy of D. J. Ruben, Francis Bitter Magnet Laboratory, Massachusetts Institute of Technology) operating at 360 and 500 MHz (¹H Larmor frequency). The 360 MHz NMR spectrometer was equipped with either a double resonance

home-built (FBML-MIT) or a triple resonance Varian-Chemagnetics probe (Palo Alto, CA), which were doubly tuned to $^{119}\text{Sn}/^1\text{H}$. The 500 MHz NMR spectrometer was equipped with a triple resonance Varian-Chemagnetics probe (Palo Alto, CA) doubly tuned to $^{15}\text{N}/^1\text{H}$. Powdered samples were packed into either 3.2 mm (26 μl fill volume) or 4 mm (80 μl fill volume) outer diameter ZrO_2 rotors equipped with Vespel drive- and top-caps. Top-caps were equipped with rubber O-ring seals to inhibit water contamination of the sample (Revolution NMR, Fort Collins, CO). Dry samples were prepared by heating to 423 K under a 10 Pa vacuum and packing the NMR rotor in an Ar-filled glovebox.

^{15}N cross polarization (CP)⁵² MAS NMR spectra were acquired with a spinning frequency set to 9 kHz ($\omega_r/2\pi$) and regulated with a Bruker (Billerica, MA) MAS controller. The recycle delay was set to 1.5 seconds, 64k co-added transients were acquired and the temperature was maintained at 290 K. The spin-lock on ^{15}N during CP was optimized to match the Hartmann-Hahn condition⁵³ under MAS with $\gamma B_1/2\pi = 50$ kHz on protons during a contact time of 2.0 ms, which was maintained constant for all samples. Proton pulses and two pulse phase modulation (TPPM) decoupling⁵⁴ were optimized for $\gamma B_1/2\pi = 83$ kHz. All spectra were referenced externally to liquid ammonia (0 ppm NH_3). CP MAS NMR revealed the bound Brønsted sites and selectively probed bound pyridine molecules. ^{15}N chemical shielding anisotropy experiments were acquired using CP MAS NMR and a spinning frequency of 5 kHz (supporting information).

For quantitative purposes, ^{15}N MAS NMR analyses used direct detection (Bloch) and spin-lattice relaxation times (T_1) were measured using either an inversion recovery or saturation recovery experiment. Typical T_1 's were on the order of 200 to 800 ms for ^{15}N and recycle delays were chosen to be $5 \times T_1$ (or greater) for all NMR experiments. All spectra were acquired using a 9 kHz spinning frequency and between 16,384 and 32,764 co-added transients. Spectra were processed using 125 Hz of exponential apodization function. Spectra fitting of the pyridine and glycine resonances were performed using a single Lorentzian and the baseline with one sine function using least squares. All quantitative data were carefully fitted to account for the spinning side band intensity of the larger CSA of bound pyridine (span, $\Omega = 360$ ppm, skew, $\kappa = 0.8$) relative to the internal ^{15}N glycine ($\Omega = 15$ ppm, $\kappa = 0.05$) standard.

^{119}Sn MAS NMR spectra were acquired by performing a Hahn-echo (^{119}Sn , $\gamma B_1/2\pi = 50$ kHz) with recycle delays between 10 and 40 s, between 8,192 and 35,850 co-added transients, and a spinning frequency

of 8 kHz. Typical T_1 's were on the order of 2 to 8 s for ^{119}Sn and recycle delays were chosen to be $5 \times T_1$ of the slowest relaxing site. ^{119}Sn spectra were referenced externally using a secondary reference solid, SnO_2 (-604.3 ppm, relative to tetramethyltin, 0 ppm).

Quantum chemical calculations

Simulations were run on a Unix cluster implementing Gaussian G09 revision B.01.⁵⁵ A 17T model of the Beta zeolite T2 site was created from the International Zeolite Association (IZA) crystallographic structure and the outer atoms were frozen with hydrogens pointing in the direction of missing oxygen atoms for cluster termination. Hybrid density functional theory (DFT) geometry optimizations and energies were run at B3LYP/Def2-TZVPD level of theory⁵⁶ and counterpoise corrections were applied to remove basis set superposition error. All of the metal atoms except Ti used an effective core potential (ECP). The reported energy values represent the electronic contribution to enthalpy and were not adjusted for the thermal correction since the vibrational frequencies of the zeolite cluster may be non-physical. Additional data were gathered at B3LYP/Def2-TZVP and Def2-TZVPPD to demonstrate convergence. Detailed descriptions of the methods used appear in the supporting information.

3.4 Results and Discussion

The adsorption of pyridine onto metal-substituted zeolites will form adducts that feature specific ^{15}N chemical shifts. The ^{15}N chemical shifts of pyridine and pyridinium (protonated pyridine) are 318 and 212 ppm, respectively, yielding a 106 ppm chemical shift span that can be used to assess the acid character of specific pyridine-acid adducts. Note that pyridine adsorption on an acid site causes changes in the nitrogen chemical shift anisotropy (CSA) component, δ_t , which lies in the plane of and tangential to the pyridine ring. This component change appears as δ_{11} and δ_{22} in the chemical shift tensor for pyridine and pyridinium, respectively.⁵⁷ Consequently, after binding to an acid, the pyridine resonances will appear at lower frequency, which is opposite to the expected trend for the interaction between electron density-withdrawing sites and electron density-shielding nuclei (see Figure 4).

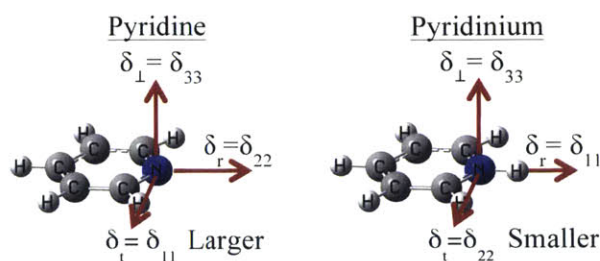


Figure 4. Rotation of CSA components into the pyridine radial δ_r , tangential δ_t , and perpendicular δ_{\perp} reference frame. The pyridine δ_t decreases upon binding to a proton or Lewis acid site, causing it to change from δ_{11} to δ_{22} in NMR nomenclature ($\delta_{33} \leq \delta_{22} \leq \delta_{11}$).

Figure 5 shows the ^{15}N chemical shift of pyridine adsorbed on a series of porous materials, including pure silica zeolites, metal-substituted and metal-impregnated zeolites, as well as mesoporous Sn-MCM-41. In the absence of framework metals, the defect-free Si-Beta showed no bands associated with pyridine, while Si-Beta containing extraframework Sn and Zr oxides showed very weak Lewis acidity, with the appearance of a ^{15}N resonance near 318 ppm. Taken together, these control experiments show that in the absence of framework metal sites, pyridine does not interact with a defect-free zeolite framework and that extra-framework heteroatoms feature ^{15}N chemical shifts on the far left extreme (high frequency side) of the chemical shift scale that correspond to weakly bound pyridine molecules. The ^{15}N pyridine chemical shifts resolve the Brønsted acids in the expected order of acid strength as follows: silanols < B-Beta < Ga-Beta < Al-Beta. The resonance at 288 ppm for weakly acidic silanols defines a lower limit of Brønsted acid strength. The fluoride synthesized Al-Beta showed a chemical shift of 212 ppm that is consistent with a fully protonated pyridine molecule, thus defining the upper limit of Brønsted acid strength in this scale.

In contrast to Brønsted acid sites, the interaction of pyridine with a Lewis acid site leads to a more diverse chemical shift range. This phenomenon can be rationalized from the Ramsey expression for NMR chemical shift by noting that the energy of the nitrogen sp^2 lone pair electron is located just below that of an anti-bonding π orbital associated with the pyridine ring.⁵⁸ Binding to a Lewis acid allows the nitrogen electron lone pair to enter a definite lower energy σ bond with each metal center, leading to larger transitions to the anti-bonding π orbital and, consequently, a smaller chemical shift component. The isotropic resonance is the average of the chemical shift components and a smaller chemical shift component moves the resonance to lower frequency (*i.e.*, closer to protonated pyridine). Interestingly,

the radial (δ_{22} in pyridine and δ_{11} in pyridinium) and perpendicular (δ_{33}) components of the chemical shift tensor are related exclusively to electronic transitions internal to the pyridine molecule. Since the lone pair is not involved in pyridine ring resonance and the pyridine geometry does not change drastically upon binding to a Lewis acid site, these chemical shift components are not significantly perturbed upon adsorption. Taken together, these features provide a robust and highly sensitive probe for assessing Lewis acid character.

For our samples, the ^{15}N pyridine chemical shift resolves the Lewis acid centers over a 20 ppm range, with the following order: $\text{Ti} < \text{Hf} < \text{Zr} < \text{Nb} < \text{Ta} < \text{Sn}$. Among the different Sn-containing structures, Sn-Beta shows the highest frequency Lewis acid character with a ^{15}N chemical shift of 260 ppm. Two overlapping ^{15}N pyridine resonances are observed for most materials, which we hypothesize correspond to the open and closed sites in analogy with the two ^{119}Sn resonances observed in the ^{119}Sn NMR spectrum of dehydrated samples for tetrahedrally-coordinated Sn atoms.^{20, 30} Sn-MFI and the mesoporous Sn-MCM-41 have similar Sn resonances centering at 262 ppm as well as a resonance near 285 ppm consistent with the presence of silanol groups in the framework. In an earlier work, Van der Waal *et al.* mention that, as a hard Lewis acid, Ti prefers hard Lewis bases such as oxygen over pyridine (a Lewis base with intermediate hardness).⁵⁹ Based on this, the authors suggest that pyridine would deprotonate a Brønsted acidic silanol group rather than coordinate directly to the Lewis acid site. However, the chemical shift of pyridine on Ti-Beta (281 ppm) is distinct from Si-Beta with defect sites (288 ppm) indicating that the data presented here does not agree with this conclusion. The chemical shift of ^{15}N pyridine adsorbed on framework Sn (ca. 263 ppm) is drastically different from that adsorbed on extraframework SnO_2 (319 ppm) and, similarly, the chemical shift of ^{15}N pyridine adsorbed on framework Zr (275 ppm) differs from that adsorbed on extraframework ZrO_2 (318 ppm). Hf and Zr have similar resonances because Hf appears below Zr in the periodic table and the elements have similar covalent atomic radii due to the Lanthanide contraction (*i.e.*, 1.50 Å vs. 1.48 Å). Nb and Ta show intermediate ^{15}N chemical shifts of 274 and 268 ppm, respectively. These metals are active in many of the same reactions as Hf, Zr and Sn and offer a higher charge to radius ratio. Tin- and tantalum-containing samples also exhibited small resonances associated with strong Brønsted acidity near 210 ppm. For tantalum, this effect may result from an inductive effect of the =O group similar to that observed in sulfated zirconia. These NMR trends are in agreement with prior work investigating probe molecule adsorption on zeolites with IR spectroscopy (*vide supra*).

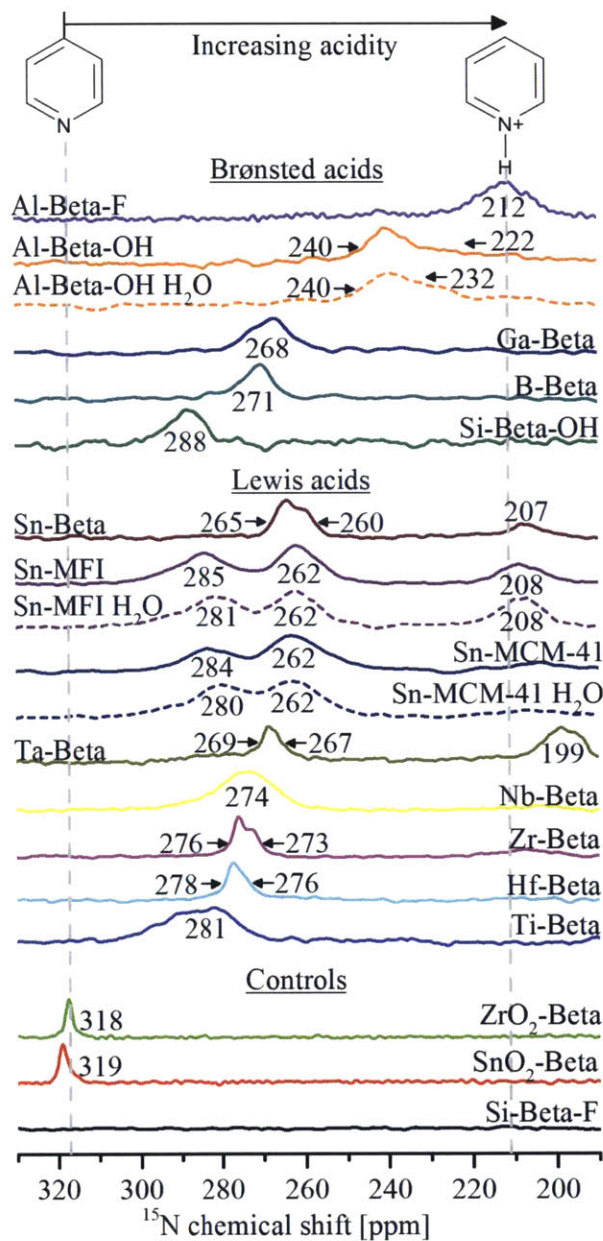


Figure 5. ^{15}N CP MAS NMR of pyridine adsorbed on metal-substituted zeolites. Spinning sidebands appear outside the field of view. Dashed lines correspond to spectra of hydrated samples. H-Al-Beta-F had a Si/Al=50, H-Al-Beta-OH had a Si/Al=19 and all other materials had Si/Metal \approx 100.

In order to understand the catalytic behavior of Lewis acid sites in the presence of water, additional MAS NMR experiments were performed to study the substituted Beta zeolites under hydrated conditions. We anticipate that water will interact strongly with the metal site in the hydrophilic materials but weaker in the hydrophobic materials, thereby influencing hydrogen bond networks near the active site.⁶⁰ For the fluoride-synthesized zeolites, the results of pyridine adsorption are

indistinguishable for dehydrated and hydrated samples, thus showing that the ^{15}N chemical shift data generated under dehydrated conditions may be applicable to hydrophobic materials under hydrated conditions. Extended silanol nests in hydrophilic materials can stabilize hydrogen bond networks and promote the presence of water in the pores. This effect can be observed from the slight changes in chemical shift for the hydroxide-synthesized and mesoporous materials that feature defect sites and terminal hydroxyl groups. As shown in Figure 5, a slight shift to lower frequency (high field shift) in the leftmost ^{15}N resonance is observed for the Sn-MFI and Sn-MCM-41 samples, which is consistent with a displacement of pyridine from the weakest sites with water.

The resonance width and chemical shift tensor provide information on the modes of complexation between pyridine and the metal center and numerical analysis of the spinning sideband pattern provides additional structural information.⁶¹ The wide resonances observed for Ti-Beta correspond to a high degree of flexibility for the pyridine-Ti adduct geometry. Slow spinning experiments to study the chemical shift anisotropy (CSA) are shown in Figure S12. Sn and Zr showed nearly identical patterns consistent with a similar orientation of the chemical shift tensor. Additionally, a hydrated Sn-Beta showed the rise of a disordered structure between 210 and 215 ppm, which we attribute to pyridine co-adsorbed with water on a metal center that acquires a Brønsted acid character.

Assessing Lewis acidity

The use of chemical shift to assess Lewis acidity enables us to establish correlations with fundamental measures of Lewis acidity. There have been many attempts to find a fundamental parameter that quantifies Lewis acidity, which has proven to be particularly difficult for solids. The simplest and most widely used measure is the binding strength of a basic molecule onto an acid site. The most fundamental description for this interaction is represented by Fukui functions that describe the electron density in a frontier orbital resulting from a small change in the total number of electrons. These functions can be used to determine degree of electrophilicity of active sites. Pearson *et al.* showed that the Mulliken electronegativity (χ) and the hardness (η), analogous to the first and second derivatives of energy with respect to number of electrons, respectively, can be used to measure Lewis acidity with more accuracy.⁶² Applying a finite difference approximation for the first derivative and three-point finite difference approximation for the second derivative leads to operational definitions in terms of ionization potential (I) and electron affinity (A) as follows:

$$\chi = -\mu = -\left(\frac{\partial E}{\partial N}\right)_V = \frac{1}{2}(I + A) \quad (1)$$

$$\eta = \frac{1}{2}\left(\frac{\partial^2 E}{\partial N^2}\right)_V = \frac{1}{2}(I - A) \quad (2)$$

Where μ is electronic chemical potential, E is the energy, N is the number of electrons, and V is the potential. As such, the Mulliken electronegativity can be interpreted as a finite difference approximation of the electronic energy with respect to the number of electrons, which provides a measure of how strongly a Lewis acid site can polarize a reactant.

Hard-soft acid base theory (HSAB) uses chemical hardness to describe deviations from a pure electronegativity analysis. Indeed, such deviations exclude the possibility of establishing a universal scale for all Lewis acid–base interactions. The HSAB theory suggests that hard acids prefer to bind with hard bases and soft acids prefer to bind with soft bases. When the difference between the highest occupied molecular orbital (HOMO) of the donor and lowest unoccupied molecular orbital (LUMO) of acceptor is large, charge control involving electrostatic interactions is dominant and hard-hard interactions are favored while, for smaller differences, frontier-orbitals at the outer edge of a molecule are dominant. In the numerical version of HSAB, the difference in electronegativity drives the electron transfer and the sum of the hardness parameters acts as a resistance leading to an overall charge transfer of ΔN where C refers to the Lewis acid and B to the base. HSAB however does not take into account the shapes and phases of the participating orbitals, says little about hard-soft complexes, and fails to explain variations in the strength of bonds.

$$\Delta N = \frac{\chi_C - \chi_B}{2(\eta_C + \eta_B)} \quad (3)$$

Several different measures of Lewis acidity have been proposed including LUMO energy, electronegativity, degree of electron transfer and strength of interaction between the acid-base pair. Corma *et al.* proposed using the LUMO energy of a mixed oxide as a measure of Lewis acidity; however the authors noted that this comparison only holds for Lewis acid sites of the same central atom, in the same valence state, and with the same coordination number.⁸ LUMO energies are difficult to obtain experimentally but correlate linearly with electron affinity.⁶³ Similarly, the HOMO energies correlate with ionization potential and the HOMO-LUMO gap is important to determine the extent of interaction between an acid base pair. The values of the relevant parameters describing Lewis acid character for different metals are summarized in Table 4.

Table 4. Experimental values for ionization potential (I), electron affinity (A), Mulliken electronegativity and hardness taken from literature.⁶²

	Ionization potential, I [kJ/mol]	Electron affinity, A [kJ/mol]	Mulliken electronegativity, χ [kJ/mol]	Hardness, η [kJ/mol]
Pyridine	900	-60	420	500
Ti	658	8	333	325
Hf	650	80	370	300
Zr	660	41	351	310
Nb	670	100	400	300
Ta	761	31	397	366
Sn	708	121	410	294
B	800	27	414	387
Ga	600	30	310	280
Al	578	44	312	267
Si	786	134	460	326
H+	1310	72	693	620
Proportional to	HOMO	LUMO	HOMO+LUMO	HOMO-LUMO

As shown in Figure 6, electron affinity and Mulliken electronegativity show a linear correlation with the experimentally determined ¹⁵N chemical shift values (averaged from the resonances of open and closed sites). Furthermore, using the proton electronegativity for Al-Beta-F shows that the linear trend extends over the entire chemical shift range spanned by Lewis and Brønsted acid sites. The observed ¹⁵N pyridine trend is noteworthy because it captures the interaction of pyridine with metal centers featuring significantly different electronic states. We note that different coordination environments often lead to different chemical shifts, especially for polarizable metal atoms. Also, nitrogen is directly bound to the metal and the lack of chemical shielding effects not directly related to the metal's ability to function as a Lewis acid points to a more fundamental association. We posit that the linear correlation between the ¹⁵N chemical shift and Mulliken electronegativity occurs because of the correspondence between the HOMO-LUMO energy gap and the ionization energy-electron affinity energy gap. The former appears in the Ramsey expression of chemical shift and the latter in the definition of Mulliken electronegativity. The correlation is facilitated by the similar M-O-Si coordination environment. The partial electron transfer (ΔN) calculated according to equation 3 does not improve the trend (see Figure S11), suggesting that the hard-soft nature of the system does not significantly perturb the chemical shift.

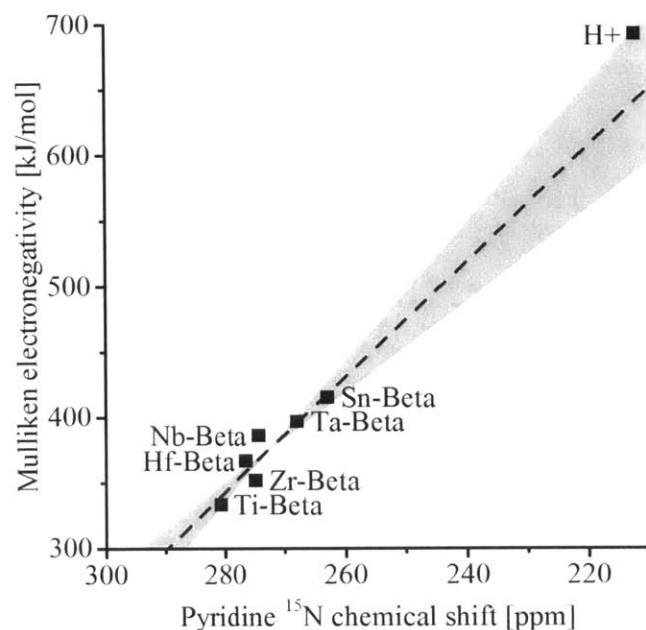


Figure 6. Experimental Mulliken electronegativity vs. pyridine ^{15}N MAS NMR chemical shift. The chemical shift shown is un-weighted average of the chemical shifts associated with open and closed sites. The dashed line and grey envelope show a regression with standard errors.

Quantum chemical calculations

The strength of interaction between the acid-base pair is proportional to orbital overlap and inversely proportional to its HOMO-LUMO energy difference. Adsorption isotherms at multiple temperatures or calorimetry can provide experimental measures of pyridine binding strength; however, these techniques have technical challenges and competing effects are difficult to separate. Evidently, covalent bonding in an acid-base pair is a function of many parameters other than the degree of electron transfer. Quantum chemical calculations are ideal to determine the metal-nitrogen bond dissociation energies and the energetics associated with active site reorganization.

Specifically, density functional theory (DFT) provides fundamental insight into the structure and bonding of the catalyst substrate complex such as bond distances and charge distributions in order to support the use of chemical shift as a proxy to evaluate Lewis acidity. DFT includes the effects of orbital overlap and provides a deeper understanding of HOMO-LUMO interactions than the electronegativity-based charge transfer model discussed earlier. Determining the pyridine dissociation energy and geometric distortion energy of the metal site can address the possibility that reactant activation can differ from adsorption enthalpy due to geometric changes induced by the flexibility of the metal in the framework.

Additionally, NMR calculations allow comparisons of calculated chemical shielding components with experimental data to validate the model and verify pyridine complexation on specific metal sites. Consistency between the two sets of data facilitates assignment of resonances and the absence of multiple pyridine binding.

To this end, we developed a 17 tetrahedral site model that incorporates both geometric constraints and local distortion of the crystal lattice. Specifically, the model fixes the outer atoms at specific crystallographic locations, but allows the inner five tetrahedral sites with their associated oxygen atoms to relax (see Figure S13). Heteroatom substitutions were confined to the T2 site of a Beta zeolite, in accordance with prior studies suggesting the preferential substitution of Sn into this site.⁶⁴ Nb and Ta exist in a +5 oxidation state and were modeled with a M=O functional group. We note that the present study did not model the preferential substitution of small B, Al and Ga atoms, which may localize to other sites. Simulations starting with two pyridines resulted in one of the two moving away from the metal site; consequently, the cluster models included only a single pyridine molecule bound to a single metal center.

The model for Sn-Beta was extended by one shell of oxygen atoms (see Figure S13) in order to allow relaxation of both shells of Si atoms near the Sn center. For group IV and V transition metal elements, the LUMO is the unfilled dz^2 orbital, which is less sensitive to the coordination geometry. In contrast, the LUMO of Sn is a linear combination of the 4 Sn-O π^* orbitals, making bonding very sensitive to coordination geometry. Sn delocalizes electron density from an incoming base to its four adjacent framework oxygen atoms, lengthening and polarizing its bonds in the process and resulting in a distortion of the crystal lattice. Even without substrate binding, X-ray adsorption spectroscopy (XAS) data on Sn-Beta had previously shown distortion of the Beta lattice to at least two Si atoms away from the Sn site.²²

Table 5. Calculated pyridine-metal (M-N) bond distances, metal-oxygen (M-O, M=O) bond distances, bond dissociation (D_0) and relaxation ($\Delta E_{M \text{ relax}}$) energies. B3LYP/Def2-TZVPD

Catalyst	M-N [Å]	M-O [Å]	M=O [Å]	D_0 [kJ/mol]	$\Delta E_{M \text{ relax}}$ [kJ/mol]
Ti-Beta	2.67	1.79	n.a.	21	24
Hf-Beta	2.58	1.94	n.a.	60	32
Zr-Beta	2.61	1.94	n.a.	53	29
Nb-Beta	2.44	1.91	1.73	91	45
Ta-Beta	2.41	1.92	1.76	105	59
Sn-Beta*	2.39	1.93	n.a.	105	69

*denotes an extended model

+ DFT methods used: B3LYP/Def2-TZVPD

Table 5 shows the results of the geometry optimization for several Lewis acid zeolites. There is a strong correlation between the dative covalent bond length and bond dissociation energy for all six substituted zeolites, which suggests that a 30 kJ/mol increase in adsorption energy brings the nitrogen 0.1 Å closer to the metal site. As shown in Figure 7, the metal-N bond dissociation energies show a strong correlation with experimental ^{15}N chemical shift values, indicating consistency between the two Lewis acidity scales. The good fit presumably results from error cancellation associated with adsorption energy as an energy difference. In Figure 7, Sn appears 23% off the trend line, likely because of limited flexibility of the cluster model combined with not accounting for expansion of the zeolite unit cell. Hf also showed a 16% difference from the trend line likely due to the presence of f-electrons, which can lead to stronger sigma bonding.⁶⁵

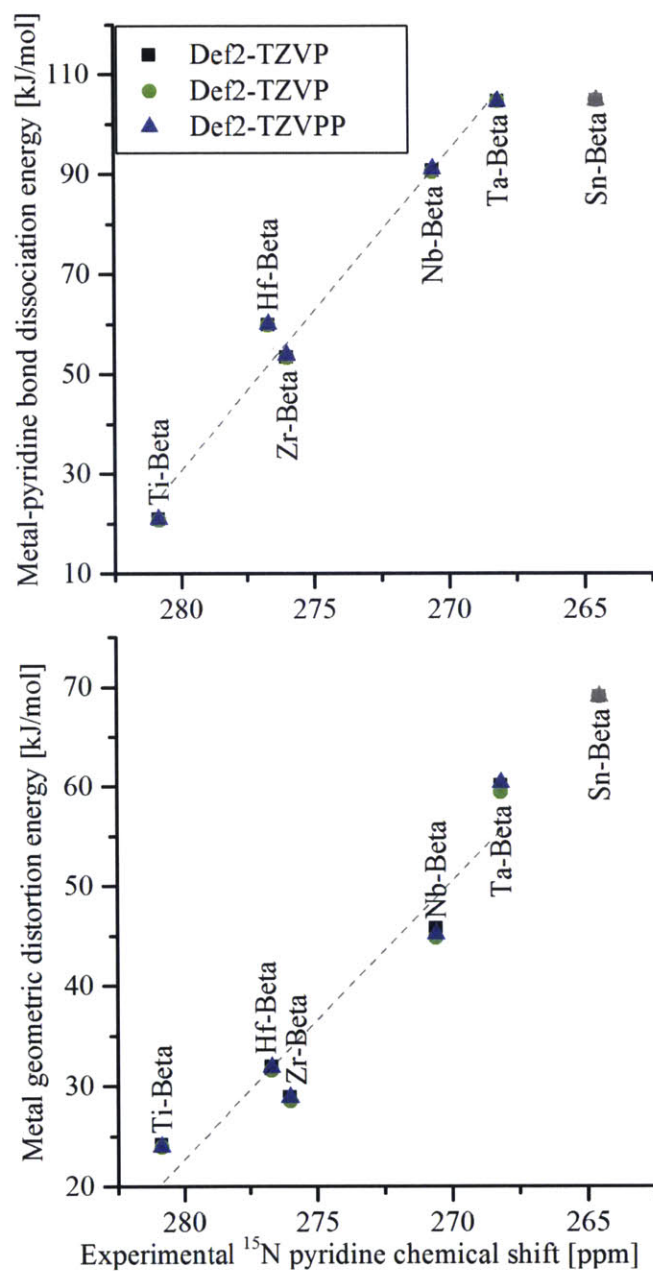


Figure 7. Distortion and dissociation energetics associated with pyridine adsorption calculated with DFT.

Allowing the metal site to return to its most stable state without pyridine resulted in a geometric distortion energy analogous to those reported by Bell *et al.*^{60a} The calculated geometric distortion energies also correlate with chemical shift. Relaxation of the metal site can recover a portion of the metal pyridine dissociation energy and the sum of the dissociation energy and the geometric distortion energy provides an estimate of the adsorption energy. The trend resembles a plot for catalyst active site distortion energy vs heteroatom radii,^{60a} potentially due to the near linear trend of chemical shift with

metal-N bond length. This may correlate to the atomic radii and polarizability discussed by Bell *et al.*^{60a} As an additional correlation illustrating Lewis acidity, pyridine Mulliken charges are plotted in Figure S14 and show increasing charge transfer to the metal cluster with increasing Lewis acidity. Def2-TZVP and Def2-TZVPP calculations trend better than Def2-TZVPD likely resulting from the greater basis set balance without diffuse functions.

As shown in Figure S14, NMR calculations on the structures showed the expected correlation between calculated chemical shielding and experimental chemical shift, suggesting the model involving a single pyridine bound directly to the metal center adequately represents the system. The simulations also showed that stronger Lewis acids had smaller chemical shift anisotropies resulting from movements of the δ_{33} chemical shift component, which is consistent with the description of the pyridine system put forth at the beginning of the discussion section. Chemical shift anisotropy contains directionally dependent information and the similar pattern suggests a similar complex structure, a requirement to function as an effective probe of Lewis acidity.

The systems of interest have a number of computational challenges, including the presence of inorganic and organic groups, high valence heavy metal atoms with relativistic corrections, aromatic bonds within the pyridine and diffuse lone pairs. These challenges are addressed in more detail in the supporting information section. We note that the largest source of error is the finite cluster size. Owing to the computational complexity of modeling an entire zeolite pore, the model neglected the effects of non-specific physisorption. Typically, physisorption resulting from van der Waals forces involves an enthalpy change as high as 40 kJ/mol. Corma *et al.* showed a 60 kJ/mol adsorption energy for toluene adsorption on fluoride synthesized Si-Beta.^{11b} Application of the dispersion-corrected ω B97X-D functional on the Sn 17T cluster model increased the binding energy by approximately 30 kJ/mol. These differences should not affect the trends between the different substituted Beta zeolites but would result in an offset when using small molecules such as pyridine and glycine to relate calculated and experimental values. A larger periodic model might better address expansion of the Beta unit cell and the potential for double Sn substitutions.

Quantifying framework sites

Direct detection methodologies using ^{15}N glycine as an internal standard were used to indirectly quantify the framework metal sites in ^{119}Sn -Beta and Zr-Beta zeolites. A linear correlation was observed between

the amount of adsorbed pyridine and framework tin content (calculated from ^{119}Sn MAS NMR data and ICP analyses) for samples with Si/Sn molar ratios ranging from ca. 100 to 350 (see Figure 8). This correlation effectively translates into a calibration curve to determine framework content of any metal. To demonstrate the applicability of the method to quantify framework atoms even in the presence of extraframework species, a pristine ^{119}Sn -Beta samples (Si/Sn = 115) was subjected to a heat treatment to convert framework tin species into extraframework SnO_2 clusters. Specifically, treating the sample at 1253 K for 10 h in dry air converted 14% of the framework atoms into extraframework species. Nitrogen adsorption data confirmed that the structure (i.e., crystallinity and micropore volume) of the zeolite structure remained intact after heat treatment (see Table S7). The ^{15}N pyridine MAS NMR quantification method effectively captured the change in framework content. Importantly, this method is general and can be applied to quantify metal centers that cannot be easily analyzed with NMR. As shown in Figure 8, the Zr content of various Zr-Beta samples could be quantified. We note that a recent infrared spectroscopy study suggested that pyridine can only access 62% of Sn sites, which contrasts the near quantitative adsorption values observed for our samples.⁶⁶ We hypothesize that the difference in dosing temperatures between both studies (423 vs 323 K) impacts the diffusion and adsorption events within the entirety of the zeolite crystal.⁶⁶

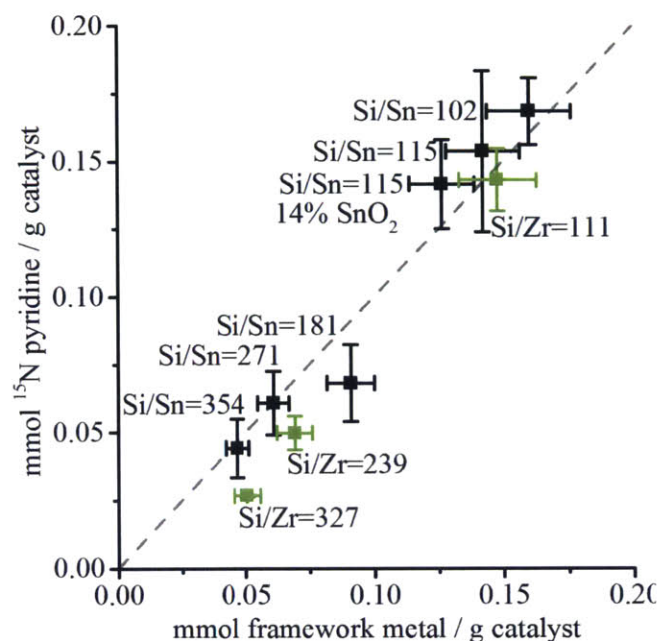


Figure 8. Quantification of adsorbed pyridine using ^{15}N MAS NMR. The dotted line represents a parity line. The Y-error bars are based on the signal-to-noise of each spectra; each experimental data point was analyzed in triplicate and the error bars represent two times the sample standard deviation. X-error bars represent the range of errors (ca. 10%) typically obtained during elemental analysis, including zeolite dissolution and ICP characterization.

3.5 Conclusion

A ^{15}N MAS NMR-based method is presented for assessing the strength and number of framework metal sites using pyridine as a probe molecule. MAS NMR analysis of the ^{15}N chemical shift of adsorbed pyridine on metal-substituted zeolites (e.g., Sn, Ti, Zr, Hf, Nb, Ta, B, Ga, and Al) shows linear correlations with several fundamental descriptors and is applicable to heteroatoms that are difficult to analyze with traditional methods. ^{15}N NMR spectra of pyridine displayed good resolution for both Lewis and Brønsted acids and control experiments showed complete resolution of framework sites from inactive SnO_2 . Spectra of these water tolerant solid acids were obtained under dehydrated and hydrated conditions, showing the role of water in hydrophilic materials. The ^{15}N chemical shift of pyridine resolved the identity of different heteroatoms in Beta zeolite, including framework sites in the presence of extraframework oxides. A linear correlation of ^{15}N chemical shift with Mulliken electronegativity was found which is consistent with HSAB theory of Lewis acidity. DFT studies demonstrated the utility of adsorption energy as a measure of Lewis acidity and illustrated the importance of considering active site reorganization when computing adsorption equilibrium. The selective insight generated by this

technique into activation of framework sites complements adsorption equilibrium data and facilitates rational catalyst selection to optimize reactant binding. Lewis acids are more diverse than Brønsted acids and this diversity offers the ability to develop highly selective processes. This method is general and can be easily implemented to compare the Lewis acid strength of samples with the same heteroatom but synthesized with different methodologies.^{26a, 26b} Recent kinetic results on the substituted Beta materials⁶⁷ suggest that higher solvent polarity results in tighter binding to the Lewis acid center and decreased flexibility in the transition state. Current efforts are focused on investigating the impact of condensed phases and solvents with different dielectric constants on binding properties.

4 Sn-Beta zeolites with borate salts catalyse the epimerization of carbohydrates via an intramolecular carbon shift²

4.1 Abstract

Carbohydrate epimerization is an essential technology for the widespread production of rare sugars. In contrast to other enzymes, most epimerases are only active on sugars substituted with phosphate or nucleotide groups, thus drastically restricting their use. Here we show that Sn-Beta zeolite in the presence of sodium tetraborate catalyses the selective epimerization of aldoses in aqueous media. Specifically, a 5 wt% aldose (for example, glucose, xylose or arabinose) solution with a 4:1 aldose:sodium tetraborate molar ratio reacted with catalytic amounts of Sn-Beta yields near-equilibrium epimerization product distributions. The reaction proceeds by way of a 1,2 carbon shift wherein the bond between C-2 and C-3 is cleaved and a new bond between C-1 and C-3 is formed, with C-1 moving to the C-2 position with an inverted configuration. This work provides a general method of performing carbohydrate epimerizations that surmounts the main disadvantages of current enzymatic and inorganic processes.

4.2 Introduction

Carbohydrate chemistry is a critical enabling technology for numerous processes in the health, food, chemical and alternative fuel industries. Of all possible pentoses and hexoses, only seven (that is, D-glucose, D-galactose, D-mannose, D-fructose, D-xylose, D-ribose and L-arabinose) are found in nature in sufficient amounts to allow their commercial production, while all others are denominated as 'rare'.⁶⁸ Despite their low natural abundance, rare sugars have enormous potential in several important applications, including their use as components for antiviral drugs,⁶⁹ low-calorie sweeteners with low glycemic indexes,⁷⁰ anti-inflammatory agents with immunosuppressive properties⁷¹ and chiral building blocks in natural products synthesis.⁷² Biochemical processes are primarily employed to transform abundant sugars into rare ones using three main classes of enzymes, namely keto-aldol isomerases, epimerases and oxidoreductases (see Figure 9). Isomerases and oxidoreductases are widely used because they are active on a wide range of simple substrates; however, such general activity is not always an advantage because it can result in the formation of side products (for example, xylose

² This chapter is adapted from Gunther, W. R.; Wang, Y.; Ji, Y.; Michaelis, V. K.; Hunt, S. T.; Griffin, R. G.; Román-Leshkov, Y., Sn-Beta zeolites with borate salts catalyse the epimerization of carbohydrates via an intramolecular carbon shift. *Nat. Commun.* **2003**, *3*, 1109.

isomerase converts glucose into fructose and simultaneously converts fructose into mannose). These processes have generated some commercially available rare sugars (for example, D-sorbitose and D-tagatose), but in most cases the complex nature of the bio-chemical process coupled with the thermodynamic limitations associated with sugar conversions performed at a strict upper bound temperature makes the synthesis and purification of rare sugars costly. In this respect, epimerases are potentially the most useful biocatalysts for the widespread production of rare sugars. They offer high specificity for products and are capable of selectively modifying sugars at multiple carbon positions (unlike isomerases, which are restricted to modifications of C-1 and C-2 positions).⁷³ For example, a 2-epimerase could replace the double keto-aldol isomerization required to convert D-xylose into D-lyxose. Unfortunately, most epimerases (with the notable exception of D-tagatose 3-epimerase) are only active on sugars that are substituted with phosphate or nucleotide groups, thus drastically restricting their use.

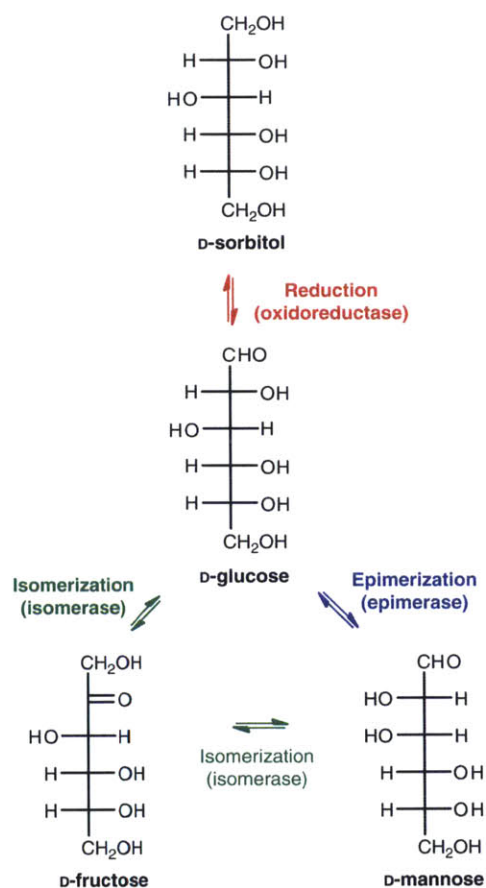


Figure 9. Representative glucose conversion pathways using biological catalysts. Enzymes comprise isomerases, oxidoreductases and epimerases.

Inorganic catalysts can provide alternative chemical pathways to those offered by biological systems. In contrast to enzymes, inorganic catalysts function over a larger range of reactant purities, temperatures, pressures and pH. For equilibrium-limited endothermic reactions, the ability to function at higher temperatures allows for operation in a regime where the equilibrium is more favorable. In addition, solid catalysts, such as zeolites, are easily separated from gas- or liquid-phase reactions and can be readily regenerated by calcination upon deactivation. The performance of the current generation of inorganic catalysts rarely matches that of their enzymatic counterparts; however, newly developed inorganic catalysts that have activities and selectivities comparable to those of enzymes will provide more efficient isomerization, epimerization and oxidation/reduction routes. This will increase the availability of rare sugars for the discovery and implementation of new applications.

Tin-containing silicates have recently emerged as a new class of inorganic solids with Lewis acid character capable of activating carbonyl functional groups in the presence of water.⁴ The pioneering work by Corma et al.^{11c, 23b, 25c, 45d} showed that Sn-Beta (that is, a zeolite with the Beta topology containing a small weight percent of tin present as isolated sites tetrahedrally coordinated in the zeolite framework) is highly active in Meerwin–Ponndorf–Verley (MPV) reduction and Baeyer–Villiger oxidation reactions. In contrast to most Lewis acids that require strictly anhydrous conditions, Sn-Beta remained active in the presence of small amounts of water. For the MPV reaction between alcohols and ketones, Corma et al.^{45d} showed that Sn incorporated in the framework of zeolite Beta has adequate Lewis acidity to polarize the carbonyl group in the ketone while providing open coordination sites for both the ketone and the alcohol. Davis et al.^{12b, 24b, 30} have recently demonstrated that Sn-Beta is active in the isomerization of sugars in bulk water and showed that it operates via chemical pathways analogous to those observed in isomerases. Sn-Beta and other tin-containing silicates have also been used for the isomerization of trioses in organic media to produce lactate derivatives.^{24c, 24d, 24f, 74}

Here we show that zeolites containing isolated Lewis acid sites used in conjunction with borate salts catalyse the epimerization of carbohydrates in a cooperative manner. This catalytic system is robust, featuring high activity and selectivity for the conversion of various aldoses over a broad range of reaction conditions. For example, a system comprising Sn-Beta and sodium tetraborate (SB) (molecular formula $\text{Na}_2[\text{B}_4\text{O}_5(\text{OH})_4]\cdot 8\text{H}_2\text{O}$) epimerizes aldoses to an equilibrium mixture containing the reactant (for example, glucose, xylose or arabinose) and the epimer (for example, mannose, lyxose and ribose, respectively), without producing significant quantities of the ketose isomer (for example, fructose,

xylulose and ribulose, respectively). We demonstrate that borates have a critical role in stabilizing the intermediate required for Sn-Beta to catalyse the epimerization by way of a 1,2 intramolecular carbon shift, whereby C-1 and C-2 undergo a transposition such that the former C-1 takes the place of C-2 with an inverted configuration. This drastically differs from the typical use of borates to shift the thermodynamic equilibrium through LeChatlier's principle by preferentially complexing with the ketose products.⁷⁵ The present work demonstrates a simple, general route for the epimerization of carbohydrates using solid Lewis acid catalysts. This catalytic system features activities and selectivities resembling those of epimerases, while also overcoming many of the drawbacks associated with biocatalytic processes.

4.3 Results

Reactivity data

Glucose reactivity data obtained with the combined use of Sn-Beta and SB show that both constituents are needed to achieve the epimerization of glucose to mannose. Specifically, when a 4:1 glucose:SB solution is used in the presence of Sn-Beta at a temperature of 358 K for 60 min, a product distribution of 84:1:15 glucose:fructose:mannose (99% of the total carbon) is generated (see Table 6, entry 4). On the contrary, when the reaction is performed under identical conditions but in the absence of borate, an 83:16:1 glucose:fructose:mannose (95% of the total carbon) distribution is obtained that is consistent with the product distribution previously reported for glucose isomerization using Sn-Beta (see Table 6, entry 5).^{12b} Additional control experiments show that under the temperature and reaction times investigated, glucose is unreactive in SB solutions or in SB solutions containing pure silica Beta zeolite (see Table 6, entries 1 and 2). We note that similar results are obtained for other aldoses (see Table 6, entries 7–14). Thus, starting from D-xylose, a 75:3:22 xylose:xylulose:lyxose (93% of total carbon) product distribution was obtained with SB, as compared with a distribution of 79:13:8 (96% of total carbon) in the absence of borate, and starting from D-arabinose with SB, a 68:1:31 arabinose:ribulose:ribose (97% of total carbon) product distribution was obtained as compared with 84:11:5 (83% of total carbon) in the absence of borate. Time studies for glucose, xylose and arabinose are shown in Table S9 to Table S11.

Table 6. Results for the isomerization/epimerization of sugars.

Entry	Sugar	Sugar:SB	Catalyst	Temp	Time	Conversion ^a	Product Distribution ^b			Total Sugar
		[mol:mol]		[K]	[min]	[%]	Reagent	Isomer	Epimer	Yield ^c
							[%]	[%]	[%]	[%]
							<i>Glucose</i>	<i>Fructose</i>	<i>Mannose</i>	
1	Glucose	4:1	None	358	60	1	100	-	-	99
2	Glucose	4:1	Si-Beta	358	60	1	100	-	-	99
3	Mannose	4:1	None	358	60	2	0	0	100	98
4	Glucose [†]	4:1	Sn-Beta	358	60	16	84	1	15	99
5	Glucose	-	Sn-Beta	358	30	21	83	16	1	95
6	Mannose*	4:1	Sn-Beta	358	60	17	14	0	86	97
							<i>Xylose</i>	<i>Xylulose</i>	<i>Lyxose</i>	
7	Xylose [†]	4:1	Sn-Beta	358	15	30	75	3	22	93
8	Xylose	-	Sn-Beta	358	15	24	79	13	8	96
9	Xylose	4:1	Sn-Beta	333	120	21	81	1	18	97
10	Xylose	-	Sn-Beta	333	120	18	83	7	10	98
							<i>Arabinose</i>	<i>Ribulose</i>	<i>Ribose</i>	
11	Arabinose [†]	4:1	Sn-Beta	358	15	34	68	1	31	97
12	Arabinose	-	Sn-Beta	358	15	30	84	11	5	83
13	Arabinose	4:1	Sn-Beta	333	120	17	84	1	15	99
14	Arabinose	-	Sn-Beta	333	120	11	91	5	4	95

Reactions were performed with a 5 wt% sugar feed (~2 mL), using the corresponding amount of catalyst to maintain a 100:1 sugar:metal molar ratio (~40 mg).

^a Conversion is defined as the ratio of moles of sugar consumed to moles sugar added initially, expressed as a percentage

^b Product distribution is the molar ratio of each sugar to the sum of the three sugars expressed as a percentage.

^c Sugar yield is the ratio of the sum of moles of the reagent, isomer and epimer sugars to moles of sugar added initially, expressed as a percentage.

[†] The epimerization product distributions at the thermodynamic equilibrium are: Glucose:Mannose = 70:30, Xylose:Lyxose = 67:33, and Arabinose:Ribose = 69:31. Values obtained from Gibbs free energies reported by Angyal.⁷⁶

* For this entry the Reagent and Epimer columns in the product distribution are exchanged so that they match the type of sugar used.

Reaction mechanism

To gain insight into the epimerization reaction mechanism, isotopically labeled glucose was reacted with the Sn-Beta/SB system and investigated using ^{13}C nuclear magnetic resonance (NMR). Before reaction, a 5 wt% D-(1- ^{13}C)glucose solution containing SB in a 4:1 glucose:SB molar ratio generates resonances at $\delta=97.0$ and 93.2 ppm, as well as a multiplet at $\delta=103.4$ – 104.5 ppm (see Figure 10a). The first two resonances correspond to the C-1 carbon of the β -pyranose and α -pyranose configurations of glucose, respectively, and the multiplet is consistent with the chemical shifts induced on C-1 by complex formation between the borate anion and the hydroxyl group at C-1.⁷⁷ Previous reports have shown that SB readily interacts with molecules containing vicinal diols, forming stable monomeric and dimeric boroxo species.⁷⁸ ^{11}B and ^{13}C NMR spectra for sugars dissolved in the presence of SB confirm the presence of monomeric and dimeric sugar–boron complexes (see Table S12 and Table S13 and Figure S15 to Figure S23). After reaction, a new set of resonances appear at $\delta=71.8$ and 72.3 ppm (see Figure 10b). Surprisingly, these resonances correspond to the two chemical shifts of D-(2- ^{13}C)mannose that are separated by ~ 0.5 ppm due to vicinal C–C coupling interactions with the α and β forms of the anomeric carbon.⁷⁹ Fractionation of the reaction mixture using high-performance liquid chromatography (HPLC) followed by ^{13}C and ^1H NMR analyses of the product fraction confirm the identity of the products (see Figure S24 and Figure S25). These results indicate that a rearrangement of the carbon backbone occurred, with C-1 and C-2 exchanging positions by way of an intramolecular carbon shift where the bond between C-2 and C-3 is cleaved and a new bond between C-1 and C-3 is formed. To obtain the epimer, the former C-1 atom (now at the C-2 position) must have an inverted configuration and the process has to be accompanied by hydride transfer steps at O-1 and O-2. An isotopic effect was not observed when the reaction was performed in deuterium oxide (D_2O), suggesting that H-D exchange processes are not involved in the kinetically relevant steps.

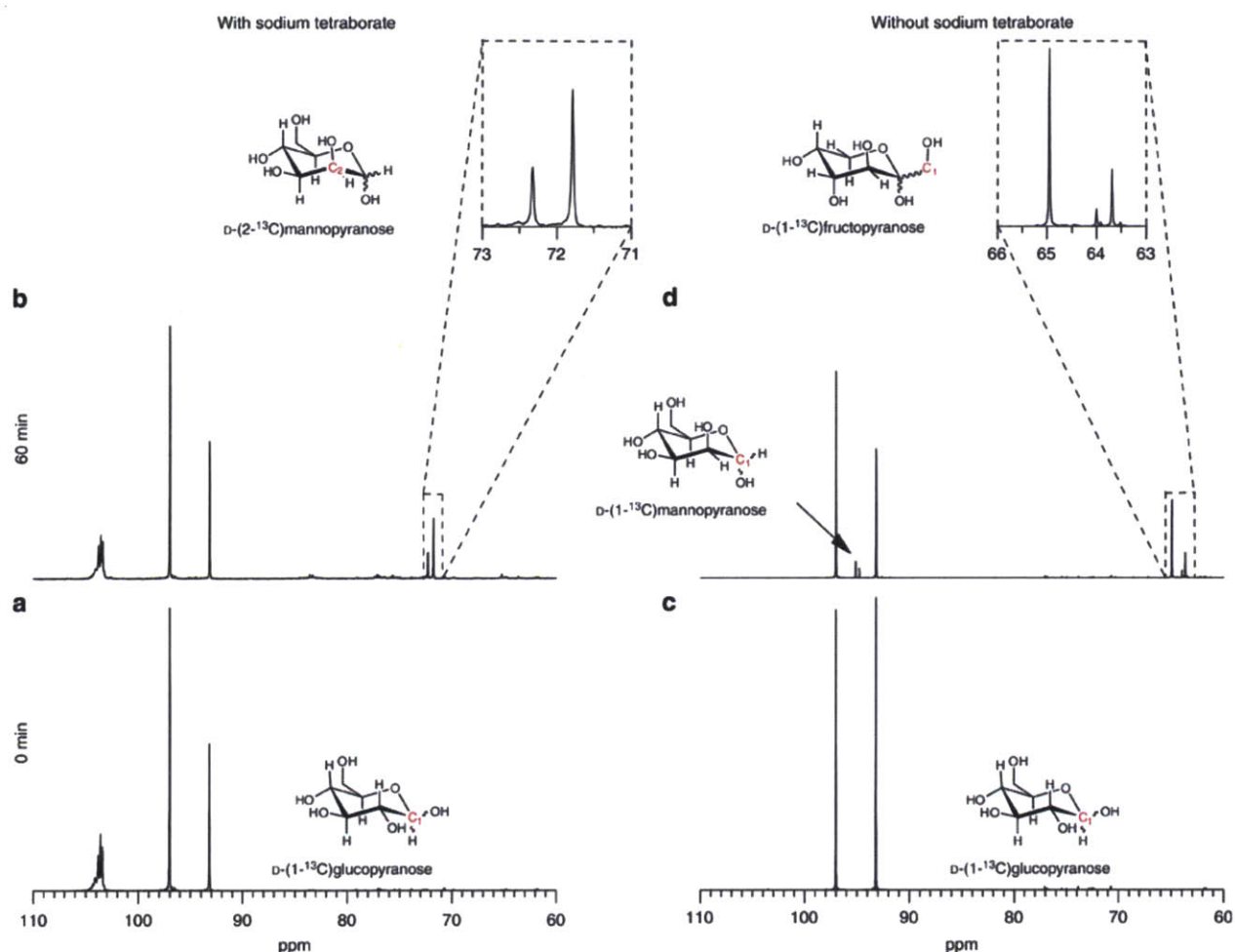


Figure 10. ^{13}C NMR spectra of reactants and products for epimerization and isomerization reactions. (a) D-(^{13}C)glucose with SB in a 4:1 glucose:SB ratio; (b) product mixture after reacting D-(^{13}C)glucose with SB in a 4:1 glucose:SB ratio and Sn-Beta; (c) D-(^{13}C)glucose; and (d) product mixture after reacting D-(^{13}C)glucose with Sn-Beta.

A similar ^{13}C NMR study performed under identical reaction conditions but in the absence of borate generates drastically different results. Before reaction, only the two resonances at $\delta=97.0$ and 93.2 ppm are observed for the 5 wt% D-(^{13}C)glucose solution (see Figure 10c). After reaction, two new sets of resonances appear: the first set at $\delta=63.7$ and 65.0 ppm corresponding to the α -furanose and β -pyranose conformations of D-(^{13}C)fructose and the second set at $\delta=94.6$ and 95.1 ppm corresponding to the β -pyranose and α -pyranose configurations of D-(^{13}C)mannose (see Figure 10d). Evidently, when the reaction is catalysed by Sn-Beta without borates, no carbon backbone rearrangement occurs and the reaction proceeds by way of an intramolecular hydride shift as reported in previous studies.^{24b}

Sugar–borate complex

To determine the role borate–sugar complex formation has on product distribution, a series of reactions varying the SB content were performed. As shown in Table 7, decreasing SB content results in a shift in the product distribution from mannose to fructose, while addition of stoichiometric or higher amounts of borate yields virtually no fructose. This indicates that epimerization and isomerization processes occur competitively. Note that the epimerization is still dominant with sub-stoichiometric amounts of borate, suggesting that the sugar–borate complex is not permanent and could form preferentially within the pores of the zeolite. Additional experiments showed that pretreating the catalyst with borate before adding the sugar or premixing the sugar with borate before adding Sn-Beta did not affect these results.

Table 7. Results for the isomerization/epimerization of sugars.

Entry	Sugar	Sugar:SB	Catalyst	Temp	Time	Conversion ^a	Product Distribution ^b			Total Sugar
		[mol:mol]		[K]	[min]	[%]	Reagent	Isomer	Epimer	Yield ^c
							[%]	[%]	[%]	[%]
<i>Borate content study</i>										
							<i>Glucose</i>	<i>Fructose</i>	<i>Mannose</i>	
1	Glucose	4:1	Sn-Beta	358	60	16	85	1	14	99
2	Glucose	10:1	Sn-Beta	358	60	31	76	3	21	91
3	Glucose	20:1	Sn-Beta	358	60	32	77	4	19	88
4	Glucose	40:1	Sn-Beta	358	60	28	78	10	12	92
<i>Catalyst study</i>										
5	Glucose	4:1	Sn-MCM-41	383	120	38	76	11	13	81
6	Glucose	4:1	Sn-MFI	358	120	7	97	0	3	95
7	Glucose	4:1	Ti-Beta	358	120	23	87	0	13	88
8	Glucose	None	Sn-MCM-41	383	120	8	93	6	1	99
9	Glucose	None	Sn-MFI	358	120	4	98	1	1	98
10	Glucose	None	Ti-Beta	358	120	9	92	6	2	99
							<i>Xylose</i>	<i>Xylulose</i>	<i>Lyxose</i>	
11	Xylose	4:1	Sn-MFI	358	120	20	84	12	4	95
12	Xylose	None	Sn-MFI	358	120	23	79	15	6	97

Reactions were performed with a 5 wt% sugar feed (~2 mL), using the corresponding amount of catalyst to maintain a 100:1 sugar:metal molar ratio (~40 mg).

^a Conversion is defined as the ratio of moles of sugar consumed to moles sugar added initially, expressed as a percentage

^b Product distribution is the molar ratio of each sugar to the sum of the three sugars expressed as a percentage.

^c Sugar yield is the ratio of the sum of moles of the reagent, isomer and epimer sugars to moles of sugar added initially, expressed as a percentage.

Solid-state magic-angle spinning (MAS) ¹³C and ¹¹B NMR spectra reveal that the sugar–borate complex exists inside the pores of the zeolite (see Figure 11). Specifically, Sn-Beta was mixed with a D-(1-¹³C)glucose solution containing SB (with molar ratios of 2:0.5:1 and 100:25:1 D-(1-¹³C)glucose:SB:Sn for ¹³C and ¹¹B, respectively) for 30 min at room temperature and then separated by vacuum filtration. The ¹³C MAS NMR spectrum of the filtered Sn-Beta contains a set of resonances at $\delta_{iso} \approx 103$ ppm that is consistent with the formation of glucose–borate complexes. Similar outcomes are observed in spectra obtained post reaction in the presence of SB. When the D-(1-¹³C)glucose solution does not contain SB or

when SB is adsorbed in the absence of glucose, the resonances at $\delta_{\text{iso}}=103$ ppm are not observed. In addition, ^{11}B MAS NMR of the D-(1- ^{13}C)glucose sample adsorbed on Sn-Beta in the presence of SB shows the characteristic four-coordinate ^{11}B resonances associated with sugar–borate complex formation. Specifically, we observe one three-coordinate ^{11}B resonance centered at $\delta=17$ ppm that is correlated with a disordered borate moiety likely due to the presence of free SB and four four-coordinate ^{11}B resonances centered at $\delta_{\text{iso}}=11, 5.5, -0.5$ and -4 ppm. The broad lineshapes observed for all the three-coordinate ^{11}B environments are due to a significant quadrupolar coupling constant of ~ 2.5 MHz and a low-asymmetry parameter ($\eta < 0.2$). In crystalline systems such as SB, a clean second-order quadrupolar pattern is observed (CQ=2.53 MHz, $\eta=0.09$ and $\delta_{\text{iso}}=19.8$ ppm); however, in a disordered solid this will cause a broadening of the resonance into a Gaussian-like lineshape as seen for SB adsorbed on Sn-Beta and D-(1- ^{13}C)glucose with SB adsorbed on Sn-Beta (see Figure 11e–g).⁸⁰ This phenomenon is not the case for the higher-symmetry four-coordinate ^{11}B resonances. The reduction in second-order quadrupolar broadening occurs due to the local symmetry being pseudo-tetrahedral (quadrupolar couplings on the order of a few 100 kHz), resulting in a near-isotropic lineshape. Of the four four-coordinate ^{11}B resonances, only the one at $\delta_{\text{iso}}=-0.5$ can correspond to B–O–B (that is, re-arrangement within SB) and B–O–Si (that is, Sn-Beta and SB interactions) environments.⁸¹ These assignments are further confirmed by the ^{11}B MAS NMR spectrum of SB adsorbed on Sn-Beta (see Figure 11f), which exhibits a broad three-coordinate ^{11}B resonance and a narrower four-coordinate ^{11}B resonance centered at $\delta_{\text{iso}}=0.5$ ppm and a shoulder at $\delta_{\text{iso}}=-0.5$ ppm. The concentration of possible B–O–Sn environments is too low to be detected with the current analytical method; therefore, the remaining four-coordinate ^{11}B resonances must correspond to sugar–borate complexes. Note that these resonances match those observed for glucose–borate complexes present in solution (see Figure S15).

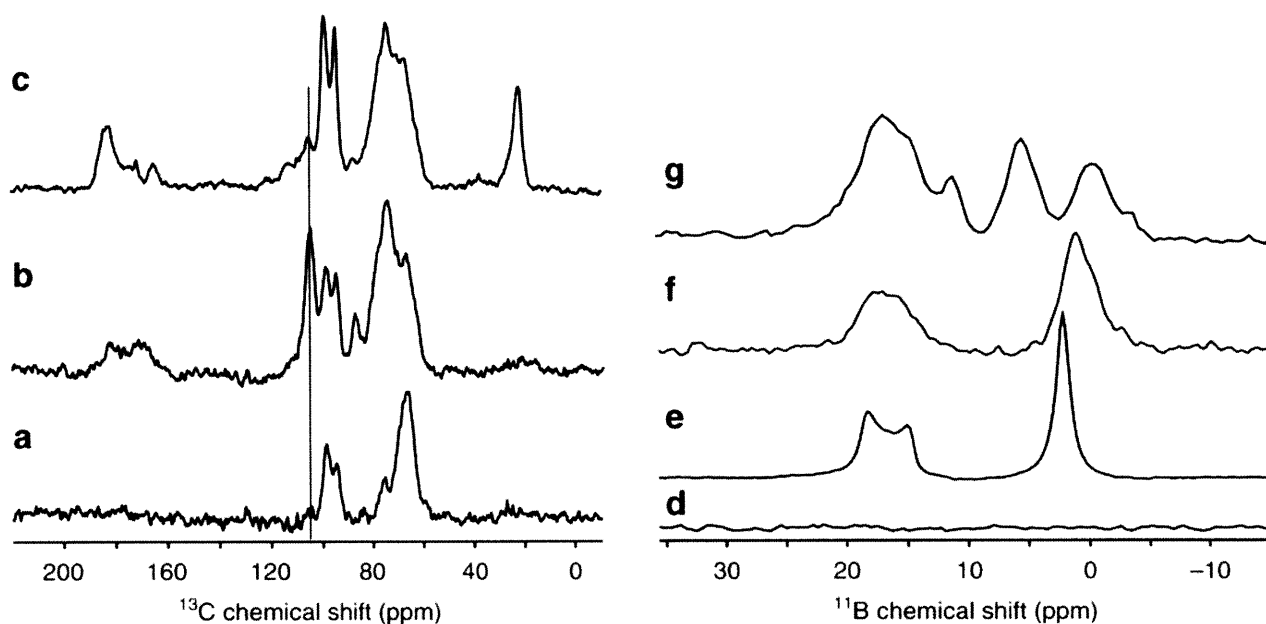


Figure 11. ^{13}C and ^{11}B solid-state MAS NMR spectra for glucose adsorbed on Sn-Beta.

(a) ^{13}C MAS NMR cross-polarization (CP) of D-(1- ^{13}C)glucose adsorbed on Sn-Beta with a 2:1 glucose:Sn molar ratio; (b) ^{13}C MAS NMR (CP) of D-(1- ^{13}C)glucose with SB in a 2:0.5:1 glucose:SB:Sn molar ratio; (c) ^{13}C MAS NMR (CP) of D-(1- ^{13}C)glucose with SB after reaction at 358 K for 30 min with a 50:12.5:1 glucose:SB:Sn molar ratio; (d) ^{11}B MAS NMR of Sn-Beta; (e) ^{11}B MAS NMR of SB; (f) ^{11}B MAS NMR of SB adsorbed on Sn-Beta with a 12.5:1 SB:Sn molar ratio; and (g) ^{11}B MAS NMR of D-(1- ^{13}C)glucose with SB adsorbed on Sn-Beta in a 2:0.5:1 glucose:SB:Sn molar ratio.

X-ray photoelectron spectroscopy (XPS) data of Sn-Beta samples containing adsorbed species show both an increase in the amount of carbon on the surface and changes in the chemical nature of surface tin sites (see Figure S26). Specifically, calcined Sn-Beta showed doublets for Sn $3d_{5/2}$ and $3d_{3/2}$ electrons with binding energies of 487.2 and 495.6 eV, respectively, which is indicative of Sn^{4+} species on the surface. Spectra for Sn-Beta containing adsorbed glucose and glucose/borate show a downward shift in the binding energy for the Sn 3d signal of ~ 0.3 and 0.9 eV, respectively. Also, these samples show an increase in the binding energy for the C 1s signal when compared with freshly calcined Sn-Beta.

To gain further insight into the nature of the interaction between the sugar–borate complex, the zeolite pore and the active site, the epimerization of sugars with Sn-MCM-41 and Sn-MFI, which are stannosilicates with pore topologies different from Beta, was investigated. Interestingly, the epimerization-promoting effect of SB was only slightly detected for Sn-MCM-41 and not observed for

Sn-MFI. For experiments performed with Sn-MCM-41 at 383 K with a 4:1 glucose:SB molar ratio, the product distributions in the presence and absence of SB are 76:11:13 (81% of total carbon) and 93:6:1 (99% of total carbon), respectively (see Table 7, entries 5 and 8). Sn-MFI experiments with glucose did not show reactivity, but this is consistent with the fact that glucose is too large to enter the pores of MFI (see Table 7, entries 6 and 9). Using xylose as the starting reagent, the product distributions in the presence and absence of SB are 84:12:4 and 79:15:6 xylose:xylulose:lyxose with sugar yields of 95% and 97%, respectively (see Table 7, entries 11 and 12). In contrast, xylose reacted with Sn-Beta and SB is almost exclusively converted into lyxose (see Table 6, entries 7 and 9).

4.4 Discussion

The results of the present study indicate that zeolites containing isolated Lewis acid sites and borate salts cooperatively catalyse the epimerization of carbohydrates. Base catalysts are typically used to produce epimers following Lobry de Bruyn-Alberda van Ekenstein pathways that produce mixtures of the ketose isomer and the aldose epimer via ene-diol transition states.⁸¹⁻⁸² A rare exception to this mechanism was discovered by Bílik, who showed that treatment with catalytic amounts of molybdic acid under acidic conditions will epimerize aldoses via transition states that promote a 1,2 carbon shift.⁸³ Many catalytic systems based on molybdate chemistry have been investigated.⁸⁴ The accepted mechanism involves the complex formation of a binuclear molybdate species with four adjacent hydroxyl groups (OH-1 to OH-4) in the sugar.⁸⁵ The molybdate species creates a rigid framework that holds the atoms in the required conformation to promote the concerted C-3 bond migration from C-2 to C-1. Similar results have been reported for homogeneous Ni²⁺ complexes with diamine co-catalysts in methanolic solutions.⁸⁶ In all cases, a rigid metal–sugar complex was required to achieve the carbon backbone rearrangement. In the present study, NMR investigations on isotopically labeled sugars show that the epimerization occurs via a 1,2 intramolecular carbon shift, which is similar to the mechanism proposed for the Bílik reaction catalysed by molybdate species. The borate–sugar complexes likely have a critical role in providing a rigid framework for the carbon shift to occur at the active site in the zeolite. This rigid complex facilitates bond bending to bring C-1 and C-3 close enough to promote bond migration.

The data suggest that a synergistic effect between the pore walls of Beta, the isolated Lewis acid sites and the sugar–borate complex has to exist for the epimerization reaction to occur selectively. The ¹³C and ¹¹B MAS NMR data show that the complex is likely present inside the pores of Sn-Beta and the XPS

data indicate that adsorbed components change the electronic environment of the Sn surface sites. The inferior epimerization performance of other pore topologies suggests the presence of a strong confining effect in the 12-membered rings of Beta. We hypothesize that the large pores of Sn-MCM-41 allow all molecules, complexed and uncomplexed, to reach and react at the active site without restriction to generate a mixture of epimers and isomers. Conversely, the pores of Sn-MFI are too small for the sugar–borate complex to enter or form inside them, but are large enough to allow uncomplexed sugar to enter and undergo normal isomerization reactions at the tin site. In Sn-Beta, the borate may preferentially reside inside the pores, form the sugar–borate complex and preferentially absorb in the pores, or form a unique complex with both the sugar and the tin site. The present reaction and NMR data cannot conclusively exclude any of these options, thus requiring further studies. We note that the epimerization chemistry is not restricted to tin-containing zeolites. Experiments with Ti-Beta using glucose under standard reaction conditions showed that this catalyst had much lower activity than Sn-Beta, but generated a similar product distribution in the presence (87:0:13 glucose:fructose:mannose) and absence (92:6:2 glucose:fructose:mannose) of SB, with carbon balances exceeding 88% (see Table 7, entries 7 and 10).

The combination of Sn-Beta and SB generates a highly active catalytic system for epimerization reactions that, unlike most epimerases, can be used to process a variety of sugars to the thermodynamic equilibrium limit (see Table 6 for calculated equilibrium compositions) without the need of prior substrate functionalization. Currently, heterogeneous catalysts containing immobilized molybdate species in ion-exchange resins represent the state-of-the-art in sugar epimerization chemistry.⁸⁷ These inorganic catalysts have been optimized to minimize deactivation; however, slow and continuous leaching of the active phase is always observed and this effect is expected to increase in the presence of dissolved anions in the feed (for example, as those encountered in lignocellulosic biomass feedstock).⁸⁷ The Sn-Beta/SB system is stable and active in the presence of high ionic strength solutions, thus offering an attractive alternative to process 'dirty' carbohydrate feeds containing dissolved anionic species that would foul catalysts based on ion-exchange resins. Importantly, the zeolite component can provide interesting reactivity pathways based on confining and shape selectivity effects induced by the micropores that are unattainable by ion-exchange resins.

Future studies geared at designing catalytic sites that allow the formation of an immobilized rigid sugar–borate complex within the zeolite pores will be critical to reduce the number of separation unit

operations by eliminating the use of complexing agents in solution. Finally, having observed C–C bond-breaking and bond-forming events associated with rigid sugar complexes activated with Sn-Beta, it is anticipated that this catalytic system may be applied to other classes of oxygenated molecules and more general reactions. We are intrigued by the potential links between the observed carbon backbone rearrangement and C–C bond-forming events in prebiotic chemistry. For instance, the formose reaction involves the bottom-up synthesis of pentoses and hexoses by a series of borate- or silicate-stabilized formaldehyde coupling sequences,⁸⁸ while the 'glyoxylate scenario' proposes glyoxylate and dihydroxyfumarate intermediates for forming carbohydrates in the presence of Lewis acidic salts.⁸⁹ Understanding such C–C coupling in carbohydrates is currently the subject of additional studies within our group.

4.5 Methods

Synthesis of Sn-Beta

Sn-Beta was synthesized according to Corma et al.,⁹⁰ as follows: 24.67 g of aqueous tetraethylammonium hydroxide (Sigma-Aldrich, 35% (w/w)) and 22.14 g of tetraethylorthosilicate (Sigma-Aldrich, 99% (w/w)) were added to a Teflon® (Polytetrafluoroethylene, [PTFE]) dish, which was stirred at room temperature for 90 min. Then, 0.380 g of tin (IV) chloride pentahydrate (Sigma-Aldrich, 98% (w/w)) dissolved in 15 g of deionized water (DI H₂O) was added dropwise. The solution was left uncovered on a stir plate for 10 h to reach 15 g of total water. Next, 2.407 g of aqueous hydrofluoric acid (Sigma-Aldrich 48% (w/w)) was added dropwise and the mixture was homogenized using a PTFE spatula, resulting in a thick gel. Then, 0.333 g of previously made Sn-Beta was seeded into the mixture, which was allowed to evaporate to a final molar composition of SiO₂/0.01 SnCl₄/0.55 TEAOH/0.54 HF/7.52 H₂O. The thick paste was transferred to a PTFE-lined stainless steel autoclave and heated to 413 K for 40 days. The solids were recovered by filtration, washed with DI H₂O, dried at 373 K and calcined at 853 K for 10 h with a 1-K min⁻¹ ramp and 1 h stops at 423 and 623 K, leading to an overall inorganic oxide yield of 80–90%.

Powder X-ray diffraction (PXRD) confirmed that the solid material has the Beta zeolite topology (see Figure S27). The ultraviolet–visible diffuse reflectance spectrum of the calcined sample shows the presence of a unique band at ~200 nm, which has been associated with Sn tetrahedrally coordinated into the zeolite framework (see Figure S28). A scanning electron microscopy (SEM) image is shown in Figure S29 and SEM energy-dispersive X-ray spectroscopy (EDS) measurements show an atomic ratio

Si:Sn of 110:1. This result is consistent with the Si:Sn of 111:1 obtained from elemental analysis (Galbraith Laboratories, Inc).

Ti-Beta was synthesized in a similar way as described in the supporting information, with an XRD shown in Figure S30.

Synthesis of other stannosilicates

Sn-MFI was synthesized according to Mal et al.,^{51a} as follows: 0.098 g of tin (IV) chloride pentahydrate (Sigma-Aldrich, 98% (w/w)) was added to 5 g of DI H₂O in a PTFE dish. Further, 8.350 g of tetraethylorthosilicate (Sigma-Aldrich, 99% (w/w)) was added and the solution was stirred for 30 min. Then, 8.966 g of aqueous tetra-n-propyl ammonium hydroxide (Alfa Aesar, 20%(w/w)) was added and the mixture was stirred uncovered for 1 h. Next, 20.083 g of DI H₂O was added and the solution was allowed to mix for 30 min to a final synthesis gel molar composition of SiO₂/0.01 SnO₂/0.44 TPAOH/34.3 H₂O. The solution was transferred to a PTFE-lined stainless steel autoclave and heated to 433 K for 48 h. After this time, the solids were repeatedly centrifuged and washed with DI H₂O, dried at 373 K, and calcined at 853 K for 10 h with a 1 K min⁻¹ ramp and 1 h stops at 423 and 623 K, leading to an overall 70–90% yield.

PXRD confirmed that the solid material has the MFI zeolite topology (see Figure S31). The ultraviolet–visible diffuse reflectance spectrum indicates Sn is in the framework (see Figure S32). SEM EDS measurements for the Sn-MFI sample show an atomic ratio Si:Sn of 180:1.

Please refer to the supporting information for a detailed description of the Sn-MCM-41 synthesis method.

Catalytic reactions

Catalysts were added at a 1:100 metal:sugar molar ratio to a 5 wt% sugar solution in a 5-ml thick-walled glass reactor containing a small magnetic stir bar (typically ~40 mg of catalyst in 2 ml of sugar solution). After taking a sample for t=0, the vial was sealed using a PTFE/silicone septa and metal crimp top, placed in a temperature-controlled oil bath and samples were taken at various times. After quenching the vial for 5 min in an ice bath, a small sample was removed using a syringe and filtered into a small vial. Next, 100 µl of the filtered sample and 20 µl of a 10 wt% mannitol solution were mixed in an HPLC vial. The

samples were analysed on an Agilent 1260 HPLC system equipped with photodiode array ultraviolet and evaporative light-scattering detectors. The reaction products were separated using a Bio-Rad Aminex HPX-87C column heated to 353 K with DI H₂O (pH=7) as the mobile phase at a flow rate of 0.6 ml min⁻¹. Xylulose and ribulose concentrations were determined using the ultraviolet detector at 210 nm. At this wavelength all other sugars had negligible ultraviolet signals. For all ultraviolet-inactive carbohydrates, the analysis was performed using the evaporative light scattering detector and Origin software (OriginLab Corp., ver. 9) for peak deconvolution when needed. The peak deconvolution function is based on Gaussian/Lorentzian fitting functions that provided an accuracy of ~8% when compared with standard mixtures.

Sugar adsorption

For the sugar adsorption studies, 100 mg of Sn-Beta was mixed with a 0.01-g ml⁻¹ sugar solution (2:0.5:1 or 100:25:1 D-(1-¹³C)glucose:SB:Sn) for 30 min at room temperature and then quickly separated by vacuum filtration and dried under vacuum at room temperature. Post-reaction catalysts were produced in a similar way starting with a 0.05-g ml⁻¹ sugar solution (50:1 D-(1-¹³C)glucose:Sn) and heating the mixture to 358 K for 30 min.

Characterization

PXRD patterns were collected using a Bruker D8 diffractometer with Cu K α radiation. SEM EDS measurements were recorded on a JEOL 6700F at an electron high tension of 10 kV. Ultraviolet-Vis measurements were recorded using a Cary 3G spectrometer with a diffuse reflectance cell after calcination without subsequent drying. Nitrogen adsorption/desorption experiments were performed on a Quantachrome Autosorb iQ apparatus.

Solution NMR was performed on a Bruker AVANCE 400 MHz spectrometer with a Magnex magnet and 5 mm double-resonance probe, which was tuned to ¹H, ¹¹B and ¹³C before use. Samples were prepared at a sugar concentration of 0.05 g ml⁻¹ using quartz NMR tubes. The spinning frequency was 20 Hz. For ¹H and ¹¹B 64 transients were taken, and for ¹³C between 1024 and 2048 transients were taken. ¹H NMR spectra were referenced with respect to residual water. ¹³C was referenced with respect to the C-1 carbon of D-glucose at 97.0 ppm as a secondary standard relative to 4,4-dimethyl-4-silapentane-1-sulphonic acid. All ¹¹B spectra were referenced using boric acid (H₃BO₃, 19.6) as a secondary standard relative to boron trifluoride etherate (BF₃ EtO₂).

^{13}C solid-state MAS NMR experiments were measured using an 11.7-T (^1H , 500.057 MHz) Magnex magnet and a home-built spectrometer (courtesy of Dr David Ruben, FBML-MIT). Experiments were performed using a 4-mm Varian-Chemagnetics MAS triple-resonance probe, doubly tuned to ^{13}C and ^1H . Powdered samples were packed into 4 mm outside diameter (o.d.) ZrO_2 rotors equipped with Vespel drive-caps and Kel-F top-caps. All ^{13}C spectra were acquired using two second recycle delays, a spinning frequency of $\omega_r/2\pi=9.00$ kHz, and between 10 240 and 35 840 co-added transients. $^{13}\text{C}\{^1\text{H}\}$ 91 cross-polarization 54,92 experiments were acquired using γB_1 of 50 kHz on ^1H and an optimized ^{13}C ramp with high-power ^1H decoupling (Two-pulse phase-modulated [TPPM], 93 γB_1 of 83 kHz). All ^{13}C spectra were referenced with respect to adamantane at 38.48 ppm (relative to neat tetramethylsilane). 43

^{11}B MAS NMR experiments were measured using a 16.4-T (^1H , 697.8 MHz) Magnex magnet and a home-built spectrometer (David Ruben, FBML-MIT). Experiments were acquired using a 3.2-mm Varian MAS triple-resonance probe, tuned to ^{11}B . Samples were packed into 3.2 mm (o.d.) ZrO_2 thin-wall rotors (36 μl fill volume). Spectra were acquired using short (20° tip-angle) quantitative pulses, recycle delays of 2 s, between 4096 and 30 720 co-added transients, and a spinning frequency of $\omega_r/2\pi=14.00$ kHz. All ^{11}B spectra were referenced using 0.1 M H_3BO_3 (19.6 ppm) as a secondary standard relative to $\text{BF}_3 \cdot \text{EtO}_2$. 76

All XPS spectra were collected using a PHI Versaprobe II equipped with a multichannel hemispherical analyser and aluminium anode X-ray source operating at 100 W with a 100- μm beam scanned over a 1.4-mm line across the sample surface. A dual-beam charge neutralization system was used with an electron neutralizer bias of 1.2 eV and an argon ion beam energy of 10 eV.

5 Catalytic consequences of borate complexation and pH on the epimerization of L-arabinose to L-ribose in water catalyzed by Sn-Beta zeolite with borate salts³

5.1 Abstract

Sn-Beta zeolite with sodium tetraborate cooperatively catalyzes the epimerization of aldoses via an intramolecular 1,2 carbon-shift mechanism. L-arabinose is one of the seven common sugars and its epimer, L-ribose, is a valuable rare sugar with applications in antiviral and anticancer agents. Here, a full factorial experimental design is performed to demonstrate the catalytic consequences of varying key reaction parameters such as pH, borate to sugar ratio, and reaction time. Reactivity data revealed that isomerization is favored under acidic pH conditions (pH < 7.0); that epimerization dominates under neutral conditions (pH ranging from 7.0 to 7.8); and that drastic inhibition of both epimerization and isomerization rates occur under basic conditions (pH > 7.8). Using a 5 wt% arabinose feed and 100:1 sugar–metal ratios at 343 K, conversions ranging from 20% to 30% were obtained with selectivities of 75%, 84%, and 91% for boron–sugar ratios of 0.2:1, 0.5:1, and 1:1, respectively. The predominance of epimerization over isomerization products with substoichiometric borate suggests that one borate can influence the reactivity of several sugar molecules and may influence the Sn active site directly. Reaction data obtained under differential conditions revealed that the epimerization reaction follows first order kinetics over a wide temperature range with an apparent activation energy of 98 kJ/mol and pre-exponential factor of $1.9 \times 10^{14} \text{ L mol Sn}^{-1} \text{ s}^{-1}$.

5.2 Introduction

Carbohydrates are involved in important biological processes and also serve as valuable building blocks in many commercial applications. For instance, the common pentose D-ribose is a major component in ribonucleic acid (RNA), adenosine triphosphate (ATP), and nicotinamide adenine dinucleotide (NADH) in metabolism. The industrial production of riboflavin also involves the use of D-ribose.⁹⁴ The rare pentose, L-ribose, has found applications in anti-viral and anti-cancer drugs because its reverse stereochemistry alters the interaction with enzymes, inhibiting the nucleoside synthesis-replication process.⁹⁵

³ This chapter is adapted from Gunther, W. R.; Duong, Q.; Román-Leshkov, Y., Catalytic consequences of borate complexation and pH on the epimerization of L-arabinose to L-ribose in water catalyzed by Sn-Beta zeolite with borate salts. *J. Mol. Catal. A: Chem.* **2013**, *379*, 294-302

Additionally, L-RNA binds tightly to natural RNA and is resistant to degradation by nucleases, allowing it to silence gene expression. Consequently, L-ribose is part of several pharmaceuticals presently on the market or undergoing clinical trials.⁹⁶ To meet the demand for such rare sugars, costly and complex biochemical⁹⁷ and synthetic organic processes are currently used to produce them from common carbohydrates.⁹⁸ Therefore, the development of simpler and more effective catalytic pathways to produce rare sugars is of great relevance.

The selective epimerization of aldoses is an attractive pathway for the production of rare sugars. L-arabinose is a common sugar found in the hemicellulose fraction of biomass. As depicted in Figure 12, arabinose is interconverted into an equilibrium mixture consisting of ca. 66% arabinose, 11% ribulose and 23% ribose in the presence of isomerase enzymes or inorganic base catalysts at 333 K.⁹⁹ Ribulose is the ketose isomer, while ribose is the aldose epimer, typically formed by way of a double isomerization process. The direct epimerization of arabinose into ribose may be accomplished using epimerase enzymes to generate a distribution of 74% arabinose and 26% ribose at 333 K. However, most epimerases only function on substrates modified with phosphate or nucleotide groups. Direct epimerization yields a product distribution that does not contain ribulose, and is therefore more amenable for purification. Epimerization of arabinose to ribose is slightly endothermic, and consequently, high temperatures lead to higher equilibrium ribose yields (see Figure S34). In this respect, inorganic catalysts may be attractive epimerization candidates given that they are not limited by temperature or substrate functionalization in the same manner as biological catalysts.⁹⁹

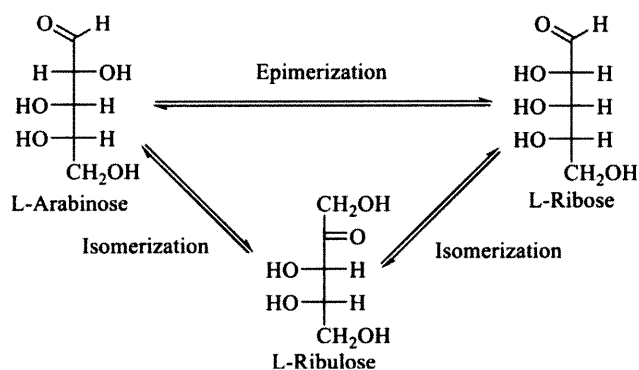


Figure 12. Schematic representation of the isomerization and epimerization of L-arabinose. The D form is the mirror image of the L form.

Hydrophobic zeolites with metal atoms substituted in the crystalline microporous framework have recently emerged as a new class of Lewis acid catalysts capable of activating carbonyl functional groups in the presence of water. The highly dispersed tetrahedrally-coordinated metal centers can accept electron pairs through empty d orbitals and expand their coordination shells from 4 to 5 or 6 sites due to their large covalent radii. Tin-containing zeolites are active in the Meerwein–Ponndorf–Verley reduction^{23b, 45d}, Baeyer–Villiger oxidation^{11c, 24a, 100}, and carbonyl-ene reaction¹⁰¹. In the context of carbohydrate chemistry, the incorporation of Sn, Ti, and Zr in the framework of Beta zeolite has found applications in the conversion of hexoses^{12b, 24b}, pentoses^{74a, 102}, and trioses^{24c, 24d, 24f, 74b} via intramolecular hydride shifts, as well as in the production of gamma-valerolactone from xylose^{23a} and alpha-hydroxyacids^{41c, 103} from C-2 and C-4 oxygenates. Recent work shows that Sn-Beta catalyzes the chiral Baeyer–Villiger oxidation of sugar derivatives.¹⁰⁴

Our recent work has shown that Sn-Beta with sodium tetraborate cooperatively catalyzes the selective epimerization of aldoses in aqueous media under mild conditions.^{24e} The reaction mechanism, investigated using ¹³C-labeled sugars and nuclear magnetic resonance (NMR), proceeds by way of a 1,2 carbon-shift mechanism whereby C1 forms a new C-C bond with C₃, while C₂ moves to the C₁ position. In the absence of the borate promoter, no carbon backbone rearrangement occurs and Sn-Beta catalyzes a regular aldose–ketose isomerization via an intramolecular hydride shift as reported in previous studies.^{12b} The epimerization mechanism is analogous to the Bilik reaction using molybdenum-based catalysts that form rigid complexes by interacting with the hydroxyl groups of C₁–C₄ in the sugar.^{85b, 87}

Isomorphous substitution of tin for silicon tetrahedrally-coordinated in the crystalline zeolite framework generates a closed site. Hydration with two water molecules produces a Sn site with octahedral coordination, while hydrolysis of one of the Sn–O–Si bridges generates an open site. For the isomerization of glucose to fructose, Bermejo-Deval and co-workers showed that the open-site in Sn-Beta promotes the ring opening and the hydride transfer steps more favorably than the closed site.³⁰ In the presence of borate, the 1,2 hydride-shift isomerization pathway is drastically inhibited in favor of a 1,2 carbon-shift epimerization pathway. Interestingly, a similar 1,2 carbon-shift product has been recently reported using Sn-Beta in methanol, although epimerization rates are lower when compared to the Sn-Beta/borate system in water.¹⁹ Borates can interact with the hydroxyl groups found in carbohydrates and with the silanol groups found near the Sn open site, both with a strong dependence on pH.¹⁰⁵ We hypothesize that the borate additive interacts with the sugar and/or the active site to

change the reaction from a hydride-shift isomerization to a carbon-shift epimerization pathway. Here, we present a full factorial experimental design to investigate the impact of pH, sugar to borate ratio, and reaction time on the epimerization of L-arabinose to L-ribose. The conversion of arabinose to ribose provided a high value added case to investigate the role of sugar–borate complexation. Understanding which species and reactions are dominant under controlled reaction conditions provides insight into the role of additives in directing the sugar conversion pathway. Thus, we show a comparison of isomerization activity with the fraction of free sugar under low borate loadings and use ^{11}B NMR and Raman spectroscopy characterization to identify sugar borate dimers and polyborates in solution. A temperature study is performed to extract kinetic parameters and optical rotation measurements are used to assess stereospecificity.

5.3 Experimental

Catalyst synthesis

Sn-Beta was synthesized as follows: 26.735 g of aqueous tetraethylammonium hydroxide (Sigma–Aldrich, 35% (w/w)) and 24.069 g of tetraethylorthosilicate (Sigma–Aldrich, 99% (w/w)) were added to a Teflon® (Polytetrafluoroethylene, [PTFE]) dish, which was magnetically stirred at room temperature for 90 min and then cooled in an ice bath. Then, 0.261 g of tin (II) chloride dihydrate (Sigma–Aldrich, 98% (w/w)) dissolved in 15 g of cold deionized water (DI H₂O) was added dropwise. Sn(II) which oxidizes to Sn(IV) in water was used in place of SnCl₄·5H₂O and has resulted in Sn-Beta consistently free of extraframework SnO₂. The solution was left uncovered on a stir plate for 10 h to reach a total mass of 35 g. Next, 2.600 g of aqueous hydrofluoric acid (Sigma–Aldrich, 48% (w/w)) was added dropwise and the mixture was homogenized using a PTFE spatula, resulting in a thick gel. Then, 0.358 g of previously-made Sn-Beta was seeded into the mixture, which was allowed to evaporate to 33.776 g, which corresponds to a final molar composition of SiO₂/0.01 SnCl₂/0.55 TEAOH/0.54 HF/7.52 H₂O. The thick paste was transferred to a 45 ml PTFE-lined stainless steel autoclave and heated to 413 K for 40 days under static conditions. The solids were recovered by filtration, washed with DI H₂O, dried at 373 K and calcined at 853 K for 10 h with a 1 K min⁻¹ ramp and 1 h stops at 423 and 623 K, leading to an overall inorganic oxide yield of 80–90%.

Powder X-ray diffraction (PXRD) patterns were collected using a Bruker D8 diffractometer with Cu K α radiation, which confirmed that the solid material has the Beta topology (see Figure S35). Ultraviolet–visible (UV–vis) measurements were recorded using a Varian Cary 5000 UV–vis–NIR spectrometer with a

diffuse reflectance cell after calcination without subsequent drying. The ultraviolet–visible diffuse reflectance spectrum of the calcined sample shows the presence of a unique band at ~200 nm, which has been associated with Sn tetrahedrally coordinated into the zeolite framework (see Figure S36); as additional confirmation of framework incorporation, ^{119}Sn NMR of an analogous sample is included in Figure S37. Sn content was measured using a Horiba Jobin Yvon ACTIVA-S ICP-AES. Catalyst samples were dissolved in a few drops of 48% HF and diluted in 2% nitric acid after evaporation of the HF.

Solutions

Within this study, the sugar content was held constant and the borate content was varied to obtain the desired ratios. The sodium to borate ratio was adjusted by mixing boric acid, sodium tetraborate, sodium metaborate and sodium hydroxide on a mass basis on a 50 ml solution scale (see Table S15). The pH was measured with a Mettler Toledo FiveEasy FE20 probe, calibrated with pH 6, 7 and 10 buffers prior to use at 298 K. For the control experiments, the pH-adjusted solutions without borate were very sensitive and were therefore measured while mixing. NMR solutions were prepared analogously in D_2O on a 5 ml scale.

Reactions

For the factorial design experiments, Sn-Beta (Si/Sn = 96) was added at a 100:1 sugar–metal molar ratio to a 5 wt% sugar solution in a 5 ml thick-walled glass reactor containing a small magnetic stir bar (typically ~40 mg of catalyst in 2 ml of sugar solution). Reactions were performed with d- and L-arabinose interchangeably with no difference in kinetics. Initial rate experiments were done with larger volumes and higher sugar–metal ratios in order to capture the low conversion data points. In order to determine the initial rates at higher temperature ranges, an arabinose to Sn ratio of 1000 or 2000 was used. The thick-walled glass vials were sealed using a PTFE/silicone septa and metal crimp top, placed in a temperature-controlled oil bath, and removed periodically to take samples. The glass reactors were quenched in ice and a small sample volume was removed. Next, 100 μl of the filtered sample and 25 μl of a 10 wt% mannitol solution were mixed in a vial. The samples were analyzed by high-performance liquid chromatography (HPLC) on an Agilent 1260 system equipped with photodiode array ultraviolet and evaporative light-scattering detectors. The reaction products were separated using a Bio-Rad Aminex HPX-87C column heated to 353 K using deionized water (pH = 7) as the mobile phase at a flow rate of 0.6 ml min^{-1} . Ribulose concentrations were determined using an ultraviolet detector at a wavelength of 210 nm. At this wavelength all other sugars had negligible ultraviolet signals. For all

ultraviolet-inactive carbohydrates, the analysis was performed using the evaporative light scattering detector. Samples were run in duplicate on the HPLC and the column was regenerated daily with 0.1 M $\text{Ca}(\text{NO}_3)_2$. Ketoses showed the strongest tendency to shift retention time in the column. Fractionation and NMR were used to check peak purity.

Conversion, selectivity, yield, and turn over frequency (TOF) are defined as follows:

$$\text{Conversion} = \frac{\text{Initial moles of reactant} - \text{Moles of reactant}}{\text{Initial moles of reactant}} \quad (4)$$

$$\text{Selectivity} = \frac{\text{Moles of product} - \text{Initial moles of product}}{\text{Initial moles of reactant} - \text{Moles of reactant}} \quad (5)$$

$$\begin{aligned} \text{Yield} &= \text{Conversion} * \text{Selectivity} \quad (6) \\ &= \frac{\text{Moles of product} - \text{Initial moles of product}}{\text{Initial moles of reactant}} \end{aligned}$$

$$\text{TOF} = \frac{\text{Moles of converted}}{\text{Moles of Sn} * \text{Time}} \quad (7)$$

Characterization

Solution NMR was performed on a Varian Inova 500 MHz spectrometer with an Oxford Instruments magnet and 5 mm double-resonance probe, which was tuned to ^1H , ^{11}B , and ^{13}C before use. Samples were prepared at a sugar concentration of 0.05 g ml^{-1} in D_2O using quartz NMR tubes. No correction was made for an isotope effect on the ion product of water. The spinning frequency was 20 Hz. For ^{11}B 128 transients were taken and for ^{13}C 1024 transients were taken. All ^{11}B spectra were referenced using boric acid (H_3BO_3 , 19.6 ppm) as a secondary standard relative to boron trifluoride etherate ($\text{BF}_3 \text{EtO}_2$). Boric acid was used as an external standard for ^{11}B NMR since the chemical shift for free borate changes with pH. A variable temperature study was also performed in 10 K increments between room temperature and 343 K. ^{13}C NMR was referenced with respect to the C-1 carbon of D-arabinose at 99.47 ppm as a secondary standard relative to 4,4-dimethyl-4-silapentane-1-sulphonic acid.

Raman spectra were acquired on a Kaiser RamanRXN1 spectrometer with a 784.807 nm exciting line from an Invictus diode laser using a HPG-785 grating and a 20 \times microscope objective. For analysis, a drop of sample was placed on a microscope slide coated with aluminum foil. Post-processing included baseline removal and normalization of the largest peak to an intensity of 1.

Optical rotation measurements were performed with a Jasco P-1010 polarimeter using the 589 nm sodium D line at room temperature. After performing separate epimerizations of L-arabinose and D-arabinose and separation of the products by HPLC, the ribose fraction was dried using a lyophilizer and redissolved in D₂O (see Figure S38). The optical rotation was measured and used to calculate the specific rotation based on the concentrations determined by HPLC using a power law calibration curve for dilute samples. Solutions were prepared 24 h prior to measurement in order to allow the sugar conformers to equilibrate.

¹¹⁹Sn solid-state MAS NMR experiments were measured using an 8.46-T (¹H, 360.336 MHz) Oxford wide bore magnet and a home-built spectrometer (courtesy of Dr. David Ruben, FBML-MIT). Experiments were performed using a 4-mm Otsuka Electronics MAS double-resonance probe, tuned to ¹¹⁹Sn. Powdered samples were packed into 4 mm outside diameter (o.d.) ZrO₂ rotors equipped with Vespel drive-caps and Kel-F top-caps with O-ring seals. Dry samples were prepared by heating to 473 K under a 0.1 mbar vacuum and loading the NMR rotor in a glovebox. ¹¹⁹Sn spectra were acquired using a Hahn-echo experiment, RD = 1.3*T₁, 50 kHz vrf, 2–125 second recycle delays, a spinning frequency of $\omega_r/2\pi = 9\text{--}10$ kHz, and between 70 and 80k co-added transients at 295 K. All ¹¹⁹Sn spectra were referenced with respect to SnO₂ at -604.3 ppm as an external standard relative to trimethyltin. A T₁ curve was generated to determine an appropriate relaxation time.

Contour plots were generated by fitting a surface to the experimental data using a linear scattered interpolant, applying five cycles of 40 × 40 point surface convolution using a 3 × 3 matrix with a central weight of 0.4, side weights of 0.1 and corner weights of 0.05, and then stretching this smoothed surface to fit the data using nonlinear parameter fitting. This method avoided data over fitting, the introduction of anomalous peaks due to cubic splines and the use of polynomial surface models which have unusual behavior at the edges of the data. In order to maintain continuity between the sodium to borate and pH plots the pH contour plots were obtained by a conformal mapping of the sodium to borate reactivity surface using a separate pH surface response model. This was possible because reactivity varied smoothly with sodium to borate ratio. Contour lines were determined using a default Origin Delaunay triangulation with B-Spline curves.

5.4 Results and discussion

Borates have found application in organic synthesis due to their ability to complex with cis-diols of organic molecules.¹⁰⁶ Thus, in the presence of borates, sugars in solution can exist as a free sugar, a one boron one sugar molecular complex (B^-L), a one boron two sugar molecular complex (B^-L_2) and/or a two boron one sugar molecular complex ($B^-)_2L$ (see Figure 13). The ribose–borate complex is ca. 41 kJ/mol more stable than the arabinose–borate complex.¹⁰⁷ Previous studies have also shown that sugar–borate complexes formed with tetrahedral borate are much stronger than those formed with trigonal borates with complexation timescales considerably faster than those involved in the epimerization reactions.⁷⁸ Borates in solution can exist in an uncharged trigonal form, a negatively charged tetrahedral form as well as an intricate polyanionic mixture (see Figure 13). The nature of the borate speciation in solution is a strong function of pH. For $pH < 5$ borate exists almost exclusively as boric acid H_3BO_3 ; for $pH > 11$ as the tetraborate ion $B(OH)_4^-$; and at intermediate pH values, as a complex mixture of trigonal borate (B), tetrahedral borate (B^-), and borate polyanions.¹⁰⁸ Sodium tetraborate (the borate salt initially used in the Sn-Beta/borate epimerization system) contains two neutral B and two negatively charged B^- species counterbalanced by two sodium cations and, due to charge neutrality arguments, the fraction of tetrahedral boron in solution is equal to the ratio of sodium to boron in the starting material. Thus sodium tetraborate has a B^-/B of 0.5 while, sodium metaborate has a B^-/B of 1. Sodium metaborate corresponds to boric acid fully titrated with sodium hydroxide (NaOH) into tetrahedral borate; therefore, titration of boric acid with NaOH provides an effective method to control the B^-/B ratio, and, consequently, reaction pH.

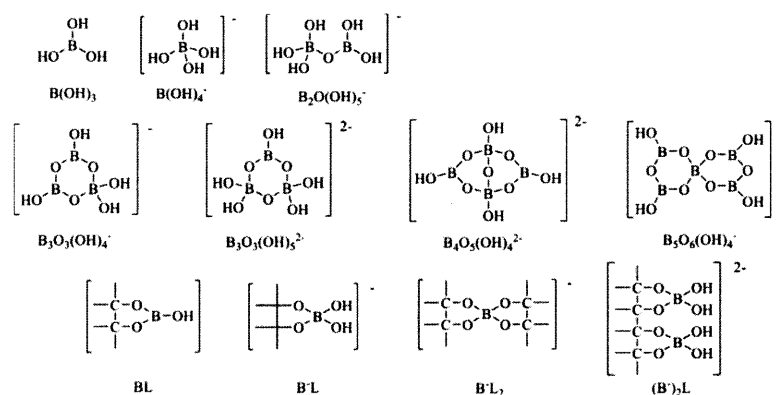


Figure 13. Schematic representation of borate species in solution and borate–sugar complexes.

Table 8 and Figure 14 show the results of a full $7 \times 4 \times 4$ factorial design involving pH, sugar to borate ratio, and reaction time as reaction variables for the epimerization of arabinose to ribose. Experiments were designed to facilitate comparison at constant B^-/B and pH. In this chapter, low pH refers to values lower than 7, near-neutral pH refers to values in the range of 7–7.8, and high pH refers to values of higher than 7.8. In order to relate reactivity to the concentration of borate species, the fraction of B^-L and B^-L_2 was determined with ^{11}B NMR at room temperature (see Table S16 and Figure S43). A separate variable temperature ^{11}B NMR study showed similar spectra up to 343 K with a shift toward monoester at higher temperatures. The ^{11}B data show that the fraction of complexed borate increases steadily with pH and that the ratio between mono and diester is almost constant across the pH spectrum.

Table 8. Full factorial design involving pH, borate to sugar ratio and reaction time as reaction variables for the epimerization of arabinose to ribose.

Entry	Borate– arabinose	B ⁻ /B	pH	BL ⁻	BL ₂ ⁻	15 min			30 min			45 min			60 min		
						C ^a [%]	S1 ^b [%]	S2 ^c [%]	C ^a [%]	S1 ^b [%]	S2 ^c [%]	C ^a [%]	S1 ^b [%]	S2 ^c [%]	C ^a [%]	S1 ^b [%]	S2 ^c [%]
1	1:0:1	0	3.75	0	0	11	11	24	14	22	27	17	27	26	18	31	26
2		0.23	6.5	0.05	0.12	31	73	5	39	71	4	44	64	5	48	60	5
3		0.41	6.97	0.15	0.26	31	87	3	40	78	2	45	75	2	49	69	4
4		0.5	7.21	0.19	0.31	28	91	3	34	89	4	37	85	4	39	85	5
5		0.64	7.5	0.24	0.38	18	65	1	27	46	1	26	59	1	29	52	1
6		1	8.37	0.38	0.46	4	7	2	3	12	5	5	9	2	9	6	1
7	0.5:1	0	3.93	0	0	7	5	20	9	17	26	11	22	26	14	25	24
8		0.22	6.51	0.06	0.13	24	64	6	30	61	8	33	55	9	35	49	8
9		0.45	7.02	0.15	0.29	30	82	3	36	77	4	39	76	5	42	69	5
10		0.5	7.11	0.16	0.33	31	84	3	35	81	4	38	80	5	41	75	6
11		0.74	7.49	0.23	0.46	30	65	1	37	60	1	41	60	2	43	58	2
12		1	8.37	0.3	0.59	12	52	2	14	56	3	17	47	3	18	49	2
13	0.4:1	0	3.98	0	0	10	13	28	13	22	29	15	27	28	19	30	25
14		0.21	6.5	0.05	0.11	22	66	8	27	60	11	30	55	12	32	52	13
15		0.45	6.97	0.15	0.3	31	72	3	37	70	3	41	63	4	45	57	4
16		0.5	7.1	0.16	0.34	29	80	3	33	80	4	37	75	5	39	73	6
17		0.78	7.5	0.24	0.5	27	70	3	33	73	3	37	69	3	40	67	4
18		1	7.88	0.3	0.59	14	69	2	16	72	4	19	70	3	18	82	4
19		1.1	8.37	0.31	0.64	9	72	4	12	67	5	16	62	5	17	56	6
20	0.2:1	0	4.1	0	0	9	15	29	14	26	30	17	31	27	20	33	24
21		0.21	6.5	0.15	0.29	19	47	11	24	43	13	26	43	15	29	42	15
22		0.46	6.99	0.15	0.29	20	59	3	25	62	4	28	57	5	30	56	6
23		0.5	7.09	0.16	0.33	26	70	4	29	69	6	31	66	7	33	60	8
24		0.8	7.5	0.26	0.48	24	75	2	30	75	4	33	74	4	34	75	4
25		1	7.83	0.28	0.59	22	67	3	27	67	4	30	69	5	34	64	5
26		1.1	8.38	0.32	0.64	21	71	4	25	71	5	27	75	6	31	64	6
27	0:0:1	na	4.51	na	na	23	46	23	28	40	29	33	36	31	35	36	35

Reactions were performed at a 100:1 sugar–metal molar ratio with a 5 wt% arabinose feed at 343 K in a stirred batch reactor using Sn-Beta with a Si/Sn of 96. B⁻/B fraction is equal to the Na/B ratio used to make the solutions. The fraction BL⁻ and BL₂⁻ represent the normalized ¹¹B NMR areas without correction for different NMR transfer efficiencies.

^a C refers to arabinose conversion.

^b S1 refers to ribose selectivity.

^c S2 refers to ribulose selectivity.

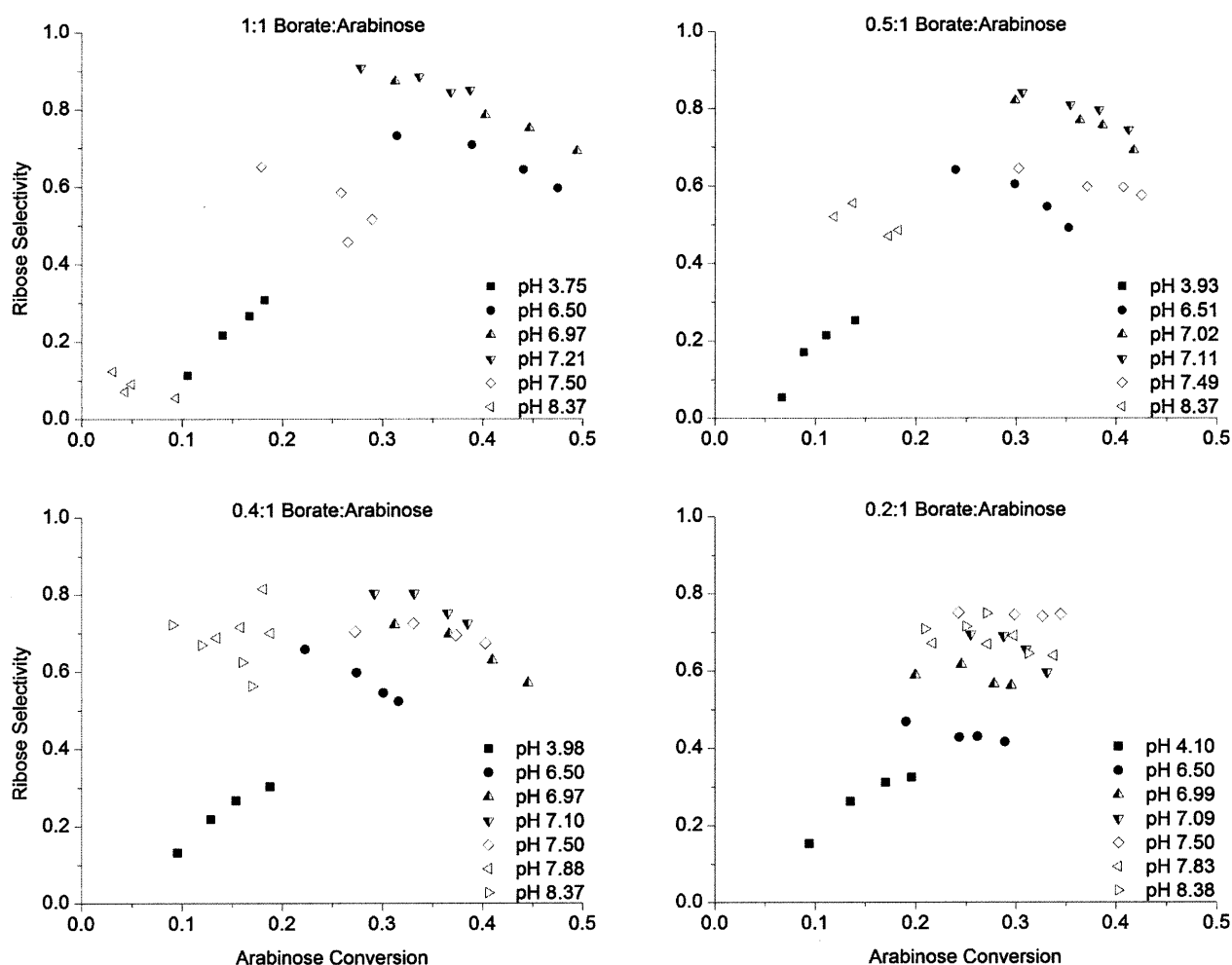


Figure 14. Factorial design for the conversion of a 5 wt% arabinose solution at 343 K using Sn-Beta and a borate co-catalyst. Reactions were performed at a 100:1 sugar–metal molar ratio with a 5 wt% arabinose feed at 343 K in a stirred batch reactor, using Sn-Beta with a Si/Sn of 96.

The experimental data show that pH has a drastic effect on epimerization selectivity and reactivity. For a solution featuring a 1:1 borate–arabinose ratio, low pH values hindered epimerization pathways, yielding low ribose selectivities <30%. In the presence of the borate additive, a conversion of 11% was obtained at a pH of 3.75 after 15 min at 343 K, whereas in the absence of borates, a conversion of 23% is achieved under similar reaction conditions, thus suggesting that borates slightly inhibit reactivity at low pH values. Conversely, at near-neutral pH conditions ribose selectivities exceeding 50% were obtained, reaching a maximum of 91% at a pH of 7.21. In the pH range of 6.5–7.5, high arabinose conversions ranging from 18% to 32% were observed after 15 min. Note that the observed product distribution contains ribose in excess of the amount predicted from the thermodynamic equilibrium, indicating that

the equilibrium is shifted toward the epimer by preferential borate–ribose complexation. At high pH values the reaction rate was drastically inhibited and the low ribose selectivity values obtained (<10%) are not quantitative since the conversion measurements are within the error of the analytical method. When the amount of borate is systematically decreased, the optimal pH to maximize epimerization activity and selectivity gradually increases. For instance, using a 0.2:1 borate–arabinose ratio, a 27% arabinose conversion with 75% selectivity to ribose is obtained at a pH of 8.38 after 45 min. These data also demonstrate that epimerization pathways continue to dominate over isomerization pathways even when substoichiometric amounts of borate are used. The low ribulose yield obtained with substoichiometric borate suggests that borate inhibits isomerization even in the presence of free sugar suggesting that the sugar borate complex is dynamic and could form preferentially in the pores of the zeolite (see Figure S40). Control experiments and mass balances accounting for >98% of the carbon exclude the possibility of low ribulose yields due to borate–ribulose complexation. These results suggest that one borate molecule may influence the reactivity of many sugar molecules in a catalytic cycle or that borate species remain inside the zeolite pores, potentially influencing the active site directly.

Borate ions are known to catalyze the isomerization of aldoses to ketoses in alkaline media.¹⁰⁹ Control experiments in the presence of borates but in the absence of Sn-Beta were performed to quantify the extent of homogeneous isomerization. Table 9 shows results for reactions performed with 1:1 borate–arabinose solutions. For all the pH values investigated, arabinose conversion never exceeded 1% even after 120 min at 343 K. Reactions performed using a combination of Si-Beta and borate were also unreactive.

Table 9. Control experiments for arabinose conversion in the presence of borates but in the absence of Sn-Beta. Reactions were performed with a 5 wt% arabinose feed at 343 K in a stirred batch reactor.

Arabinose– Borate	B ⁻ /B	pH	Conversion [%]	
			60 min	120 min
1:01	0	3.75	<1	<1
	0.23	6.5	<1	<1
	0.41	6.97	<1	<1
	0.64	7.5	<1	<1
	1	8.37	<1	<1

Figure 15 shows a series of contour plots mapping the dynamic arabinose conversion and ribose yield as a function of pH ratio and borate–sugar ratio (see Figure S41 for ribulose study). Note that a near-linear relationship exists between the NaOH–HBO₃ ratio and pH, which is characteristic of weak acid titrations (see Figure S42). Ribose selectivity and arabinose conversion rates reached their maximum values in near-neutral pH conditions and rapidly tailed off at either extremes of the NaOH–HBO₃ range investigated, thus leading to the appearance of a sharp maximum in ribose yield in the contour plot. In the range where maximum reactivity and selectivity is observed, the ratio of tetragonal to trigonal boron species (i.e. B⁻/B) is ca. ~0.5. Diverting from this B⁻/B ratio leads to sharp decreases in activity and selectivity, possibly suggesting that both species are required to promote the epimerization pathway. Note that tetragonal borate readily interacts with internal diols in the sugar backbone, whereas trigonal borate can react with hydroxyl groups, such as those present in the Sn open site or in the silanols present next to the Sn open site, via an sp³d intermediate.¹⁰⁵ The rate constant for arabinose conversion in the presence of borate under acidic conditions is approximately half of that calculated in the absence of borate, thus suggesting that while trigonal borate does not appreciably bind to arabinose it can inhibit the reaction presumably by interacting with the Sn site. Additionally, the low ribulose selectivity and low unaccounted carbon suggest the isomerization is virtually shut down at neutral pH conditions. Consequently, borate binding may impact the binding of arabinose to the active site and alter elementary steps involved in the hydride shift isomerization mechanism.³⁰ Studies are currently underway to determine if Sn–O–B are formed during the reaction.

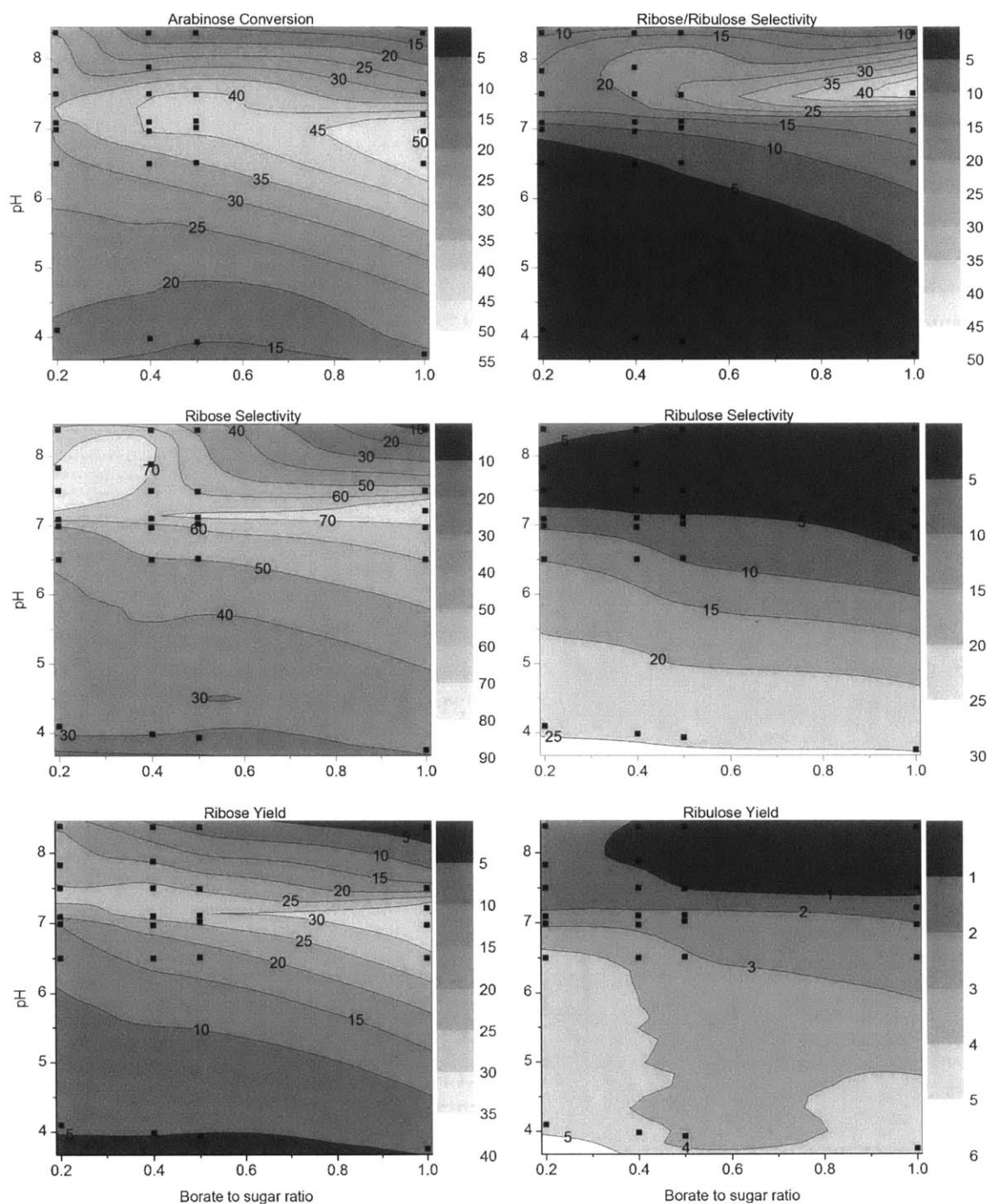


Figure 15. Contour plots as a function of borate to sugar ratio and pH at 60 minutes for: (a) arabinose conversion, (b) ratio of ribose to ribulose selectivities (i.e., instantaneous selectivity of ribose), (c) ribose selectivity, (d) ribulose selectivity, (e) ribose yield, (f) ribulose yield. The response surface lies the within experimental error of all experimental points which are labeled with dots on the plot. Reactions were performed at a 100:1 sugar–metal molar ratio with a 5 wt% arabinose feed at 343 K in a stirred batch reactor, using Sn-Beta with a Si/Sn of 96.

The mechanism for the Bilik reaction involves the formation of a rigid complex between three to four hydroxyl groups of the sugar and a molybdate dimer.^{85b} Since polyborates occur in near-neutral pH conditions it is plausible that an analogous rigid complex could be formed between a borate dimer and the sugar. Therefore, Raman spectroscopy was used to probe borate-containing solutions at different pH values for the presence of polyborates. As shown in Figure 16, the resulting spectra clearly show bands at 872 and 745 cm^{-1} corresponding to $\text{B}(\text{OH})_3$ and $\text{B}(\text{OH})_4^-$ species, respectively; however, no evidence for polyborate species with a sharp maximum at near-neutral pH conditions was found.¹⁰⁸ Resonances corresponding to borate chains were less apparent likely because sugar complexation affects their vibrational frequencies or because they are, in fact, a minor component in the solution. A mechanism that requires polyborates would be difficult to rationalize in the context of steric effects inside the pores of the zeolite and also in view of the carbon-shift epimerization recently observed with Sn-Beta in methanol.

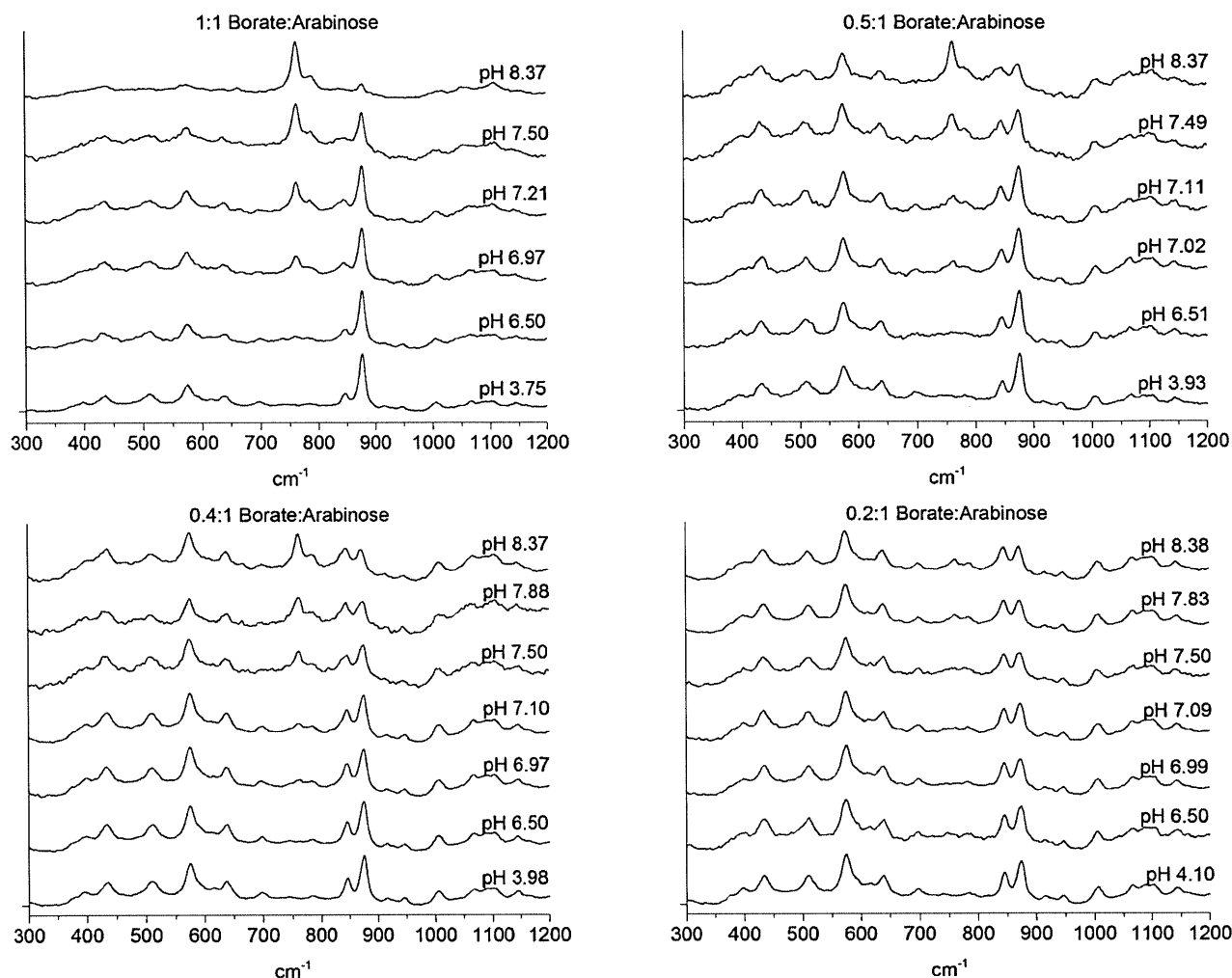


Figure 16. Raman spectra for 5 wt% arabinose solutions with borate obtained at 298 K.

^{11}B NMR was used to further study the complete inhibition of isomerization and epimerization reactions observed under basic conditions (see Figure S43 and Table S16). At high pH values, the formation of B^-L_2 complexes is slightly favored. We hypothesize that the B^-L_2 complexes formed within the pores may cause pore blocking. Also, the B^-L_2 complexes also lack open B-O-H bonds, effectively decreasing the number of available protons that may participate during key reaction steps, including ring-opening/closing sequences and product desorption from the site.^{30, 110} Interestingly, Figure S43 shows a ^{11}B resonance at 10.9 ppm in the BL_2^- region that reaches a maximum as a function of pH for a given borate–arabinose ratio. The pH value at which this maximum is observed increases as the borate–arabinose ratio decreases. A compensation effect is seen wherein the fraction of the BL_2^- species increases in such a way that the ratio of BL_2^- to BL^- remains roughly constant with decreasing borate loadings. Although the presence or absence of B^-L_2 complexes cannot fully explain the inhibition or

promotion of reactivity, further studies are required to understand the role of hydroxyl species on reactions rates.

Kinetic parameters were extracted for arabinose conversion under epimerization conditions. Prior to acquiring reactivity data, an appropriate stirring speed was selected to avoid external intermolecular mass transfer limitations, and a Madon-Boudart test was performed to rule out internal mass transfer limitations. As shown in Figure 17 and Figure S44, the initial epimerization TOFs remained constant for identical catalyst volumes with zeolites featuring Si/Sn ratios ranging from 98 to 367, thus showing the absence of intra-pore diffusion artifacts at the reaction conditions of interest. Next, the reaction order was determined by varying the feed concentration under differential conditions over a wide range of concentrations (see Figure 18 and Figure S45). Turnover rates were determined by normalizing the moles of arabinose converted by the total moles of Sn on each catalyst at conversion levels <15%. As shown in Figure 18, arabinose epimerization follows first order kinetics, thus suggesting that sugar coverage at the active site is low under the reaction conditions investigated. An Arrhenius plot was used to calculate an apparent activation energy of 98 kJ/mol and pre-exponential factor of $1.9 \times 10^{14} \text{ L mol Sn}^{-1} \text{ s}^{-1}$ for the epimerization reaction (see Figure 19, Table S17 and Figure S46). Ribose selectivity remained high for all temperatures investigated, indicating that homogeneous side reactions were not dominant. The amount of ribose formed from ribulose isomerization (i.e., 1,2 hydride-shift pathway) with respect to that formed from arabinose epimerization (i.e., 1,2 carbon-shift pathway) was estimated from ^{13}C NMR data of reaction products obtained using $[^{13}\text{C}_1]$ arabinose feeds. A 5:1 arabinose–borate solution reacted at pH 7.21 for 60 min yielded ca. 29% $[^{13}\text{C}_2]$ ribose C_1 , 4% $[^{13}\text{C}_1]$ ribose, and 2% $[^{13}\text{C}_1]$ ribulose. The ratio of $[^{13}\text{C}_1]$ ribose to $[^{13}\text{C}_1]$ ribulose is approximately equal to the isomerization thermodynamic equilibrium value (see Figure S47 and Figure S48). The NMR data for reactions performed with stoichiometric borate show that a similar product distribution is obtained to that of the 5:1 arabinose:borate case. Further, initial rate data show that the $[^{13}\text{C}_2]$ ribose and the $[^{13}\text{C}_1]$ ribulose selectivity remains constant at low conversions, which is consistent with a reaction pathway that does not involve ribulose as an intermediate (see Table S18). These data suggest that the observed arabinose consumption corresponds predominantly to ribose production via the 1,2 carbon-shift epimerization pathway.

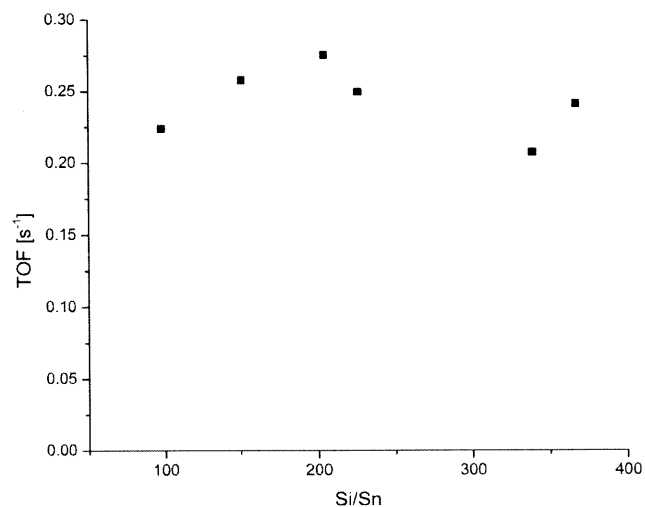


Figure 17. Madon-Boudart diffusion test at 343 K. Experiments were performed with 20 mg of Sn-Beta and a sufficient volume of 5 wt% arabinose to achieve a 2000 sugar–metal ratio in a stirred batch reactor.

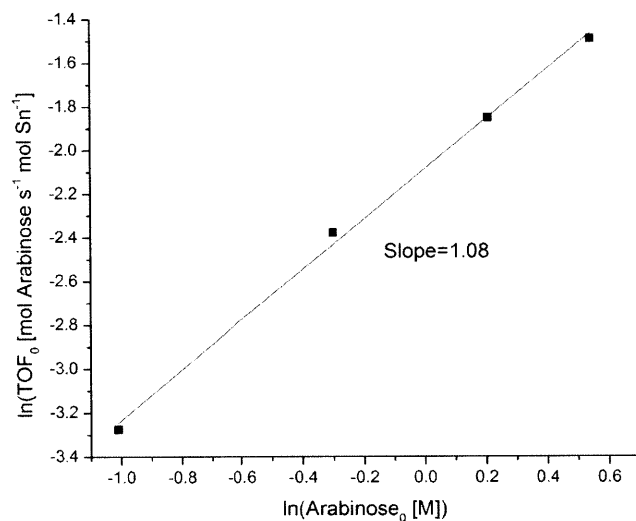


Figure 18. Reaction order plot for initial rates at 343 K and 1000:1 sugar–metal with a 5 wt% arabinose 1:1 borate–arabinose solution at pH 7.21 in a stirred batch reactor. The catalyst used was Sn-Beta with a Si/Sn of 98.

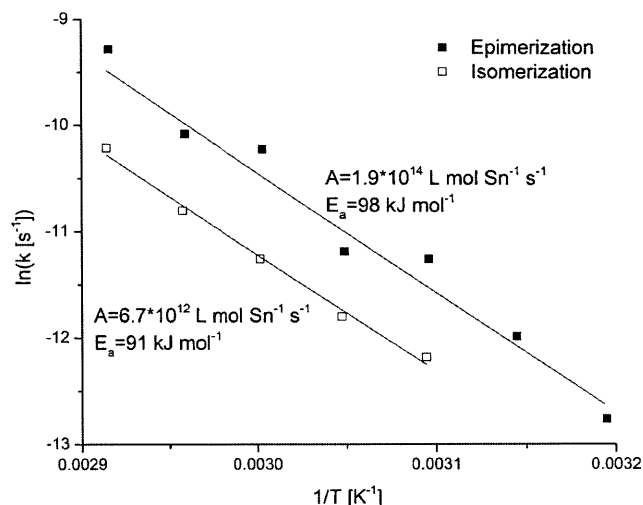


Figure 19. Arrhenius plot for first order epimerization and isomerization reactions with 1000:1 sugar–metal. Epimerization reactions were performed with a 5 wt% arabinose 1:1 borate–arabinose feed at pH 7.21 in a stirred batch reactor using Sn-Beta with a Si/Sn of 98. Isomerization was performed unbuffered with 5 wt% arabinose.

Analogous kinetic experiments were performed in the absence of borate. An apparent activation energy of 91 kJ/mol and a pre-exponential factor of $6.7 \times 10^{12} \text{ L mol Sn}^{-1} \text{ s}^{-1}$ were obtained for arabinose isomerization (see Table S17 and Figure S49). These values are similar to the energy barriers previously calculated for glucose.³⁰ Thus, under optimal conditions, the epimerization rate constant at 343 K ($0.23 \text{ L mol Sn}^{-1} \text{ s}^{-1}$) is roughly twice that of the isomerization without borate ($0.093 \text{ L mol Sn}^{-1} \text{ s}^{-1}$) and the similarities between the isomerization and epimerization kinetics are consistent with a common intermediate such as the open chain form of the sugar. The differences in rates are mostly associated with differences in the pre-exponential factors. The higher pre-exponential factor observed for the epimerization of borates may result from more favorable open vs. closed site distribution in the presence of borate or due to a dual Lewis acid activation wherein borate contributes to spatially arrange the sugar in a more desirable configuration near the active site.

Optical rotation measurements demonstrated the stereospecific nature of the epimerization reaction. The specific rotation of a sugar varies with solvent and borate concentration, and requires time to equilibrate, making it difficult to determine an enantiomeric excess.¹¹¹ Optical rotation results shown in Table 10, confirm the stereospecific nature of the epimerization reaction using Sn-Beta in conjunction with borate salts.

Table 10. Optical rotation measurement used to assess stereospecificity.

Carbohydrate ^a	$[\alpha]_D$
Literature D-ribose ¹¹²	-18.8 to -23.7
Literature L-ribose ¹¹²	18.7–24.0
Ribose from D-arabinose	-14
Ribose from L-arabinose	21

^a Literature values are at 274 K while experimental values are at 298 K.

5.5 Conclusion

A full $7 \times 4 \times 4$ factorial experimental design for NaOH–HBO₃ (i.e., pH), sugar to borate ratio, and reaction time facilitated optimization of ribose production and showed that low pH values favored isomerization pathways, near-neutral pH values favored epimerization pathways and high pH values inhibited both epimerization and isomerization. Optimal pH values ranging from 7.0 to 7.5 and high borate to sugar ratios were found to promote borate complexation with the sugar, effectively decreasing the concentration of free arabinose and promoting epimerization via a 1,2 carbon-shift mechanism. Importantly, 1,2 carbon-shift epimerization products dominated most product distributions even when using substoichiometric amounts of borate, thus suggesting a potential interaction of borate species with the active site that inhibits isomerization pathways. Reactivity and ¹¹B NMR characterization data showed that although the fraction of complexed sugar (B⁻L and B⁻L₂) increases with pH, reactivity declines at high pH values, thus indicating that the fraction of complexed borate is not a sufficient descriptor of reactivity. The maximum in reactivity as a function of pH is consistent with both charged and uncharged borates partitioning into the zeolite and participating in the reaction. The Sn-Beta/borate system shows high epimerization activity at low temperature following a first order rate law over a wide temperature range. Optical rotation measurements confirmed the stereospecific nature of the epimerization reaction. The isolated Lewis acid sites inside the hydrophobic zeolite present an interesting opportunity to study the Sn-borate catalytic pair and the unusual C-C bond-forming and bond-breaking events it promotes. Future studies are geared at understanding the nature of the borate interaction with the active site.

6 Mechanistic implications of a novel tin borate nanostructure on the epimerization of glucose with Sn-Beta zeolite

6.1 Abstract

Sn-Beta zeolite with sodium tetraborate cooperatively catalyzes the epimerization of aldoses via an intramolecular 1,2 carbon shift mechanism. The present work describes a detailed mechanistic study using nuclear magnetic resonance spectroscopy to probe the structure of the glucose-borate-tin complex formed within the zeolite and provide evidence for the pseudocatalytic behavior of borate. The reaction can occur via a Bilik-type mechanism or a retro-Aldol/Aldol addition sequence. Deuterium labeling experiments showed that the deuterium was retained on the same carbon before and after the carbon shift reaction. Reactions performed with sugars deoxygenated at various C positions demonstrated the importance of oxygens at C-1, C-2 and C-3. The absence of a secondary kinetic isotope effect for a [3-2H]glucose showed that C-3 does not undergo sp^3 to sp^2 hybridization, which would have been characteristic of a retro-Aldol reaction. In order to identify which chemical functionality was effecting this transformation, NMR proximity measurements were performed. $^{13}\text{C}\{^{11}\text{B}\}$ rotational-echo double-resonance (REDOR) NMR showed that borate was bound to C-1 and C-2 of glucose and $^{11}\text{B}\{^{13}\text{C}\}$ REDOR revealed that the borate complexed to the tin site is tetrahedral. $^{13}\text{C}\{^{119}\text{Sn}\}$ REDOR indicated that in the presence of borate, either glucose C-1, C-2, and C-3 are closest to the Sn site or that a higher fraction of glucose is bound to Sn. 2D ^{13}C - ^{13}C radio frequency-driven recoupling (RFDR) NMR showed that glucose was present in the pyranose form. The structure reveals how borate could bring C-1 close enough to C-3 in the presence of the Sn to facilitate bond migration. Based on this information and additional computational analysis, it was possible to determine the structure of the glucose-borate-tin complex at the active site, further supporting a concerted Bilik-type epimerization reaction involving the Sn and borate.

6.2 Introduction

Pure silica zeolites containing isolated metal atoms have recently emerged as a new class of water-tolerant Lewis acid catalysts capable of activating carbonyl groups.¹¹ The hydrophobic pores of these molecular sieves exclude bulk water similar to certain pockets within enzymes and the metal atoms function analogously to enzyme cofactors. In particular, Beta zeolites have a 3D intersecting pore structure with large 0.65-nm pores that facilitate small molecule transport to internal catalytic sites

within the large surface area. These atomically dispersed metal catalytic sites incorporate into the crystalline framework of the zeolite and are tetrahedrally coordinated under dehydrated conditions, but adopt a pseudo-octahedral geometry upon the adsorption of two water molecules. The key to unique catalytic activity is the ability to hydrolyze one of the four metal-O-Si bonds of the framework that are normally intact to form an open site. This results in a dual Lewis acid/base character, which is useful for cooperative catalysis. By contrast, extraframework metal oxide species form an octahedral geometry and display very different catalytic activity. Several methods are available to distinguish between framework and extraframework sites, including dynamic nuclear polarization (DNP) NMR and pyridine adsorption.⁴² These methods utilize solid-state NMR (ssNMR) to interrogate metal atoms within zeolite pores where surface characterization techniques would fail.

The water-tolerant Sn-beta zeolite is an effective catalyst for the conversion of glucose to fructose.^{12b} One way to modify the properties of the Sn active site in the hydrophobic zeolite is through the incorporation of a sodium tetraborate (STB) promoter. This enables cooperative catalysis and tuning of the product distribution. Borate is known to interact with cis-diols such as those present in sugar molecules and, similar to sulfated zirconia, borate can also interact with catalysts to form borated zirconia, titania and stannia. Additionally, borate can interact with silica surfaces such as SBA-15.¹⁴ Given that boron has a single bond radii of 0.85 Å compared to 1.16 Å for Si, borate may fit in the Sn-Beta open site in a manner analogous to complexation with cis-diols. As such, borate can promote stronger complexation and alter the geometry of reactant adsorption, potentially leading to different reaction pathways. In the borate-promoted Sn-Beta catalyst, boron, silicon and Sn are positioned at the metal-nonmetal boundary and are known to be active in C-C bond forming reactions, which are important in catalysis. They also have increasing electronegativity in the order Sn<Si<B, suggesting that the incorporation of borate may improve the Lewis acidity of the metal active site. Thus, these elements are natural choices for a catalyst and promoter pair.¹⁷

The ability of boron to expand its coordination shell from trivalent to tetravalent allows it to temporarily form and break bonds to the reactant and catalyst active site. Boron has three valence electrons ($2s^2 2p^1$) which can form a trigonal planar sp^2 hybrid, such as $B(OH)_3$. This structure is stabilized by electron donation from the filled oxygen p_z orbitals to the unfilled $2p_z$ orbital on the boron through the π -bonding framework. However, in this structure, boron is electron deficient (6 shared electrons, unsatisfied octet) and therefore acts as a Lewis acid. Addition of an electron donor to this structure leads to a negatively

charged tetrahedral anion with sp^3 hybridization. Borate is known to catalyze Aldol reactions through tight 6-membered transition states and can also undergo addition with itself to form rigid structures that potentially facilitate more complex reactions.¹⁶

Previous work showed that Sn-Beta zeolites with STB catalyzed the epimerization of carbohydrates in aqueous media through an intramolecular carbon shift.¹¹³ Specifically, addition of STB to the Sn-Beta-catalyzed conversion of glucose flipped the product distribution from fructose to mannose and conversion to mannose occurs through an unusual 1,2 C-C bond shift reaction. Glucose conversion to fructose however occurs through a 1,2 hydride shift isomerization reaction. A full factorial experimental design provided additional insight into the catalytic consequences of varying key reaction parameters such as pH and borate loading.⁵⁰ Isomerization occurs under acidic conditions, epimerization dominates under near-neutral conditions, and inhibition of both pathways occurs under basic conditions. The dominance of epimerization over isomerization with substoichiometric borate suggests that borate acts pseudo-catalytically, potentially through esterification of the Sn open site.

In general, the treatment of certain α -hydroxy aldehydes and ketones with a base or Brønsted or Lewis acid can lead to a number of 1,2 carbon bond shift reactions, which result in an isomeric product. This 1,2 rearrangement is classified based on the specific type of substrate or reaction conditions used. For example, an acid-catalyzed transformation of 1,2-diols to ketones or aldehydes via this unusual bond migration is referred to as the pinacol rearrangement.¹¹⁴ Several variations on pinacol-type rearrangement reactions have been described in which the bond migration is driven by different vicinal electrophilic carbon centers to produce a carbonyl group. Relevant to this work is the rearrangement of α -hydroxy ketones, which is referred to as either an acyloin or α -ketol rearrangement. In its most basic sense, an α -ketol rearrangement involves the 1,2 C-C bond migration toward the electrophilic carbonyl carbon center. When a rigid complex with molybdcic acid catalyzes this α -ketol transformation, the reaction is more specifically known as the Bilik reaction.^{85b}

Another mechanism for the 1,2 C-C shift is a retro-Aldol/Aldol addition sequence involving formation of an enol intermediate. An enol and carbonyl can form a C-C bond through an Aldol reaction. Enols are typically trapped through the addition of boron, lithium or trimethylsilyl (TMS) groups. Specifically, boron enolates can form tight six membered transition states that lead to stereoselective Aldol products. The use of silyl enol ethers in Aldol reactions with Lewis acid catalysis is known as the

Mukaiyama Aldol reaction, which proceeds through an open transition state and has less stereoselectivity.¹¹⁵

The present mechanistic study utilizes rotational-echo double-resonance (REDOR) NMR to characterize active sites within the porous Sn-Beta zeolite in order to develop molecular level understanding of how borate interacts with Sn-Beta. REDOR NMR is a ssNMR-based technique that measures the proximity of isolated spin pairs, typically up to 6 Å. In ssNMR, magic angle spinning (MAS) mimics the molecular motion in liquids and averages out the dipolar interaction. Synchronizing a pulse sequence with rotor rotation can, however, selectively reintroduce the dipolar interaction between nuclei under MAS. This allows for the transfer of spin polarization from the observed nuclei to neighboring atoms and the resultant dipolar interaction is inversely proportional to the cube of the distance between the nuclei. For isolated spin pairs, it is possible to fit accurate distances that can be used to infer the structure of an active site complex such as glucose-borate-Sn. Here, structural data from REDOR NMR together with kinetic analyses provided an accurate description of the epimerization mechanism for the Sn-Beta-catalyzed conversion of glucose to mannose. Additionally, density functional theory (DFT) calculations were performed to show that borate binding to the Sn site is energetically favorable, which is consistent with borate acting pseudocatalytically. DFT confirmed that borate can bind through esterification to the Sn open site and may alter adsorption geometry. These data together support a concerted Bilik-type mechanism for the borate promoted Sn-Beta catalyzed reaction system.

6.3 Results

While a 1,2 bond migration occurs in the sodium tetraborate promoted Sn-Beta catalyzed conversion of aldoses, the C-3 center stereochemistry remains unchanged, which is characteristic of a limited set of stereospecific carbon shift mechanisms.⁵⁰ The reaction can proceed through a two-step mechanism involving consecutive retro-Aldol/Aldol reactions or a concerted α -ketol rearrangement. The retro-Aldol/Aldol sequence can start from two different conformations. In the first, no reorientation is necessary whereas the second conformation requires rotation and translation to the opposite side, thus making this second conformation less likely.

In the context of molybdc acid-catalyzed epimerization of aldoses, a concerted α -ketol rearrangement is known as the Bilik reaction. The Bilik reaction applies to aldoses containing at least 4 carbons and requires 3-4 Mo-O-C bonds with C-1 through C-4 in the sugar.^{85b} Similar to the 1,2 hydride transfer for

the conversion of glucose to fructose with Sn-Beta, a Bilik reaction involves a C-2 atom behaving as a nucleophile and migrating with the remainder of the sugar backbone to the electrophilic C-1 center. The Bilik reaction must proceed in a mild acidic solution and leads to an equilibrium mixture of epimeric aldoses without production of the complementary ketose. Vlachos et al. suggested that isomerization and the Bilik reaction comprise glucose coordinating via oxygen 1 and 2 to the Sn center.¹¹⁶ The concerted α -ketol arrangement maintains stereochemistry as clearly shown in Figure 20.

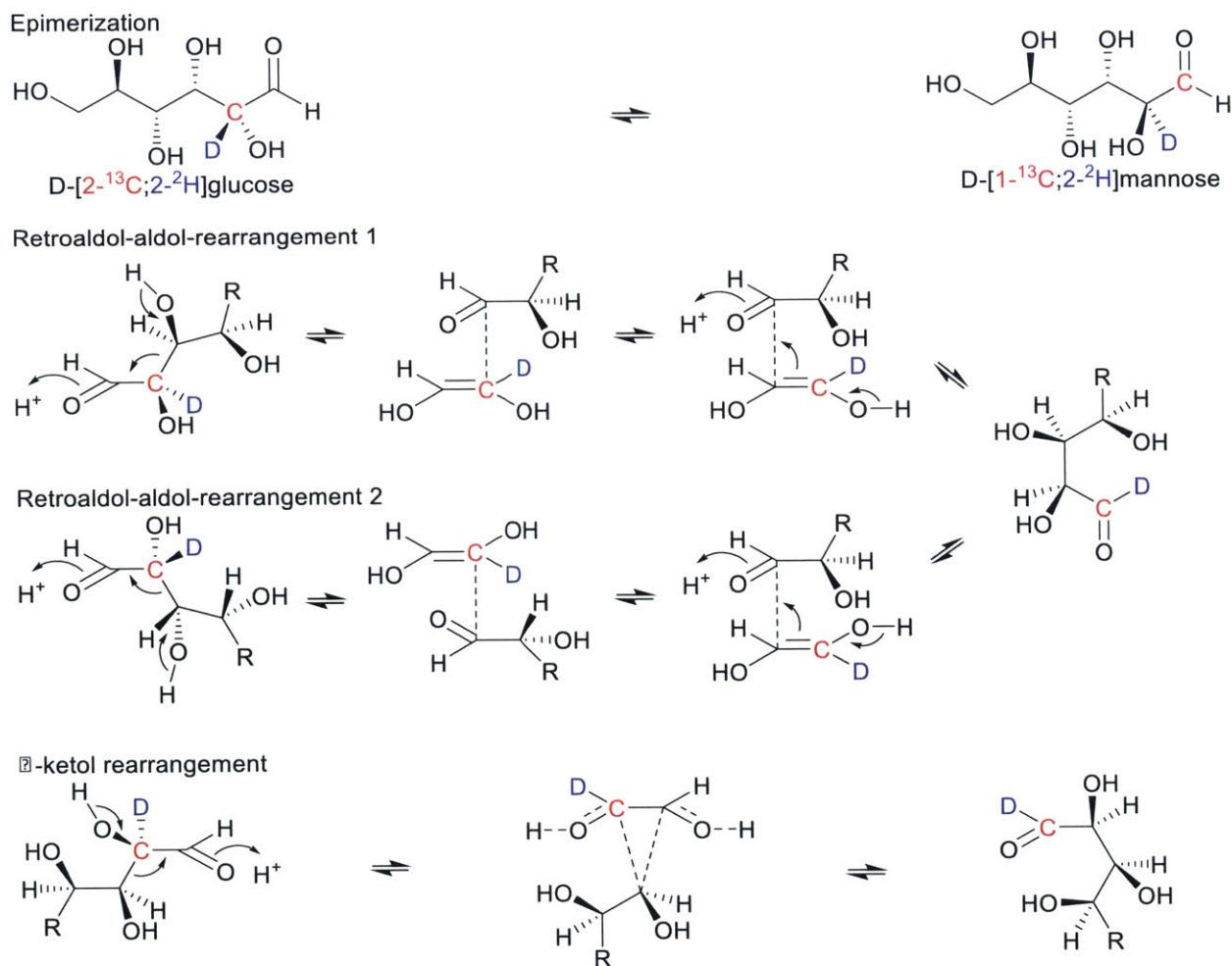


Figure 20. Epimerization mechanism with retention of stereochemistry at C-3.

Both of these mechanisms are known to occur in nature.¹¹⁷ The catalyzed conversion of acetoxy acids into methyl-branched dihydroxy acids proceeds via α -ketol rearrangement, whereas the L-ribulose-5-phosphate-4-epimerase reaction and bacterial class II aldolases includes a retroaldol-aldol mechanism. Another example of this transformation is the deoxyxylulose phosphate pathway, though

which of the two mechanisms actually occurs is not definitively known. These reactions often involve a divalent cation acting as a Lewis acid. In enzymes, acid and base functionalities are provided by carefully placed acidic and basic amino acid residues. In the context of Sn-Beta, the acid and base functionalities could result from the Sn-Beta open site or soft enolization.^{41a, 60a}

One way to distinguish between a retro-Aldol/Aldol versus Bilik mechanism is to look for the formation of an enol intermediate, which is consistent with a retro-Aldol/Aldol sequence. Direct spectroscopic detection of enols is difficult due to the low reactant concentration and position within the zeolite pores. As an alternative, a deuterium labeling approach can be applied to indirectly detect enol intermediates since the formation of enols is often associated with loss of deuterium. However, a careful analysis of the reaction pathways shown in Figure 20 indicates that in a special case, loss of deuterium is not required for enol formation through the retro-Aldol/Aldol sequence when C-3 is a leaving group. If the enol species is long-lived and undergoes keto-enol tautomerization, then it is possible that the deuterium is instead exchanged. In order to determine whether the epimerization reaction potentially passes through an enol, glucose labeled in position 2 with deuterium was used. Epimerization of D-[2-¹³C;2-²H]glucose, fractionation of the products and ¹³C NMR showed the mannose reaction product retained the deuterium at the labeled carbon, indicating that the reaction likely does not involve the formation of an enol. Retention of deuterium also showed that a hydride transfer did not occur. Given that these experiments did not clearly differentiate between the retro-Aldol/Aldol versus Bilik reaction, another set of analyses was subsequently performed.

Kinetic isotope effects can provide a more direct approach to distinguish between these two mechanisms. A kinetic isotope effect measures the change in the chemical reaction rate upon substituting one of the atoms in the reactant molecule with one of its isotopes. There are two types of kinetic isotope effect. Primary kinetic isotope effects result from breaking a bond directly to the labeled atom, whereas secondary kinetic isotope effects result from a labeled atom bound to the atom undergoing bond formation/breakage. The 2-fold increase in mass moving from a H to ²H leads to much larger effects and can produce a 10-20% change in the rate depending on the hybridization of the carbon to which the deuterium is bound. In the Bilik mechanism, C-3 remains at sp³ hybridization throughout and would not exhibit a kinetic isotope effect. In the retro-Aldol/Aldol addition sequence, C-3 undergoes sp³ to sp² rehybridization during the retro-Aldol step and sp² to sp³ rehybridization in the subsequent Aldol step. For [3-²H]glucose, the retro-Aldol step would lead to a normal kinetic isotope

effect while the Aldol step would lead to an inverse kinetic isotope effect in which the rate increases upon deuterium substitution. However, these two opposing effects would likely not cancel but the rate-determining step would be dominant. By virtue of being intermediates, the fragments are at a higher energy than the nearly energetically equivalent reactant and product and the Aldol sequence would not be rate limiting.

A 50:50 mixture of glucose and [3-²H]glucose was reacted to 20% conversion with STB promoted Sn-Beta to determine if the C-3 undergoes sp³ to sp² rehybridization due to the retro-Aldol reaction. In the proposed retro-Aldol reaction, deuterium would slow the conversion of [3-²H]glucose relative to unlabeled glucose leading to a deuterium-enriched glucose mixture. Isotopic enrichment was measured using HPLC fractionation, lyophilization, derivatization and GC-MS. The derivatization reagent and fragment ions were chosen based on published work involving the use of GC-MS to characterize glucose deuterium enrichment.¹¹⁸ As shown in Figure 21, glucose deuterium enrichments before and after the epimerization reaction were identical. By contrast, analogous experiments performed with enzymes have shown a significant 10-19% kinetic isotope effect for a retro-Aldol/Aldol sequence.¹¹⁹ Even accounting for the 20% conversion, the measured deuterium enrichment is still significantly less than the expected kinetic isotope effect for a retro-Aldol/Aldol sequence. These results are therefore consistent with the Bilik mechanism but not the retro-Aldol/Aldol sequence.

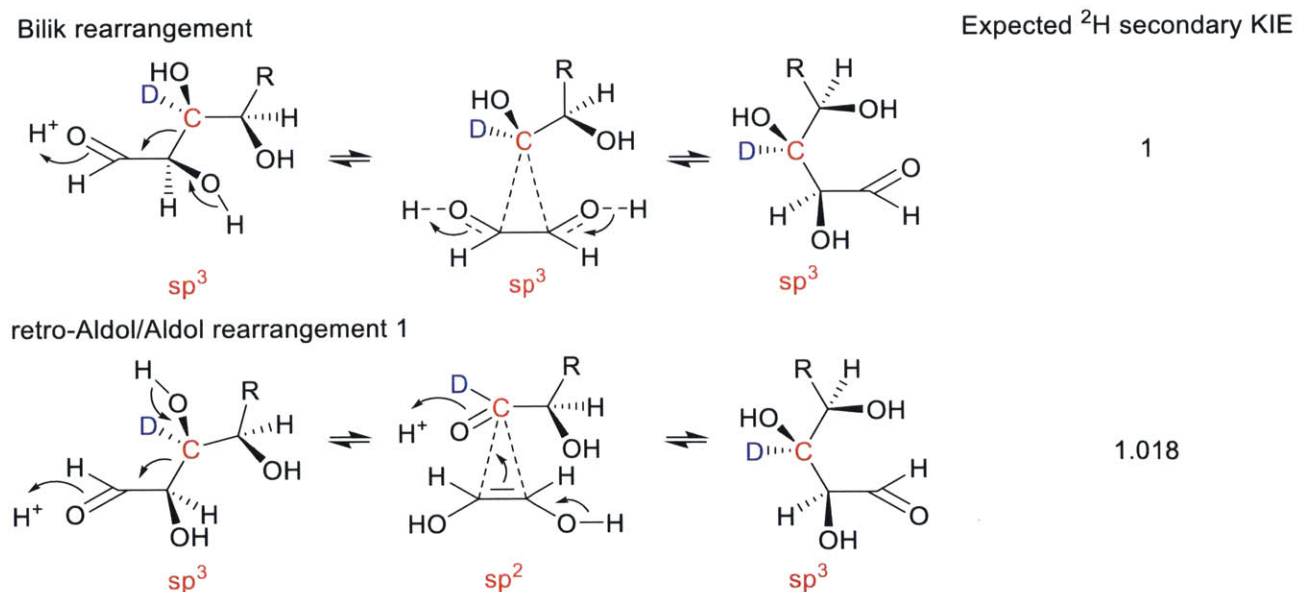


Figure 21. Competitive kinetic isotope study.

Table 11. Results from competitive kinetic isotope study using aldonitrile pentapropionate derivatives and GC-MS.

Sample		Fraction unlabeled glucose	
		m/z 284	m/z 370
Before reaction	Average	0.486	0.503
	Standard deviation	0.003	0.001
After reaction	Average	0.486	0.502
	Standard deviation	0.002	0.001

Substrate specificity

Experiments with deoxygenated sugars showed that the C-1, C-2 and C-3 oxygen atoms were essential for the epimerization to happen selectively. In tandem, reactions performed using singly deoxygenated sugars showed which hydroxyls are necessary for the epimerization to happen selectively. C-2 deoxy proceeded through an uncharacterized reaction with borate. 3-deoxy-D-glucose does not lead to epimerization but 4-deoxy-D-glucose does epimerize, illustrating the importance of hydroxyls at C-3. In the Bilik reaction C-3 deoxy glucose or mannose leads irreversibly to the 3-deoxy-fructose.¹²⁰ The reverse reaction does not occur since C-1 of the ketose lies outside the ring preventing the formation of a rigid complex with the hydroxyl groups at C-1 and C-2. In the Bilik epimerization, 4-deoxy-glucose shows reduced epimerization activity, and the small amount of activity observed may invoke complexation with the C-5 hydroxyl.⁸⁵

Recently, Bermejo-Deval et al. demonstrated that Sn-Beta in a saturated NaCl solution can catalyze the slow epimerization of glucose via a mechanism similar to the Bilik reaction, which involved retention of the deuterium.^{18a} The rate of our sodium tetraborate promoted Sn-Beta catalyzed reaction is more than an order of magnitude faster than the Sn-Beta saturated NaCl reaction rate. Taken together, these results support a similar Bilik-type mechanism in our STB promoted Sn-Beta system but with a different catalytic functionality effecting these transformations as compared to the NaCl Sn-Beta system.

Structural Characterization

Having gained insight into the reaction mechanism, it is informative to next determine which catalytic functions are effecting the transformations described above. This study focused on the mechanistic implications of a novel Sn-O-B nanostructure on the epimerization of glucose with Sn-Beta zeolite. As one of the possible mechanisms, the Bilik reaction requires 4 metal-O-C bonds, which creates a rigid complex that facilitates the concerted C-C bond shift. Three oxygens are required but four can be used.

A similar C-C bond shift mechanism may occur for the borate system and we sought to determine the glucose-borate-Sn structure, specifically if it contains four metal-O-C bonds. It is possible that glucose forms a rigid structure with the borate and Sn site similar to that formed by molybdic acid in the Bilik epimerization reaction.

For the Sn-Beta/borate system, solid state ^{13}C and ^{11}B NMR spectroscopy revealed that the sugar-borate complex exists inside the pores of the zeolite.^{24e} Figure 22 shows a proposed adsorption complex involving borate binding to the Sn-Beta open site as it would to the glucose C-1 and C-2 cis diol. The rigidity of this structure may place strain on bonds similar to the rigid molybdic acid complex in the Bilik reaction. Preliminary DFT structure optimization indicated that the sodium cation balancing the tetrahedral borate situates itself inside a 5-membered ring defined by the Sn and B. While the 1,2 carbon shift likely occurs in a transitory open chain form, the proposed adsorbed structure shows how borate could bring C-1 close enough to C-3 in the presence of the Sn to facilitate the bond migration. The borate can block the Sn open site hydroxyl and therefore inhibit the isomerization pathway.¹¹⁶ Additionally, hydroxyl deprotonation can form a bound alkoxide with increased electron density at the carbon center, potentially facilitating this rearrangement. Simplified representations of the proximity measurements used to define the structure appear on the right in Figure 22.

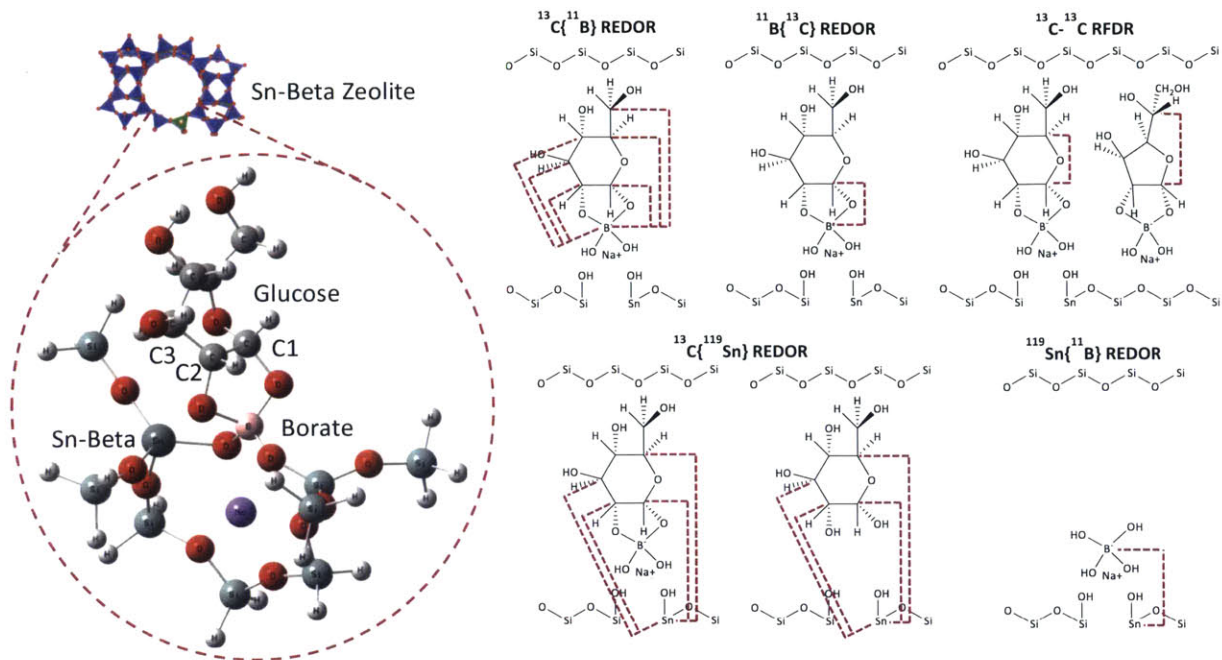


Figure 22. DFT based hypothetical structure of glucose-borate-tin complex featuring Sn-O-B-O-Si nanostructure and proximity measurements used to 'triangulate' the structure.

Based on the proposed structure of the borate-Sn-glucose complex, a potential explanation for the observed stereochemistry is as follows. The borate could hold the C-1 to C-2 enol fragment to prevent it from rotating such that only one face is accessible to a molecule bound at the Sn site. Additionally, binding of the C-3 aldehyde fragment to the Sn site may restrict rotation of its carbonyl group. In order for this stereochemistry to be valid, sugars with different C-3 stereocenters must be in the open chain form. Alternatively, Sn can bridge the C-1 and C-3 oxygens and is known to catalyze a retro-Aldol fragmentation with this geometry.¹²¹ Within this proposed structure, species including both the borate and glucose may dissociate through hydrolysis of the ester bonds. The ability of the borate to remain at the active site may explain its pseudo-catalytic behavior. A number of other promoted active sites are known, including phosphorus-promoted ZSM-5, which is important in fluid catalytic cracking.

$^{13}\text{C}\{^{11}\text{B}\}$ REDOR performed on all six singly ^{13}C -labeled glucose molecules inside the Sn-Beta zeolite showed borate was bound to positions C-1 and C-2 but not C-3, C-4, C-5 and C-6.

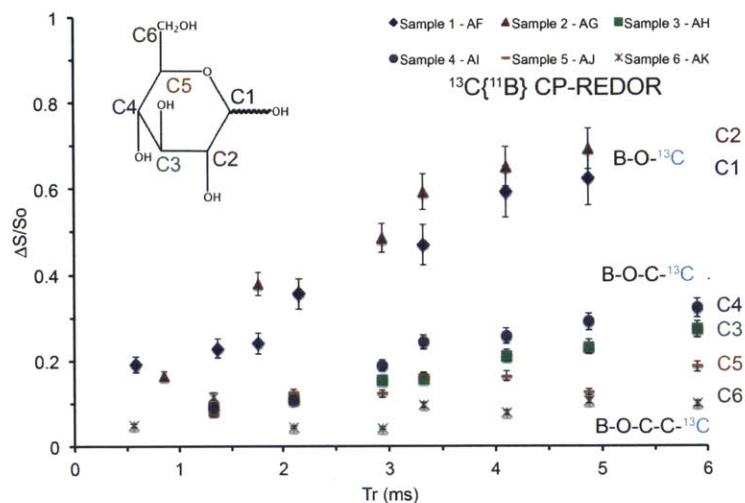


Figure 23. Carbon observed boron dephased distance measurements using singly labeled ^{13}C glucose 4:1 sodium tetraborate.

In the isomerization hydride transfer mechanism, the Sn interacts with C-1 and C-2, which may not be possible with borate. In its most basic sense, REDOR involves siphoning off spin polarization on the observed nucleus into the dephased nucleus and measuring the decreased intensity of the observed nucleus. A caveat to consider when using REDOR is that distance fitting only works with an isolated spin pair. For NMR correlation, proximity presents another limitation because dipolar coupling scales as the inverse cube of the distance between nuclei. Furthermore, coupling maxes out at 9 \AA for ^1H - ^1H interactions.

Based on the REDOR curves, the distance between C-1/C-2 and boron was found to be $2.5 \pm 0.1 \text{ \AA}$, the distance between C-3/C-4 and boron was $4.2 \pm 0.15 \text{ \AA}$ and the distance between C-5/C-6 and boron was $5.1 \pm 0.3 \text{ \AA}$. $^{11}\text{B}\{^{13}\text{C}\}$ REDOR showed the complexed borate was tetrahedral.

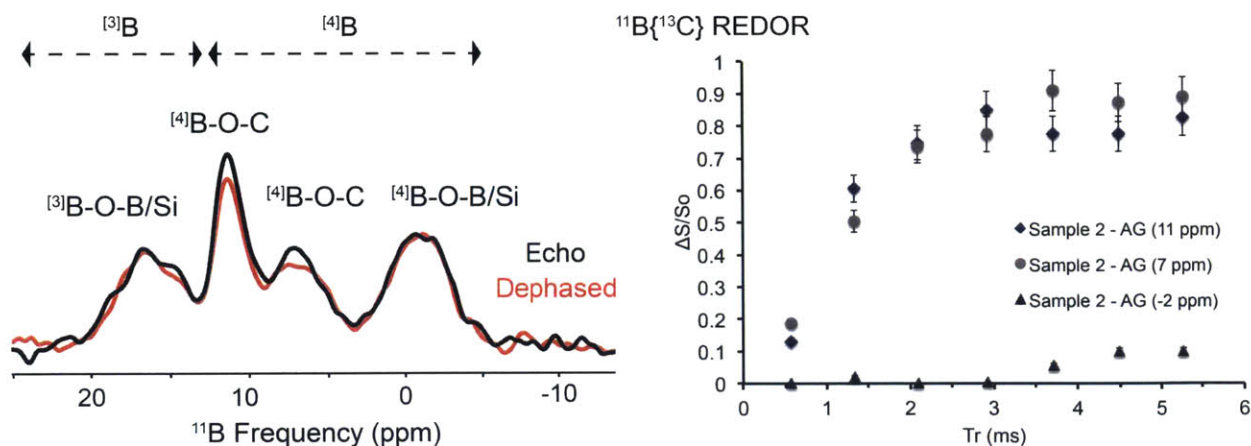


Figure 24. Boron observed carbon dephased distance measurements.

To extend on this concept and determine how borate affects reactant complexation, $^{13}\text{C}\{^{119}\text{Sn}\}$ REDOR was performed as illustrated in Figure 25. The largest decrease in intensity occurs for glucose C-1, indicating it is the closest carbon to the Sn. C-2 and C-3 are also nearby while C-5 is far away. Glucose borate complex, which is not near a Sn, does not exhibit an intensity decrease and thus fitting a distance requires the fraction of bound complexes. The larger decrease in intensity observed with borate compared to free glucose could result from closer glucose binding or from a higher fraction of glucose bound to the Sn site.

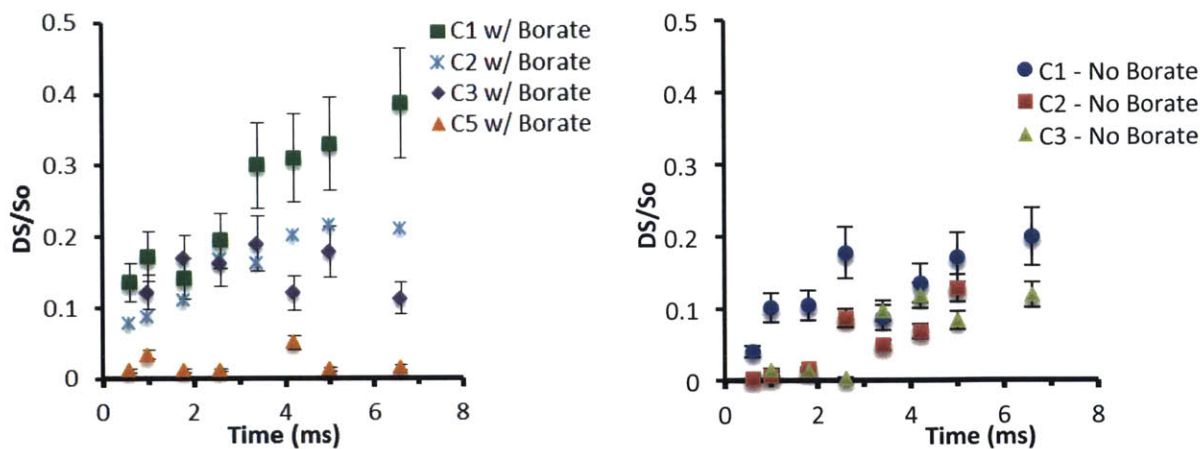


Figure 25. $^{13}\text{C}\{^{119}\text{Sn}\}$ REDOR ssNMR curves show that C-1, C-2 and C-3 are closest to the Sn site and that glucose adsorption is stronger with borate.

As shown in Figure 26, ^{13}C - ^{13}C RFDR spectra revealed a C-1 to C-5 cross peak appearing at short mixing times. This is consistent with the majority of the sugar being present in the pyranose form in the zeolite.

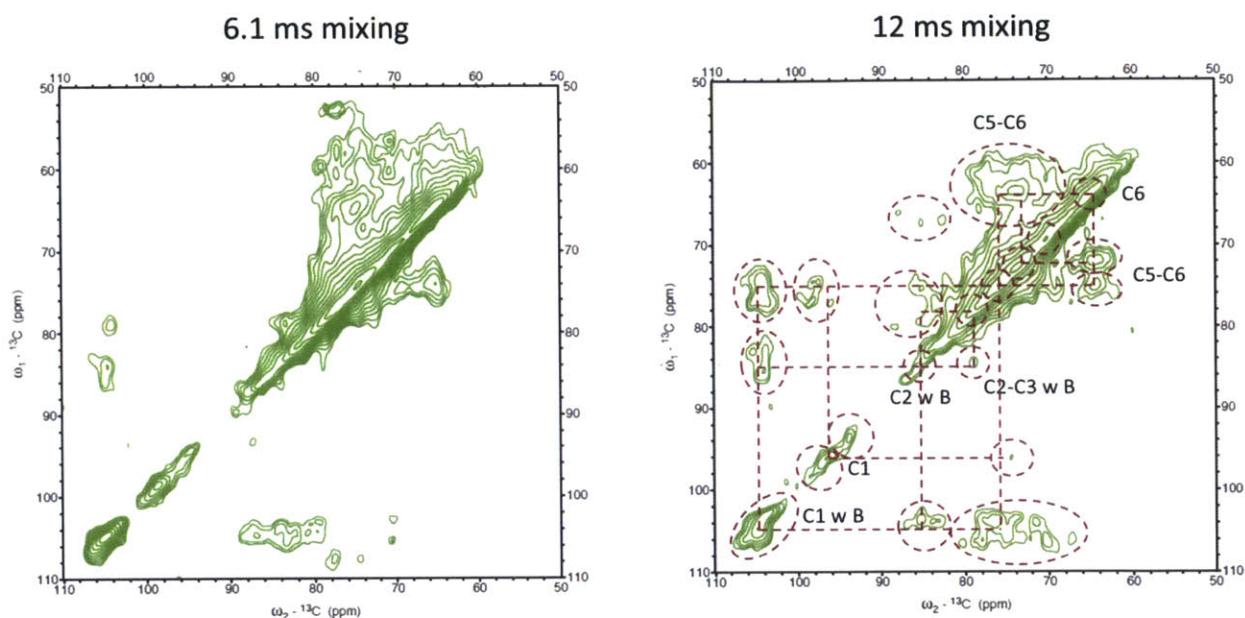


Figure 26. ^{13}C - ^{13}C RFDR ssNMR shows that C-1 and C-5 may be close together, which is consistent with the pyranose form of glucose.

As shown in Figure 27, ^{119}Sn ssNMR of dry Sn-Beta showed new resonances on addition of borate, confirming sodium tetraborate-Sn interactions and the relatively sharp resonances are consistent with a Sn-O-B-O-Si nanostructure.

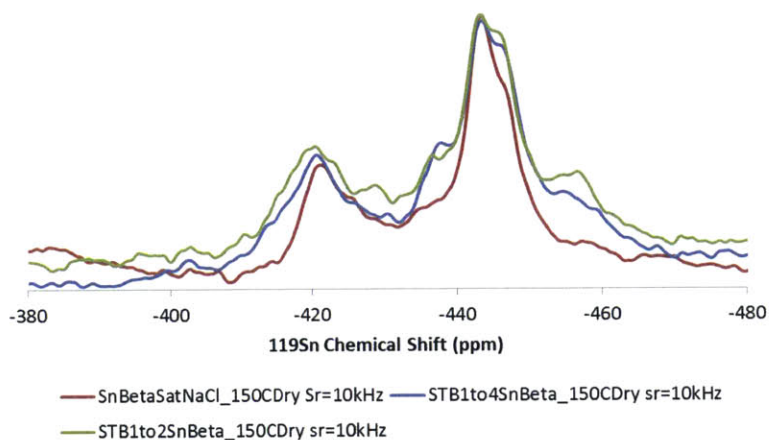


Figure 27. ^{119}Sn NMR of borate adsorbed on Sn-Beta showing the appearance of two new resonances at -437 and -456 ppm.

6.4 Conclusion

Lewis acids catalyze many industrially relevant reactions and the ability to perform Lewis acid catalysis heterogeneously and in the presence of water holds great potential. A current challenge in catalysis is to create nanostructured active sites to mimic the highly selective behavior of enzymes. Many enzymes activate carbonyls when two Lewis acid sites are in close proximity. By analogy, when two Lewis acid sites are tethered together, dramatic rate enhancement has been observed.⁴ Many studies thus far have focused on utilizing unmodified zeolites, but a number of advances towards cooperative catalysis with the application of multi-component systems. Evidence suggests that promoter incorporation can enhance reactant complexation, alter adsorption geometry, and lead to different pathways.

Previous work has shown that sodium borate promoted Sn-Beta can catalyze the epimerization of aldoses in a manner analogous to enzymes.¹¹³ In the borate Sn-Beta system, epimerization proceeds through an unusual C-C bond shift reaction that is similar to the Bilik reaction or retro-Aldol/Aldol addition sequence. This work describes a detailed mechanistic study that seeks to address how borate promoted Sn-Beta can enable aldose epimerization. The observation of enolization and kinetic experiments with deoxygenated and deuterated sugars support a retro-Aldol/Aldol addition. Initially, borate is bound to C-1 and C-2 of glucose and brings C-1, C-2, and C-3 close to the Sn site, which facilitates bond rearrangement. The pseudocatalytic behavior of borate likely results from esterification to the open Sn site, such that stereochemistry within the molecule is preserved. Many different promoters may be incorporated within Sn-Beta to function over a wide pH range and, in general, components within this system may be interchanged to provide finer tuning of product distribution. The production of these advanced catalytic materials with molecular control over the placement of single and multicomponent active sites allows for highly selective chemical transformations.

Lewis acids are more diverse than Brønsted acids and this diversity offers the ability to develop highly selective processes through the incorporation of different promoters. Aside from borate, other sugar complexing agents such as silicate, vanadate, germinate, arsenite, molybdate and aluminate could provide a series of promoters that function across the pH spectrum. For example, molybdate forms reversible complexes under acidic conditions and borate does so under neutral conditions.^{88a} In addition to the complexing agents, other cations such as Cs, which displays basic properties, could be used to replace sodium. In general, the ability to form nanostructures at the open sites of zeolites provides a rich combination of the metal, promoter anion and counter-balancing cation in order to tailor the active

site. Additionally, the presence of two components in close proximity may allow a reactant to bind to one site while the other site facilitates a reaction further away.

7 Concluding Remarks and Future Directions

Catalysts play an important role in many chemical processes, ranging from petrochemical conversions to oxygenate valorization. Zeolite catalysis in particular has found numerous applications in high-temperature gas phase reactions. For example, the use of acidic zeolites in place of non-structured clays for the catalytic cracking of oil can minimize the formation of coke.¹²² The gradual shift from coal to oil and natural gas feedstocks has driven many advances within the field of catalysis, including the catalytic conversion of oxygenates. Relevant to this work are the development of the TS-1 catalyst and hydrophobic zeolites. Lewis acid catalysis typically necessitates strictly anhydrous conditions, but the development of hydrophobic zeolites has removed this constraint. One important example is the Sn-Beta zeolite, which shows similar performance to enzymes in the isomerization of glucose to fructose but is also much more stable.^{12b} Since glucose to fructose conversion is a large bio-catalytic process, the application of Sn-Beta could conceivably improve the economics of high-fructose corn syrup production.

At the present time, oxygenate processing offers a host of new opportunities and challenges. The catalytic technology required to convert oxygenates into many chemical precursors and molecules with beneficial blending properties for fuels is not fully developed. Specifically, C-C bond forming reactions such as Aldol and formose chemistry are needed to upgrade short chain molecules into fungible fuels. A current challenge in catalysis is to create nanostructured active sites to mimic the behavior of enzymes in these types of reactions. Many enzymes activate carbonyls when two Lewis acid sites are in close proximity. By analogy, when two Lewis acid sites are tethered together, dramatic rate enhancement has been observed in MPV and Michael additions.⁴ Much work thus far has focused on utilizing unmodified zeolites, but there is great potential for cooperative catalysis with the application of multi-component systems. Evidence suggests that promoters can enhance reactant complexation, alter adsorption geometry, and lead to different pathways. Within zeolite catalysis, significant research has been conducted on Al-substituted Brønsted acid zeolites, while comparatively little has been performed on other Lewis acidic heteroatom substitutions. As such, there is substantial room for improvement. Another active area of catalysis research encompasses the development of methods to characterize reactions inside zeolites. Methods are also required to verify framework incorporation of metal sites. There are several techniques to characterize zeolites, such as solid-state NMR (ssNMR), infrared spectroscopy, and synchrotron-based analyses, but they each have their own limitations. Thus, there is significant room for method development.

Chemical functionalities may be rationally placed at an active site to generate high degrees of catalytic activity and selectivity. This process requires atomic level understanding of structure-activity relations, which may be achieved through the combined application of synthesis and spectroscopy. One type of hydrophobic zeolites is Sn-Beta zeolite, which shows unique catalytic activity in a wide range of reactions due to its open site and consequent dual acid/base character.¹¹⁶ Modifying Sn-Beta with promoters may further allow the selective activation of functional groups, which is important for oxygenate conversions containing complex mixtures.

The goal of this thesis was to develop molecular level understanding of Lewis acid sites within hydrophobic zeolites and to tailor those sites for directing reactivity. Spectroscopy and mechanistic studies were performed to characterize the active sites. Additionally, Lewis acid sites were tailored through the application of promoters and the resultant changes in reactivity were assessed through kinetic measurements. This thesis focused on the fluoride-synthesized Beta zeolites substituted with transition and post-transition metal heteroatoms and established ssNMR-based methods for their characterization. The reactions and promoters discussed within this work encompassed the conversion of oxygenates in water and cis-diol complexing agents, respectively.

The use of DNP ssNMR resulted in improved ¹¹⁹Sn NMR sensitivity and enabled analysis of natural abundance Sn-Beta in order to distinguish framework and extraframework Sn sites. Subsequent studies described a general method to distinguish Sn site configurations using the ¹⁵N chemical shift of the probe molecule pyridine. The pyridine chemical shift also provided a measure of Lewis acid strength that correlated with electronegativity and was equally applicable under dehydrated and hydrated conditions. Through the application of single pulse ssNMR, it was also possible to assess the number of framework metal sites in the presence of extraframework metal oxides. With these characterization tools, a molecular level understanding of Sn-Beta zeolites was developed and further studies using promoters to modify the metal active sites were performed. Sodium tetraborate-promoted Sn-Beta was shown to cooperatively catalyze the epimerization of aldoses via an unusual 1,2 carbon shift reaction. By contrast, Sn-Beta alone catalyzed a 1,2 hydride transfer isomerization reaction. Kinetic experiments then showed that isomerization occurred under acidic conditions, epimerization dominated under neutral conditions, and inhibition of both processes occurred under basic conditions. Furthermore, epimerization remained dominant with substoichiometric borate, indicating that one borate could influence the reactivity of

multiple aldoses and potentially interact with the active site directly. Using NMR proximity measurements, it was ultimately possible to determine the structure of the glucose-borate-tin complex at the active site, which supported a Bilik-type epimerization reaction.

7.1 Future work

Spectroscopic characterization of zeolites

Since DNP NMR provides improved sensitivity that may lead to informative multidimensional experiments, a natural extension of the Sn DNP work is to investigate interactions of molecules with the Lewis acid sites. However, the tetrachloroethane solvent used in this study is very nonpolar and may not dissolve oxygenates. As such, other solvents that form a glass at cryogenic temperatures and do not interact with the Sn site are of interest. For aqueous reactions, a mixture of water and the chemical of interest as the cryoprotectant may work. Preliminary experiments with glycerol/H₂O/Sn-Beta have shown consistently high enhancements. In addition, hydrated conditions likely allowed protons to closely approach the active site, thereby boosting the polarization transfer efficiency.

Direct DNP may provide sufficient localized signal enhancement to observe long-lived reaction intermediates on the surface of a catalyst. Using radicals that enter the pores but do not interact with the Lewis acid sites or doping the samples with paramagnetic metals containing unpaired electrons such as gadolinium may facilitate direct and solvent free DNP.

DNP also opens up other methods to distinguish framework and extraframework sites. NMR has provided significant insight into the Sn-Beta zeolite owing to the spin $\frac{1}{2}$ ¹¹⁹Sn, but limited work has been done on analogous quadrupolar catalysts. For over 63% of the elements, the only NMR active isotopes are quadrupolar, which leads to broad spectra and poor cross polarization efficiencies.¹²³ For low to moderately quadrupolar nuclei, DNP can compensate for the low sensitivity of multiquantum (MQ) MAS experiments, which can remove second-order quadrupolar broadening. For highly quadrupolar nuclei such as Zr and Hf, calcining the zeolite in a ¹⁷O atmosphere and performing ssNMR may facilitate an indirect characterization of framework incorporation via bridging metal-O-Si bonds.

In terms of locating the framework metal sites, Brouwer and Levitt previously showed that it was possible to determine crystallographic sites using 2D ²⁹Si NMR.¹²⁴ Additional work has been conducted on symmetry-based recoupling methods. However, the gyromagnetic ratio for ²⁹Si limits dipolar coupling

to 5 Å. A potential solution to determine the crystallographic location of heteroatom substitution could be to couple a ^{29}Si - ^{29}Si 2D with a heteroatom in a 3D experiment. Such a technique may provide an alternative to synchrotron-based techniques.

By nature, NMR selectively displays active sites with an attached pyridine, which may not give a complete representation of competitive adsorption with water. Therefore, the effects of water are inferred mainly from changes in the ^{15}N chemical shift. Quantifying the loading of pyridine under hydrated conditions may be informative. Additionally, it may be useful to study the kinetics and activation barrier of water adsorption from the variation in D_2O line width with changing temperatures.

The work presented here focused on pyridine, but other probe molecules such as ^{31}P trimethylphosphine (TMP) may allow for faster acquisition. ^{31}P trimethylphosphine in particular is 100% naturally abundant and possesses an intrinsically more sensitive nucleus, though it is pyrophoric (oxygen sensitive).¹²⁵ Thus far, ^{15}N pyridine can only provide two overlapping resonances in the 1D that likely correspond to the open and closed sites, but enriched ^{15}N pyridine sample did not permit 2D NMRs since such spectra typically involve 64-128 increments. That is, 2D NMRs would require at least 64-stacked 1D spectra and thus a prohibitive amount of time. The application of heteronuclear correlation methods with ^{31}P trimethylphosphine may provide information on the protons polarizing the probe nuclei and on the presence of open metal sites, which are important for reactivity. Preliminary experiments suggest that $^{31}\text{P}\{^1\text{H}\}$ HETCOR for TMP bound to closed sites only shows polarization from the methyl groups while TMP bound to open sites can be polarized from both methyl and -OH protons. With the ability to distinguish open and closed sites, it may be possible to show intrinsic differences in the tendency of different active site metals to form open sites. Hydrolysis of one of the metal-O-Si bonds leads to metal-OH and Si-OH groups, which facilitates cooperative acid/base catalysis with the Lewis acid metal center. The necessity of the open site may explain differences in activity between Ti, Sn, Zr and Hf metal centers since it depends on the amount of framework open sites and not just of framework metal. Based on preliminary findings, Sn-Beta appears to contain a significant fraction of open sites; Ti-Beta contains a small amount; and Hf, Zr, Nb and Ta had essentially none.

Cooperative catalysis and the role of promoters

The work presented here on the sodium borate promoted Sn-Beta system opens up many interesting avenues for future consideration. To understand the role of confinement and hydrophobic effects within

the zeolite, it would be informative to try other frameworks containing Sn. Our findings showed that Sn incorporated into the mesoporous matrix MCM-41 had low activity and selectivity, potentially indicating that confinement effects are important. Triflate metal salts that can survive for short periods in water could allow for a comparison of catalysts with and without any pore structure. Furthermore, grafting isolated transition metal catalysts on quartz could facilitate spectroscopic characterization with IR.

As an extension of the kinetic study described in Chapter 5, it would be informative to determine the equilibrium loading of sodium, borate and glucose between the Sn-Beta zeolite and solution. This would provide insight into how solution species concentration affects observed reactivity, which could help extend a differential model of the reaction network incorporating sugar-borate equilibrium. Additionally, analyzing the distribution of species in solution may address whether the formation of two sugar-one boron complexes can account for the absence of isomerization and epimerization at high pH. These loading studies can be carried out using ssNMR and ICP. However, a potential complication that could affect borate-cis diol complexation is ion exchange with the zeolite silanol protons. The findings in Chapter 5 showed that the fraction of one boron-one sugar and one boron-two sugar complexes changes with temperature, so NMR experiments performed under variable temperatures might be informative. To investigate the species within zeolites under reaction conditions, it is also possible to use diffusion ordered spectroscopy with high-resolution magic angle spinning to see if these complexes diffuse.

With the borate-promoted Sn-Beta system, future studies may also attempt to resolve the finer details of the epimerization mechanism. It would be informative to perform the $^{13}\text{C}\{^{11}\text{B}\}$ REDOR with erythrose in order to study the adsorption geometry of an open chain sugar. Performing flow reactor stability experiments with Sn-Beta plus borate may distinguish whether slow ion exchange or other processes are affecting catalysis. This can be coupled with characterization methods to analyze the spent catalysts. From a commercial standpoint, it would also be interesting to determine the effects of binders and extrusion on catalyst behavior and particularly diffusion. Prior DFT work showed that borate binds to the Sn site, but a complete DFT model of the full epimerization mechanism was not yet developed. Though the present work focuses on the role of borate in the epimerization reaction, it is conceivable that sodium from the sodium tetraborate plays a significant role in shifting the reaction pathway. Further experiments to elucidate the role of sodium could include quenching the reaction via the addition of another component such as methanol. Methanol will bind to and volatilize trigonal borate. Given that

the epimerization reactions proceed through a retro-Aldol/Aldol addition sequence, it would be interesting to characterize other C-C bond formation between other oxygenates.

7.2 Limitations of this work

Sn-Beta zeolites have shown high activity and selectivity in a wide variant of reactions, however the current study has a number of limitations. In general, the ability of a zeolite framework to form different polymorphs and stacking disorders may relieve stress and facilitate the incorporation of large heteroatoms into the zeolite. Beta zeolites consist of a mixture of polymorphs, but many other commercially important frameworks do not. Though Beta zeolites have large 12-membered rings that allow bigger molecules to react, extra-large pore zeolites are difficult to synthesize and are not stable. Additionally, the formation of open sites may be specific to certain metals and zeolite frameworks. Another factor to consider is the cost of zeolite synthesis. Particularly, synthesis of the Sn-Beta zeolite also requires the use of an organic structure-directing agent, which is burned off during calcination. This along with the fluoride hydrothermal synthesis adds to the cost of manufacturing for commercialization. In the system studied, borate is present as a homogeneous co-catalyst necessitating removal post reaction.

A number of ssNMR-based techniques were developed in this study including dynamic nuclear polarization and the use of a general probe molecule to characterize Lewis acid sites within zeolites. DNP demonstrated the ability to dramatically boost the signal, but it is not quantitative. The application of REDOR to active site structure determination of heterogeneous catalysts is also quite novel. A caveat to consider when using REDOR is that distance fitting only works with an isolated spin pair. For NMR correlation, proximity presents another limitation because dipolar coupling scales as the inverse cube of the distance between nuclei. Furthermore, coupling maxes out at 9 Å for strong ^1H - ^1H interactions. Despite these limitations, ssNMR allows for determining the structure of the active site and is often the method of choice for disordered sites.

7.3 Future perspective

Lewis acids are more diverse than Brønsted acids and this diversity offers the ability to develop highly selective processes through the incorporation of different promoters. Aside from borate, it would be informative to study other sugar complexing agents such as silicate, vanadate, germinate, arsenite, molybdate and aluminate, which could provide a series of promoters that function across the pH

spectrum. For example, molybdate forms reversible complexes under acidic conditions and borate does so under neutral conditions.^{88a} In addition to the complexing agents, other cations such as Cs, which displays basic properties, could be used to replace sodium. In general, the ability to form nanostructures at the open sites of zeolites provides a rich combination of the metal, promoter anion and counterbalancing cation in order to tailor the active site. Additionally, the presence of two components in close proximity may allow a reactant to bind to one site while the other site facilitates a reaction further away. Understanding exchange at the open site is useful since the promotional effects of ions on Sn-Beta have shown great potential.

The application of borate promoted Sn-Beta to gas phase reactions could avoid the need to add borate homogeneously. In terms of gas phase reactions, it may also be informative to investigate whether CO can insert into the Sn-OH to form a surface bound formate species that could add to or reduce other species. In these multi-component systems, cooperative catalysis with diverse functionality may be the most interesting reactions to study. Previously, Corma et al. demonstrated the ability to form Pt nanoparticles on top of Sn sites.¹²⁶ Other transition metals are known to bind alkenes. For instance, Zn and Ga modified Al-Beta activates C-H bonds for the conversion of light alkanes to olefins and aromatics.¹²⁷ By analogy with borated zirconia as a superacid, borated Sn-Beta may have Brønsted acidic properties. As an alternative approach, it would be interesting to study the reverse structure in which a Brønsted acidic promoter is supported on a metal site capable of dehydrogenation activity.

As inorganic analogs of enzymes, certain catalysts enable selective chemical transformations at lower temperatures. Inorganic materials are however more robust than enzymes and heterogeneous catalysts allow for easy separation from the reaction mixture. Pertaining to oxygenate conversion, enzymes have evolved into very active and selective catalytic systems and serve as a good model for optimizing catalyst design. The development of water-tolerant Lewis acids enables inorganic materials to behave like hydrophobic pockets within enzymes. By analogy with the isomerases and epimerases in Sn-Beta zeolite, many other biomimetic catalysts exist such as Cu-MOR, which resembles methane monooxygenases.¹²⁸ In addition to the enzymes themselves, inorganic catalysis can benefit from techniques that have traditionally been used for structural biology, such as ssNMR in the determination of enzyme active site structure. Studies on structure activity relations may enable the rational design of catalysts.

This thesis sought to enhance the fundamental understanding of existing catalysts and identify methods to modify their properties. The work presented here demonstrates a robust system for modification of Lewis acid zeolites through the application of promoters in order to control reactivity. It establishes the feasibility of self-assembled nanostructures for cooperative catalysis. While our findings focused on one particular catalyst pair, they may provide a framework for future studies with other advanced catalytic materials.

8 References

1. Yoneyama, M. W. *Catalysts: Petroleum and Chemical Process*; Menlo Park, USA, 2010.
2. Chheda, J. N.; Huber, G. W.; Dumesic, J. A., Liquid-phase catalytic processing of biomass-derived oxygenated hydrocarbons to fuels and chemicals. *Angew. Chem., Int. Ed.* **2007**, *46* (38), 7164-7183.
3. Bruijninx, P. C. A.; Weckhuysen, B. M., Shale Gas Revolution: An Opportunity for the Production of Biobased Chemicals? *Angewandte Chemie International Edition* **2013**, *52* (46), 11980-11987.
4. Roman-Leshkov, Y.; Davis, M. E., Activation of Carbonyl-Containing Molecules with Solid Lewis Acids in Aqueous Media. *ACS Catal.* **2011**, *1* (11), 1566-1580.
5. Lewis, G. N., *Valence and the structure of atoms and molecules*. The Chemical Catalog Company, Inc.: New York, 1923; p 172.
6. Nakon, R.; Rechani, P. R.; Angelici, R. J., Copper(II) complex catalysis of amino acid ester hydrolysis. A correlation with complex stability. *J Am Chem Soc* **1974**, *96* (7), 2117-20.
7. Pearson, R. G.; Songstad, J., Application of the principle of hard and soft acids and bases to organic chemistry. *J. Am. Chem. Soc.* **1967**, *89* (8), 1827-36.
8. Corma, A.; Garcia, H., Lewis Acids: from conventional homogeneous to green homogeneous and heterogeneous catalysis. *Chem. Rev. (Washington, DC, U. S.)* **2003**, *103* (11), 4307-4365.
9. Cejka, J.; Kubicka, D., Zeolites and Other Micro- and Mesoporous Molecular Sieves. In *Kirk-Othmer Encyclopedia of Chemical Technology*, 5th ed.; Kroschwitz, J. I.; Seidel, A., Eds. John Wiley & Sons, Inc.: Hoboken, NJ, 2007; Vol. 26, p 1052 pp.
10. Martinez, C.; Corma, A., Inorganic molecular sieves: Preparation, modification and industrial application in catalytic processes. *Coord. Chem. Rev.* **2011**, *255* (13-14), 1558-1580.
11. (a) Zhu, Y.; Chuah, G.; Jaenicke, S., Al-free Zr-zeolite beta as a regioselective catalyst in the Meerwein-Ponndorf-Verley reaction. *Chem. Commun. (Cambridge, U. K.)* **2003**, (21), 2734-2735; (b) Blasco, T.; Cambor, M. A.; Corma, A.; Esteve, P.; Guil, J. M.; Martinez, A.; Perdigon-Melon, J. A.; Valencia, S., Direct Synthesis and Characterization of Hydrophobic Aluminum-Free Ti-Beta Zeolite. *J. Phys. Chem. B* **1998**, *102* (1), 75-88; (c) Corma, A.; Nemeth, L. T.; Renz, M.; Valencia, S., Sn-zeolite beta as a heterogeneous chemoselective catalyst for Baeyer-Villiger oxidations. *Nature (London, U. K.)* **2001**, *412* (6845), 423-425.
12. (a) Boronat, M.; Concepcion, P.; Corma, A.; Renz, M., Peculiarities of Sn-Beta and potential industrial applications. *Catal. Today* **2007**, *121* (1-2), 39-44; (b) Moliner, M.; Roman-Leshkov, Y.; Davis, M. E., Tin-containing zeolites are highly active catalysts for the isomerization of glucose in water. *Proc. Natl. Acad. Sci. U. S. A.* **2010**, *107* (14), 6164-6168, S6164/1-S6164/8.
13. Derewinski, M.; Sarv, P.; Sun, X.; Muller, S.; van Veen, A. C.; Lercher, J. A., Reversibility of the Modification of HZSM-5 with Phosphate Anions. *J. Phys. Chem. C* **2014**, *118* (12), 6122-6131.
14. Eswaramoorthi, I.; Dalai, A. K., Synthesis, characterization and catalytic performance of boron substituted SBA-15 molecular sieves. *Microporous Mesoporous Mater.* **2006**, *93* (1-3), 1-11.
15. Pyykkoe, P.; Atsumi, M., Molecular single-bond covalent radii for elements 1-118. *Chem. - Eur. J.* **2009**, *15* (1), 186-197.
16. Hoffmann, R. W.; Ditrich, K.; Froech, S., Stereoselective syntheses of alcohols, XXV. Generation of enol borates and their addition to aldehydes. *Liebigs Ann. Chem.* **1987**, (11), 977-85.
17. Carey, F.; Sundberg, R., Carbon-Carbon Bond-Forming Reactions of Compounds of Boron, Silicon, and Tin. In *Part B: Reactions and Synthesis*, Springer Berlin Heidelberg: 2001; Vol. Pt. B, pp 547-593.
18. (a) Bermejo-Deval, R.; Orazov, M.; Gounder, R.; Hwang, S.-J.; Davis, M. E., Active Sites in Sn-Beta for Glucose Isomerization to Fructose and Epimerization to Mannose. *ACS Catal.* **2014**, *4* (7), 2288-2297; (b) Tolborg, S.; Sadaba, I.; Osmundsen, C. M.; Fristrup, P.; Holm, M. S.; Taarning, E.,

- Tin-containing Silicates: Alkali Salts Improve Methyl Lactate Yield from Sugars. *ChemSusChem* **2015**, *8* (4), 613-617.
19. Bermejo-Deval, R.; Gounder, R.; Davis, M. E., Framework and Extraframework Tin Sites in Zeolite Beta React Glucose Differently. *ACS Catal.* **2012**, *2* (12), 2705-2713.
 20. Lewis, J. D.; Van de Vyver, S.; Crisci, A. J.; Gunther, W. R.; Michaelis, V. K.; Griffin, R. G.; Román-Leshkov, Y., A Continuous Flow Strategy for the Coupled Transfer Hydrogenation and Etherification of 5-(Hydroxymethyl)furfural using Lewis Acid Zeolites. *ChemSusChem* **2014**, *7* (8), 2255-2265.
 21. (a) Tang, B.; Dai, W.; Wu, G.; Guan, N.; Li, L.; Hunger, M., Improved Postsynthesis Strategy to Sn-Beta Zeolites as Lewis Acid Catalysts for the Ring-Opening Hydration of Epoxides. *ACS Catalysis* **2014**, *4* (8), 2801-2810; (b) Wolf, P.; Valla, M.; Rossini, A. J.; Comas-Vives, A.; Nunez-Zarur, F.; Malaman, B.; Lesage, A.; Emsley, L.; Coperet, C.; Hermans, I., NMR Signatures of the Active Sites in Sn- β Zeolite. *Angew. Chem., Int. Ed.* **2014**, *53* (38), 10179-10183.
 22. Bare, S. R.; Kelly, S. D.; Sinkler, W.; Low, J. J.; Modica, F. S.; Valencia, S.; Corma, A.; Nemeth, L. T., Uniform Catalytic Site in Sn- β -Zeolite Determined Using X-ray Absorption Fine Structure. *Journal of the American Chemical Society* **2005**, *127* (37), 12924-12932.
 23. (a) Bui, L.; Luo, H.; Gunther, W. R.; Roman-Leshkov, Y., Domino Reaction Catalyzed by Zeolites with Bronsted and Lewis Acid Sites for the Production of γ -Valerolactone from Furfural. *Angew. Chem., Int. Ed.* **2013**, *52* (31), 8022-8025; (b) Corma, A.; Domine, M. E.; Nemeth, L.; Valencia, S., Al-Free Sn-Beta Zeolite as a Catalyst for the Selective Reduction of Carbonyl Compounds (Meerwein-Ponndorf-Verley Reaction). *J. Am. Chem. Soc.* **2002**, *124* (13), 3194-3195.
 24. (a) Luo, H. Y.; Bui, L.; Gunther, W. R.; Min, E.; Roman-Leshkov, Y., Synthesis and Catalytic Activity of Sn-MFI Nanosheets for the Baeyer-Villiger Oxidation of Cyclic Ketones. *ACS Catal.* **2012**, *2* (12), 2695-2699; (b) Roman-Leshkov, Y.; Moliner, M.; Labinger, J. A.; Davis, M. E., Mechanism of Glucose Isomerization Using a Solid Lewis Acid Catalyst in Water. *Angew. Chem., Int. Ed.* **2010**, *49* (47), 8954-8957, S8954/1-S8954/8; (c) Li, L.; Stroobants, C.; Lin, K.; Jacobs, P. A.; Sels, B. F.; Pescarmona, P. P., Selective conversion of trioses to lactates over Lewis acid heterogeneous catalysts. *Green Chem.* **2011**, *13* (5), 1175-1181; (d) de Clippel, F.; Dusselier, M.; Van Rompaey, R.; Vanelderen, P.; Dijkmans, J.; Makshina, E.; Giebel, L.; Oswald, S.; Baron, G. V.; Denayer, J. F. M.; Pescarmona, P. P.; Jacobs, P. A.; Sels, B. F., Fast and Selective Sugar Conversion to Alkyl Lactate and Lactic Acid with Bifunctional Carbon-Silica Catalysts. *J. Am. Chem. Soc.* **2012**, *134* (24), 10089-10101; (e) Gunther, W. R.; Wang, Y.; Ji, Y.; Michaelis, V. K.; Hunt, S. T.; Griffin, R. G.; Román-Leshkov, Y., Sn-Beta zeolites with borate salts catalyse the epimerization of carbohydrates via an intramolecular carbon shift. *Nat Commun* **2012**, *3*, 1109; (f) Holm, M. S.; Saravanamurugan, S.; Taarning, E., Conversion of Sugars to Lactic Acid Derivatives Using Heterogeneous Zeotype Catalysts. *Science (Washington, DC, U. S.)* **2010**, *328* (5978), 602-605.
 25. (a) Moliner, M., State of the art of Lewis acid-containing zeolites: lessons from fine chemistry to new biomass transformation processes. *Dalton Trans.* **2014**, *43* (11), 4197-4208; (b) Dusselier, M.; Van Wouwe, P.; Dewaele, A.; Makshina, E.; Sels, B. F., Lactic acid as a platform chemical in the biobased economy: the role of chemocatalysis. *Energy Environ. Sci.* **2013**, *6* (5), 1415-1442; (c) Boronat, M.; Concepcion, P.; Corma, A.; Renz, M.; Valencia, S., Determination of the catalytically active oxidation Lewis acid sites in Sn-beta zeolites, and their optimization by the combination of theoretical and experimental studies. *J. Catal.* **2005**, *234* (1), 111-118.
 26. (a) Hammond, C.; Conrad, S.; Hermans, I., Simple and Scalable Preparation of Highly Active Lewis Acidic Sn- β . *Angew. Chem., Int. Ed.* **2012**, *51* (47), 11736-11739; (b) Dijkmans, J.; Gabriels, D.; Dusselier, M.; de, C. F.; Vanelderen, P.; Houthoofd, K.; Malfliet, A.; Pontikes, Y.; Sels, B. F., Productive sugar isomerization with highly active Sn in dealuminated β zeolites. *Green Chem.* **2013**, *15* (10), 2777-2785; (c) Li, P.; Liu, G.; Wu, H.; Liu, Y.; Jiang, J.-g.; Wu, P., Postsynthesis and

- Selective Oxidation Properties of Nanosized Sn-Beta Zeolite. *J. Phys. Chem. C* **2011**, *115* (9), 3663-3670; (d) Chang, C.-C.; Wang, Z.; Dornath, P.; Cho, H. J.; Fan, W., Rapid synthesis of Sn-Beta for the isomerization of cellulosic sugars. *RSC Adv.* **2012**, *2* (28), 10475-10477.
27. Mal, N. K.; Ramaswamy, V.; Ganapathy, S.; Ramaswamy, A. V., Synthesis of tin-silicalite molecular sieves with MEL structure and their catalytic activity in oxidation reactions. *Appl. Catal., A* **1995**, *125* (2), 233-45.
28. (a) Lafon, O.; Rosay, M.; Aussenac, F.; Lu, X.; Trebosc, J.; Cristini, O.; Kinowski, C.; Touati, N.; Vezin, H.; Amoureux, J.-P., Beyond the Silica Surface by Direct Silicon-29 Dynamic Nuclear Polarization. *Angew. Chem., Int. Ed.* **2011**, *50* (36), 8367-8370, S8367/1-S8367/16; (b) Renault, M.; Pawsey, S.; Bos, M. P.; Koers, E. J.; Nand, D.; Tommassen-van Boxtel, R.; Rosay, M.; Tommassen, J.; Maas, W. E.; Baldus, M., Solid-State NMR Spectroscopy on Cellular Preparations Enhanced by Dynamic Nuclear Polarization. *Angew. Chem., Int. Ed.* **2012**, *51* (12), 2998-3001, S2998/1-S2998/6; (c) Rossini, A. J.; Zagdoun, A.; Lelli, M.; Gajan, D.; Rascon, F.; Rosay, M.; Maas, W. E.; Coperet, C.; Lesage, A.; Emsley, L., One hundred fold overall sensitivity enhancements for Silicon-29 NMR spectroscopy of surfaces by dynamic nuclear polarization with CPMG acquisition. *Chem. Sci.* **2012**, *3* (1), 108-115; (d) Bayro, M. J.; Debelouchina, G. T.; Eddy, M. T.; Birkett, N. R.; MacPhee, C. E.; Rosay, M.; Maas, W. E.; Dobson, C. M.; Griffin, R. G., Intermolecular Structure Determination of Amyloid Fibrils with Magic-Angle Spinning and Dynamic Nuclear Polarization NMR. *J. Am. Chem. Soc.* **2011**, *133* (35), 13967-13974; (e) Linden, A. H.; Lange, S.; Franks, W. T.; Akbey, U.; Specker, E.; van Rossum, B.-J.; Oschkinat, H., Neurotoxin II Bound to Acetylcholine Receptors in Native Membranes Studied by Dynamic Nuclear Polarization NMR. *J. Am. Chem. Soc.* **2011**, *133* (48), 19266-19269; (f) Gelis, I.; Vitzthum, V.; Dhimole, N.; Caporini, M. A.; Schedlbauer, A.; Carnevale, D.; Connell, S. R.; Fucini, P.; Bodenhausen, G., Solid-state NMR enhanced by dynamic nuclear polarization as a novel tool for ribosome structural biology. *J. Biomol. NMR* **2013**, *56* (2), 85-93; (g) Hall, D. A.; Maus, D. C.; Gerfen, G. J.; Inati, S.; Becerra, L. R.; Dahlquist, F. W.; Griffin, R. G., Polarization-enhanced NMR spectroscopy of biomolecules in frozen solution. *Science (Washington, D. C.)* **1997**, *276* (5314), 930-932.
29. Protesescu, L.; Rossini, A. J.; Kriegner, D.; Valla, M.; de Kergommeaux, A.; Walter, M.; Kravchyk, K. V.; Nachttegaal, M.; Stangl, J.; Malaman, B.; Reiss, P.; Lesage, A.; Emsley, L.; Coperet, C.; Kovalenko, M. V., Unraveling the Core-Shell Structure of Ligand-Capped Sn/SnOx Nanoparticles by Surface-Enhanced Nuclear Magnetic Resonance, Moessbauer, and X-ray Absorption Spectroscopies. *ACS Nano* **2014**, *8* (3), 2639-2648.
30. Bermejo-Deval, R.; Assary, R. S.; Nikolla, E.; Moliner, M.; Roman-Leshkov, Y.; Hwang, S.-J.; Palsdottira, A.; Silverman, D.; Lobo, R. F.; Curtiss, L. A.; Davis, M. E., Metalloenzyme-like catalyzed isomerizations of sugars by Lewis acid zeolites. *Proc. Natl. Acad. Sci. U. S. A.* **2012**, *109* (25), 9727-9732, S9727/1-S9727/19.
31. Kiesewetter, M. K.; Corzilius, B.; Smith, A. A.; Griffin, R. G.; Swager, T. M., Dynamic Nuclear Polarization with a Water-Soluble Rigid Biradical. *J. Am. Chem. Soc.* **2012**, *134* (10), 4537-4540.
32. Wada, T.; Yamanaka, M.; Fujihara, T.; Miyazato, Y.; Tanaka, K., Experimental and Theoretical Evaluation of the Charge Distribution over the Ruthenium and Dioxolene Framework of [Ru(OAc)(dioxolene)(terpy)] (terpy = 2,2':6',2''-terpyridine) Depending on the Substituents. *Inorg. Chem.* **2006**, *45* (22), 8887-8894.
33. Zagdoun, A.; Rossini, A. J.; Gajan, D.; Bourdolle, A.; Ouari, O.; Rosay, M.; Maas, W. E.; Tordo, P.; Lelli, M.; Emsley, L.; Lesage, A.; Coperet, C., Non-aqueous solvents for DNP surface enhanced NMR spectroscopy. *Chem. Commun. (Cambridge, U. K.)* **2012**, *48* (5), 654-656.

34. Van der Wel, P. C. A.; Hu, K.-N.; Lewandowski, J.; Griffin, R. G., Dynamic Nuclear Polarization of Amyloidogenic Peptide Nanocrystals: GNNQQNY, a Core Segment of the Yeast Prion Protein Sup35p. *J. Am. Chem. Soc.* **2006**, *128* (33), 10840-10846.
35. (a) Rossini, A. J.; Zagdoun, A.; Lelli, M.; Canivet, J.; Aguado, S.; Ouari, O.; Tordo, P.; Rosay, M.; Maas, W. E.; Coperet, C.; Farrusseng, D.; Emsley, L.; Lesage, A., Dynamic Nuclear Polarization Enhanced Solid-State NMR Spectroscopy of Functionalized Metal-Organic Frameworks. *Angew. Chem., Int. Ed.* **2012**, *51* (1), 123-127; (b) Lesage, A.; Lelli, M.; Gajan, D.; Caporini, M. A.; Vitzthum, V.; Mieville, P.; Alauzun, J.; Roussey, A.; Thieuleux, C.; Mehdi, A.; Bodenhausen, G.; Coperet, C.; Emsley, L., Surface enhanced NMR spectroscopy by dynamic nuclear polarization. *J. Am. Chem. Soc.* **2010**, *132* (44), 15459-61; (c) Lelli, M.; Gajan, D.; Lesage, A.; Caporini, M. A.; Vitzthum, V.; Mieville, P.; Heroguel, F.; Rascon, F.; Roussey, A.; Thieuleux, C.; Boualleg, M.; Veyre, L.; Bodenhausen, G.; Coperet, C.; Emsley, L., Fast Characterization of Functionalized Silica Materials by Silicon-29 Surface-Enhanced NMR Spectroscopy Using Dynamic Nuclear Polarization. *J. Am. Chem. Soc.* **2011**, *133* (7), 2104-2107; (d) Rossini, A. J.; Zagdoun, A.; Hegner, F.; Schwarzwalder, M.; Gajan, D.; Coperet, C.; Lesage, A.; Emsley, L., Dynamic Nuclear Polarization NMR Spectroscopy of Microcrystalline Solids. *J. Am. Chem. Soc.* **2012**, *134* (40), 16899-16908; (e) Kobayashi, T.; Lafon, O.; Lilly Thankamony, A. S.; Slowing, I. I.; Kandel, K.; Carnevale, D.; Vitzthum, V.; Vezin, H.; Amoureux, J.-P.; Bodenhausen, G.; Pruski, M., Analysis of sensitivity enhancement by dynamic nuclear polarization in solid-state NMR: a case study of functionalized mesoporous materials. *Phys. Chem. Chem. Phys.* **2013**, *15* (15), 5553-5562.
36. Lafon, O.; Thankamony, A. S. L.; Kobayashi, T.; Carnevale, D.; Vitzthum, V.; Slowing, I. I.; Kandel, K.; Vezin, H.; Amoureux, J.-P.; Bodenhausen, G.; Pruski, M., Mesoporous Silica Nanoparticles Loaded with Surfactant: Low Temperature Magic Angle Spinning ^{13}C and ^{29}Si NMR Enhanced by Dynamic Nuclear Polarization. *J. Phys. Chem. C* **2013**, *117* (3), 1375-1382.
37. (a) Bajaj, V. S.; Farrar, C. T.; Hornstein, M. K.; Mastovsky, I.; Viereg, J.; Bryant, J.; Elena, B.; Kreischer, K. E.; Temkin, R. J.; Griffin, R. G., Dynamic nuclear polarization at 9 T using a novel 250 GHz gyrotron microwave source. *J. Magn. Reson.* **2011**, *213* (2), 404-409; (b) Barnes, A. B.; Markhasin, E.; Daviso, E.; Michaelis, V. K.; Nanni, E. A.; Jawla, S. K.; Mena, E. L.; DeRocher, R.; Thakkar, A.; Woskov, P. P.; Herzfeld, J.; Temkin, R. J.; Griffin, R. G., Dynamic nuclear polarization at 700 MHz/460 GHz. *J. Magn. Reson.* **2012**, *224*, 1-7; (c) Becerra, L. R.; Gerfen, G. J.; Temkin, R. J.; Singel, D. J.; Griffen, R. G., Dynamic nuclear polarization with a cyclotron resonance maser at 5 T. *Phys. Rev. Lett.* **1993**, *71* (21), 3561-4.
38. (a) Bui, L.; Luo, H.; Gunther, W. R.; Román-Leshkov, Y., Domino Reaction Catalyzed by Zeolites with Brønsted and Lewis Acid Sites for the Production of γ -Valerolactone from Furfural. *Angew. Chem. Int. Ed.* **2013**, *52* (31), 8022-8025; (b) Corma, A.; Domine, M. E.; Nemeth, L.; Valencia, S., Al-Free Sn-Beta Zeolite as a Catalyst for the Selective Reduction of Carbonyl Compounds (Meerwein-Ponndorf-Verley Reaction). *J. Am. Chem. Soc.* **2002**, *124* (13), 3194-3195.
39. (a) Corma, A.; Renz, M., A general method for the preparation of ethers using water-resistant solid Lewis acids. *Angew. Chem., Int. Ed.* **2007**, *46* (1+2), 298-300; (b) Jae, J.; Mahmoud, E.; Lobo, R. F.; Vlachos, D. G., Cascade of Liquid-Phase Catalytic Transfer Hydrogenation and Etherification of 5-Hydroxymethylfurfural to Potential Biodiesel Components over Lewis Acid Zeolites. *ChemCatChem* **2014**, *6* (2), 508-513.
40. (a) Hammond, C.; Conrad, S.; Hermans, I., Simple and Scalable Preparation of Highly Active Lewis Acidic Sn- β . *Angew. Chem. Int. Ed.* **2012**, *51* (47), 11736-11739; (b) Corma, A.; Nemeth, L. T.; Renz, M.; Valencia, S., Sn-zeolite beta as a heterogeneous chemoselective catalyst for Baeyer-Villiger oxidations. *Nature* **2001**, *412*, 423-425; (c) Renz, M.; Blasco, T.; Corma, A.; Fornés, V.; Jensen, R.; Nemeth, L., Selective and Shape-Selective Baeyer-Villiger Oxidations of Aromatic

Aldehydes and Cyclic Ketones with Sn-Beta Zeolites and H₂O₂. *Chemistry – A European Journal* **2002**, *8* (20), 4708-4717.

41. (a) Van de Vyver, S.; Odermatt, C.; Romero, K.; Prasomsri, T.; Roman-Leshkov, Y., Solid Lewis Acids Catalyze the Carbon-Carbon Coupling between Carbohydrates and Formaldehyde. *ACS Catal.* **2015**, *5* (2), 972-977; (b) Pacheco, J. J.; Davis, M. E., Synthesis of terephthalic acid via Diels-Alder reactions with ethylene and oxidized variants of 5-hydroxymethylfurfural. *Proc. Natl. Acad. Sci. U. S. A.* **2014**, *111* (23), 8363-8367; (c) Dusselier, M.; Van Wouwe, P.; De Smet, S.; De Clercq, R.; Verbelen, L.; Van Puyvelde, P.; Du Prez, F. E.; Sels, B. F., Toward Functional Polyester Building Blocks from Renewable Glycolaldehyde with Sn Cascade Catalysis. *ACS Catal.* **2013**, *3* (8), 1786-1800.
42. Gunther, W. R.; Michaelis, V. K.; Caporini, M. A.; Griffin, R. G.; Roman-Leshkov, Y., Dynamic Nuclear Polarization NMR Enables the Analysis of Sn-Beta Zeolite Prepared with Natural Abundance ¹¹⁹Sn Precursors. *J. Am. Chem. Soc.* **2014**, *136* (17), 6219-6222.
43. Harris, R. K.; Becker, E. D., NMR nomenclature: nuclear spin properties and conventions for chemical shifts - IUPAC recommendations. *J. Magn. Reson.* **2002**, *156* (2), 323-326.
44. Emeis, C. A., Determination of integrated molar extinction coefficients for infrared absorption bands of pyridine adsorbed on solid acid catalysts. *J. Catal.* **1993**, *141* (2), 347-54.
45. (a) de la Torre, O.; Renz, M.; Corma, A., Biomass to chemicals: Rearrangement of β-pinene epoxide into myrtanal with well-defined single-site substituted molecular sieves as reusable solid Lewis-acid catalysts. *Applied Catalysis A: General* **2010**, *380* (1-2), 165-171; (b) Heitmann, G. P.; Dahlhoff, G.; Hölderich, W. F., Modified Beta zeolites as catalysts for the Beckmann rearrangement of cyclohexanone oxime. *Applied Catalysis A: General* **1999**, *185* (1), 99-108; (c) Corma, A.; Llabres i. Xamena, F. X.; Prestipino, C.; Renz, M.; Valencia, S., Water Resistant, Catalytically Active Nb and Ta Isolated Lewis Acid Sites, Homogeneously Distributed by Direct Synthesis in a Beta Zeolite. *J. Phys. Chem. C* **2009**, *113* (26), 11306-11315; (d) Corma, A.; Domine, M. E.; Valencia, S., Water-resistant solid Lewis acid catalysts: Meerwein-Ponndorf-Verley and Oppenauer reactions catalyzed by tin-beta zeolite. *J. Catal.* **2003**, *215* (2), 294-304.
46. Roy, S.; Bakhmutsky, K.; Mahmoud, E.; Lobo, R. F.; Gorte, R. J., Probing Lewis Acid Sites in Sn-Beta Zeolite. *ACS Catal.* **2013**, *3* (4), 573-580.
47. (a) Laurence, C.; Graton, J.; Gal, J.-F., An Overview of Lewis Basicity and Affinity Scales. *J. Chem. Educ.* **2011**, *88* (12), 1651-1657; (b) Laurence, C.; Gal, J.-F., *Lewis basicity and affinity scales: data and measurement*. John Wiley & Sons: Hoboken, N.J., 2009; (c) Li, G.; Pidko, E. A.; Hensen, E. J. M., Synergy between Lewis acid sites and hydroxyl groups for the isomerization of glucose to fructose over Sn-containing zeolites: a theoretical perspective. *Catal. Sci. Technol.* **2014**, *4* (8), 2241-2250; (d) Yang, G.; Pidko, E. A.; Hensen, E. J. M., The Mechanism of Glucose Isomerization to Fructose over Sn-BEA Zeolite: A Periodic Density Functional Theory Study. *ChemSusChem* **2013**, *6* (9), 1688-1696.
48. Brunner, E.; Pfeifer, H., NMR spectroscopic techniques for determining acidity and basicity. *Mol. Sieves* **2008**, *6* (Acidity and Basicity), 1-43.
49. (a) Ripmeester, J. A., Surface acid site characterization by means of CP/MAS nitrogen-15 NMR. *J. Am. Chem. Soc.* **1983**, *105* (9), 2925-7; (b) Michel, D.; Germanus, A.; Pfeifer, H., Nitrogen-15 nuclear magnetic resonance spectroscopy of adsorbed molecules. *J. Chem. Soc., Faraday Trans. 1* **1982**, *78* (1), 237-54; (c) Lezcano-Gonzalez, I.; Vidal-Moya, A.; Boronat, M.; Blasco, T.; Corma, A., Modelling active sites for the Beckmann rearrangement reaction in boron-containing zeolites and their interaction with probe molecules. *Phys. Chem. Chem. Phys.* **2010**, *12* (24), 6396-6403; (d) Freude, D.; Pfeifer, H.; Schmidt, A.; Staudte, B., Characterization of acid centers in HY zeolite by NMR studies of the interaction of hydroxyl groups with pyridine. *Z. Phys. Chem. (Leipzig)* **1984**, *265* (2), 250-6.

50. Gunther, W. R.; Duong, Q.; Roman-Leshkov, Y., Catalytic consequences of borate complexation and pH on the epimerization of L-arabinose to L-ribose in water catalyzed by Sn-Beta zeolite with borate salts. *J. Mol. Catal. A: Chem.* **2013**, *379*, 294-302.
51. (a) Mal, N. K.; Ramaswamy, V.; Rajamohanam, P. R.; Ramaswamy, A. V., Sn-MFI molecular sieves: synthesis methods, ²⁹Si liquid and solid MAS-NMR, ¹¹⁹Sn static and MAS NMR studies. *Microporous Mater.* **1997**, *12* (4-6), 331-340; (b) Gaydhankar, T. R.; Joshi, P. N.; Kalita, P.; Kumar, R., Optimal synthesis parameters and application of Sn-MCM-41 as an efficient heterogeneous catalyst in solvent-free Mukaiyama-type aldol condensation. *J. Mol. Catal. A: Chem.* **2007**, *265* (1-2), 306-315.
52. Pines, A.; Gibby, M. G.; Waugh, J. S., Proton-enhanced NMR of dilute spins in solids. *The Journal of Chemical Physics* **1973**, *59* (2), 569-590.
53. Pines, A.; Gibby, M. G.; Waugh, J. S., Proton-enhanced nuclear induction spectroscopy. Method for high-resolution NMR of dilute spins in solids. *J. Chem. Phys.* **1972**, *56* (4), 1776-7.
54. Bennett, A. E.; Rienstra, C. M.; Auger, M.; Lakshmi, K. V.; Griffin, R. G., Heteronuclear decoupling in rotating solids. *J. Chem. Phys.* **1995**, *103* (16), 6951-8.
55. Frisch, M. J.; Trucks, G. W.; Schlegel, H. B.; Scuseria, G. E.; Robb, M. A.; Cheeseman, J. R.; Scalmani, G.; Barone, V.; Mennucci, B.; Petersson, G. A.; Nakatsuji, H.; Caricato, M.; Li, X.; Hratchian, H. P.; Izmaylov, A. F.; Bloino, J.; Zheng, G.; Sonnenberg, J. L.; Hada, M.; Ehara, M.; Toyota, K.; Fukuda, R.; Hasegawa, J.; Ishida, M.; Nakajima, T.; Honda, Y.; Kitao, O.; Nakai, H.; Vreven, T.; Montgomery Jr., J. A.; Peralta, J. E.; Ogliaro, F.; Bearpark, M. J.; Heyd, J.; Brothers, E. N.; Kudin, K. N.; Staroverov, V. N.; Kobayashi, R.; Normand, J.; Raghavachari, K.; Rendell, A. P.; Burant, J. C.; Iyengar, S. S.; Tomasi, J.; Cossi, M.; Rega, N.; Millam, N. J.; Klene, M.; Knox, J. E.; Cross, J. B.; Bakken, V.; Adamo, C.; Jaramillo, J.; Gomperts, R.; Stratmann, R. E.; Yazyev, O.; Austin, A. J.; Cammi, R.; Pomelli, C.; Ochterski, J. W.; Martin, R. L.; Morokuma, K.; Zakrzewski, V. G.; Voth, G. A.; Salvador, P.; Dannenberg, J. J.; Dapprich, S.; Daniels, A. D.; Farkas, Ö.; Foresman, J. B.; Ortiz, J. V.; Cioslowski, J.; Fox, D. J. *Gaussian 09*, Gaussian, Inc.: Wallingford, CT, USA, 2009.
56. (a) Weigend, F.; Ahlrichs, R., Balanced basis sets of split valence, triple zeta valence and quadruple zeta valence quality for H to Rn: Design and assessment of accuracy. *Phys. Chem. Chem. Phys.* **2005**, *7* (18), 3297-3305; (b) Andrae, D.; Haeussermann, U.; Dolg, M.; Stoll, H.; Preuss, H., Energy-adjusted ab initio pseudopotentials for the second and third row transition elements. *Theor. Chim. Acta* **1990**, *77* (2), 123-41; (c) Metz, B.; Stoll, H.; Dolg, M., Small-core multiconfiguration-Dirac-Hartree-Fock-adjusted pseudopotentials for post-d main group elements: Application to PbH and PbO. *J. Chem. Phys.* **2000**, *113* (7), 2563-2569.
57. Solum, M. S.; Altman, K. L.; Strohmeier, M.; Berges, D. A.; Zhang, Y.; Facelli, J. C.; Pugmire, R. J.; Grant, D. M., ¹⁵N Chemical Shift Principal Values in Nitrogen Heterocycles. *J. Am. Chem. Soc.* **1997**, *119* (41), 9804-9809.
58. Ramsey, N. F., Electron coupled interactions between nuclear spins in molecules. *Phys. Rev.* **1953**, *91*, 303-7.
59. van der Waal, J. C.; Tan, K.; van Bekkum, H., Zeolite titanium beta: a selective and water resistant catalyst in Meerwein-Ponndorf-Verley-Oppenauer reactions. *Catal. Lett.* **1996**, *41* (1,2), 63-67.
60. (a) Li, Y.-P.; Head-Gordon, M.; Bell, A. T., Analysis of the Reaction Mechanism and Catalytic Activity of Metal-Substituted Beta Zeolite for the Isomerization of Glucose to Fructose. *ACS Catal.* **2014**, *4* (5), 1537-1545; (b) Boronat, M.; Corma, A.; Renz, M.; Viruela, P. M., Predicting the activity of single isolated Lewis acid sites in solid catalysts. *Chem. - Eur. J.* **2006**, *12* (27), 7067-7077.

61. Fenzke, D.; Hunger, M.; Pfeifer, H., Determination of nuclear distances and chemical-shift anisotropy from proton MAS NMR sideband patterns of surface hydroxyl groups. *J. Magn. Reson.* **1991**, *95* (3), 477-83.
62. Pearson, R. G., Absolute electronegativity and hardness: application to inorganic chemistry. *Inorg. Chem.* **1988**, *27* (4), 734-40.
63. Zhan, C.-G.; Nichols, J. A.; Dixon, D. A., Ionization Potential, Electron Affinity, Electronegativity, Hardness, and Electron Excitation Energy: Molecular Properties from Density Functional Theory Orbital Energies. *J. Phys. Chem. A* **2003**, *107* (20), 4184-4195.
64. Shetty, S.; Pal, S.; Kanhere, D. G.; Goursot, A., Structural, electronic, and bonding properties of zeolite Sn-beta: A periodic density functional theory study. *Chem. - Eur. J.* **2006**, *12* (2), 518-523.
65. Marschner, C., Hafnium: stepping into the limelight! *Angew. Chem., Int. Ed.* **2007**, *46* (36), 6770-6771.
66. Dijkmans, J.; Dusselier, M.; Gabriels, D.; Houthoofd, K.; Magusin, P.; Huang, S.; Pontikes, Y.; Trekels, M.; Vantomme, A.; Giebeler, L.; Oswald, S.; Sels, B., Cooperative Catalysis for Multistep Biomass Conversion with Sn/Al Beta Zeolite. *ACS Catal.* **2014**.
67. Luo, H.; Consoli, D.; Gunther, W.; Roman-Leshkov, Y., Investigation of the reaction kinetics of isolated Lewis acid sites in Beta zeolites for the Meerwein-Ponndorf-Verley reduction of methyl levulinate to gamma-valerolactone. *J. Catal.* **2014**.
68. Granstrom, T. B.; Takata, G.; Tokuda, M.; Izumori, K., Izumoring: a novel and complete strategy for bioproduction of rare sugars. *J Biosci Bioeng* **2004**, *97* (2), 89-94.
69. Gumina, G.; Song, G. Y.; Chu, C. K., L-Nucleosides as chemotherapeutic agents. *FEMS Microbiol. Lett.* **2001**, *202* (1), 9-15.
70. Lu, Y.; Levin, G. V.; Donner, T. W., Tagatose, a new antidiabetic and obesity control drug. *Diabetes, Obes. Metab.* **2008**, *10* (2), 109-134.
71. Hossain, M. A.; Wakabayashi, H.; Goda, F.; Kobayashi, S.; Maeba, T.; Maeta, H., Effect of the immunosuppressants FK506 and D-allose on allogenic orthotopic liver transplantation in rats. *Transplant. Proc.* **2000**, *32* (7), 2021-2023.
72. Huwig, A.; Emmel, S.; Jakel, G.; Giffhorn, F., Enzymic synthesis of L-tagatose from galactitol with galactitol dehydrogenase from *Rhodobacter sphaeroides* D. *Carbohydr. Res.* **1998**, *305* (3-4), 337-339.
73. Allard, S. T. M.; Giraud, M. F.; Naismith, J. H., Epimerases: structure, function and mechanism. *Cell. Mol. Life Sci.* **2001**, *58* (11), 1650-1665.
74. (a) Holm, M. S.; Pagan-Torres, Y. J.; Saravanamurugan, S.; Riisager, A.; Dumesic, J. A.; Taarning, E., Sn-Beta catalyzed conversion of hemicellulosic sugars. *Green Chem.* **2012**, *14* (3), 702-706; (b) Pescarmona, P. P.; Janssen, K. P. F.; Delaet, C.; Stroobants, C.; Houthoofd, K.; Philippaerts, A.; De Jonghe, C.; Paul, J. S.; Jacobs, P. A.; Sels, B. F., Zeolite-catalysed conversion of C3 sugars to alkyl lactates. *Green Chem.* **2010**, *12* (6), 1083-1089.
75. Huang, R.; Qi, W.; Su, R.; He, Z., Integrating enzymatic and acid catalysis to convert glucose into 5-hydroxymethylfurfural. *Chem. Commun. (Cambridge, U. K.)* **2010**, *46* (7), 1115-1117.
76. Angyal, S. J., Composition and conformation of sugars in solution. *Angew. Chem., Int. Ed. Engl.* **1969**, *8* (3), 157-66.
77. Smoum, R.; Rubinstein, A.; Srebnik, M., Combined ¹H, ¹³C and ¹¹B NMR and mass spectral assignments of boronate complexes of D-(+)-glucose, D-(+)-mannose, methyl- α -D-glucopyranoside, methyl- β -D-galactopyranoside and methyl- α -D-mannopyranoside. *Magn. Reson. Chem.* **2003**, *41* (12), 1015-1020.
78. van den Berg, R.; Peters, J. A.; van, B. H., The structure and (local) stability constants of borate esters of mono- and disaccharides as studied by ¹¹B and ¹³C NMR spectroscopy. *Carbohydr. Res.* **1994**, *253*, 1-12.

79. Walker, T. E.; London, R. E.; Whaley, T. W.; Barker, R.; Matwiyoff, N. A., Carbon-13 nuclear magnetic resonance spectroscopy of [1-¹³C] enriched monosaccharides. Signal assignments and orientational dependence of geminal and vicinal carbon-carbon and carbon-hydrogen spin-spin coupling constants. *J. Am. Chem. Soc.* **1976**, *98* (19), 5807-13.
80. Michaelis, V. K.; Aguiar, P. M.; Kroeker, S., Probing alkali coordination environments in alkali borate glasses by multinuclear magnetic resonance. *J. Non-Cryst. Solids* **2007**, *353* (26), 2582-2590.
81. (a) Bray, P. J., NMR and NQR studies of boron in vitreous and crystalline borates. *Inorg. Chim. Acta* **1999**, *289* (1-2), 158-173; (b) Du, L.-S.; Stebbins, J. F., Nature of Silicon-Boron Mixing in Sodium Borosilicate Glasses: A High-Resolution ¹¹B and ¹⁷O NMR Study. *J. Phys. Chem. B* **2003**, *107* (37), 10063-10076.
82. Angyal, S. J., The Lobry de Bruyn-Alberda van Ekenstein transformation and related reactions. *Top. Curr. Chem.* **2001**, *215* (Glycoscience), 1-14.
83. Bilik, V., Reactions of saccharides catalyzed by molybdate ions. II. Epimerization of D-glucose and D-mannose. *Chem. Zvesti* **1972**, *26* (2), 183-6.
84. (a) Zhao, S.; Petrus, L.; Serianni, A. S., 1-Deoxy-D-xylulose: Synthesis Based on Molybdate-Catalyzed Rearrangement of a Branched-Chain Aldotetrose. *Org. Lett.* **2001**, *3* (24), 3819-3822; (b) Stockman, R.; Dekoninck, J.; Sels, B. F.; Jacobs, P. A., The catalytic epimerization of sugars over immobilized heptamolybdate: comparison of resins, layered double hydroxides and mesoporous silica as support. *Stud. Surf. Sci. Catal.* **2005**, *156* (Nanoporous Materials IV), 843-850.
85. (a) Hayes, M. L.; Pennings, N. J.; Serianni, A. S.; Barker, R., Epimerization of aldoses by molybdate involving a novel rearrangement of the carbon skeleton. *J. Am. Chem. Soc.* **1982**, *104* (24), 6764-9; (b) Petrus, L.; Petrusova, M.; Hricoviniova, Z., The Bilik reaction. *Top. Curr. Chem.* **2001**, *215* (Glycoscience), 15-41.
86. Tanase, T.; Shimizu, F.; Kuse, M.; Yano, S.; Hidai, M.; Yoshikawa, S., Novel C-2 epimerization of aldoses promoted by nickel(II) diamine complexes, involving a stereospecific pinacol-type 1,2-carbon shift. *Inorg. Chem.* **1988**, *27* (23), 4085-94.
87. Koeckritz, A.; Kant, M.; Walter, M.; Martin, A., Rearrangement of glucose to mannose catalyzed by polymer-supported Mo catalysts in the liquid phase. *Appl. Catal., A* **2008**, *334* (1-2), 112-118.
88. (a) Benner, S. A.; Kim, H.-J.; Kim, M.-J.; Ricardo, A., Planetary organic chemistry and the origins of biomolecules. *Cold Spring Harbor Perspect. Biol.* **2010**, *2* (7), No pp. given; (b) Kim, H.-J.; Ricardo, A.; Illangkoon, H. I.; Kim, M. J.; Carrigan, M. A.; Frye, F.; Benner, S. A., Synthesis of Carbohydrates in Mineral-Guided Prebiotic Cycles. *J. Am. Chem. Soc.* **2011**, *133* (24), 9457-9468; (c) Lambert, J. B.; Gurusamy-Thangavelu, S. A.; Ma, K., The Silicate-Mediated Formose Reaction: Bottom-Up Synthesis of Sugar Silicates. *Science (Washington, DC, U. S.)* **2010**, *327* (5968), 984-986.
89. (a) Sagi, V. N.; Punna, V.; Hu, F.; Meher, G.; Krishnamurthy, R., Exploratory Experiments on the Chemistry of the "Glyoxylate Scenario": Formation of Keto-Sugars from Dihydroxyfumarate. *J. Am. Chem. Soc.* **2012**, *134* (7), 3577-3589; (b) Eschenmoser, A., The search for the chemistry of life's origin. *Tetrahedron* **2007**, *63* (52), 12821-12844.
90. Renz, M.; Blasco, T.; Corma, A.; Fornes, V.; Jensen, R.; Nemeth, L., Selective and shape-selective Baeyer-Villiger oxidations of aromatic aldehydes and cyclic ketones with Sn-beta zeolites and H₂O₂. *Chem. - Eur. J.* **2002**, *8* (20), 4708-4717.
91. (a) Agency, O. f. E. C. a. D. I. E. *Energy Technology Perspectives 2012: Pathways to a Clean Energy System*; Paris, 2012; (b) Agency, O. f. E. C.-o. a. D. I. E. *Technology Roadmap: Energy and GHG Reductions in the Chemical Industry via Catalytic Processes*; Paris, 2013; (c) Ren, T.; Patel, M.; Blok, K., Olefins from conventional and heavy feedstocks: Energy use in steam cracking and

- alternative processes. *Energy (Amsterdam, Neth.)* **2005**, *31* (4), 425-451; (d) Cherest, M.; Felkin, H.; Prudent, N., Torsional strain involving partial bonds. The stereochemistry of the lithium aluminum hydride reduction of some simple open-chain ketones. *Tetrahedron Lett.* **1968**, (18), 2199-204.
92. Pines, A.; Gibby, M. G.; Waugh, J. S., Proton-enhanced NMR of dilute spins in solids. *J. Chem. Phys.* **1973**, *59* (2), 569-90.
 93. Morcombe, C. R.; Zilm, K. W., Chemical shift referencing in MAS solid state NMR. *J. Magn. Reson.* **2003**, *162* (2), 479-486.
 94. Wolf, R.; Reiff, F.; Wittmann, R.; Butzke, J. Process for the preparation of riboflavin. 1982.
 95. Okano, K., Synthesis and pharmaceutical application of L-ribose. *Tetrahedron* **2009**, *65* (10), 1937-1949.
 96. Wymer, N.; Taylor, P. Process for the production of L-ribose and other rare sugars using mannitol-1-dehydrogenase. WO2007021879A2, 2007.
 97. Hu, C.; Li, L.-Z.; Zheng, Y.-Y.; Rui, L.-L.; Hu, C.-Y., Perspectives of biotechnological production of L-ribose and its purification. *Appl. Microbiol. Biotechnol.* **2011**, *92* (3), 449-455.
 98. Akagi, M.; Omae, D.; Tamura, Y.; Ueda, T.; Kumashiro, T.; Urata, H., A practical synthesis of L-ribose. *Chem. Pharm. Bull.* **2002**, *50* (6), 866-868.
 99. Tewari, Y. B.; Goldberg, R. N., An investigation of the equilibriums between aqueous ribose, ribulose, and arabinose. *Biophys. Chem.* **1985**, *22* (3), 197-204.
 100. Corma, A.; Navarro, M. T.; Renz, M., Lewis acidic Sn(IV) centers - grafted onto MCM-41 - as catalytic sites for the Baeyer-Villiger oxidation with hydrogen peroxide. *J. Catal.* **2003**, *219* (1), 242-246.
 101. Corma, A.; Renz, M., Water-resistant Lewis-acid sites: carbonyl-ene reactions catalyzed by tin-containing, hydrophobic molecular sieves. *ARKIVOC (Gainesville, FL, U. S.)* **2007**, (8), 40-48.
 102. (a) Choudhary, V.; Pinar, A. B.; Sandler, S. I.; Vlachos, D. G.; Lobo, R. F., Xylose Isomerization to Xylulose and its Dehydration to Furfural in Aqueous Media. *ACS Catal.* **2011**, *1* (12), 1724-1728; (b) Choudhary, V.; Sandler, S. I.; Vlachos, D. G., Conversion of Xylose to Furfural Using Lewis and Bronsted Acid Catalysts in Aqueous Media. *ACS Catal.* **2012**, *2* (9), 2022-2028; (c) Lew, C. M.; Rajabbeigi, N.; Tsapatsis, M., Tin-containing zeolite for the isomerization of cellulosic sugars. *Microporous Mesoporous Mater.* **2012**, *153*, 55-58.
 103. Dusselier, M.; Van Wouwe, P.; de Clippel, F.; Dijkmans, J.; Gammon, D. W.; Sels, B. F., Mechanistic Insight into the Conversion of Tetrose Sugars to Novel α -Hydroxy Acid Platform Molecules. *ChemCatChem* **2013**, *5* (2), 569-575.
 104. Paris, C.; Moliner, M.; Corma, A., Metal-containing zeolites as efficient catalysts for the transformation of highly valuable chiral biomass-derived products. *Green Chem.* **2013**, *15* (8), 2101-2109.
 105. Irwin, A. D.; Holmgren, J. S.; Zerda, T. W.; Jonas, J., Spectroscopic investigations of borosiloxane bond formation in the sol-gel process. *J. Non-Cryst. Solids* **1987**, *89* (1-2), 191-205.
 106. *Organic Reactions*. John Wiley & Sons, Inc.: Hoboken, NJ, 2004.
 107. Sponer, J. E.; Sumpter, B. G.; Leszczynski, J.; Sponer, J.; Fuentes-Cabrera, M., Theoretical study on the factors controlling the stability of the borate complexes of ribose, arabinose, lyxose, and xylose. *Chem. - Eur. J.* **2008**, *14* (32), 9990-9998.
 108. Maeda, M.; Hirao, T.; Kotaka, M.; Kakihana, H., Raman spectra of polyborate ions in aqueous solutions. *J. Inorg. Nucl. Chem.* **1979**, *41* (8), 1217-20.
 109. Mendicino, J. F., Effect of borate on the alkali-catalyzed isomerization of sugars. *J. Am. Chem. Soc.* **1960**, *82*, 4975-9.

110. Assary, R. S.; Curtiss, L. A., Theoretical Study of 1,2-Hydride Shift Associated with the Isomerization of Glyceraldehyde to Dihydroxyacetone by Lewis Acid Active Site Models. *J. Phys. Chem. A* **2011**, *115* (31), 8754-8760.
111. Adam, D.; Jennings, R. P., Effects of borax on the polarization of sugar solutions. *Proc. Annu. Congr. S. Afr. Sugar Technol. Ass.* **1966**, *40*, 206-13.
112. Phelps, F. P.; Isbel, H. S.; Pigman, W., Mutarotation of β -D-ribose and β -L-ribose. *J. Am. Chem. Soc.* **1934**, *56*, 747-8.
113. Gunther, W. R.; Wang, Y.; Ji, Y.; Michaelis, V. K.; Hunt, S. T.; Griffin, R. G.; Roman-Leshkov, Y., Sn-Beta zeolites with borate salts catalyze the epimerization of carbohydrates via an intramolecular carbon shift. *Nat. Commun.* **2012**, *3* (Oct.), 2122/1-2122/8.
114. Song, Z.-L.; Fan, C.-A.; Tu, Y.-Q., Semipinacol Rearrangement in Natural Product Synthesis. *Chemical Reviews* **2011**, *111* (11), 7523-7556.
115. Mukaiyama, T.; Narasaka, K.; Banno, K., New aldol type reaction. *Chem. Lett.* **1973**, (9), 1011-14.
116. Rai, N.; Caratzoulas, S.; Vlachos, D. G., Role of Silanol Group in Sn-Beta Zeolite for Glucose Isomerization and Epimerization Reactions. *ACS Catalysis* **2013**, *3* (10), 2294-2298.
117. Dickschat, J. S., Isoprenoids in three-dimensional space: the stereochemistry of terpene biosynthesis. *Nat. Prod. Rep.* **2011**, *28* (12), 1917-1936.
118. Antoniewicz, M. R.; Kelleher, J. K.; Stephanopoulos, G., Measuring Deuterium Enrichment of Glucose Hydrogen Atoms by Gas Chromatography/Mass Spectrometry. *Anal. Chem. (Washington, DC, U. S.)* **2011**, *83* (8), 3211-3216.
119. Lee, L. V.; Vu, M. V.; Cleland, W. W., ¹³C and Deuterium Isotope Effects Suggest an Aldol Cleavage Mechanism for L-Ribulose-5-phosphate 4-Epimerase. *Biochemistry* **2000**, *39* (16), 4808-4820.
120. Bilik, V.; Petrus, L., Reactions of saccharides catalyzed by molybdate ions; Part XXIV. Selective transformation of 3-deoxy-D-arabino-hexose and 3-deoxy-D-ribo-hexose to 3-deoxy-D-erythro-hexulose. *Collect. Czech. Chem. Commun.* **1978**, *43* (4), 1159-62.
121. Osmundsen, C. M.; Holm, M. S.; Dahl, S.; Taarning, E., Tin-containing silicates: structure-activity relations. *Proc. R. Soc. A* **2012**, *468* (2143), 2000-2016.
122. Plank, C. J.; Rosinski, E. J. Catalytic cracking of hydrocarbons with a crystalline zeolite catalyst composite. US3140249 A, 1964.
123. MacKenzie, K. J. D., *Multinuclear Solid-State Nuclear Magnetic Resonance of Inorganic Materials*. Pergamon: 2002; p 740 pp.
124. Brouwer, D. H.; Kristiansen, P. E.; Fyfe, C. A.; Levitt, M. H., Symmetry-Based ²⁹Si Dipolar Recoupling Magic Angle Spinning NMR Spectroscopy: A New Method for Investigating Three-Dimensional Structures of Zeolite Frameworks. *J. Am. Chem. Soc.* **2005**, *127* (2), 542-543.
125. Chu, Y.; Yu, Z.; Zheng, A.; Fang, H.; Zhang, H.; Huang, S.-J.; Liu, S.-B.; Deng, F., Acidic Strengths of Bronsted and Lewis Acid Sites in Solid Acids Scaled by ³¹P NMR Chemical Shifts of Adsorbed Trimethylphosphine. *J. Phys. Chem. C* **2011**, *115* (15), 7660-7667.
126. Concepcion, P.; Perez, Y.; Hernandez-Garrido, J. C.; Fajardo, M.; Calvino, J. J.; Corma, A., The promotional effect of Sn-beta zeolites on platinum for the selective hydrogenation of α,β -unsaturated aldehydes. *Phys. Chem. Chem. Phys.* **2013**, *15* (29), 12048-12055.
127. Al-Yassir, N.; Akhtar, M. N.; Al-Khattaf, S., Physicochemical properties and catalytic performance of galloaluminosilicate in aromatization of lower alkanes: a comparative study with Ga/HZSM-5. *J. Porous Mater.* **2012**, *19* (6), 943-960.
128. Narsimhan, K.; Michaelis, V. K.; Mathies, G.; Gunther, W. R.; Griffin, R. G.; Roman-Leshkov, Y., Methane to Acetic Acid over Cu-Exchanged Zeolites: Mechanistic Insights from a Site-Specific Carbonylation Reaction. *J. Am. Chem. Soc.* **2015**, *137* (5), 1825-1832.

129. (a) Pourpoint, F.; Thankamony, A. S. L.; Volklinger, C.; Loiseau, T.; Trebosc, J.; Aussenac, F.; Carnevale, D.; Bodenhausen, G.; Vezin, H.; Lafon, O.; Amoureux, J.-P., Probing 27Al-13C proximities in metal-organic frameworks using dynamic nuclear polarization enhanced NMR spectroscopy. *Chem. Commun. (Cambridge, U. K.)* **2014**, *50* (8), 933-935; (b) Song, C.; Hu, K.-N.; Joo, C.-G.; Swager, T. M.; Griffin, R. G., TOTAPOL: A Biradical Polarizing Agent for Dynamic Nuclear Polarization Experiments in Aqueous Media. *J. Am. Chem. Soc.* **2006**, *128* (35), 11385-11390.
130. Matsuki, Y.; Maly, T.; Ouari, O.; Karoui, H.; Le Moigne, F.; Rizzato, E.; Lyubenova, S.; Herzfeld, J.; Prisner, T.; Tordo, P.; Griffin, R. G., Dynamic Nuclear Polarization with a Rigid Biradical. *Angew. Chem., Int. Ed.* **2009**, *48* (27), 4996-5000, S4996/1-S4996/8.
131. (a) Blanc, F.; Chong, S. Y.; McDonald, T. O.; Adams, D. J.; Pawsey, S.; Caporini, M. A.; Cooper, A. I., Dynamic Nuclear Polarization NMR Spectroscopy Allows High-Throughput Characterization of Microporous Organic Polymers. *J. Am. Chem. Soc.* **2013**, *135* (41), 15290-15293; (b) Zagdoun, A.; Casano, G.; Ouari, O.; Lapadula, G.; Rossini, A. J.; Lelli, M.; Baffert, M.; Gajan, D.; Veyre, L.; Maas, W. E.; Rosay, M.; Weber, R. T.; Thieuleux, C.; Coperet, C.; Lesage, A.; Tordo, P.; Emsley, L., A Slowly Relaxing Rigid Biradical for Efficient Dynamic Nuclear Polarization Surface-Enhanced NMR Spectroscopy: Expedient Characterization of Functional Group Manipulation in Hybrid Materials. *J. Am. Chem. Soc.* **2012**, *134* (4), 2284-2291.
132. Rosay, M.; Tometich, L.; Pawsey, S.; Bader, R.; Schauwecker, R.; Blank, M.; Borchard, P. M.; Cauffman, S. R.; Felch, K. L.; Weber, R. T.; Temkin, R. J.; Griffin, R. G.; Maas, W. E., Solid-state dynamic nuclear polarization at 263 GHz: spectrometer design and experimental results. *Phys. Chem. Chem. Phys.* **2010**, *12* (22), 5850-5860.
133. Herzfeld, J.; Berger, A. E., Sideband intensities in NMR spectra of sample spinning at the magic angle. *J. Chem. Phys.* **1980**, *73* (12), 6021-30.
134. Bonino, F.; Damin, A.; Bordiga, S.; Lamberti, C.; Zecchina, A., Interaction of CD3CN and Pyridine with the Ti(IV) Centers of TS-1 Catalysts: a Spectroscopic and Computational Study. *Langmuir* **2003**, *19* (6), 2155-2161.
135. Chen, J.; Wright, P. A.; Natarajan, S.; Thomas, J. M., Understanding the Brønsted acidity of SAPO-5, SAPO-17, SAPO-18 and SAPO-34 and their catalytic performance for methanol conversion to hydrocarbons. *Stud. Surf. Sci. Catal.* **1994**, *84* (ZEOLITES AND RELATED MICROPOROUS MATERIALS, PT. C), 1731-8.
136. Corma, A.; Orozco, L. M.; Renz, M., From MOFs to zeolites: zirconium sites for epoxide rearrangement. *New J. Chem.* **2013**, *37* (11), 3496-3502.
137. Grimme, S., Density functional theory with London dispersion corrections. *Wiley Interdiscip. Rev.: Comput. Mol. Sci.* **2011**, *1* (2), 211-228.
138. Climent, M. J.; Corma, A.; De Frutos, P.; Iborra, S.; Noy, M.; Veltz, A.; Concepcion, P., Chemicals from biomass: Synthesis of glycerol carbonate by transesterification and carbonylation with urea with hydrotalcite catalysts. The role of acid-base pairs. *J. Catal.* **2010**, *269* (1), 140-149.
139. Japan National Institute of Advanced Industrial Science and Spectral Database for Organic Compounds.
140. Vuorinen, T.; Serianni, A. S., Synthesis of D-erythro-2-pentulose and D-threo-2-pentulose and analysis of the carbon-13 and proton NMR spectra of the 1-13C- and 2-13C-substituted sugars. *Carbohydr. Res.* **1991**, *209*, 13-31.
141. Omicron Biochemicals Product Index.
142. Bock, K.; Pedersen, C., Carbon-13 nuclear magnetic resonance spectroscopy of monosaccharides. *Adv. Carbohydr. Chem. Biochem.* **1983**, *41*, 27-66.
143. Angyal, S. J.; Bethell, G. S., Conformational analysis in carbohydrate chemistry. III. The carbon-13 N.M.R. spectra of the hexuloses. *Aust. J. Chem.* **1976**, *29* (6), 1249-65.

144. Du Mortier, C.; De Lederkremer, R. M., A new synthesis of 3-deoxy-D-arabino-hexose and its tautomeric equilibrium. *J. Carbohydr. Chem.* **1984**, *3* (2), 219-28.
145. Szarek, W. A.; Rafka, R. J.; Yang, T.-F.; Martin, O. R., Structure-sweetness relationships for fructose analogs. Part III. 3-Deoxy-D-erythro-hexulose (3-deoxy-D-fructose): composition in solution and evaluation of sweetness. *Can. J. Chem.* **1995**, *73* (10), 1639-44.
146. Kato, H.; Nguyen, V. C.; Shinoda, T.; Sekiya, F.; Hayase, F., Metabolism of 3-deoxyglucosone, an intermediate compound in the Maillard reaction, administered orally or intravenously to rats. *Biochim. Biophys. Acta, Gen. Subj.* **1990**, *1035* (1), 71-6.
147. Matsumoto, K.; Ebata, T.; Koseki, K.; Okano, K.; Kawakami, H.; Matsushita, H., A novel synthesis of 4-deoxy-D-lyxo-hexose (4-deoxy-D-mannose) from 1,6-anhydro-3,4-dideoxy- β -D-glycero-hex-3-enopyranose-2-ulose (levoglucosenone). *Carbohydr. Res.* **1993**, *246*, 345-52.
148. Guerard, C.; Alphand, V.; Archelas, A.; Demuynck, C.; Hecquet, L.; Furstoss, R.; Bolte, J., Transketolase-mediated synthesis of 4-deoxy-D-fructose 6-phosphate by epoxide-hydrolase-catalysed resolution of 1,1-diethoxy-3,4-epoxybutane. *Eur. J. Org. Chem.* **1999**, (12), 3399-3402.
149. Allscher, T.; Kluefers, P.; Labisch, O., On the basics of carbohydrate-metal chemistry: complexes of palladium(II) with hydroxyaldehyde and -ketone hydrates. *Carbohydr. Res.* **2007**, *342* (11), 1419-1426.

9 Supporting information

9.1 Dynamic Nuclear Polarization NMR Enables the Analysis of Sn-Beta Zeolite Prepared with Natural Abundance ^{119}Sn Precursors

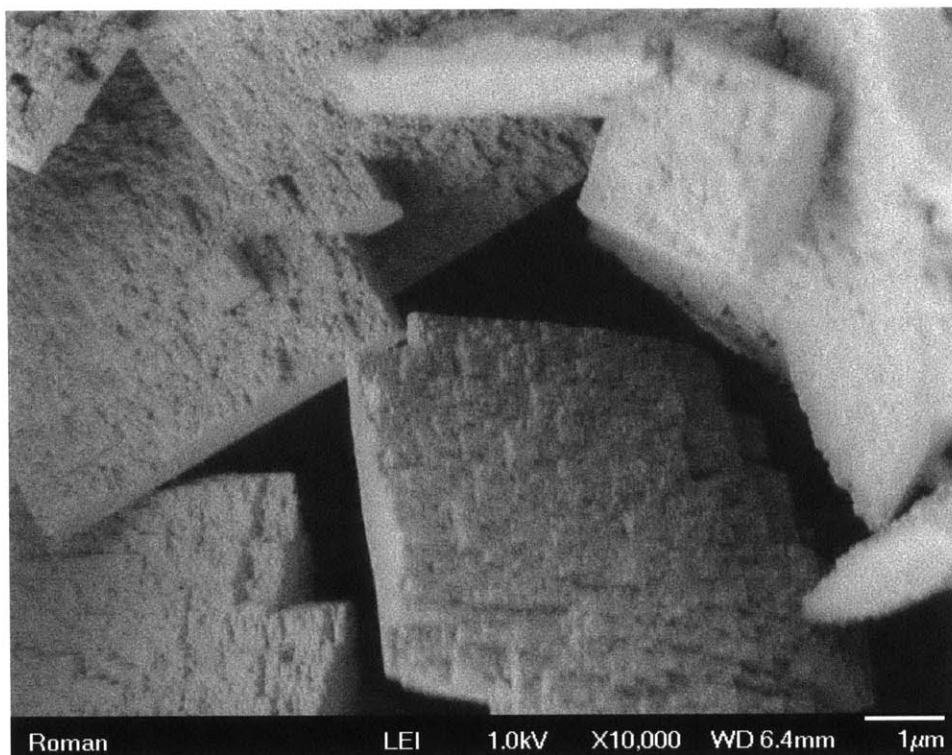


Figure S1. Scanning electron microscopy image of enriched Sn-Beta illustrating crystal dimensions over which polarization must diffuse. Note the crystal size may be much smaller than the aggregates.

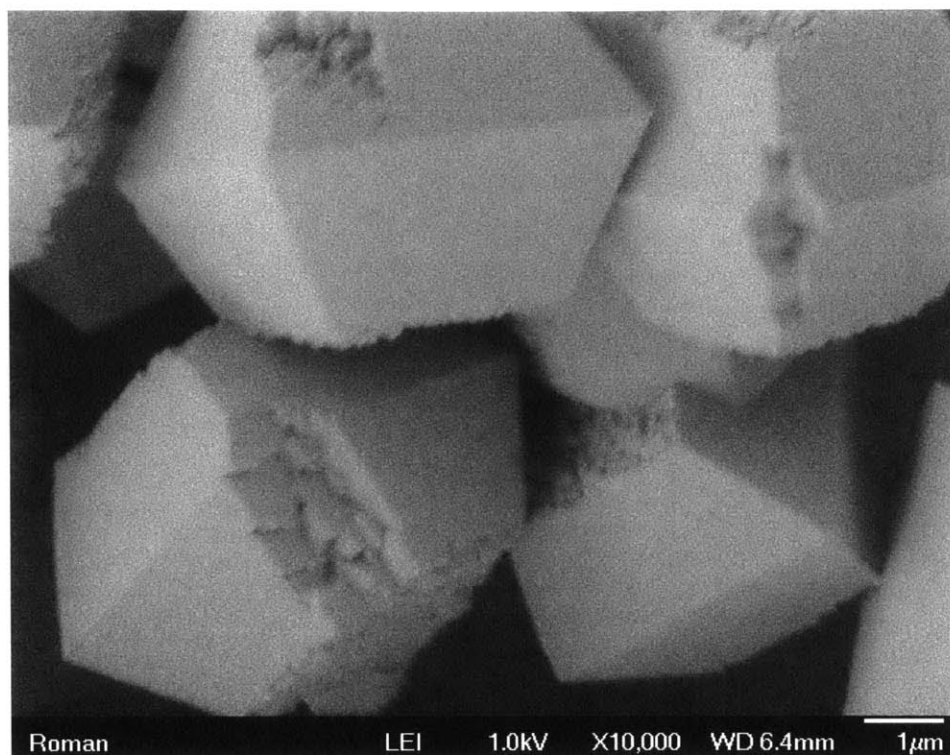


Figure S2. Scanning electron microscopy (SEM) images of natural abundance Sn-Beta showing zeolite crystal dimensions.

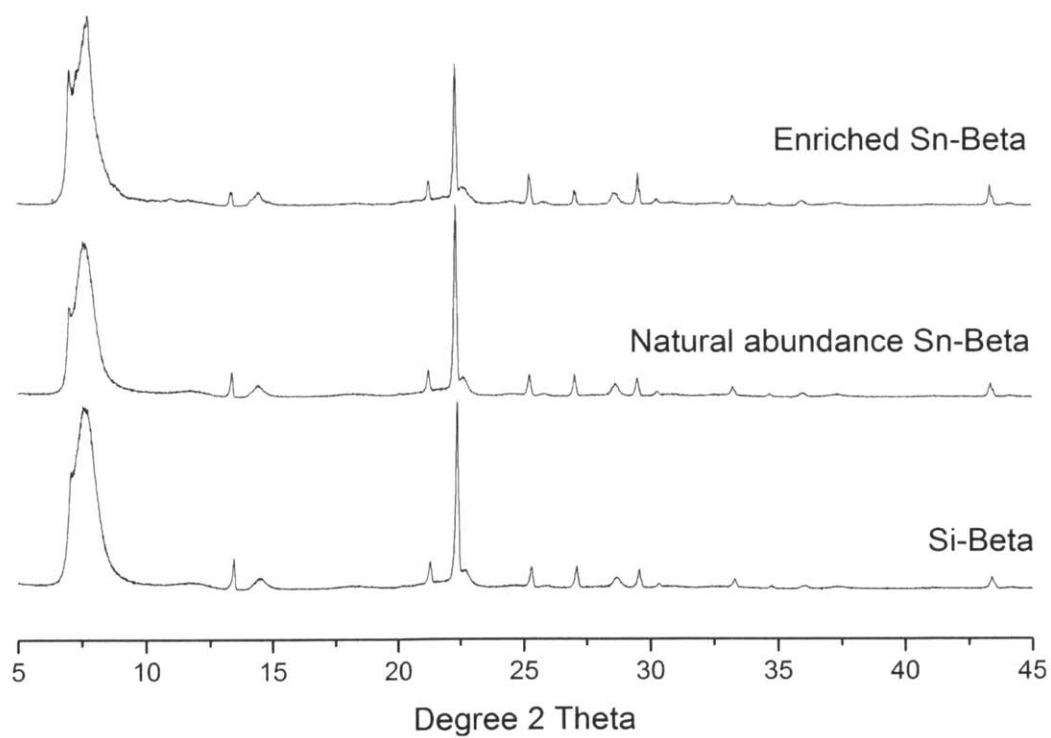


Figure S3. Powder X-ray diffraction patterns of Sn-Beta zeolites.

Table S1. Metal content calculated from ICP measurements and pore volumes of Sn-Beta samples.

Material	Si/Sn	Total pore volume [cm ³ /g]	Micropore volume [cm ³ /g]
Enriched Sn-Beta	102	0.663	0.208
Natural abundance Sn-Beta	89	0.393	0.212

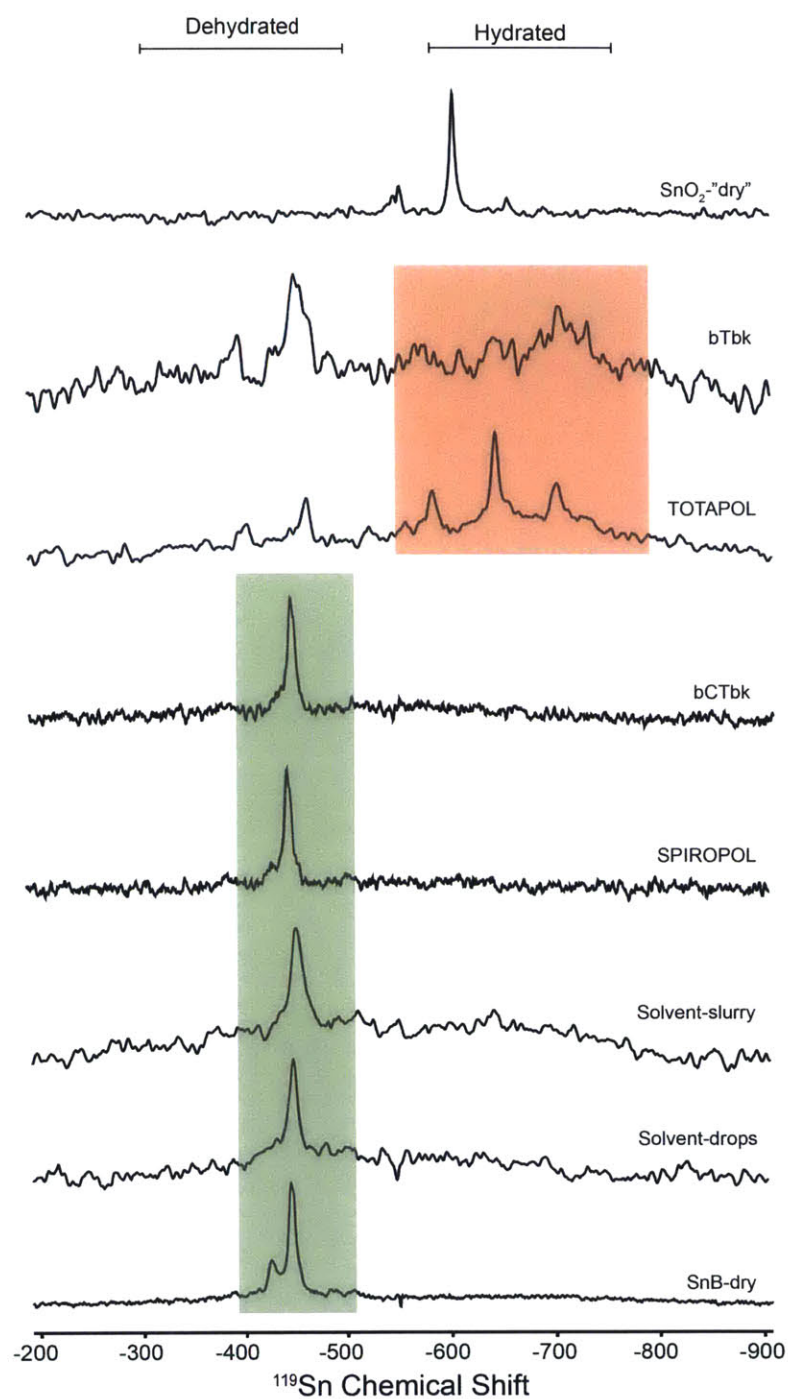


Figure S4. ^{119}Sn MAS NMR spectra (8.4 T) of ^{119}Sn -enriched Sn-Beta obtained without DNP (i.e., no microwaves and a sample temperature of 300 K) showing the zeolite remains dehydrated and the solvent/radical combination does not interfere with the Sn site (green) or it does interfere with the Sn site (red). All spectra shown were acquired using a 4 mm ZrO_2 rotor (80 ul fill volume); experimental times varied between 48 and 96 hours.

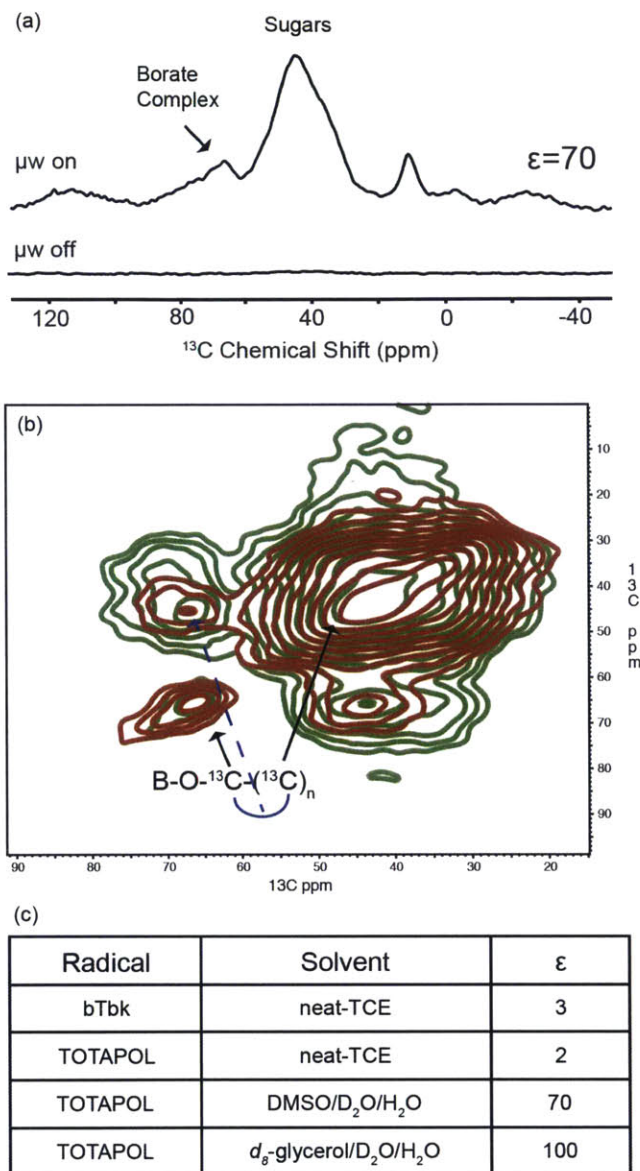


Figure S5. ^{13}C DNP NMR data acquired at 212 MHz / 140 GHz on a glucose Sn-Beta zeolite with borate salt using 8 W of microwave power at 85 K. (a) $^{13}\text{C}\{^1\text{H}\}$ microwave on and off spectrum using 10 mM TOTAPOL and DMSO/D₂O/H₂O glassing/cryoprotecting agent, (b) ^{13}C - ^{13}C Proton-Driven Spin Diffusion (PDS) correlation experiment acquired using 5 (rust) and 40 (green) ms of mixing and (c) enhancement results using 10 mM of bTbk or TOTAPOL in various glassing agents.

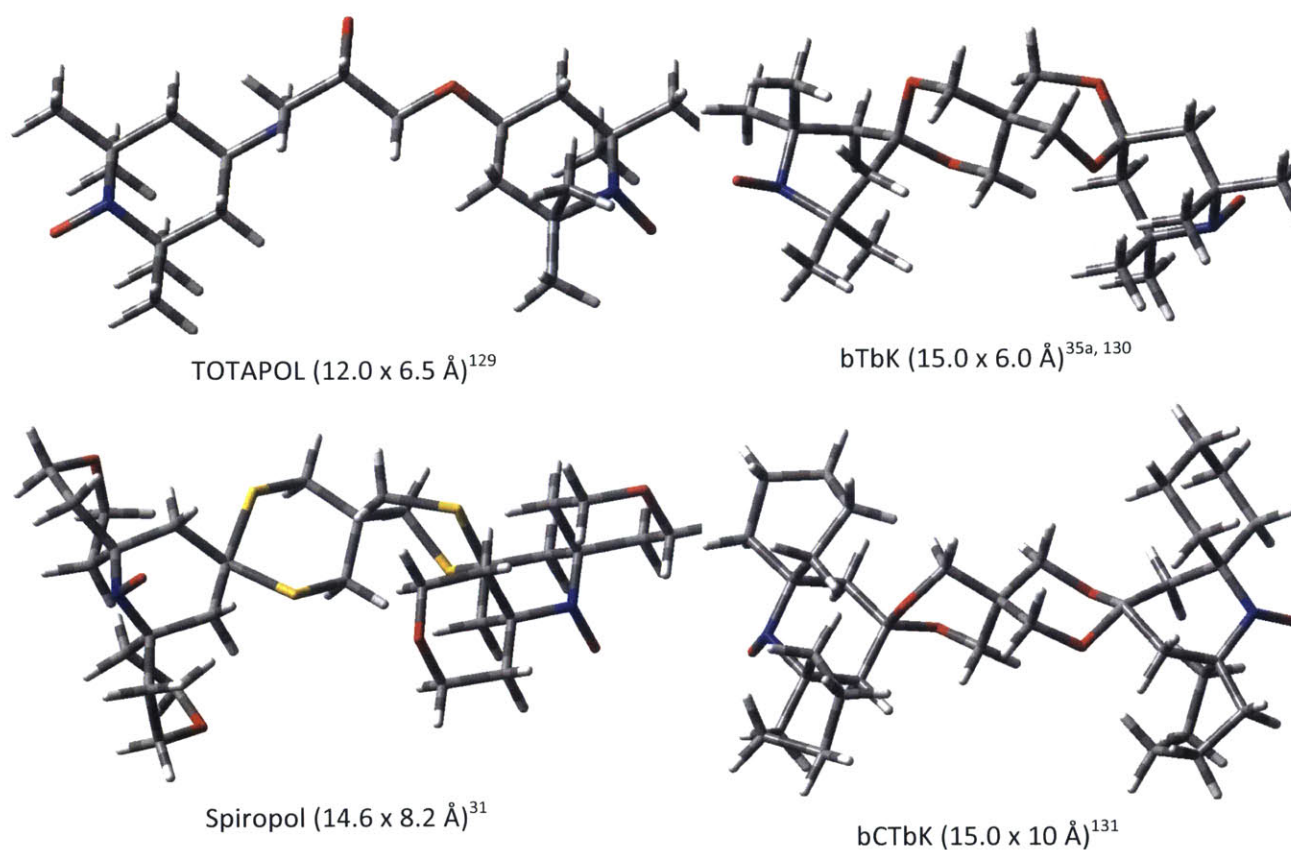


Figure S6. 3-D structural representations and dimensions of the biradicals used in this study. The atoms are colored in the following manner: blue for nitrogen, red for oxygen, yellow for sulfur, grey for carbon, and white for hydrogen.

Catalyst Synthesis

Sn-Beta was synthesized as follows: 26.735 g of aqueous tetraethylammonium hydroxide (Sigma–Aldrich, 35% (w/w)) and 24.069 g of tetraethylorthosilicate (Sigma–Aldrich, 99% (w/w)) were added to a Teflon® (Polytetrafluoroethylene, [PTFE]) dish, which was magnetically stirred at room temperature for 90 min and then cooled in an ice bath. Then, 0.261 g of tin (II) chloride dihydrate (Sigma–Aldrich, 98% (w/w)) dissolved in 15 g of cold deionized water (DI H₂O) was added dropwise. Sn(II) which oxidizes to Sn(IV) in water was used in place of SnCl₄•5H₂O and has resulted in Sn-Beta consistently free of extraframework SnO₂.⁵⁰ The solution was left uncovered on a stir plate for 10 h to reach a total mass of 35 g. Next, 2.600 g of aqueous hydrofluoric acid (Sigma–Aldrich, 48% (w/w)) was added dropwise and the mixture was homogenized using a PTFE spatula, resulting in a thick gel. Then, 0.358 g of previously-made Sn-Beta was seeded into the mixture, which was allowed to evaporate to 33.776 g, which corresponds to a final molar composition of SiO₂/0.01 SnCl₂/0.55 TEAOH/0.54 HF/7.52 H₂O. The thick

paste was transferred to a 45 ml PTFE-lined stainless steel autoclave and heated to 413 K for 40 days under static conditions. The solids were recovered by filtration, washed with DI H₂O, dried at 373 K and calcined at 853 K for 10 h with a 1 K min⁻¹ ramp and 1 h stops at 423 and 623 K, leading to an overall inorganic oxide yield of 80–90%. Enriched samples were prepared with 82% ¹¹⁹SnCl₂. We note that the resulting samples have been used in isomerization/epimerization reactivity studies and show identical results to those obtained with a zeolite prepared under identical conditions but using a Sn(IV) salt.⁵⁰ This confirms that the Sn(II) atoms oxidize to Sn(IV) during synthesis and are tetrahedrally incorporated into the zeolite framework.

Zeolite Characterization

Powder X-ray diffraction (PXRD) patterns were collected using a Bruker D8 diffractometer with Cu K α radiation. Ultraviolet–visible (UV–vis) measurements were recorded using a Varian Cary 5000 UV–vis–NIR spectrometer with a diffuse reflectance cell after calcination without subsequent drying. The ultraviolet–visible diffuse reflectance spectrum of the calcined sample shows the presence of a unique band at 200 nm, which has been associated with Sn tetrahedrally coordinated into the zeolite framework. Sn content was measured using a Horiba Jobin Yvon ACTIVA-S ICP-AES. Catalyst samples were dissolved in a few drops of 48% HF and diluted in 2% nitric acid after evaporation of the HF. SEM spectra were recorded on a JEOL 6700F at an electron high tension of 1 kV. Nitrogen adsorption/desorption experiments were performed on a Quantachrome Autosorb iQ apparatus. Micropore volume was measured using a P/P₀ of 0.01. X-band EPR was performed at 90 K on SPIROPOL and bCTbk over 24 hours; no evidence of Sn-radical reactivity was observed.

DNP Sample Preparation

In a typical preparation, 100 mg of zeolite was dried under vacuum at 473K and transferred into a glovebox. The zeolite powder was prepacked into 3.2 mm sapphire rotors. Small aliquots of 10 mM biradical (i.e. bTbk, TOTAPOL, SPIROPOL and bCTbk) in 1,1,2,2-tetrachloroethane (TCE) were added to the rotor of either dry (packed under N₂ atmosphere) or wet (in-air) Sn-Beta zeolites using a glass Hamilton syringe. The TCE solution was prepared outside the glovebox and without special anhydrous treatment. The hydrophobic zeolite readily adsorbs TCE as seen by the slight contraction of the sample volume. Note that although incipient wetness impregnation methods are typically used to analyze porous materials, the highest enhancements observed in this study involved a slurry. Thus, in the present study, there does not appear to be a tradeoff between sample volume and radical solution.

When treating the sample, we ensured that the whole sample contained in the rotor was exposed to solvent. Full solvation was easily observed by watching the solvent penetrate down the transparent sapphire rotor. Zeolites readily adsorb liquid and we note that the final state of the sample was paste-like. To ensure full wetting of the zeolite with this methodology, we performed three different control experiments to capture potential irregularities in radical distribution throughout the sample: 1) we allowed the solvent to penetrate the sample contained in the rotor by dripping the solvent/radical mixture with a pipette without further disruption (this is the standard method used for all experiments in this work); 2) we thoroughly mixed the zeolite and the solvent/radical mixture in a mortar and pestle and then packed the rotor; and 3) we introduced the solvent/radical mixture directly into the rotor and stirred the sample with a small spatula to enhance the wetting/mixing process. Analyzing these three samples, we noticed virtually identical behavior in terms of relaxation and enhancements for all samples. Samples were sealed inside the rotors using silicone plugs and hydrated samples were exposed to ambient conditions prior to adding the radical solution. Centrifugation provided a means to speed up the process. Identical protocols were carried out for TOTAPOL, bTbk, Spiropol and bCTbk. For the ^{13}C experiments samples were ground in an agate mortar and pestle.

DNP MAS NMR

$^{119}\text{Sn}\{^1\text{H}\}$ DNP MAS NMR experiments were performed on a 9.4 T Bruker Avance III DNP NMR spectrometer equipped with a 263 GHz gyrotron delivering high power microwaves to the sample.¹³² Experimental data were recorded using a 3.2 mm triple resonance (HXY) MAS probe doubly tuned to ^1H ($L = 400$ MHz) and ^{119}Sn ($L = 150$ MHz). The ^1H field position was set to the maximum field position for bTbk, bCTbk and TOTAPOL and shifted by ~ 50 kHz for SPIROPOL. All DNP NMR data were acquired under MAS, $\omega_r/2\pi$ of 10,000 (3) Hz, a sample temperature of $T = 100$ K, a recycle delay of $1.3 \times T_B$ and between 512 and 20,480 co-added transients. $^{119}\text{Sn}\{^1\text{H}\}$ cross-polarization MAS experiments were acquired using a mixing time of 2 or 6 ms for the hydrated and dehydrated samples, respectively. Data were acquired using high power ^1H ($\omega_1/2\pi = 71$ kHz) decoupling using SPINAL-64, the Hartmann-Hahn match condition was optimized with $\omega_1/2\pi = 70$ kHz for ^{119}Sn and placing a ramp on ^1H 's. Spectra were referenced with respect to tin oxide (SnO_2 , -604.3 ppm) at room temperature ($T = 298$ K) and cross-polarization was initially setup on triphenyl tin chloride in TCE/bCTbk at 100 K ($\epsilon = 20$). Contact times were optimized for the respective Sn-Beta samples.

$^{13}\text{C}\{^1\text{H}\}$ DNP MAS NMR experiments were performed on a home-built spectrometer (courtesy of Dr. David Ruben, FBML, MIT), consisting of a 212 MHz (^1H , 5 T) NMR magnet and a 140.6 GHz gyrotron generating high-power microwaves up to 14 W.¹³¹ Spectra were recorded on a home-built cryogenic 4 mm quadrupole resonance (^1H , ^{13}C , ^{15}N & e-) DNP NMR probe equipped with a Kel-F stator (Revolution NMR, Fort Collins, CO). Microwaves are guided to the sample via a circular overmoded waveguide whose inner surface has been corrugated to reduce mode conversion and ohmic losses. Sample temperatures were maintained at 85 (± 1) K, with a spinning frequency, $\omega_r/2\pi = 4,500$ (2) Hz. $^{13}\text{C}\{^1\text{H}\}$ Cross Polarization (CP) and Proton-Driven Spin Diffusion (PDS) experiments were acquired using a 1.5 ms contact time. A series of PDS mixing times were collected ranging from 5 to 40 ms with 64 increments. High-power TPPM proton decoupling (^1H $\omega_1/2\pi = 100$ kHz) was used during acquisition. Buildup times (T_B) were determined using a saturation recovery experiment, recycle delay was chosen as $T_B \times 1.3$, yielding optimum sensitivity per unit of time. Microwave power was kept constant at 8 W using a PID control interfaced within Labview. ^1H cross-effect conditions were optimized for bTbk and TOTAPOL by sweeping the main NMR field using a ± 750 Gauss sweep coil. Samples were contained in 4 mm sapphire rotors equipped with a Vespel drive tip and Kel-F spacer using either neat-TCE, 60/30/10 v/v d_8 -glycerol/ $\text{D}_2\text{O}/\text{H}_2\text{O}$ or 60/30/10 DMSO/ $\text{D}_2\text{O}/\text{H}_2\text{O}$.

^{119}Sn MAS NMR

Magic-angle spinning nuclear magnetic resonance (MAS NMR) experiments were performed on a custom designed spectrometer (courtesy of D. J. Ruben, Francis Bitter Magnet Laboratory, Massachusetts Institute of Technology) operating at 360 MHz (^1H , 8.4 T). The spectrometer was equipped with either a double resonance homebuilt (FBML-MIT) or a triple resonance Varian-Chemagnetics probe (Palo Alto, CA) which were singly and doubly tuned to ^{119}Sn and $^{119}\text{Sn}/^1\text{H}$, respectively. Powdered samples were packed into 4 mm (80 μl , fill volume) outer diameter ZrO_2 rotors equipped with Vespel drive- and top-caps. Topcaps were equipped with rubber O-ring seals, inhibiting water contamination within the sample (Revolution NMR, Fort Collins, CO) and solvent evaporation over the experiment. Dehydrated enriched ^{119}Sn , Sn-Beta samples were prepared by heating to 473 K under a 0.1 mbar vacuum and packing the NMR rotor in an Ar-filled glovebox. ^{119}Sn MAS NMR spectra were acquired using either a Hahn-echo (^{119}Sn , $\omega_1/2\pi = 50$ kHz) or CP experiments with recycle delays between 4 and 30 seconds. All spectra were acquired with a spinning frequency, $\omega_r/2\pi = 8,000$ (5) Hz and between 32,384 and 172,800 scans. CP experiments were acquired with contact times between 0.4 and 4 ms and high-power ^1H decoupling (TPPM, $\omega_1/2\pi = 83$ kHz). ^{119}Sn spectra were referenced with

powdered SnO₂ (-604.3 ppm) as an external standard relative to trimethyltin (0 ppm). Sample temperatures were maintained between 294 and 300 K.

9.2 Interrogating Lewis acid character of metal sites in Beta zeolites with ¹⁵N pyridine MAS NMR

Table S2. NMR parameters for the metal-beta zeolites

NMR Species	N.A.	Spin	Q.M.	Gyro	Recep. ¹ H
¹¹⁹ Sn	7.7	1/2	n.a.	-10.03	4.5E ⁻³
⁴⁷ Ti	7.4	5/2	30.2	-1.51	1.5E ⁻⁴
⁴⁹ Ti	5.4	7/2	24.7	-1.51	2E ⁻⁴
⁹¹ Zr	11.2	5/2	-17.6	-2.49	1.1E ⁻³
⁹³ Nb	100	9/2	-32	-6.5	0.48
¹⁷⁷ Hf	18.6	7/2	336	1.08	2.6E ⁻⁴
¹⁷⁹ Hf	13.6	9/2	379	-0.6	7.4E ⁻⁵
¹⁸¹ Ta	99.9	7/2	317	3.24	3.7E ⁻²

Pyridine – Span, $\Omega = 620$ ppm, Skew, $\kappa = 0.46$ and $\delta_{iso} = -63$ ppm

Pyridinium – $\Omega = 351$, $\kappa = 0.618$ and $\delta_{iso} = -169.3$ ppm

Note: The isotropic chemical shift (δ_{iso}) is given by the trace of the chemical shift tensor components (*i.e.*, δ_{11} , δ_{22} and δ_{33})

$$\delta_{iso} = \frac{(\delta_{11} + \delta_{22} + \delta_{33})}{3} \quad (S1)$$

The overall breadth of the shielding tensor is described by the span, Ω , and the relative magnitude of the components by the skew, κ , using the Herzfeld-Berger convention.¹³³

$$\Omega = \delta_{11} - \delta_{33} \quad (S2)$$

$$\kappa = \frac{3(\delta_{22} - \delta_{iso})}{\Omega} \quad (S3)$$

Table S3. Probe molecule adsorption frequencies on zeolites using IR spectroscopy

Catalyst	Pyridine frequency [cm^{-1}]
Ti-Beta ^{21a, 45d}	1452
Zr-Beta ^{21a}	1445
Nb-Beta ^{45c}	1450
Ta-Beta ^{45c}	1450
Sn-Beta ^{21a, 45d}	1452
Ga-Beta ^{45a}	1457
Al-Beta ^{45a, 45b, 45d}	1452
Protonated ^{45b, 45c}	1550

Table S4. Probe molecule adsorption frequencies on zeolites using IR spectroscopy

Catalyst	Deuterated acetonitrile frequency [cm^{-1}]
Physisorbed ^{12a}	2268
Silanol ^{12a}	2276
TS-1 ¹³⁴	2302
Sn-MFI ¹²¹	2310
Sn-MCM-41 ¹²¹	2312
Sn-Beta closed ^{25c}	2308
Sn-Beta open ^{25c}	2316
Brønsted ¹³⁵	2290

Table S5. Probe molecule adsorption frequencies on zeolites using IR spectroscopy

Catalyst	Cyclohexanone frequency [cm^{-1}]
Si-Beta ^{45d}	1713
SnO ₂ -Beta ^{45d}	1713
Ti-Beta ^{45a, 45d}	1681
Zr-Beta ^{45a, 136}	1676
Nb-Beta ^{45a, 45c}	1670
Ta-Beta ^{45a, 45c}	1670
Sn-Beta ^{45a, 45d}	1665

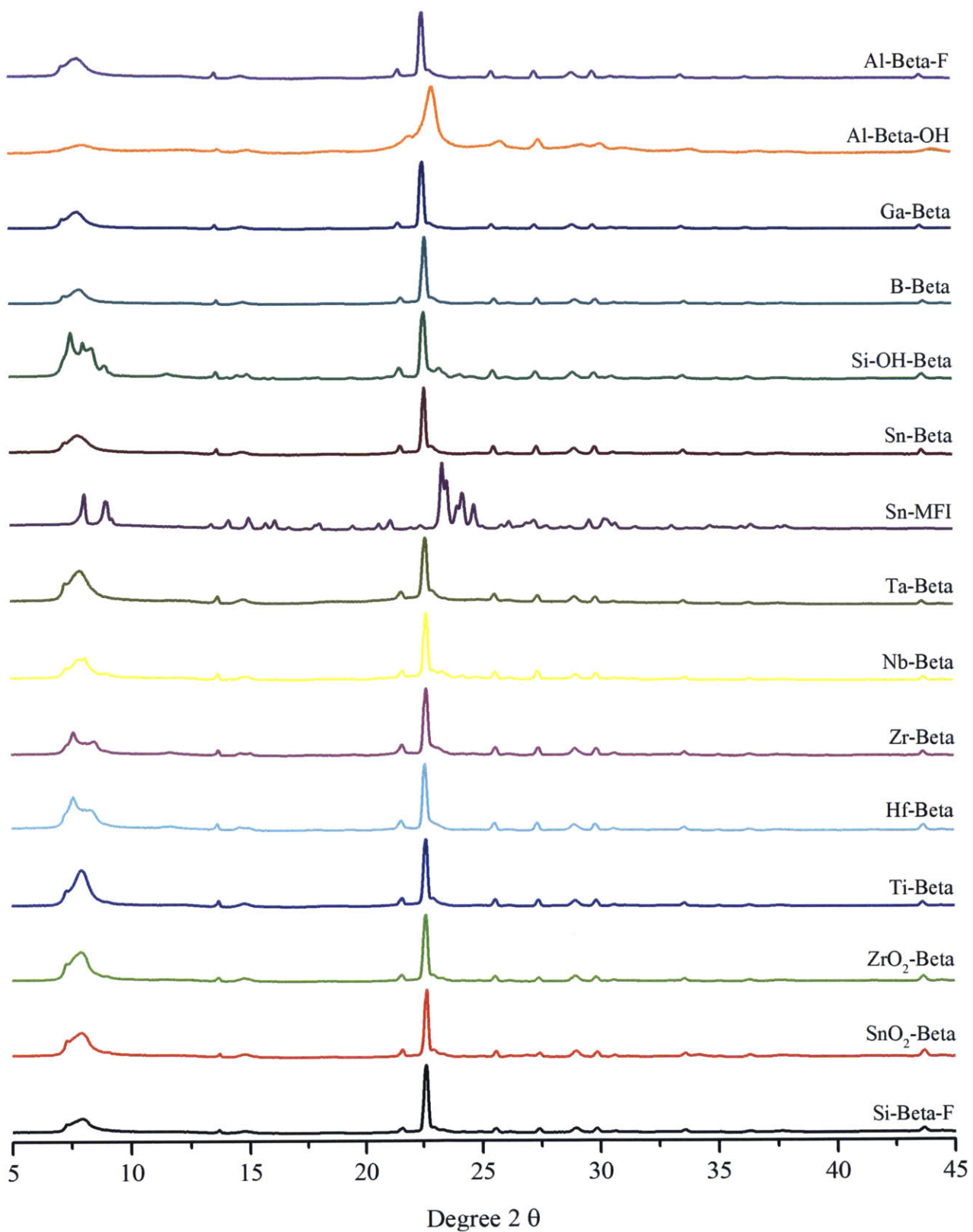


Figure S7. Powder X-Ray diffraction patterns for calcined catalysts

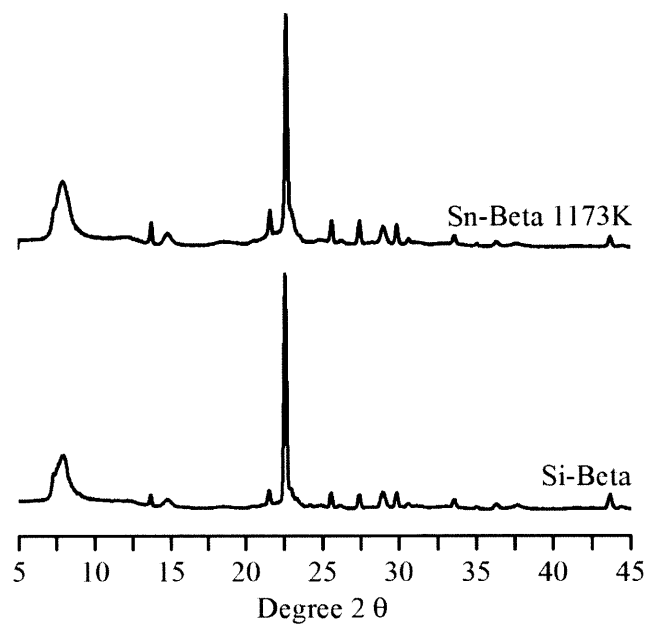


Figure S8. Powder X-Ray diffraction patterns for heat treated Sn-Beta catalyst

Table S6. Metal content in each solid material

Material	Si/M
Al-Beta-F	44
Al-Beta-OH	19
Ga-Beta	221
B-Beta	64
Sn-Beta	354
Sn-Beta	271
Sn-Beta	181
Sn-Beta	115
Sn-Beta 900°C	115
Sn-Beta	102
Sn-MFI	197
Sn-MCM-41	126
Ta-Beta	123
Nb-Beta	104
Zr-Beta	327
Zr-Beta	239
Zr-Beta	111
Hf-Beta	136
Ti-Beta	126

Table S7. Surface area measurements

Material	Micropore volume [cc/g]	Total pore volume [cc/g]
Sn-Beta 853 K	2.138e-01	3.122e-01
Sn-Beta 1173 K	2.085e-01	2.807e-01

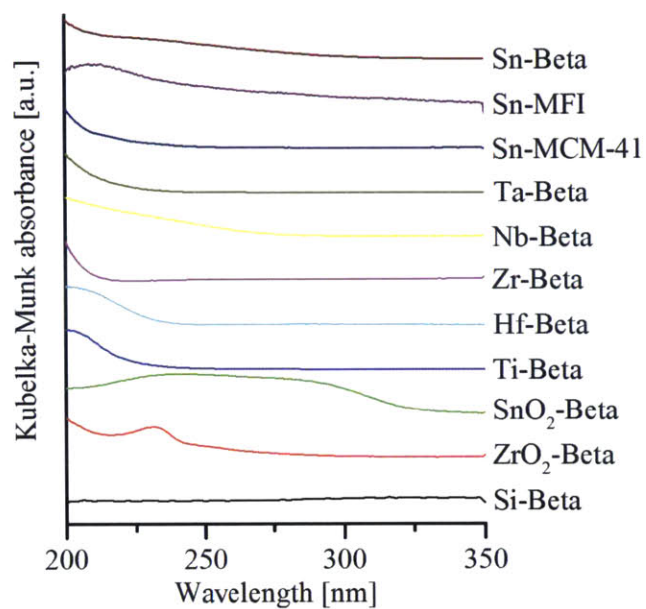


Figure S9. Diffuse reflectance ultraviolet spectra

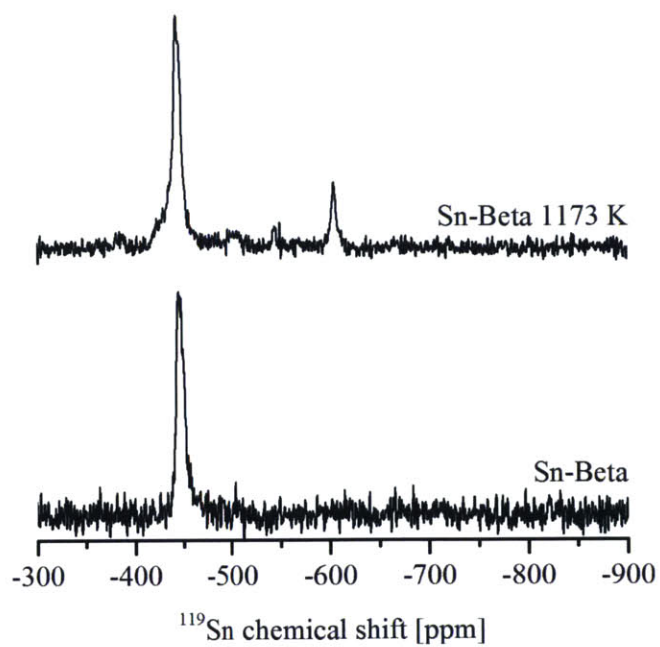


Figure S10. ^{119}Sn MAS NMR of heat treated SnBeta catalysts

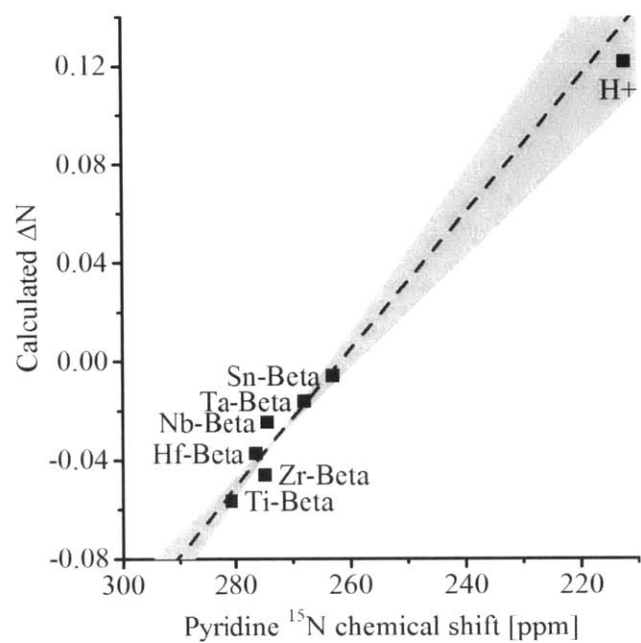


Figure S11. Calculated ΔN vs. pyridine ^{15}N chemical shift shows a linear trend. The dashed line is placed as a guide for the reader.

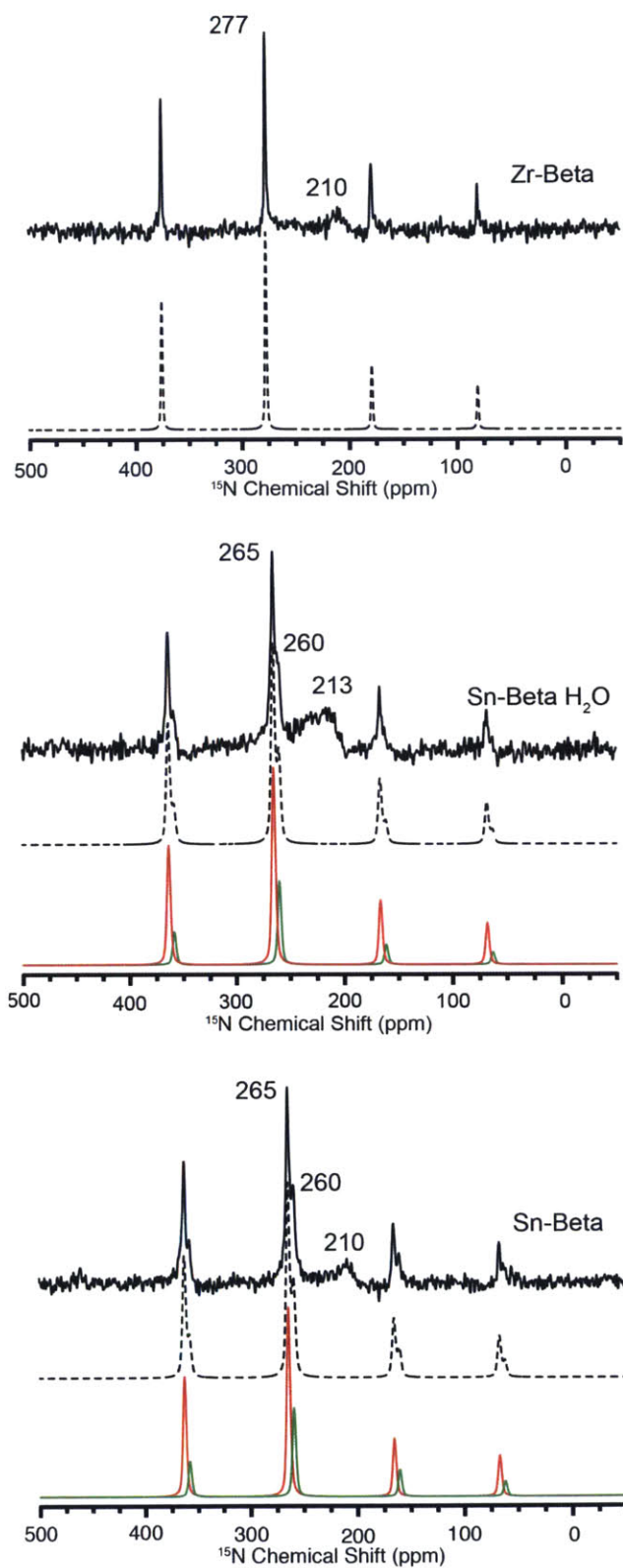


Figure S12. ^{15}N metal---pyridine bound spectra at $\omega_r/2\pi = 5$ kHz shows chemical shifts assigned to framework metal sites (high frequency 260-280 ppm) and Brønsted protons (low frequency ~ 210 ppm).

Table S8. Chemical shift anisotropy parameters for three samples shown above with span Ω and skew κ . The Sn-Beta samples appeared to contain two distinct sites 1 and 2.

Sample	δ_{iso} (ppm, ± 0.5)	Ω (ppm, ± 20)	κ (± 0.3)
Sn-Beta (1)	264.5	350	1.0
Sn-Beta (2)	259.5	350	0.3
Sn-Beta-Wet (1)	264.5	380	0.6
Sn-Beta-Wet (2)	259.5	320	0.7
Zr-Beta	277.0	390	0.7

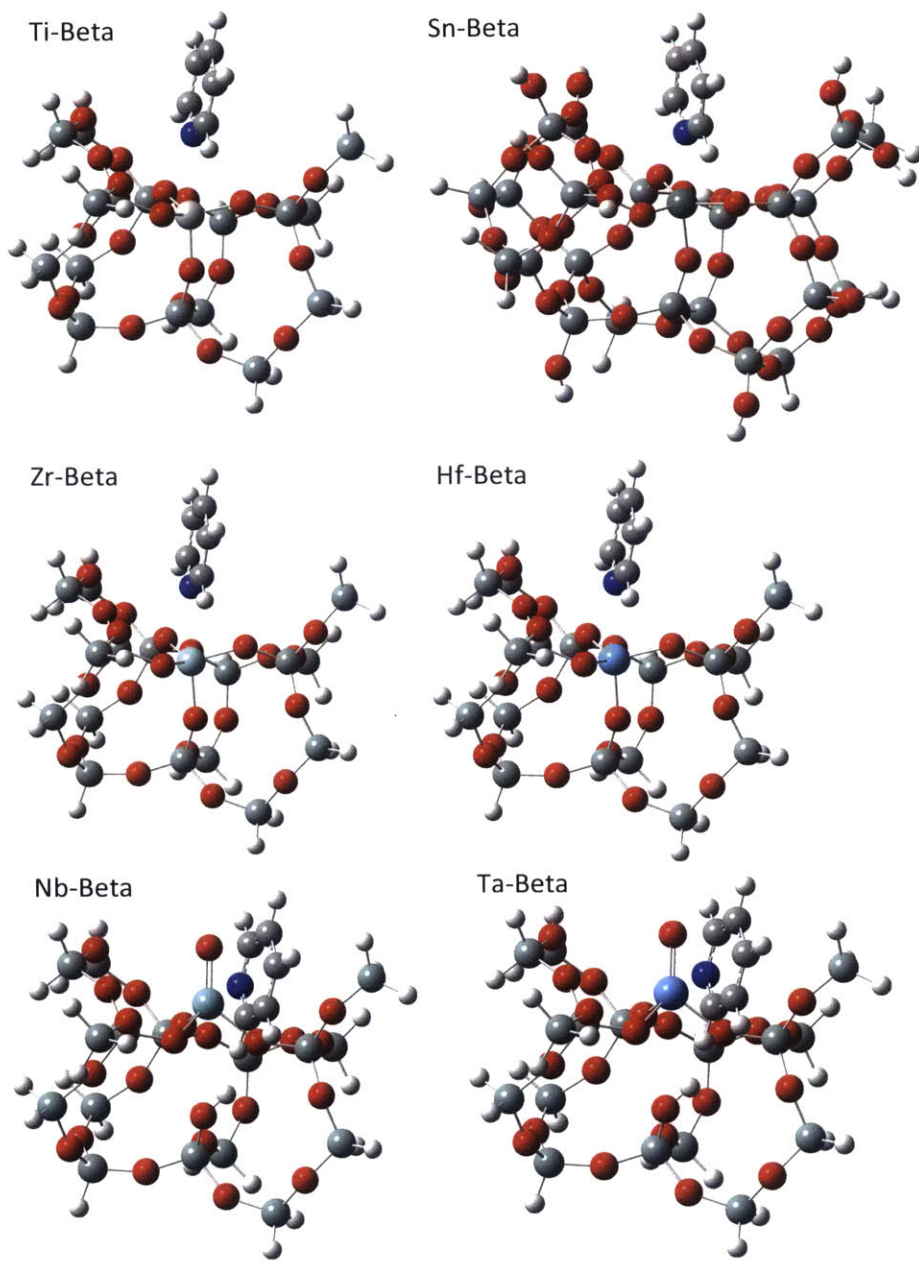


Figure S13. Structures of active site models with adsorbed pyridine

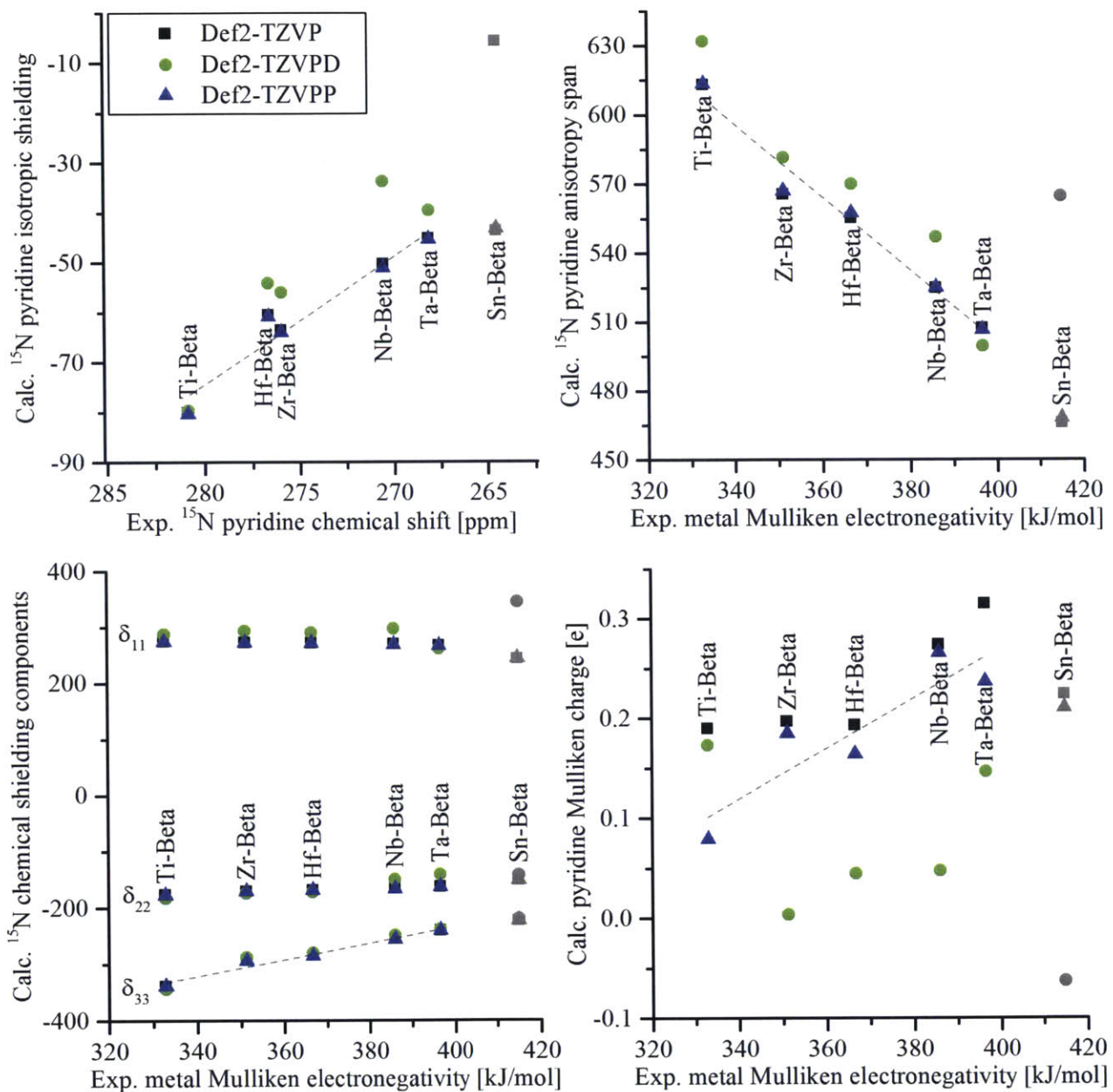


Figure S14. Calculated NMR parameters and Mulliken charge on the pyridine

Supporting information methods

Quantum chemical calculations

Basis sets were downloaded from the Environmental Molecular Sciences Laboratory (EMSL) basis set library within the Pacific Northwest National Laboratory. The chosen basis set, Def2-TZVP, is appropriate for making quantitative comparisons with typical atomization energy errors of 3 kJ/mol per atom.^{56a} This valence triple zeta basis set includes relativistic contractions necessary for heavier atoms, polarization

functions and a small electron core potential to model heavier atom energetics more accurately. Additionally, the Def2 basis sets were designed to give similar errors across the periodic table and describe experimental polarizability, and were available for all of the elements involved. The lighter atoms were modeled with the same basis set to ensure equitable basis set representation and charge distribution between the atoms. This is particularly important for NMR calculations, which are very sensitive to the electron density around a nucleus. High-level pseudo triple zeta basis sets accounting for core electrons are required for NMR calculations. For Def2-TZVPD, the pyridine, metal site, four adjacent framework oxygen atoms and four adjacent Si atoms were supplemented by diffuse functions, which are important for describing weak interactions such as hydrogen bonds, the lone pairs on the pyridine N and the high-valence state of the metal. Tight basis sets (i.e. without diffuse functions) sometimes have advantageous canceling of systematic errors and were used to verify convergence.

The B3LYP functional was the standard for many years, models organic molecules well, and facilitates comparison with other work, though it may not model inorganic materials well. Incorporation of dispersion interactions through a functional such as ω B97X-D may avoid overestimating inter-nuclear distances and improve the results,¹³⁷ however the net effect of dispersion is difficult to account for without a complete model of the zeolite pore. A first principles functional such as PBE may represent the organic and inorganic portions moderately well. The DFT calculated parameters represent that of the lowest energy state rather than that of a conformational average. Active sites were considered local and no periodic interaction considerations were considered. Double Sn substitutions were not considered. Terminal Si-H distances were set to 1.3 Å based on an unconstrained geometry optimization. The model did not incorporate expansion of the Beta zeolite unit cell due to heteroatom substitution and the 17T model does not fully incorporate weak interactions with the zeolite pore walls.

Determination of the metal-nitrogen dissociation energy, D_0 , involved calculating the energy of the zeolite and pyridine with ghost atoms in place of the missing atoms and subtracting these energies from that of the combined structure. The ghost atoms are used to perform a counterpoise correction in order to remove basis set superposition error. D_0 is an artificially high energy since small shifts of the metal out of the framework can strengthen the metal-nitrogen bond while weakening the metal-oxygen bonds. D_0 effectively measures the former while neglecting the latter, which can be problematic with weak interactions, near linear dependence, and basis set superposition error. For small solvents such as

water, the coordination of two molecules to form a pseudo octahedral structure presumably would lead to a different value.

9.3 Sn-Beta zeolites with borate salts catalyse the epimerization of carbohydrates via an intramolecular carbon shift

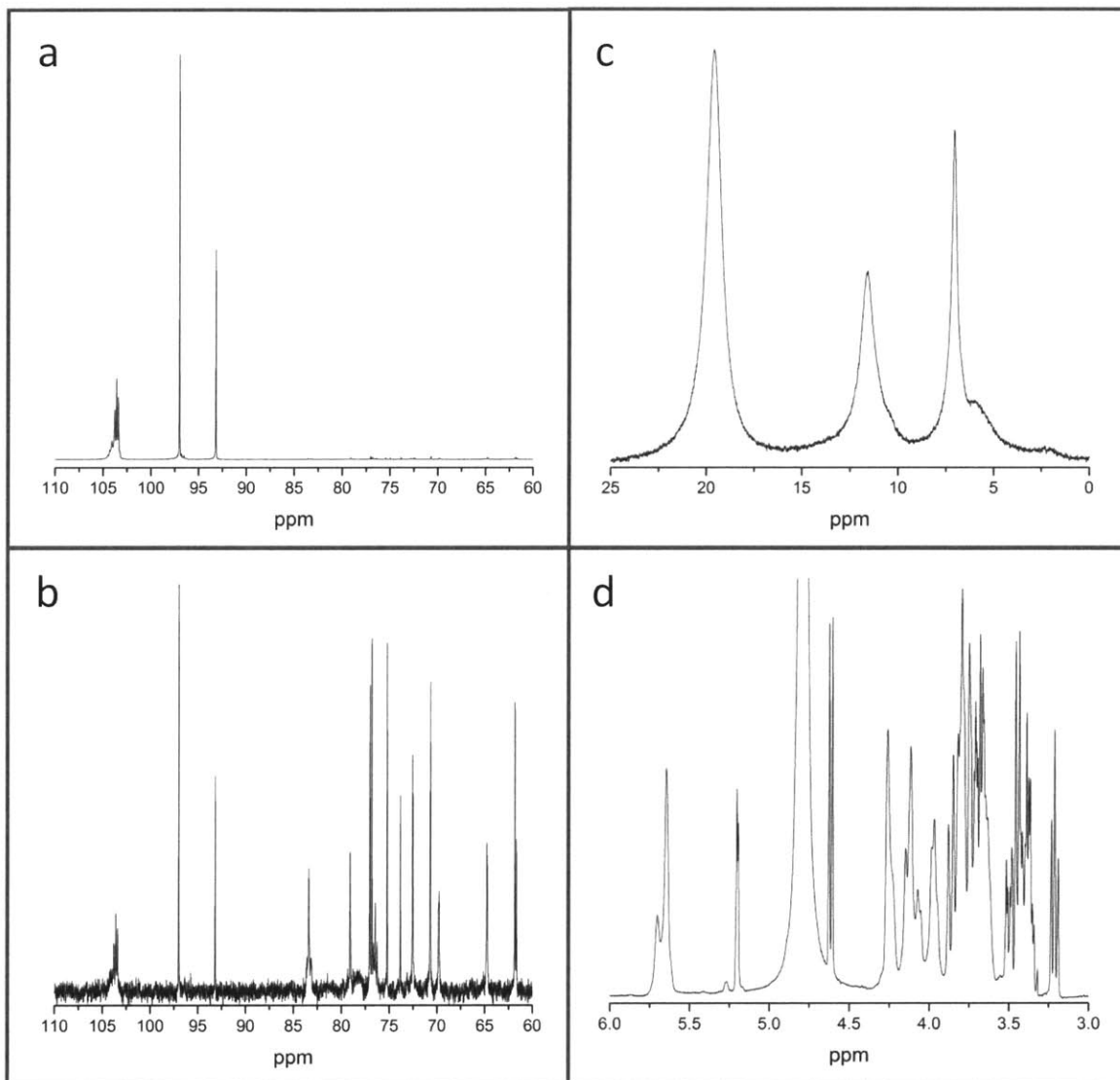


Figure S15. Solution NMR spectra for D-glucose with a 4:1 sugar:SB molar ratio in H₂O. a) ¹³C NMR of D-(1-¹³C)glucose, b) ¹³C NMR of D-glucose, c) ¹¹B NMR, d) ¹H NMR

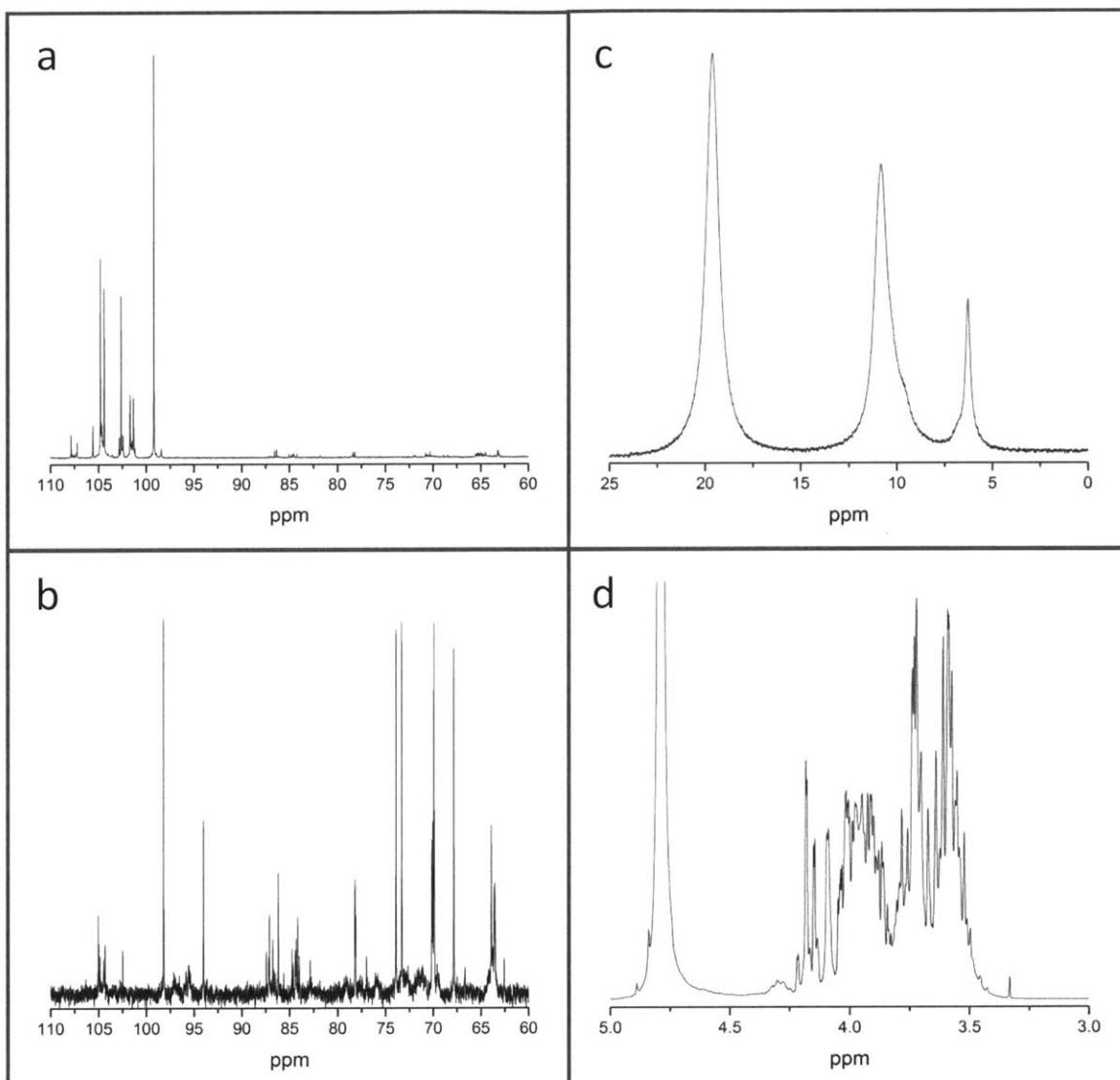


Figure S16. Solution NMR spectra for D-fructose with a 4:1 sugar:SB molar ratio in H₂O. a) ¹³C NMR of D-(2-¹³C)fructose, b) ¹³C NMR of D-fructose, c) ¹¹B NMR, d) ¹H NMR

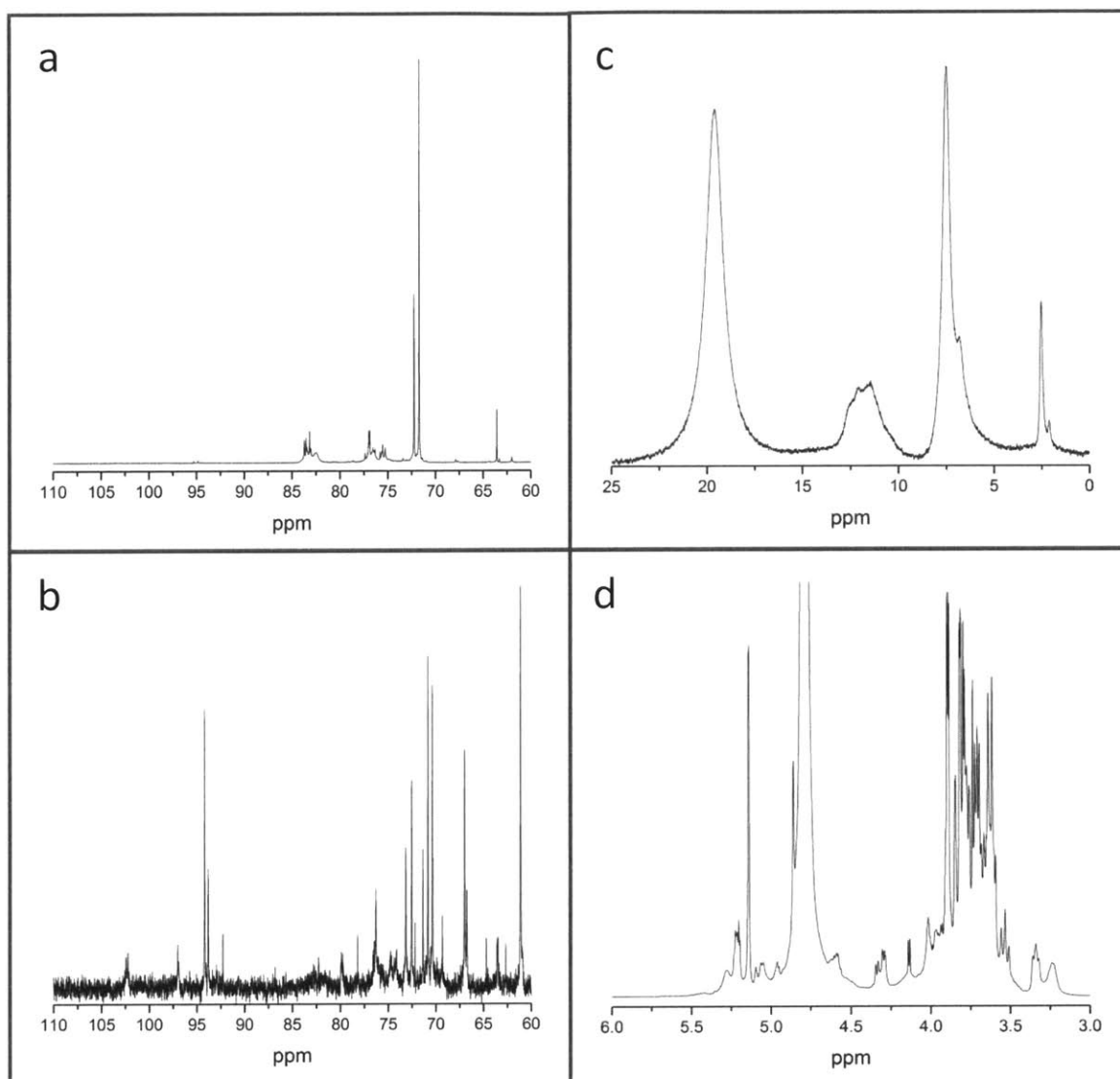


Figure S17. Solution NMR spectra for D-mannose with a 4:1 sugar:SB molar ratio in H₂O. a) ¹³C NMR of D-(2-¹³C)mannose, b) ¹³C NMR of D-mannose, c) ¹¹B NMR, d) ¹H NMR

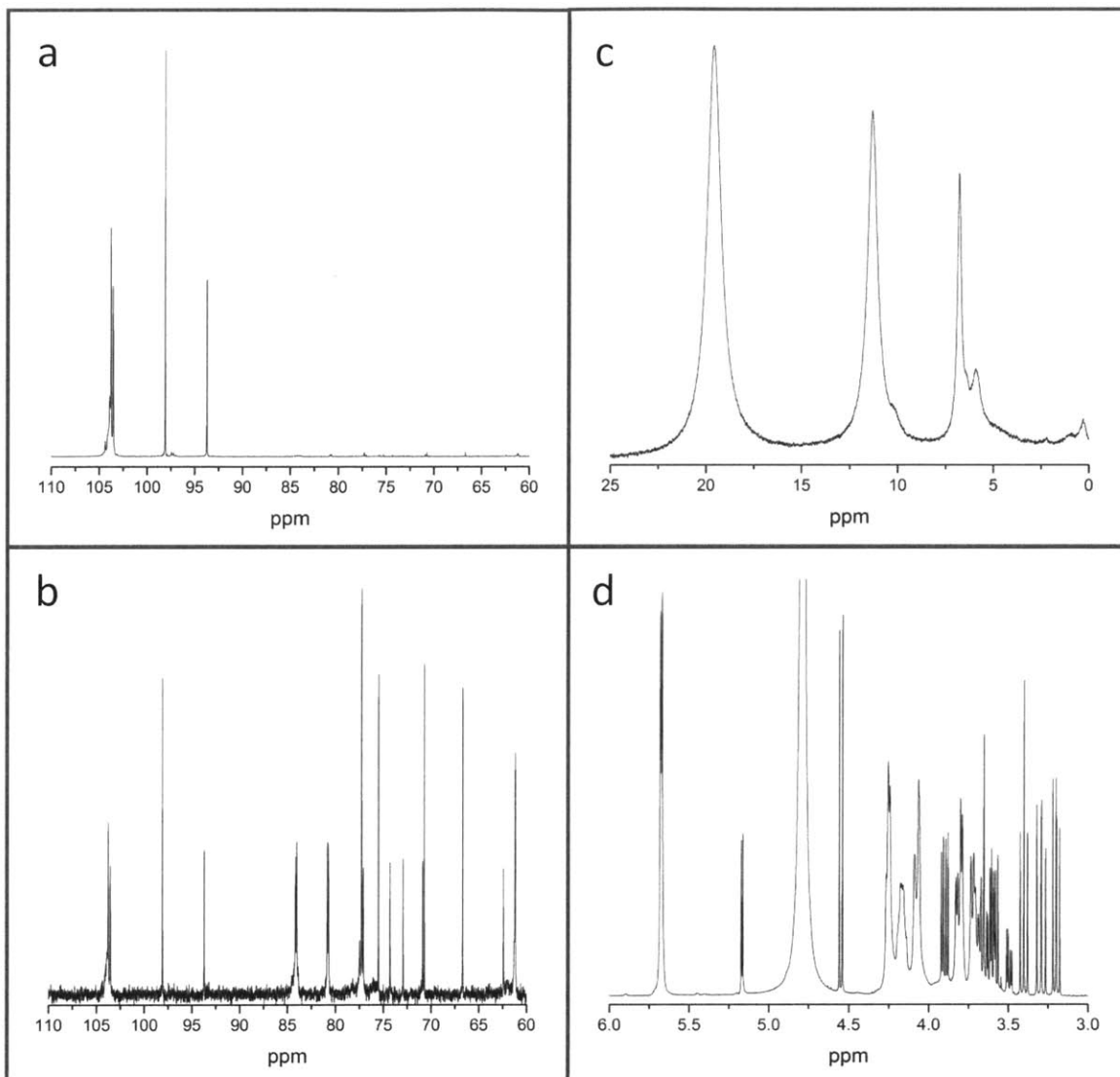


Figure S18. Solution NMR spectra for D-xylose with a 4:1 sugar:SB molar ratio in H₂O. a) ¹³C NMR of D-(1-¹³C)xylose, b) ¹³C NMR of D-xylose, c) ¹¹B NMR, d) ¹H NMR

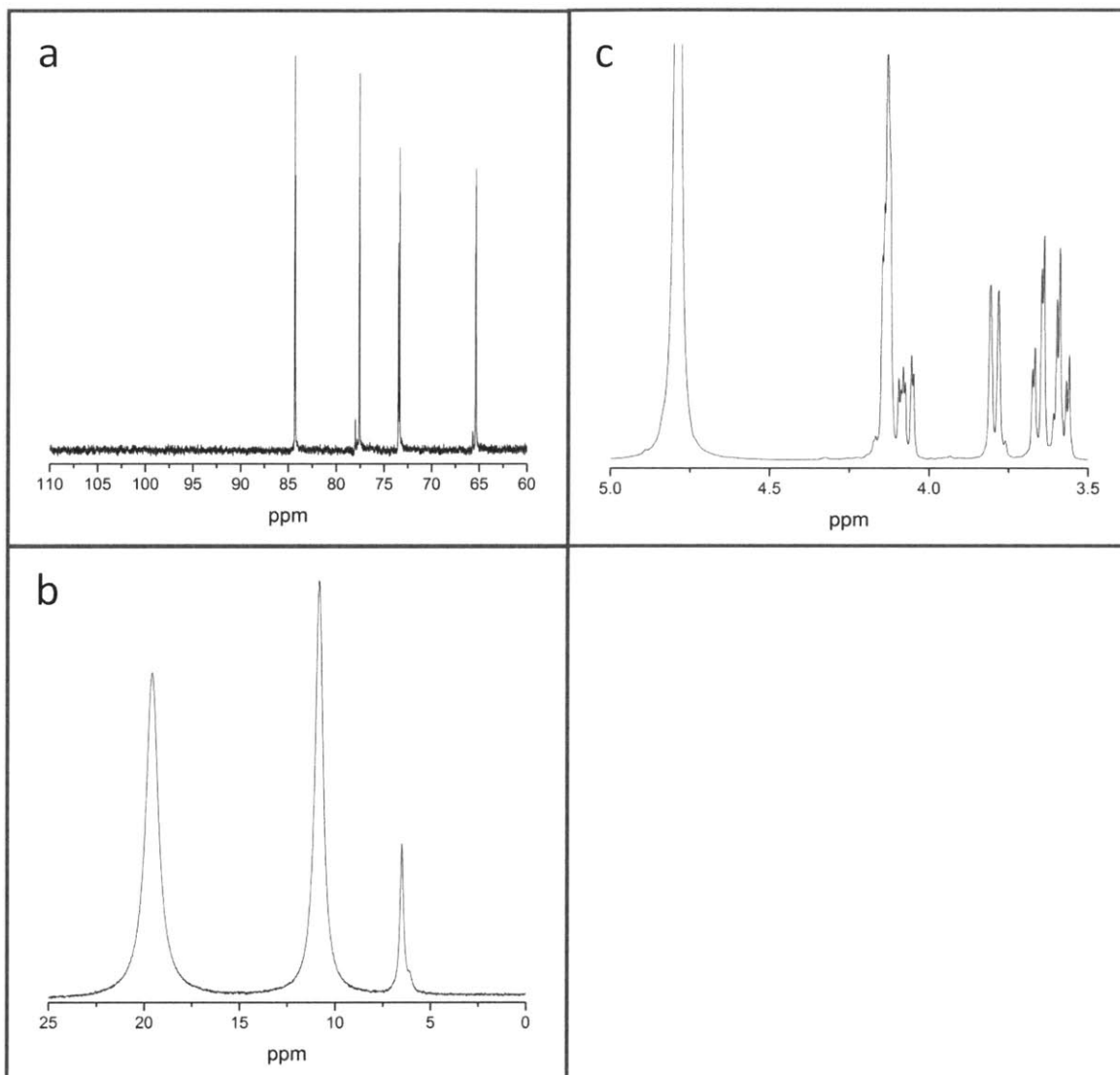


Figure S19. Solution NMR spectra for D-xylulose with a 4:1 sugar:SB molar ratio in H₂O. a) ¹³C NMR of D-xylulose, b) ¹¹B NMR, and c) ¹H NMR

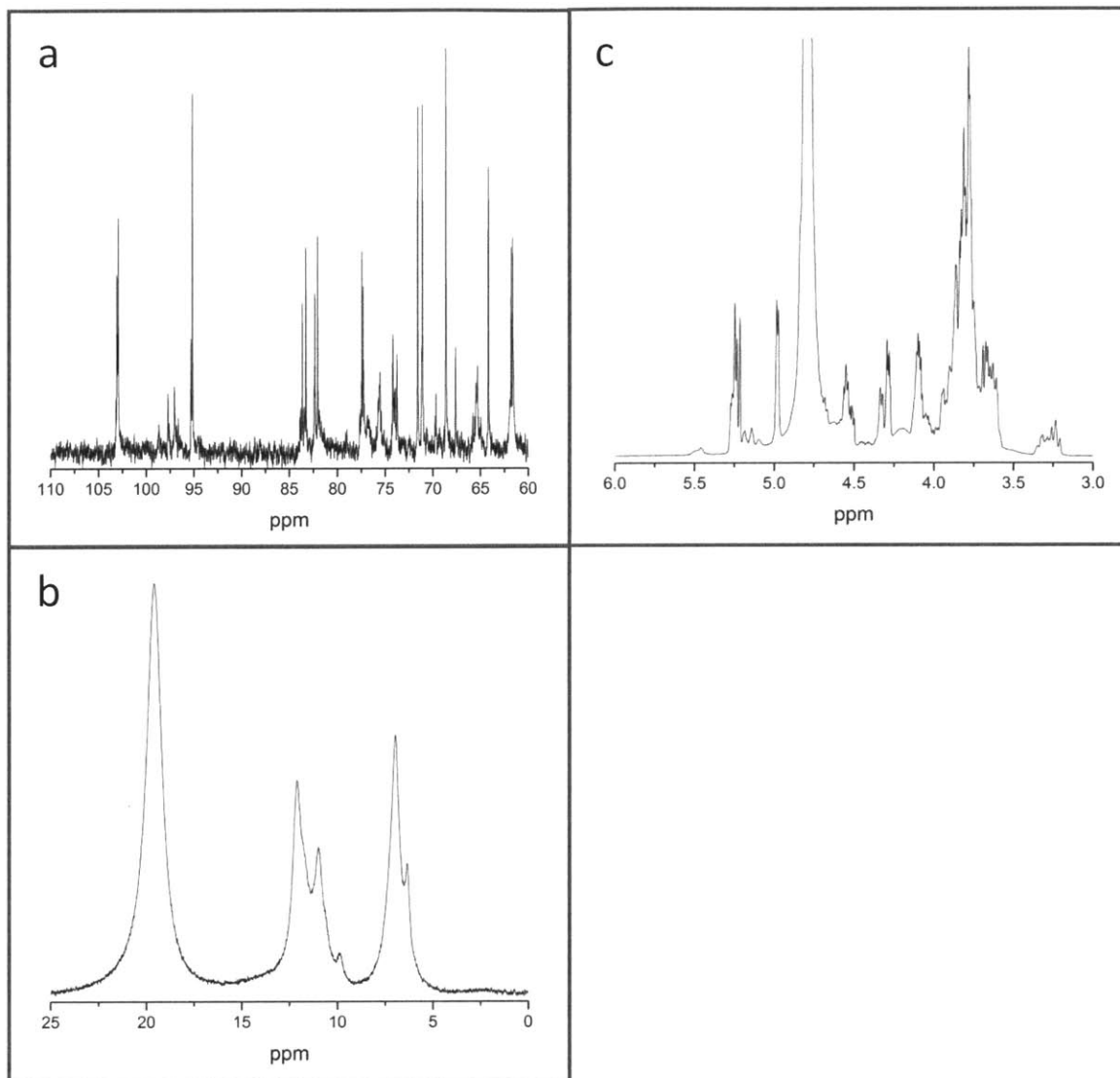


Figure S20. Solution NMR spectra for D-lyxose with a 4:1 sugar:SB molar ratio in H₂O. a) ¹³C NMR of D-lyxose, b) ¹¹B NMR, and c) ¹H NMR

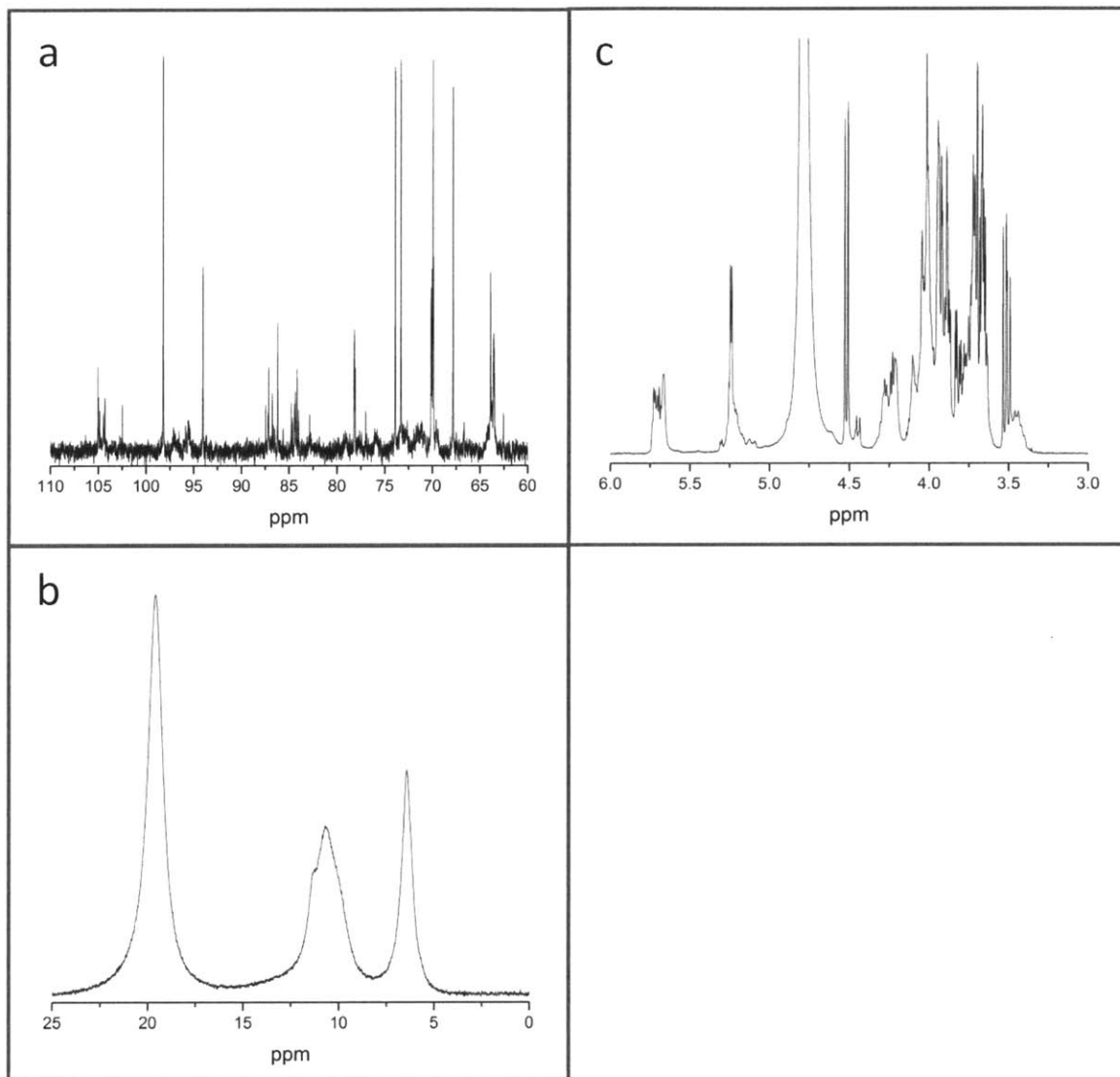


Figure S21. Solution NMR spectra for D-arabinose with a 4:1 sugar:SB molar ratio in H₂O. a) ¹³C NMR of D-arabinose, b) ¹¹B NMR, and c) ¹H NMR

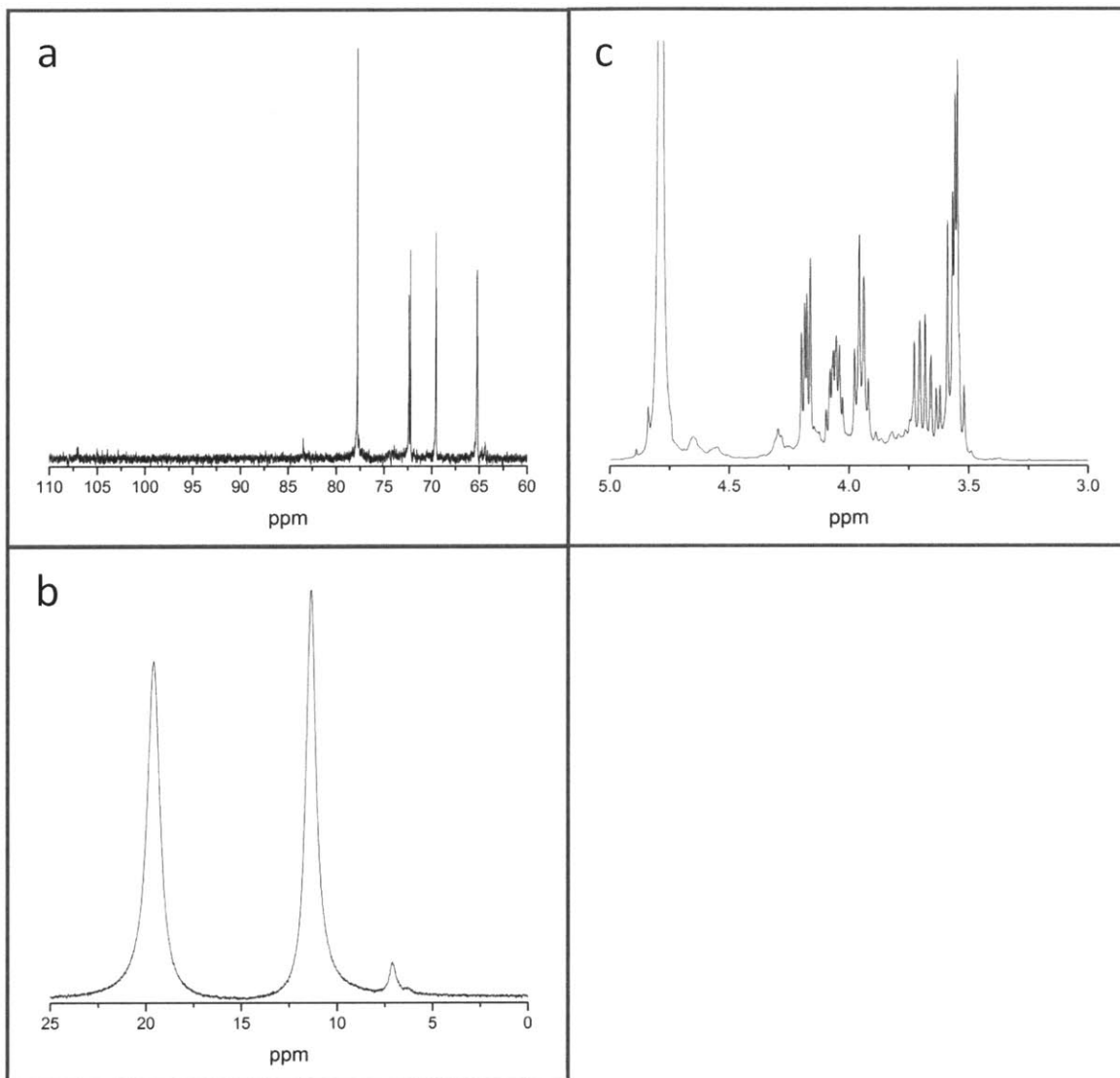


Figure S22. Solution NMR spectra for D-ribulose with a 4:1 sugar:SB molar ratio in H₂O. a) ¹³C NMR of D-ribulose, b) ¹¹B NMR, and c) ¹H NMR

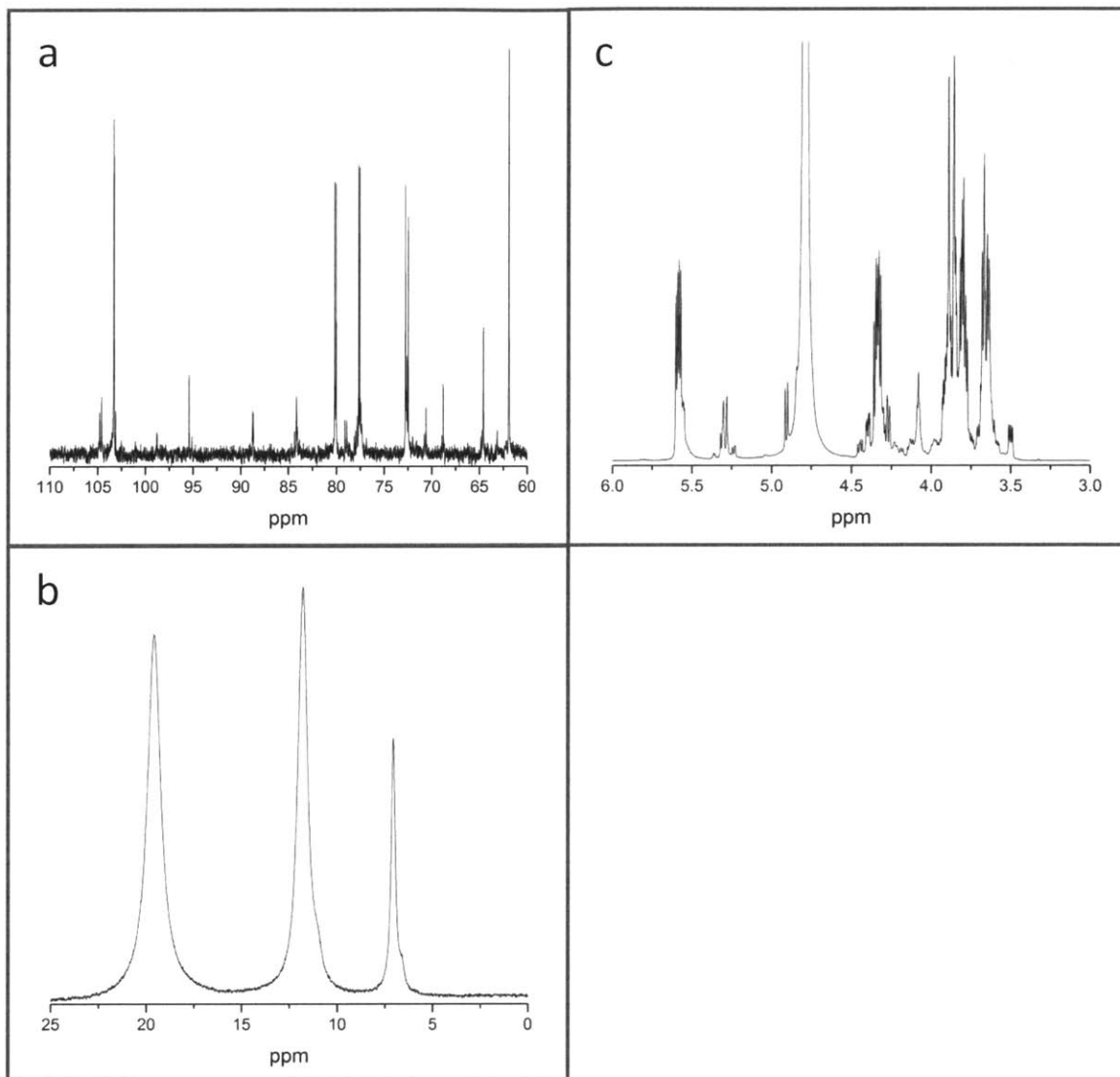


Figure S23. Solution NMR spectra for D-ribose with a 4:1 sugar:SB molar ratio in H₂O. a) ¹³C NMR of D-ribose, b) ¹¹B NMR, and c) ¹H NMR

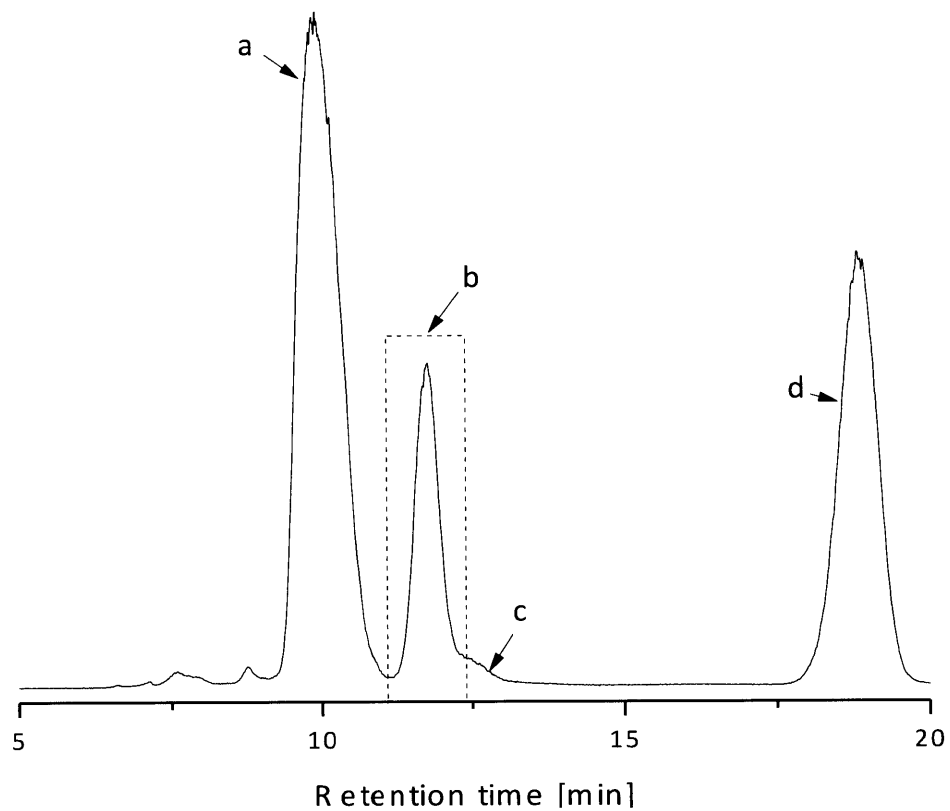


Figure S24. HPLC chromatograph of a 5 wt% D-(1-¹³C)glucose solution with a 4:1 glucose:SB molar ratio, reacted at 358 K for 60 min. The peaks correspond to a) glucose, b) mannose, c) fructose, and d) internal standard. The dotted line around peak b represents the fraction collected by fractionation and analyzed by ¹H and ¹³C NMR (see Figure S32).

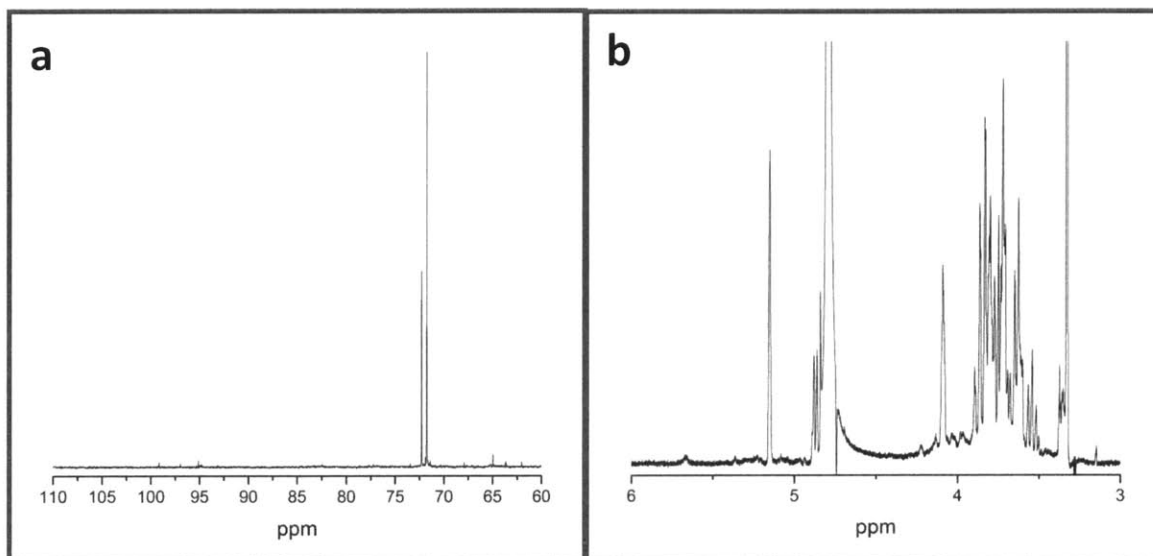


Figure S25. Solution NMR spectra of the product fraction obtained by HPLC from a 5 wt% D-(1-¹³C)glucose solution with a 4:1 glucose:SB molar ratio, reacted at 358K for 60 min (see dotted line in Figure S31). a) ¹³C NMR and b) ¹H NMR.

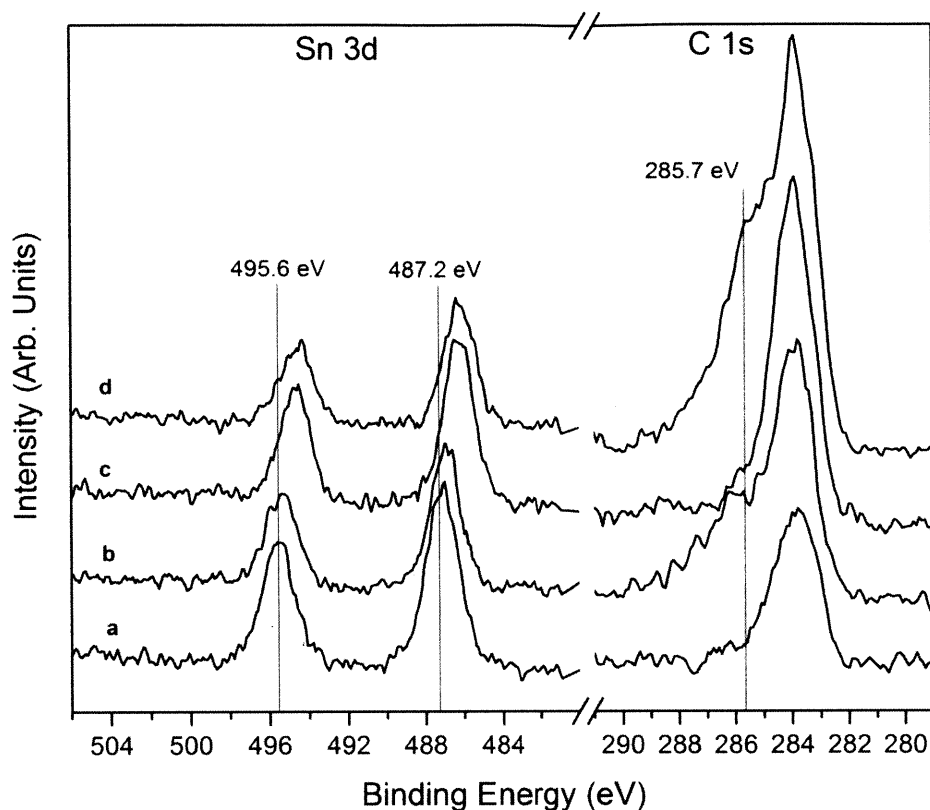


Figure S26. XPS spectra for Sn 3d and C 1s. a) calcined Sn-Beta; b) Sn-Beta with adsorbed glucose; c) Sn-Beta with adsorbed potassium borate; and d) Sn-Beta with adsorbed glucose and potassium borate. Potassium borate instead of sodium borate was used in these measurements to avoid obfuscation of the Sn 3d signal by the sodium $KL_{23}L_{23}$ Auger signal. The Sn 3d signals for calcined Sn-Beta were located at 487.2 eV and 495.6 eV, which is consistent with tetrahedral coordination of Sn in the framework. The presence of glucose lowered the binding energy by ~ 0.3 eV, while the presence of either borate or a glucose/borate mixture decreased the binding energy by ~ 0.9 eV. The observed downward shift in binding energy signifies a change in the electronic environment of the Sn surface sites that has been attributed to adsorbed species or a possible structural modification.¹³⁸ For these samples, the C 1s signal is at a higher binding energy than the adventitious carbon signal. These data suggest the presence of the glucose-borate complex on the surface of the catalyst.

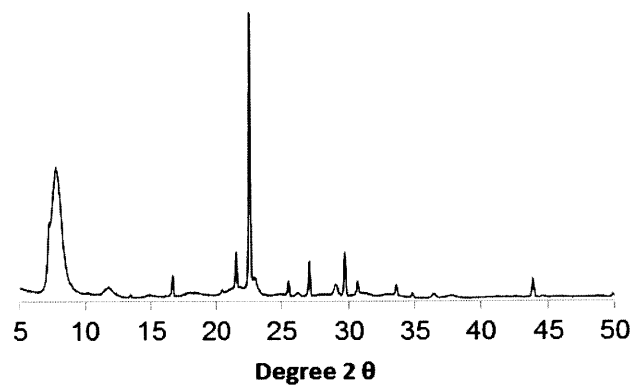


Figure S27. Powder X-ray diffraction pattern of Sn-Beta.

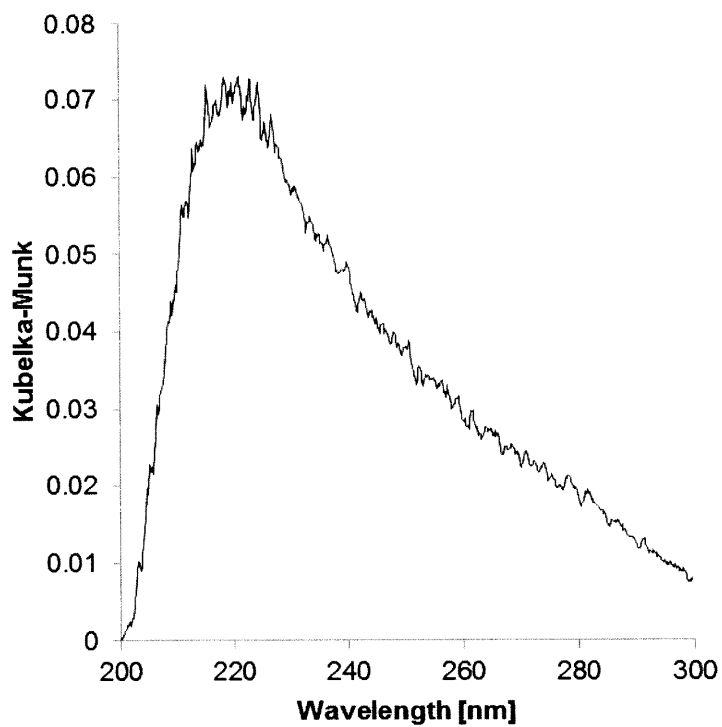


Figure S28. UV-Vis diffuse reflectance of Sn-Beta.

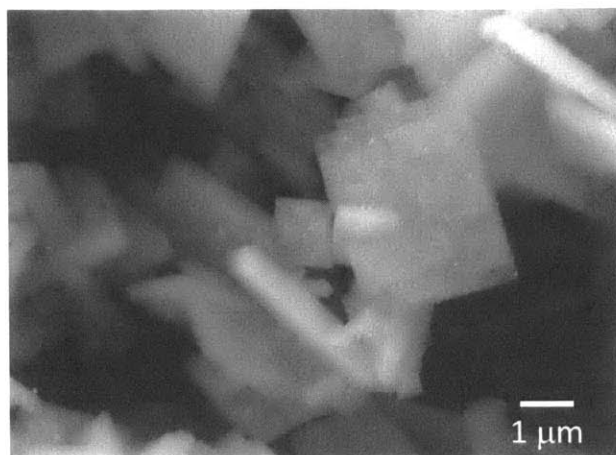


Figure S29. SEM image of Sn-Beta zeolite.

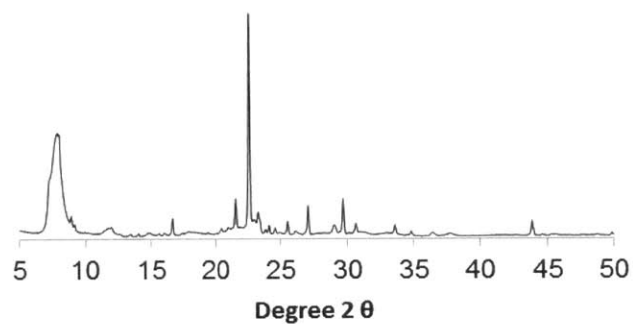


Figure S30. Powder X-ray diffraction pattern of Ti-Beta.

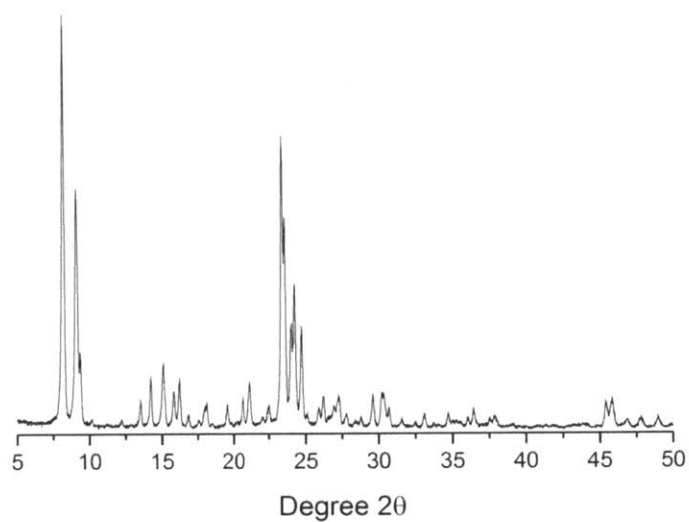


Figure S31. Powder X-ray diffraction patterns of Sn-MFI.

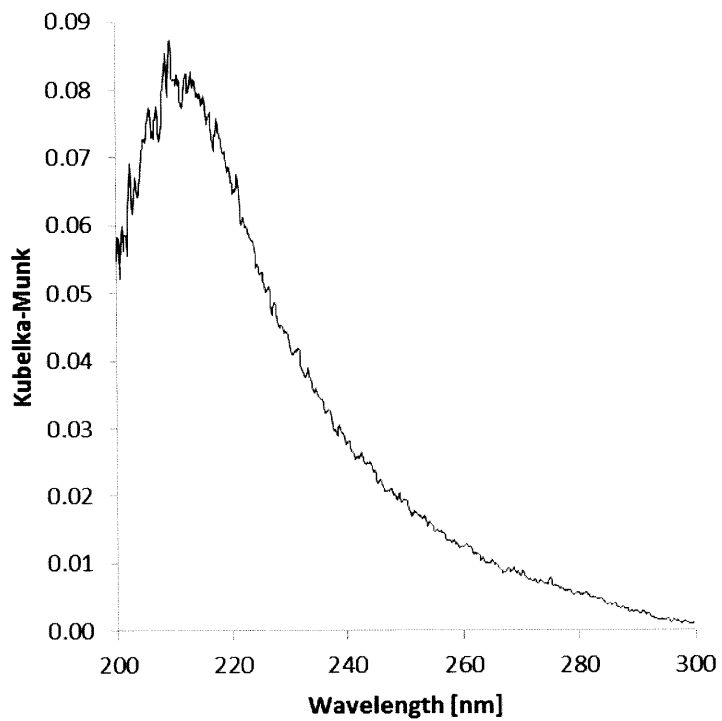


Figure S32. UV-Vis diffuse reflectance of Sn-MFI.

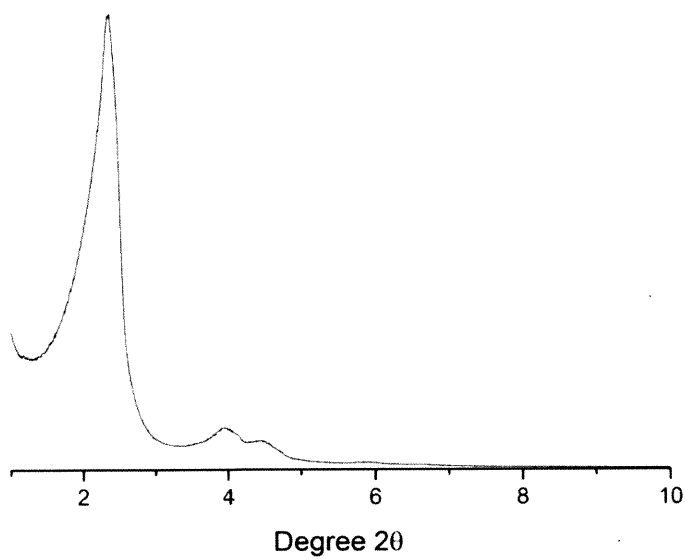


Figure S33. Powder X-ray diffraction pattern of Sn-MCM-41.

Table S9. Time study for the epimerization of glucose with SB.

<i>Without Sodium Borate</i>						<i>With 4:1 Sodium Borate</i>				
Time [min]	Conversion [%]	Reagent [%]	Isomer [%]	Epimer [%]	Sugar Yield [%]	Conversion [%]	Reagent [%]	Isomer [%]	Epimer [%]	Sugar Yield [%]
15	15	90	10	0	95	11	89	0	11	100
30	21	83	16	1	95	14	87	0	13	99
45	27	79	19	2	93	17	85	0	15	98
60	29	76	21	3	93	16	84	1	15	99
90	35	71	25	4	92	19	83	1	16	97
120	40	67	28	5	90	20	82	1	17	98

Reactions were performed at 358 K with a 5 wt% sugar feed, using the corresponding amount of catalyst to maintain a 100:1 sugar:metal molar ratio.

Table S10. Time study for the epimerization of xylose with SB. Reactions were performed at 358 K with a 5 wt% sugar feed, using the corresponding amount of catalyst to maintain a 100:1 sugar:metal molar ratio.

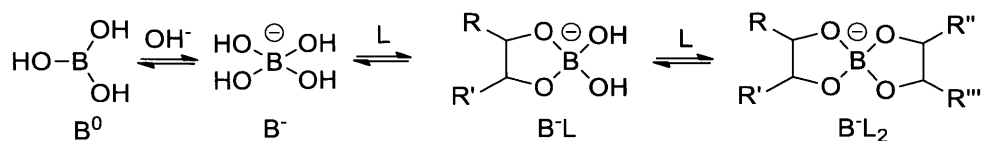
<i>Without Sodium Borate</i>						<i>With 4:1 Sodium Borate</i>				
Time [min]	Conversion [%]	Reagent [%]	Isomer [%]	Epimer [%]	Sugar Yield [%]	Conversion [%]	Reagent [%]	Isomer [%]	Epimer [%]	Sugar Yield [%]
15	24	79	13	8	96	30	75	3	22	93
30	34	71	15	14	93	36	72	4	24	90

Table S11. Time study for the epimerization of arabinose with SB.

<i>Without Sodium Borate</i>						<i>With 4:1 Sodium Borate</i>				
Time [min]	Conversion [%]	Reagent [%]	Isomer [%]	Epimer [%]	Sugar Yield [%]	Conversion [%]	Reagent [%]	Isomer [%]	Epimer [%]	Sugar Yield [%]
15	23	84	11	5	92	34	68	1	31	97
30	28	80	12	8	90	40	63	2	35	95

Reactions were performed at 358 K with a 5 wt% sugar feed, using the corresponding amount of catalyst to maintain a 100:1 sugar:metal molar ratio.

Table S12. ^{11}B chemical shifts of borate esters taken from Bekkum et al.⁷⁸ The values have been adjusted to the standard ^{11}B chemical reference.



Ester type	^{11}B Chemical Shift [ppm]	
	B ⁻ L	B ⁻ L ₂
1,2-Bidentate	7.0 to 4.7	11.9 to 7.7
1,3-Bidentate	1.7 to 1.1	1.2 to 0.6
1,3,5-Tridentate	1.5 to 0.2	

Table S13. ^{13}C chemical shifts of sugars. Note: ^1H NMR assignments can be found in the respective references.

Sugar	Conformation	Chemical Shifts [ppm]						Reference
		C1	C2	C3	C4	C5	C6	
Glucose	α -pyranose	93.2	72.6	73.9	70.8	72.6	61.8	139
	β -pyranose	97.0	75.3	76.9	70.8	77.0	61.9	139
	α -furanose	97.0	77.7	76.6	78.8	70.7	64.2	78
Fructose	β -pyranose	64.7	98.9	68.4	70.5	70.0	64.2	139
	α -furanose	63.6	104.0	82.8	75.7	80.8	60.9	139
	β -furanose	62.8	101.9	75.6	75.2	81.8	62.8	139
Mannose	α -pyranose	95.0	71.8	71.3	68.0	73.4	62.1	139
	β -pyranose	94.7	72.2	74.1	67.7	77.1	62.1	139
Xylose	α -pyranose	93.3	72.6	73.9	70.5	62.0		139
	β -pyranose	97.7	75.1	76.9	70.3	66.2		139
	α -furanose	96.0	77.8	76.2	79.3	61.6		78
Xylulose	α -furanose	63.9	107.2	82.0	77.3	73.4		140
	β -furanose	64.5	104.4	77.7	76.4	71.3		140
Lyxose	α -pyranose	95.2	71.2	71.7	68.6	64.1		139
	β -pyranose	95.2	71.2	73.7	67.7	65.1		139
Arabinose	α -pyranose	97.9	69.6	73.6	73.0	67.4		139
	β -pyranose	93.7	69.8	69.8	69.6	63.6		139
	β -furanose	96.7	77.8	75.8	82.9	62.7		78
Ribulose	α -furanose	64.3	104.0	71.9	71.6	72.9		140
	β -furanose	64.0	107.0	77.3	72.0	72.2		140
Ribose	α -pyranose	95.0	71.5	70.7	68.8	64.5		141
	β -pyranose	95.3	72.5	70.4	68.7	64.5		141
	α -furanose	97.8	72.4	71.5	84.5	62.9		141
	β -furanose	102.4	76.7	71.9	84.0	64.0		141

Table S14. Metal content in each solid material.

Material	Si/M	Total pore volume [cm ³ /g]	Micropore volume [cm ³ /g]	BET surface area [m ² /g]
Sn-Beta	111 ^[a]	0.36	0.17	n.d.
Ti-Beta	140 ^[b]	0.31	0.17	n.d.
Sn-MFI	180 ^[b]	0.25	0.10	n.d.
Sn-MCM-41	125 ^[b]	0.89	n.d.	900.20

[a] Measured by elemental analysis

[b] Measured by energy dispersive X-ray spectroscopy

Supplementary Methods

Synthesis of Ti-Beta

Ti-Beta was synthesized according to Moliner et al,^{12b} as follows: 26.02 g of aqueous tetraethylammonium hydroxide (Sigma-Aldrich, 35% (w/w)) and 23.789 g of tetraethylorthosilicate (Sigma-Aldrich, 99% (w/w)) were added to a PTFE dish which was stirred at room temperature for 90 min and then an additional 15 g of DI H₂O was added. Next, 0.327 g of titanium (IV) isopropoxide (Sigma-Aldrich, 97% (w/w)) was added dropwise. The solution was left uncovered on a stir plate for 10 h to reach 15 g of total water. Next, 2.538 g of aqueous hydrofluoric acid (Sigma-Aldrich 48% (w/w)) was added dropwise and the mixture was homogenized using a PTFE spatula resulting in a thick gel. Then, 0.348 g of previously made Si-Beta was seeded into the mixture, which was allowed to evaporate to a final molar composition of SiO₂ / 0.01 TiO₂ / 0.54 TEAOH / 0.53 HF / 6.6 H₂O. The thick paste was transferred to a PTFE-lined stainless steel autoclave and heated to 413 K for 14 days. The solids were recovered by filtration, washed with DI H₂O, dried at 373 K, and calcined at 853 K for 10 h with a 1 K/min ramp and 1 h stops at 423 K and 623 K leading to an overall 80-90% yield.

XRD confirmed that the solid material has the Beta zeolite topology (Figure S30). SEM EDS measurements show an atomic ratio Si:Ti of 140:1.

Synthesis of Sn-MCM-41

Sn-MCM-41 was synthesized according to Kumar et al,^{51b} as follows: 3.059 g of fumed silica (Sigma-Aldrich, 99.8%) was added slowly to 5.513 g of aqueous tetramethylammonium hydroxide (Sigma-Aldrich, 25% (w/w)) with constant stirring. Then, 0.181 g of tin (IV) chloride pentahydrate dissolved in 6.198 g of DI H₂O and added dropwise to the first mixture. Next, 4.426 g of hexadecyltrimethylammonium bromide (Sigma-Aldrich, 98% (w/w)) dissolved in 12.395 g of DI H₂O was added. The thick gel was stirred for 2 h, transferred to a PTFE-lined stainless steel autoclave and heated

to 383 K for 72 h. The final molar composition was $\text{SiO}_2 / 0.01 \text{ SnCl}_4 / 0.24 \text{ C}_{16}\text{TABr} / 0.3 \text{ TMAOH} / 25 \text{ H}_2\text{O}$. The solid was recovered by filtration, extensively washed with DI H_2O , dried at 373 K, and calcined at 853 K for 10 h with a 1 K/min ramp and 1 h stops at 423 K and 623 K.

PXRD confirmed that the solid material has the MCM mesoporous topology (Figure S33). SEM EDS measurements for the Sn-MCM-41 sample show an atomic ratio Si:Sn of 125:1. BET measurements demonstrate that the material is mesoporous (see Table S14).

Note on HPLC analysis

The HPX-87C column separates sugars by using calcium ions bound to a sulfonated divinyl benzene-styrene copolymer to complex with sugar isomers and change their retention time. Over time, repeated injections of sodium tetraborate (SB) can lead to ion exchange of Ca^{2+} ions out of the column, causing decreased separation quality and shifts in retention times. For this reason, the column was regenerated with 0.1 M $\text{Ca}(\text{NO}_3)_2$ on a daily basis while taking care to purge out loose calcium before sample analysis. Ketoses showed the strongest tendency to shift retention time. Fractionation and NMR were used to check peak purity. An alternate sample preparation procedure involves treating the sample with an acidic cation exchange resin followed by an anion exchange resin. The first resin removes sodium cations and acidifies the sample thereby promoting dissociation of the sugar borate complex. Next, the anion exchange resin removes borate anions.

9.4 Catalytic consequences of borate complexation and pH on the epimerization of L-arabinose to L-ribose in water catalyzed by Sn-Beta zeolite with borate salts

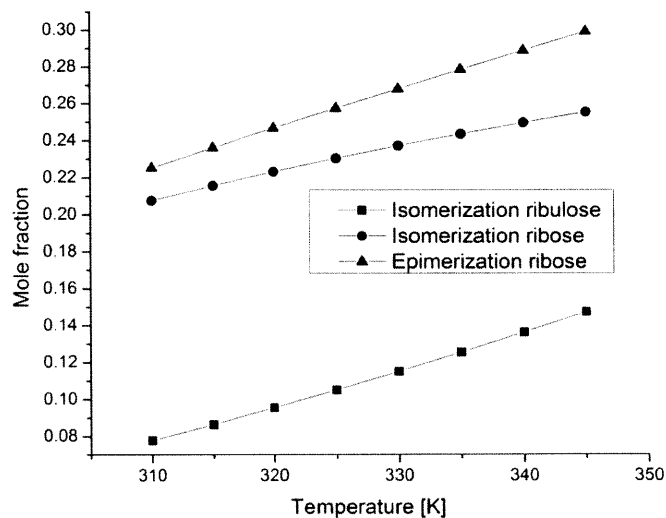


Figure S34. Isomerization and epimerization equilibrium calculated based on Tewari⁹⁹

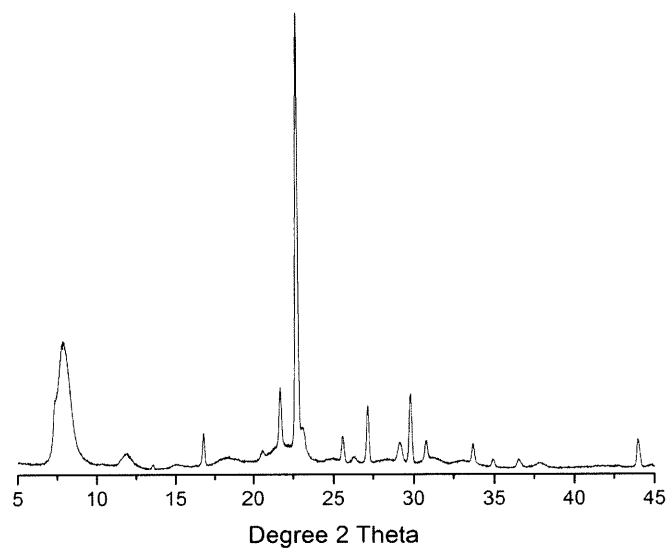


Figure S35. XRD of Sn-Beta

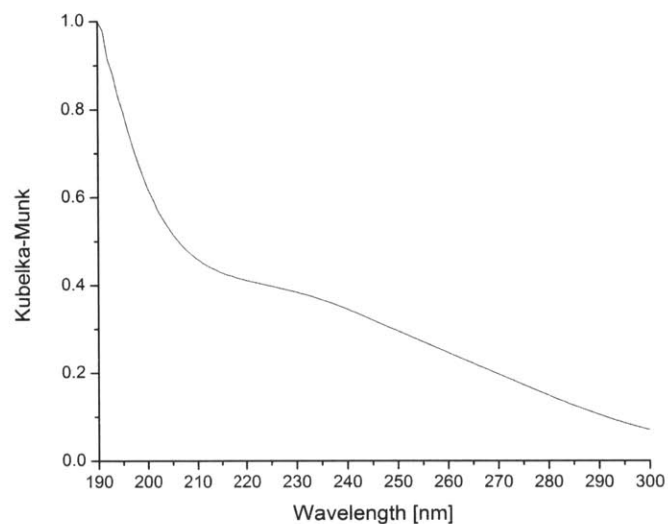


Figure S36. Diffuse-reflectance ultraviolet spectra of Sn-Beta

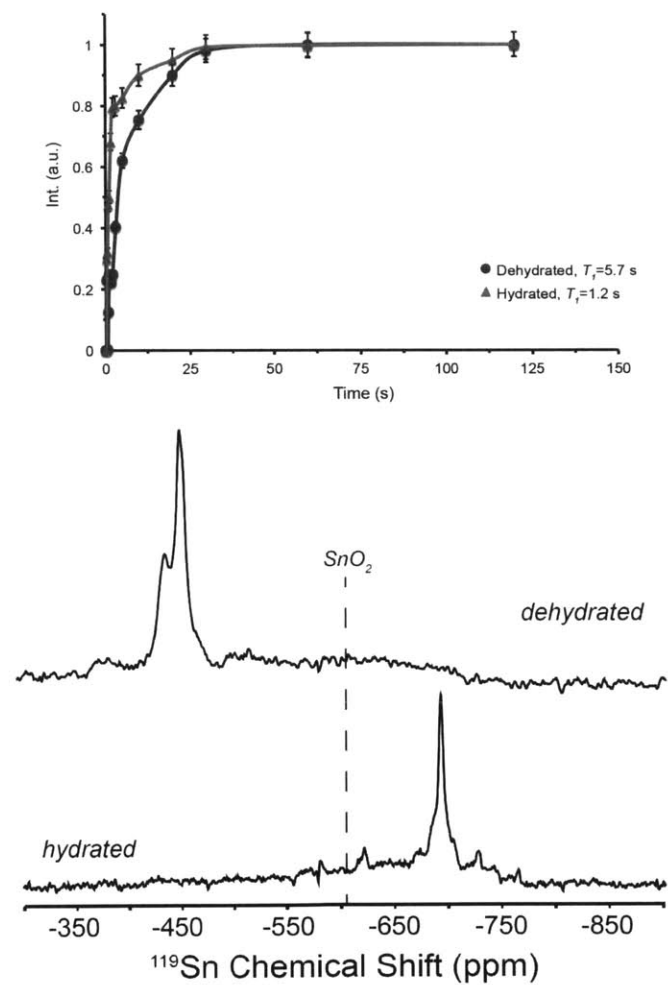


Figure S37. ^{119}Sn NMR of Sn-Beta

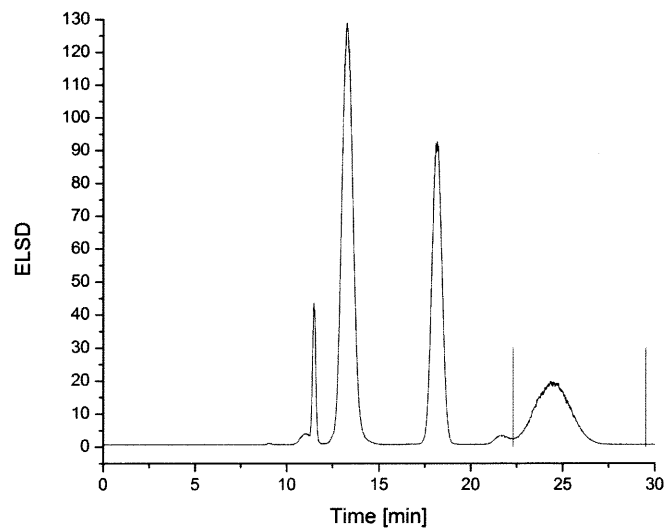


Figure S38. Ribose HPLC fraction used for polarimetry

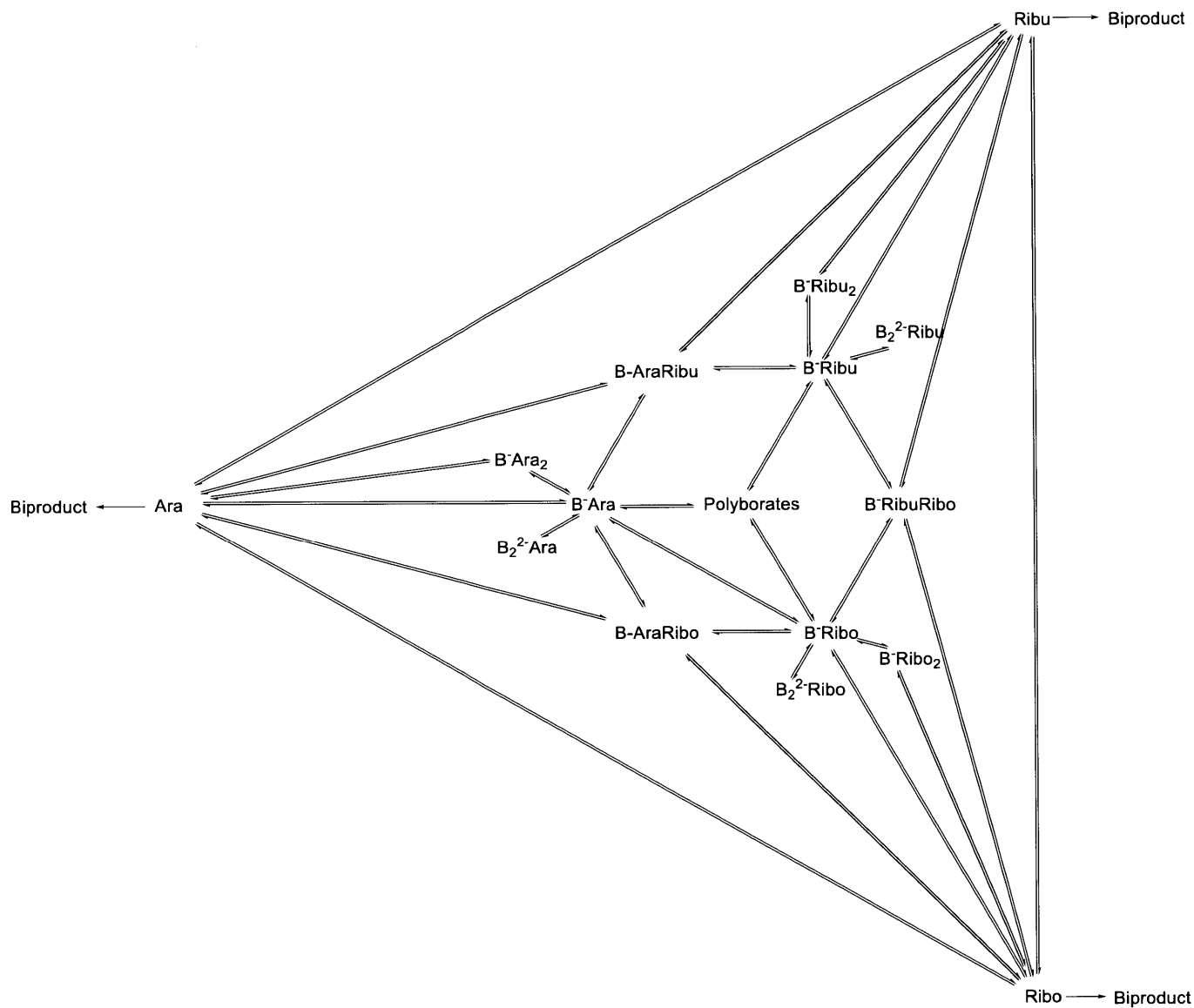


Figure S39. Sugar borate complexation

Table S15. Feed solutions for full factorial design involving pH, borate to sugar ratio and reaction time as reaction variables for the epimerization of arabinose to ribose.

Entry	Borate: Arabinose	B-/B	pH	Molar Ratio of Components				
				Arabinose	Boric acid	Sodium tetraborate	Sodium metaborate	Sodium hydroxide
1	1:1	0.00	3.75	1	1	0	0	0
2		0.23	6.50	1	0.550	0.113	0	0
3		0.41	6.97	1	0.175	0.206	0	0
4		0.50	7.21	1	0	0.25	0	0
5		0.64	7.50	1	0	0.179	0.284	0
6		1.00	8.37	1	0	0	1	0
7	0.5:1	0.00	3.93	1	0.5	0	0	0
8		0.22	6.51	1	0.285	0.054	0	0
9		0.45	7.02	1	0.05	0.113	0	0
10		0.50	7.11	1	0	0.125	0	0
11		0.74	7.49	1	0	0.066	0.235	0
12		1.00	8.37	1	0	0	0.5	0
13	0.4:1	0.00	3.98	1	0.4	0	0	0
14		0.21	6.5	1	0.23	0.043	0	0
15		0.45	6.97	1	0.04	0.09	0	0
16		0.50	7.10	1	0	0.1	0	0
17		0.78	7.50	1	0	0.044	0.225	0
18		1.00	7.88	1	0	0	0.4	0
19		1.10	8.37	1	0	0	0.4	0.0395
20	0.2:1	0.00	4.10	1	0.2	0	0	0
21		0.21	6.50	1	0.115	0.021	0	0
22		0.46	6.99	1	0.015	0.046	0	0
23		0.50	7.09	1	0	0.05	0	0
24		0.80	7.50	1	0	0.019	0.124	0
25		1.00	7.83	1	0	0	0.2	0
26		1.10	8.38	1	0	0	0.2	0.019

Reactions were performed at a 100:1 sugar:metal molar ratio with a 5 wt% arabinose feed at 343 K in a stirred batch reactor with Sn-Beta with a Si/Sn of 96.

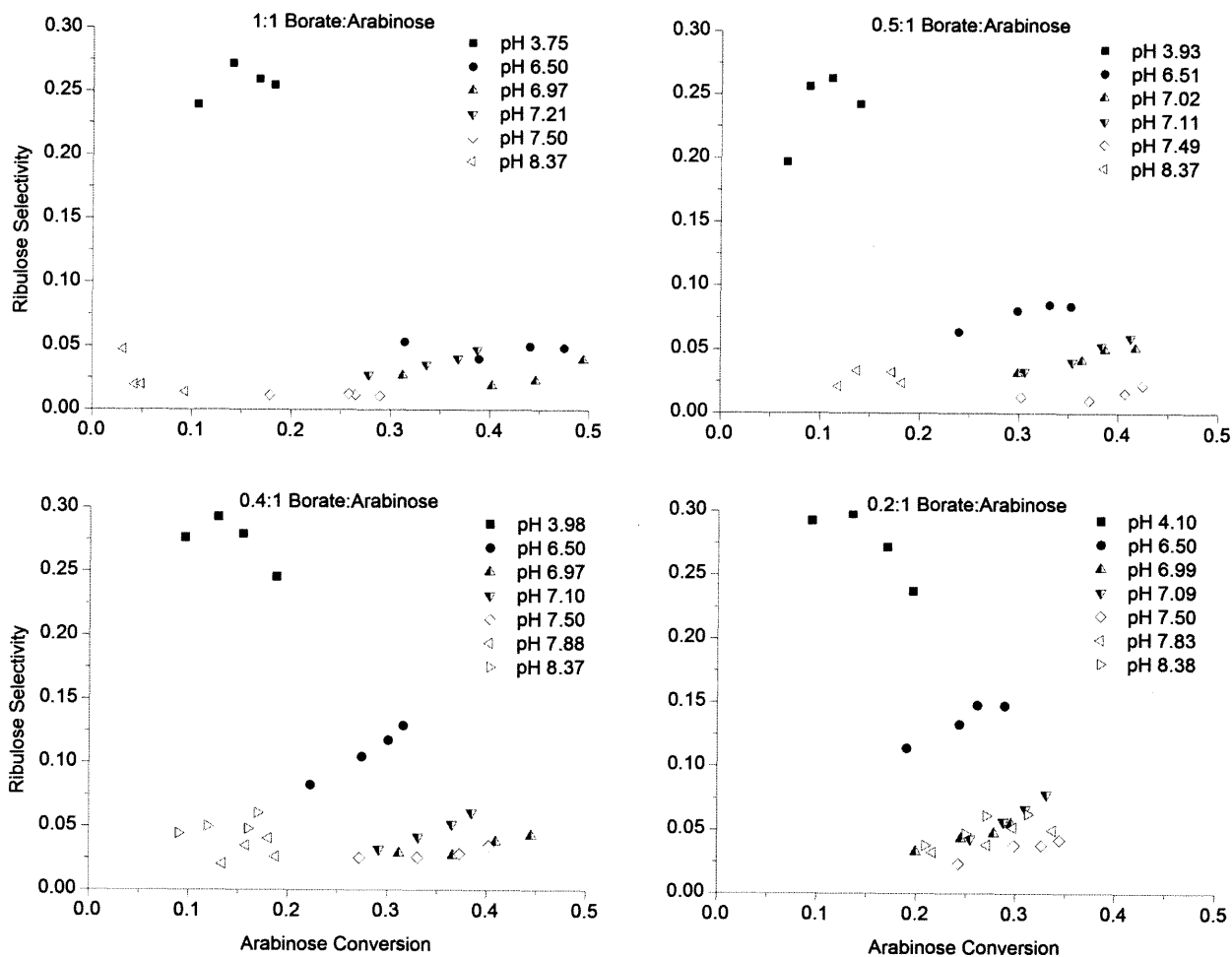


Figure S40. Factorial design for isomerization of arabinose to ribulose. Reactions were performed at a 100:1 sugar:metal molar ratio with a 5 wt% arabinose feed at 343 K in a stirred batch reactor using Sn-Beta with a Si/Sn of 96.

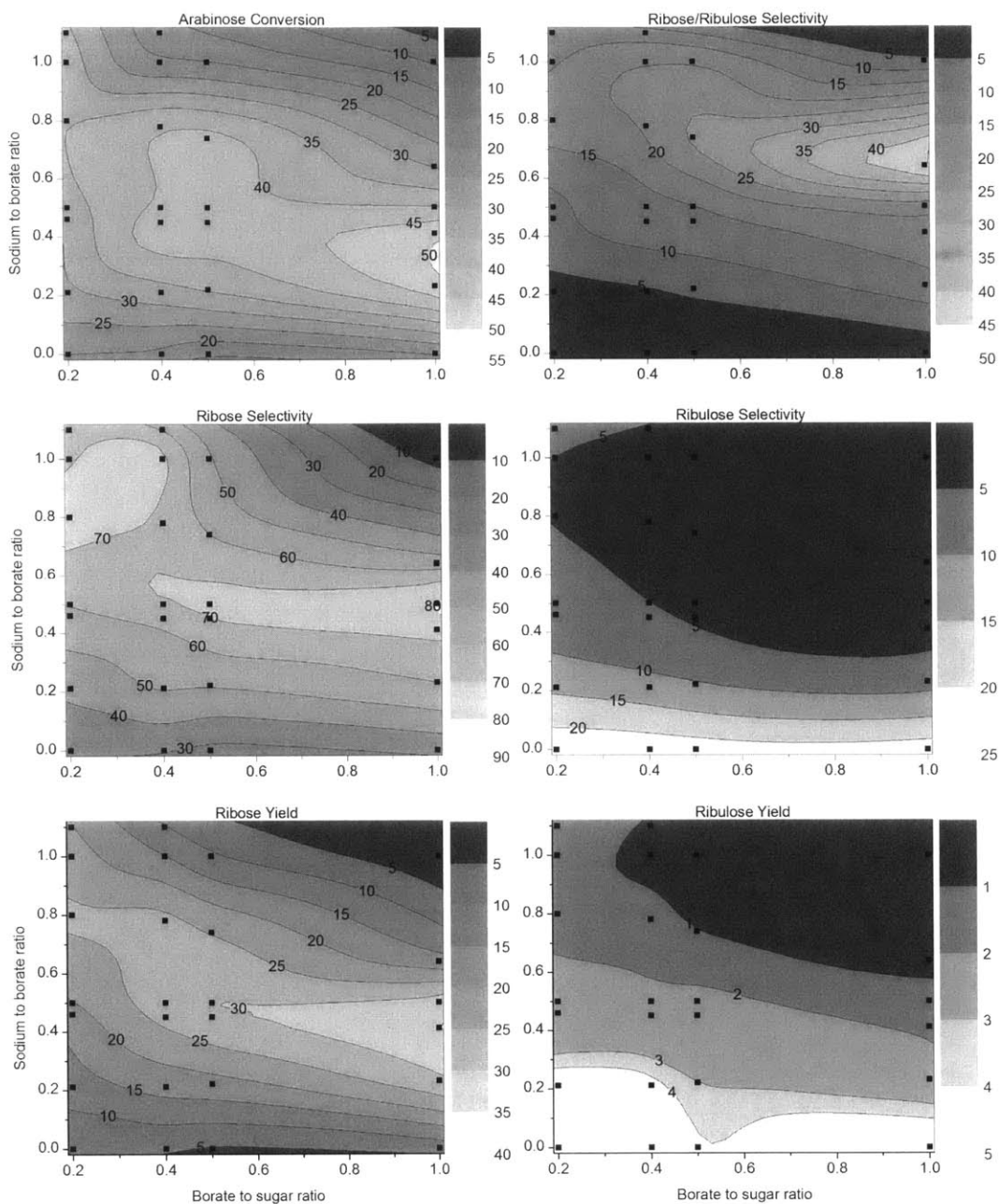


Figure S41. Contour plots as a function of borate to sugar ratio and sodium to borate ratio at 60 minutes for: a) arabinose conversion, b) ratio of ribose to ribulose selectivities (i.e., instantaneous selectivity of ribose), c) ribose selectivity, d) ribulose selectivity, e) ribose yield, f) ribulose yield. The response surface passes within experimental error of all experimental points which are labeled with dots on the plot. Reactions were performed at a 100:1 sugar:metal molar ratio with a 5 wt% arabinose feed at 343 K in a stirred batch reactor, using Sn-Beta with a Si/Sn of 96.

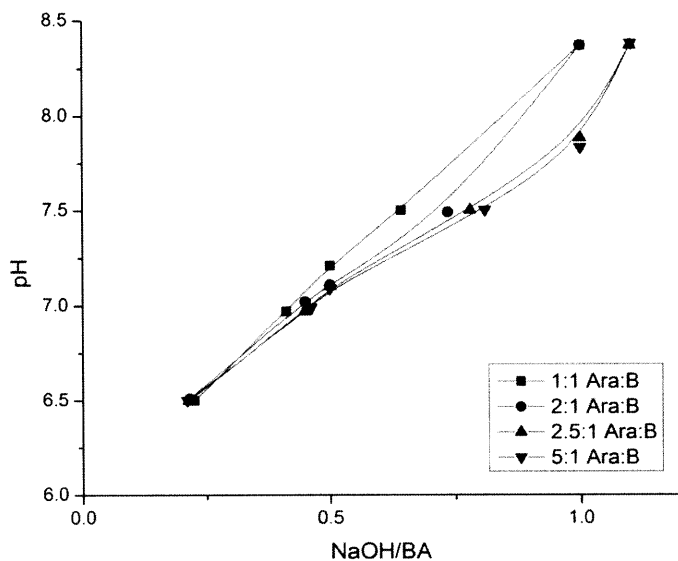


Figure S42. pH dependence on sodium to borate ratio measured at 298 K

The pH is linear with the amount of sodium hydroxide added according to the Henderson–Hasselbalch equation.

$$pH = pK_a + \log \left(\frac{[A^-]}{[HA]} \right) \quad (S4)$$

With decreasing B, all of the curves approach the steepest curve, which is the one calculated for a normal weak acid. At these low concentrations, the only species that need be considered would be B and AB⁻. At higher borate concentrations there are signs of association.

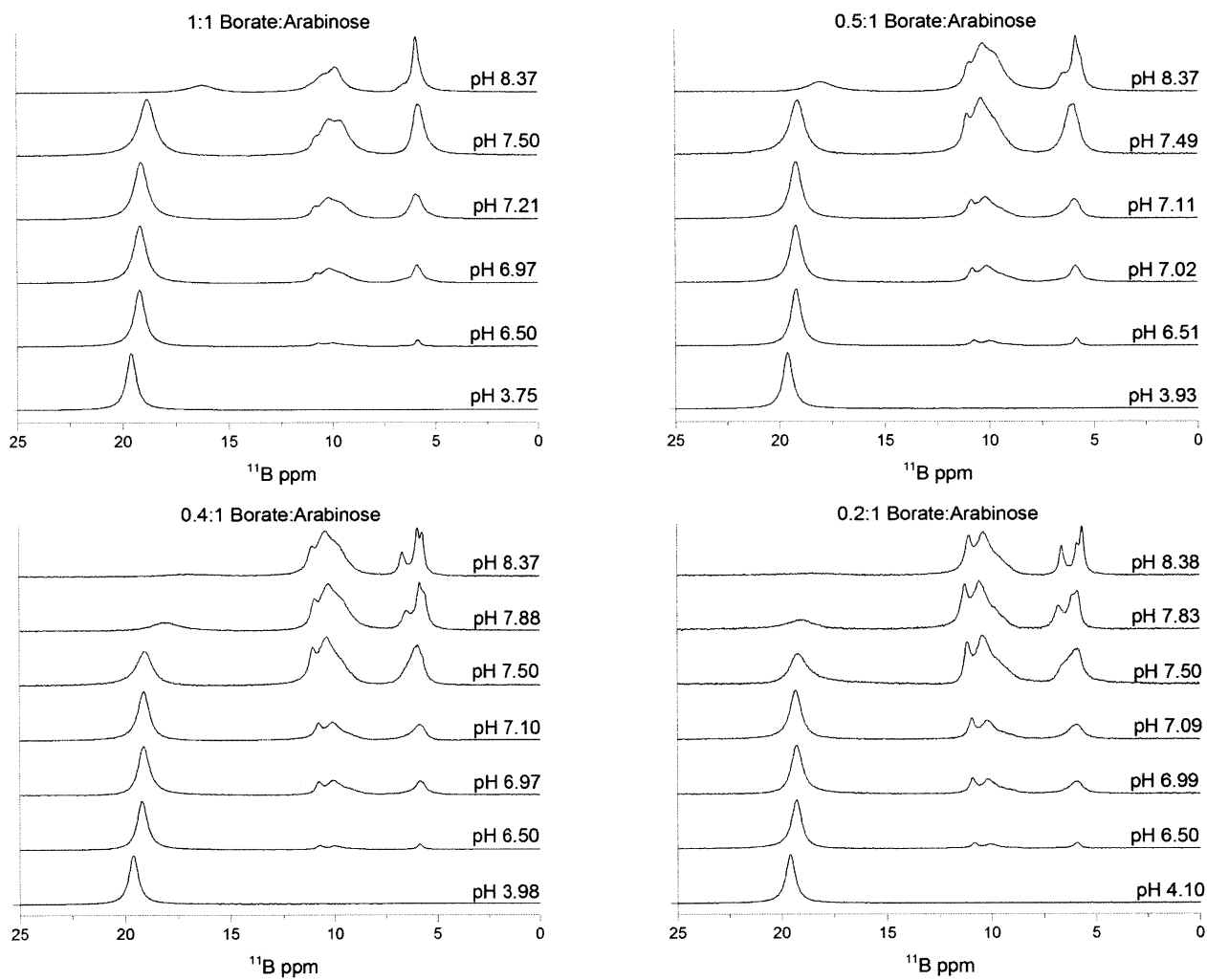


Figure S43. ^{11}B NMR performed on 5 wt% arabinose solutions with borate at 298 K

Table S16. Summary of ^{11}B NMR chemical shifts

Arabinose: Borate	B-/B	pH	Fraction (δ ppm)	Fraction (δ ppm)	Fraction (δ ppm)	Fraction (δ ppm)	Fraction (δ ppm)	Fraction (δ ppm)	Fraction (δ ppm)
1:1	0.00	3.75	1 19.61						
	0.23	6.50	0.83 19.21	0.02 10.75	0.11 9.98			0.05 5.86	
	0.41	6.97	0.54 19.18	0.03 10.82	0.14 10.18	0.08 9.50	0.07 5.87	0.14 5.87	
	0.50	7.21	0.49 19.12	0.03 10.86	0.16 10.25	0.14 9.57	0.07 6.01	0.12 5.79	
	0.64	7.50	0.38 18.82	0.02 10.82	0.17 10.22	0.19 9.54	0.07 5.91	0.17 5.69	
	1.00	8.37	0.17 16.24		0.24 10.49	0.23 9.81	0.01 6.58	0.35 5.91	
2:1	0.00	3.93	1 19.61						
	0.22	6.51	0.80 19.20	0.03 10.75	0.11 9.96			0.06 5.85	
	0.45	7.02	0.55 19.20	0.05 10.83	0.18 10.14	0.07 9.40	0.04 5.99	0.12 5.87	
	0.50	7.11	0.49 19.20	0.06 10.88	0.23 10.18	0.05 9.44	0.05 6.27	0.12 5.89	
	0.74	7.49	0.30 19.13	0.06 11.07	0.27 10.41	0.13 9.72	0.24 6.03		
	1.00	8.37	0.13 18.00	0.05 10.98	0.26 10.37	0.27 9.70	0.04 6.49	0.25 5.82	
2.5:1	0.00	3.98	1 19.62						
	0.21	6.5	0.82 19.20	0.04 10.74	0.08 9.96	0.01 9.05		0.05 5.85	
	0.45	6.97	0.54 19.12	0.06 10.78	0.19 10.06	0.06 9.30	0.01 6.51	0.14 5.82	
	0.50	7.10	0.50 19.12	0.08 10.80	0.23 10.08	0.03 9.29	0.07 6.15	0.09 5.79	
	0.78	7.50	0.26 19.09	0.07 11.07	0.32 10.40	0.10 9.69	0.10 6.28	0.15 5.90	
	1.00	7.88	0.13 18.08	0.06 10.97	0.29 10.34	0.23 9.66	0.07 6.48	0.14 5.85	0.07 5.59
	1.10	8.37	0.07 16.97	0.06 11.11	0.35 10.47	0.22 9.79	0.08 6.67	0.13 5.95	0.08 5.70
5:1	0.00	4.10	1 19.59						
	0.21	6.50	0.80 19.29	0.05 10.83	0.08 10.03	0.01 9.03		0.06 5.93	

	0.46	6.99	0.55 19.26	0.08 10.91	0.17 10.15	0.05 9.35		0.16 5.96	
	0.50	7.09	0.50 19.32	0.09 10.94	0.20 10.18	0.04 9.34		0.17 5.97	
	0.80	7.50	0.26 19.15	0.08 11.14	0.27 10.41	0.13 9.63	0.07 6.48	0.18 5.92	
	1.00	7.83	0.16 19.11	0.13 11.27	0.37 10.54	0.07 9.77	0.08 6.78	0.12 6.13	0.07 5.86
	1.10	8.38	0.09 18.81	0.13 11.07	0.40 10.36	0.09 9.61	0.09 6.62	0.08 5.90	0.12 5.64

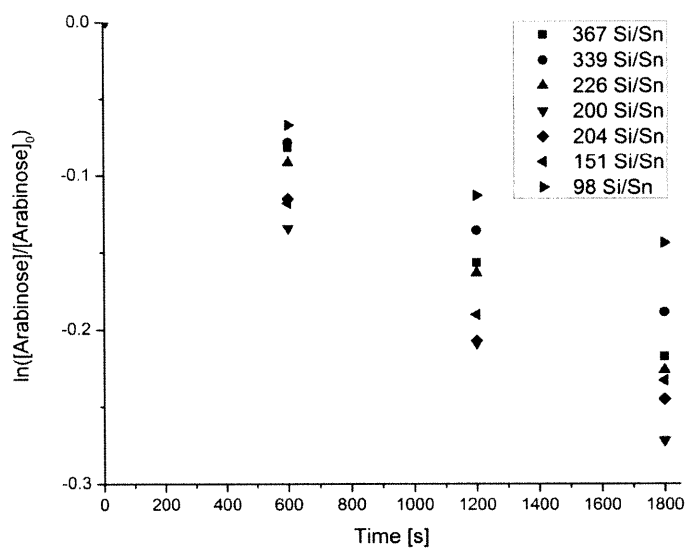


Figure S44. Madon-Boudart test at 343 K Experiments were performed with 20 mg of catalyst and a sufficient volume of 5 wt% arabinose to achieve 2000 sugar:metal in a stirred batch reactor.

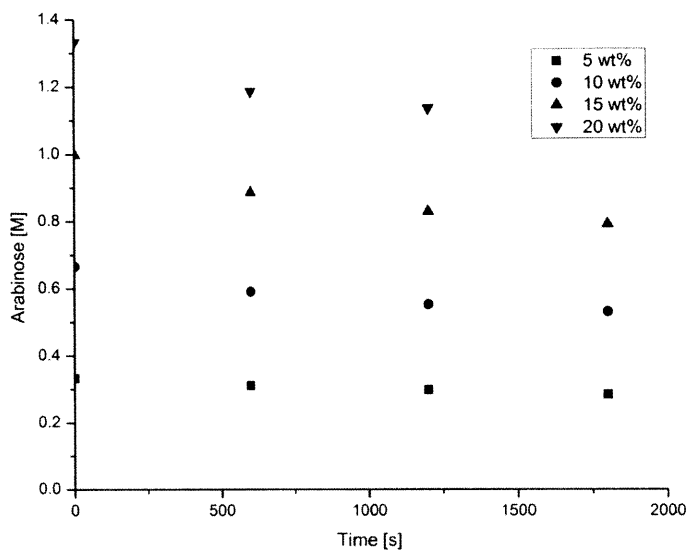


Figure S45. Reaction order plot for initial rates at 343 K and 1000:1 sugar:metal. Reactions were performed with a 5 wt% arabinose feed in a stirred batch reactor using Sn-Beta with a Si/Sn of 98.

Table S17. Arrhenius kinetic data for epimerization and isomerization. Epimerization reactions were performed with a 5 wt% arabinose 1:1 borate:sugar feed at pH 7.21 in a stirred batch reactor using Sn-Beta with a Si/Sn of 98. Isomerization was performed unbuffered with 5 wt% arabinose.

T [K]	k epimerization [s ⁻¹]	k isomerization [s ⁻¹]
313	2.9*10 ⁻⁶	
318	6.2*10 ⁻⁶	
323	1.3*10 ⁻⁵	5.1*10 ⁻⁶
328	1.4*10 ⁻⁵	7.5*10 ⁻⁶
333	3.6*10 ⁻⁵	1.3*10 ⁻⁵
338	4.2*10 ⁻⁵	2.0*10 ⁻⁵
343	9.3*10 ⁻⁵	3.7*10 ⁻⁵

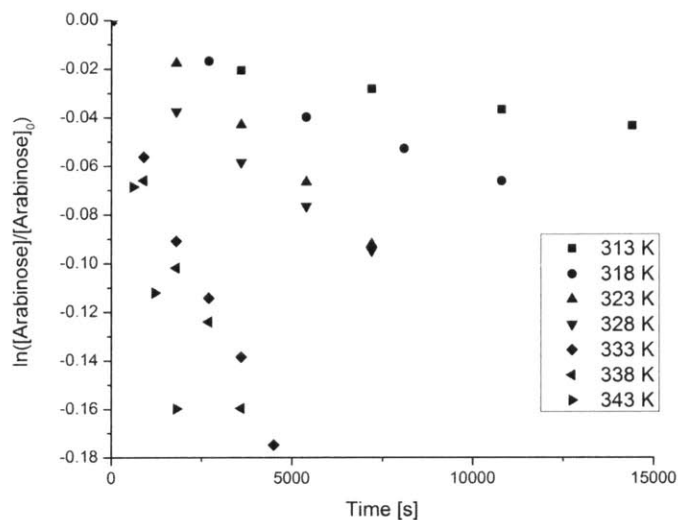


Figure S46. Arrhenius plot for first order epimerization reaction with 1000:1 sugar:metal. Epimerization reactions were performed with a 5 wt% arabinose 1:1 borate:sugar feed at pH 7.21 in a stirred batch reactor using Sn-Beta with a Si/Sn of 98. Isomerization was performed unbuffered with 5 wt% arabinose.

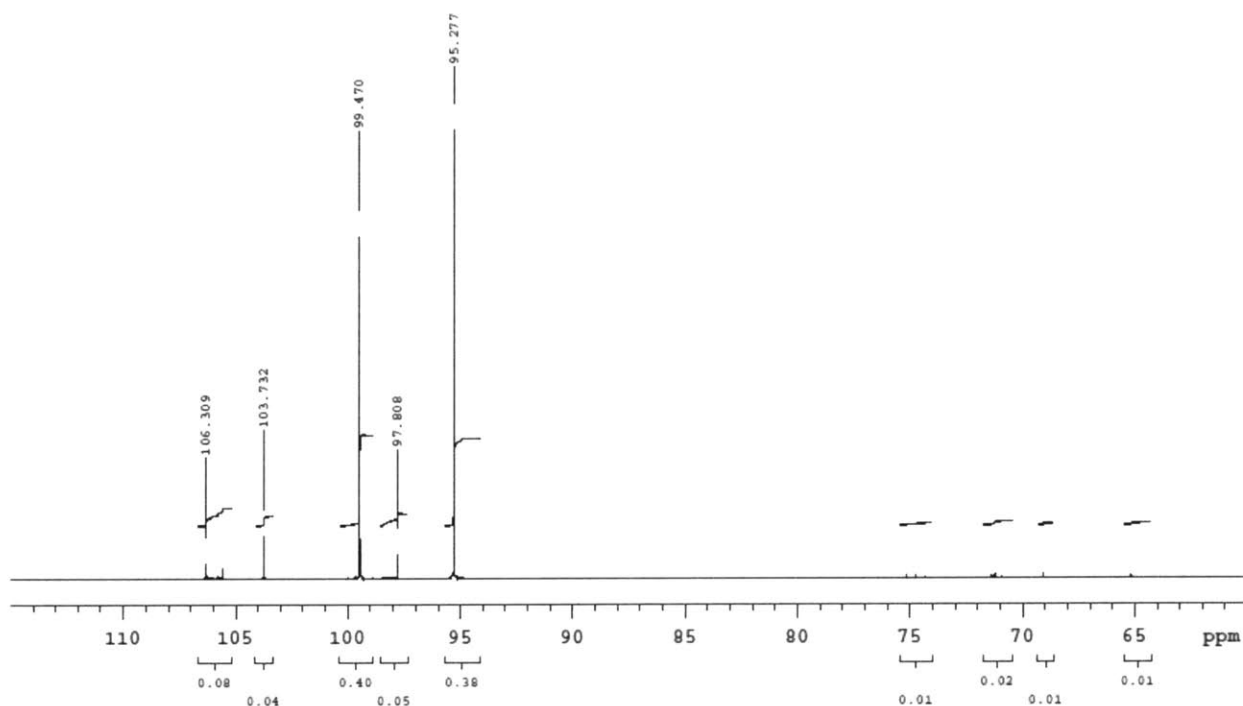


Figure S47. ^{13}C NMR of L- $^{13}\text{C}_1$ arabinose with 5:1 sugar:borate at pH 7.09 in D_2O .

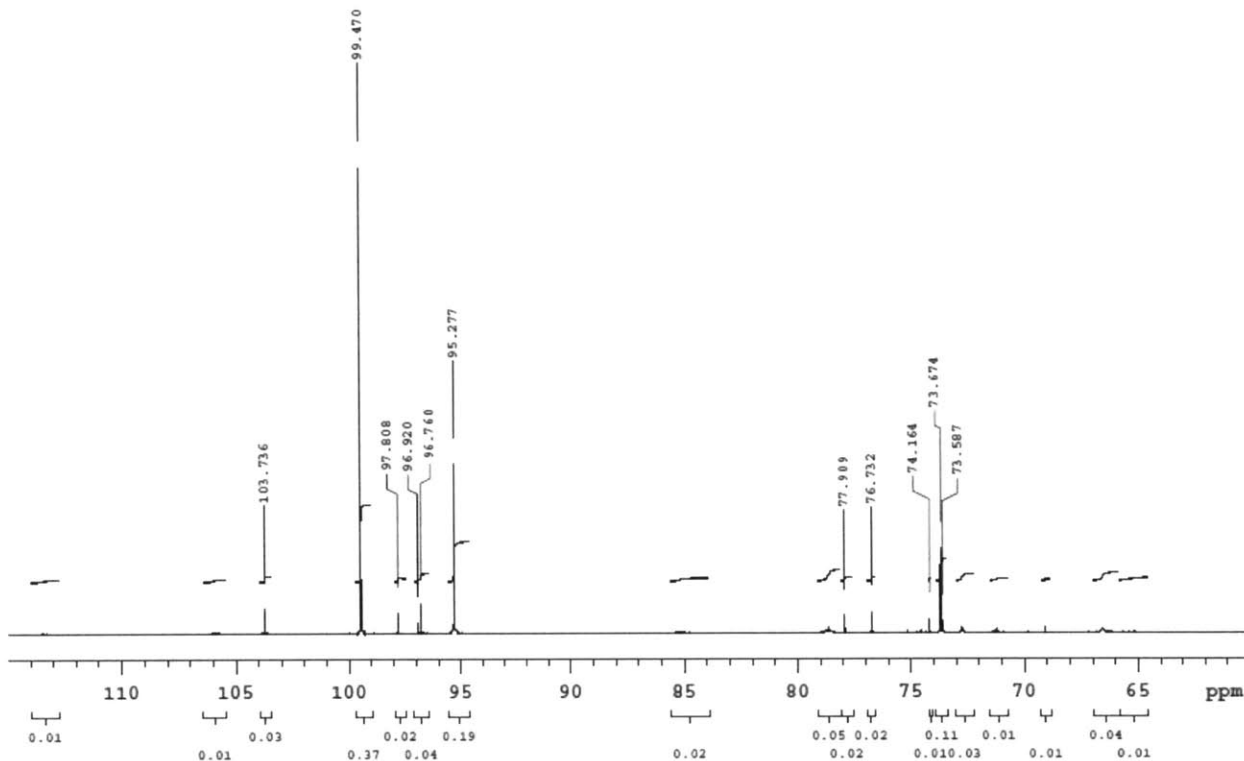


Figure S48. ^{13}C NMR of L- $^{13}\text{C}_1$ Arabinose with 5:1 sugar:borate at pH 7.09 in D_2O after reaction with 100:1 sugar:Sn-Beta at 343 K for 60 minutes.

Table S18. Epimerization of L-arabinose with 1000:1 sugar:metal, performed with a 5 wt% arabinose 1:1 borate:arabinose feed at pH 7.21 in a stirred batch reactor using Sn-Beta with a Si/Sn of 98.

Time [seconds]	Conversion [%]	Ribose Selectivity [%]	Ribulose Selectivity [%]
600	6	60	2
1200	9	69	2
1800	12	70	2

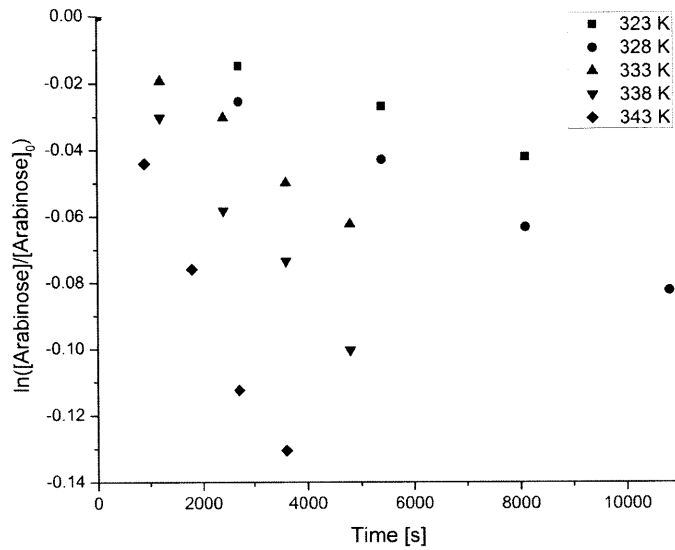


Figure S49. Arrhenius plot for first order isomerization reaction. Reactions were performed at a 1000:1 sugar:metal molar ratio with a 5 wt% arabinose feed at 343 K in a stirred batch reactor using Sn-Beta with a Si/Sn of 98.

$$k \frac{L}{\text{mol Sn} \cdot \text{s}} * 0.05 \frac{\text{g}}{\text{mL}} * \frac{\text{mol}}{150.13 \text{ g}} * \frac{\text{mol Sn}}{1000 \text{ mol Ara}} * \frac{1000 \text{ mL}}{L} = 6.21 * 10^{10} \text{ s}^{-1} \quad (\text{S5})$$

$$[\alpha]_{\lambda}^T = \frac{\alpha}{lc} \quad (\text{S6})$$

$[\alpha]$ = specific rotation

α = optical rotation

l = cell path in decimeters

c = concentration in g mL^{-1}

D-ribose

$$[\alpha]_{\lambda}^T = \frac{-0.1011}{1 \text{ dm} * 0.072 \text{ g mL}^{-1}} = -14$$

L-ribose

$$[\alpha]_{\lambda}^T = \frac{0.1663}{1 \text{ dm} * 0.0081 \text{ g mL}^{-1}} = 21$$

9.5 Mechanistic implications of a novel Sn-O-B-O-Si nanostructure on the epimerization of glucose with Sn-Beta zeolite

Table S19. Literature ¹³C chemical shifts referenced to 0.5% DSS in D₂O under MAS

		C-1	C-2	C-3	C-4	C-5	C-6	
glucose	α-pyr	94.1	73.7	75.0	71.8	73.5	62.8	142
	β-pyr	97.9	76.3	77.9	71.8	78.0	62.9	142
	β-fur	105.0	83.0		83.3			142
mannose	α-pyr	96.2	72.9	72.5	69.2	74.6	63.3	142
	β-pyr	95.8	73.5	75.3	69.0	78.4	63.3	142
fructose	α-pyr	67.1		72.1	72.5			143
	β-pyr	65.9	100.3	69.6	71.7	71.2	65.3	143
	α-fur	65.0	106.7	84.1	78.2	83.4	63.1	143
	β-fur	64.8	103.8	77.6	76.6	82.8	64.4	143
2-deoxy-D-glucose/ 2-deoxy-D-mannose	α-pyr	93.3	39.5	70.0	73.2	74.0	62.8	142
	β-pyr	95.3	41.7	72.6	72.9	78.0	63.1	142
3-deoxy-D-glucose =3-deoxy-D-ribo-hexose	α-pyr	93.0	68.6	35.9	66.4	74.3	62.8	142
	β-pyr	100.0	70.9	40.5	66.5	84.0	63.1	142
	α-fur	98.6	75.1	33.1	78.8	72.8	64.7	142
	β-fur	103.8	77.7	34.9	79.2	75.1	65.0	142
3-deoxy-D-mannose =3-deoxy-D-arabino-hexose	α-pyr	94.7	70.0	35.2	63.8	75.6	63.2	144
	β-pyr	96.7	69.8	39.0	63.6	81.9	63.5	144
	α-fur	104.1	77.3	34.3	80.2	74.9	64.9	144
3-deoxy-D-fructose =3-deoxy-D-erythro-hexulose	α-pyr		98.4					145
	β-pyr	69.6 66.0	99.4	43.5	69.2 67.0	67.0 69.2	66.0 69.6	145
	fur		107.5 107.8					145
	keto		213.9					145
	pyr	70.1	100.1	35.1	70.0 67.7	67.7 70.0	66.8	146
4-deoxy-D-glucose =4-deoxy-D-xylo-hexose	α-pyr	94.8	75.3	70.5	36.3	69.0	65.8	142
	β-pyr	98.3	78.1	74.4	36.3	72.5	65.7	142
4-deoxy-D-mannose =4-deoxy-D-lyxo-hexose	α-pyr	97.4	71.5	67.5	31.9	71.7	67.0	147
	β-pyr	96.8	72.7	70.8	31.3	75.4	66.7	147
4-deoxy-D-fructose-6-phosphate =4-deoxy-D-threo-hexulose-6-phosphate	α-fur	65.1	109.3	80.1	36.8	77.6	68.6	148
	β-fur	65.2	105.1	78.9	34.7	72.9	69.3	148
erythrose	α-fur	98.0	73.6	71.8	74.1			142

	β -fur	103.6	78.9	72.9	73.6			142
	hydrate	92.0	76.1	74.2	65.2			142
threose	α -fur	104.6	83.2	77.6	75.5			142
	β -fur	99.1	78.7	77.4	73.0			142
	hydrate	92.3	75.8	73.4	65.6			142
erythrose	keto	67.5	213.9	77.5	64.6			149
glyceraldehyde	hydrate	92.4	76.7	64.6				142
glycolaldehyde	hydrate	92.4	67.2					142
formaldehyde	hydrate	84.5						142

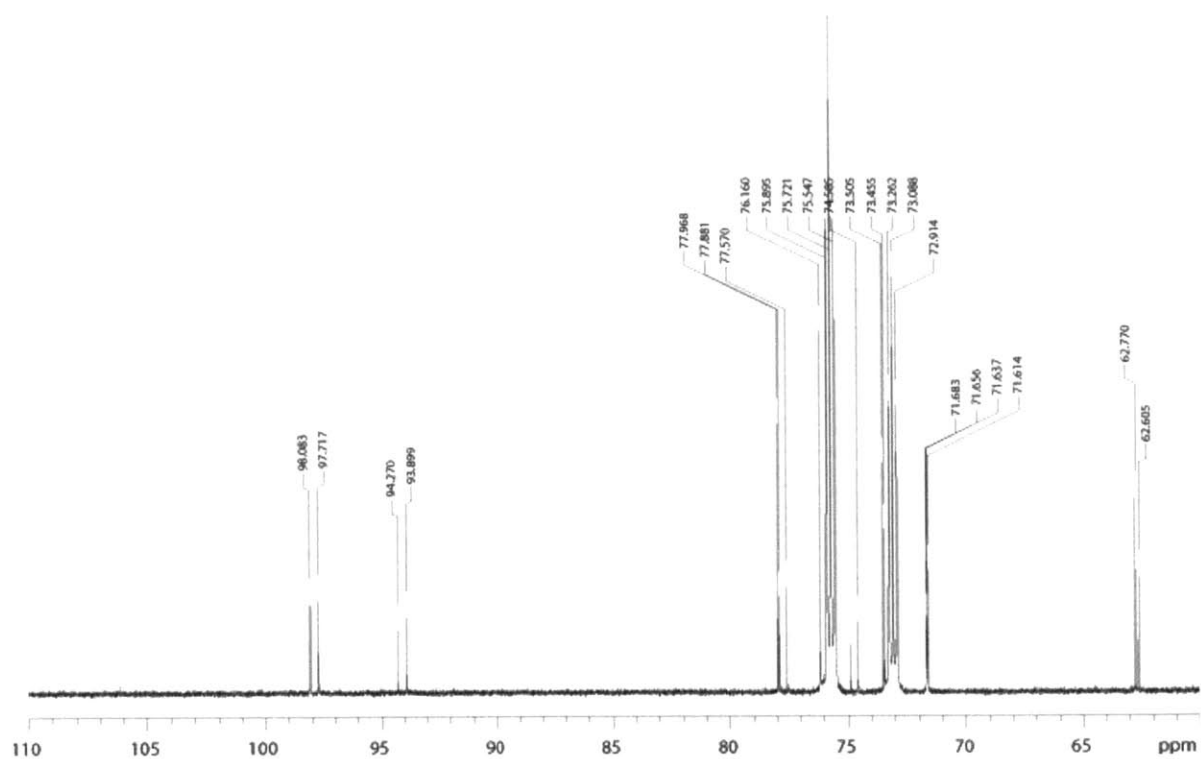


Figure S50. $[2-^{13}\text{C};2-^2\text{H}]$ glucose ^{13}C spectra

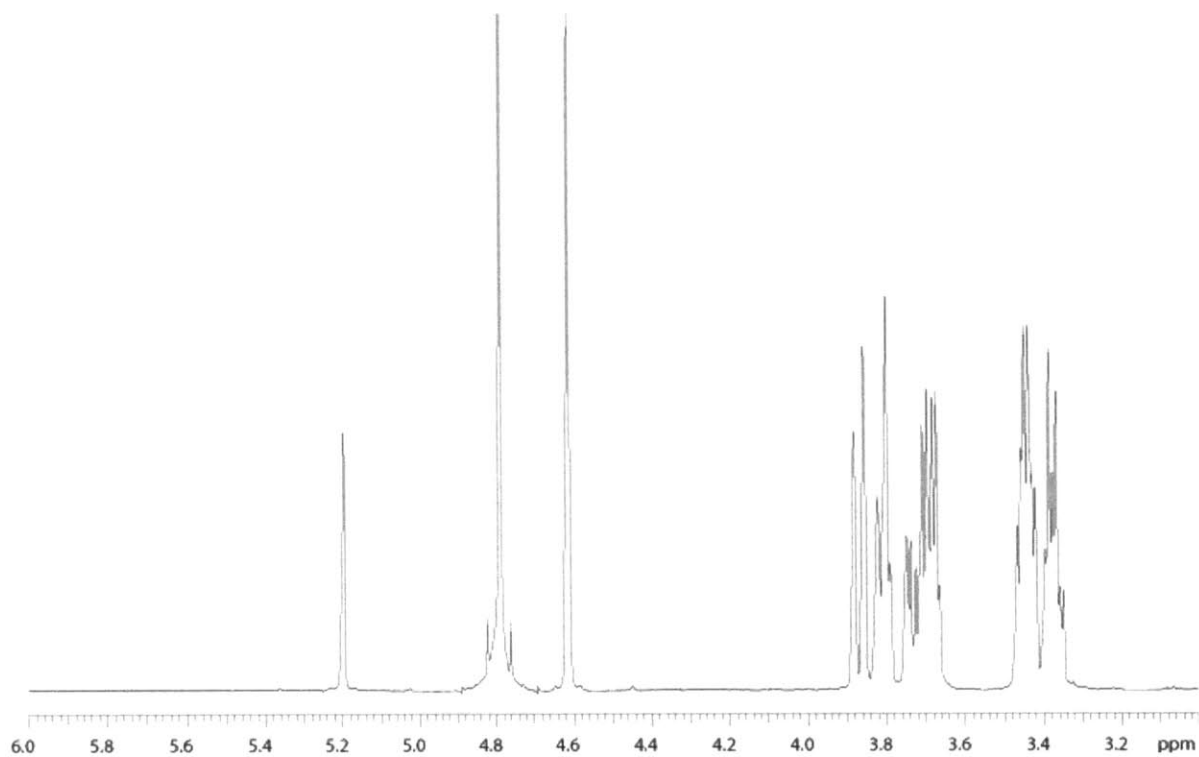


Figure S51. [2-¹³C;2-²H]glucose ¹H spectra

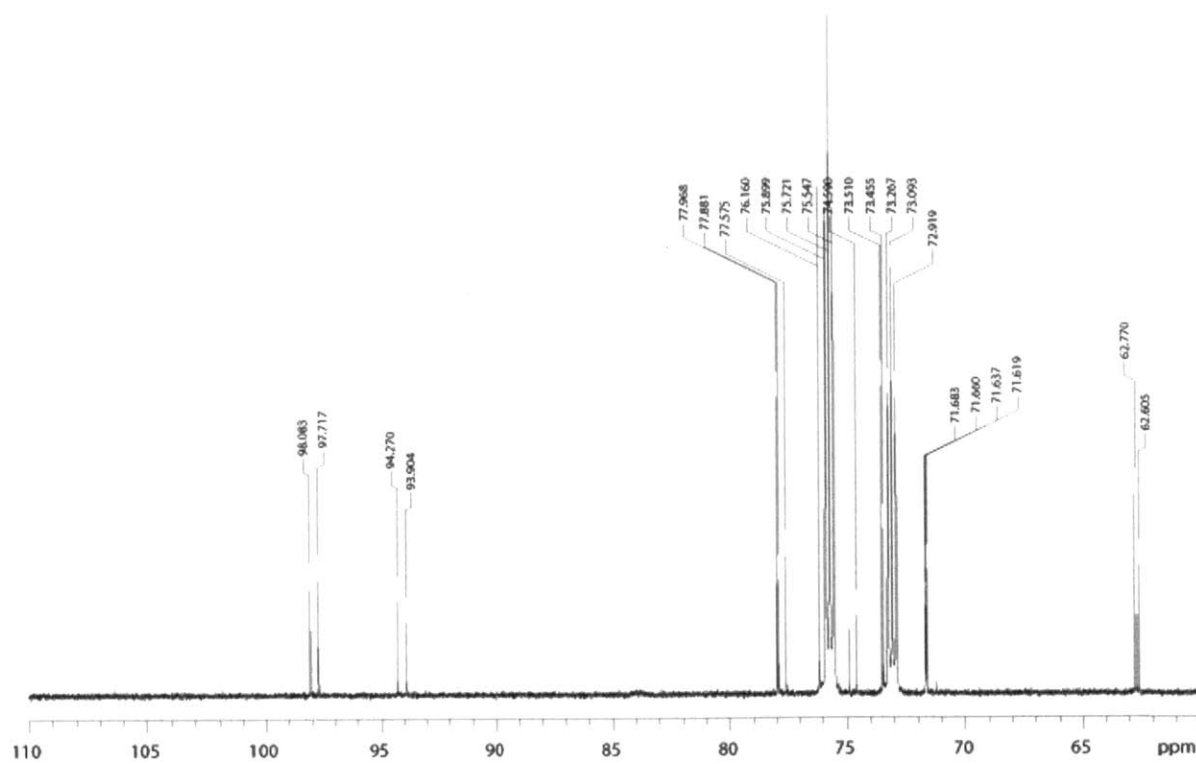


Figure S52. [2-¹³C;2-²H]glucose 4:1 sodium tetraborate with 100:1 Si-Beta at 85°C for 2 h glucose fraction ¹³C spectra

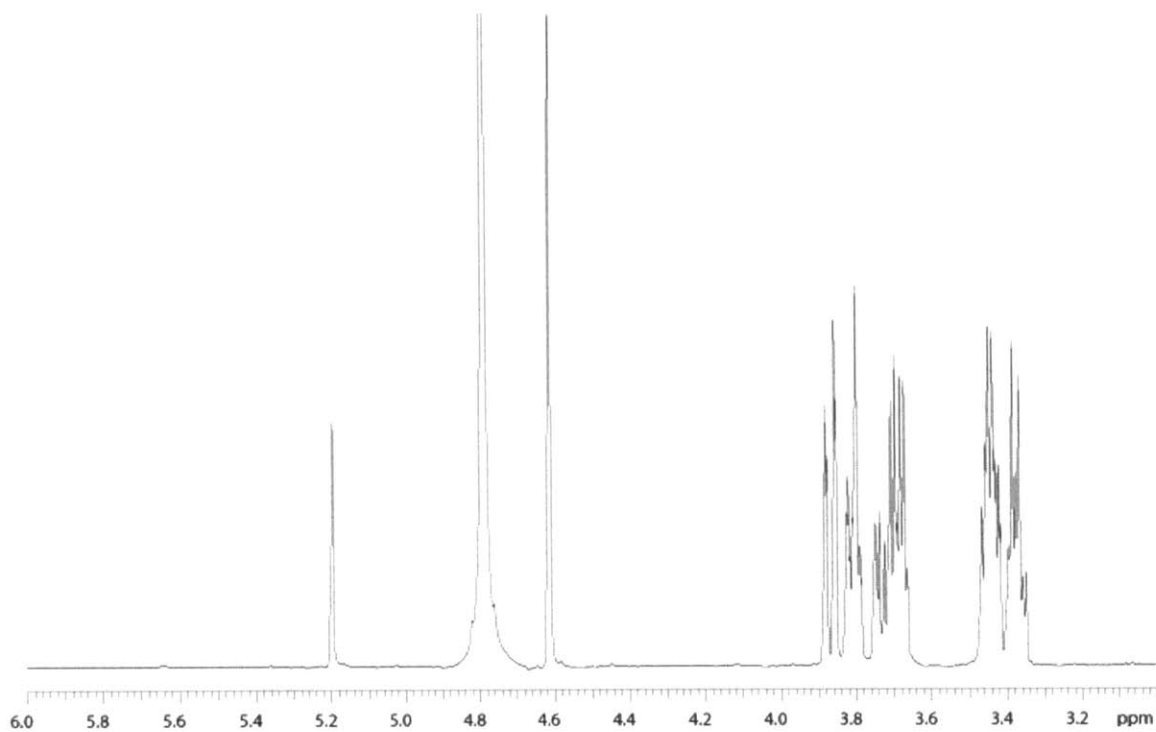


Figure S53. [2-¹³C;2-²H]glucose 4:1 sodium tetraborate with 100:1 Si-Beta at 85°C for 2 h glucose fraction ¹H spectra

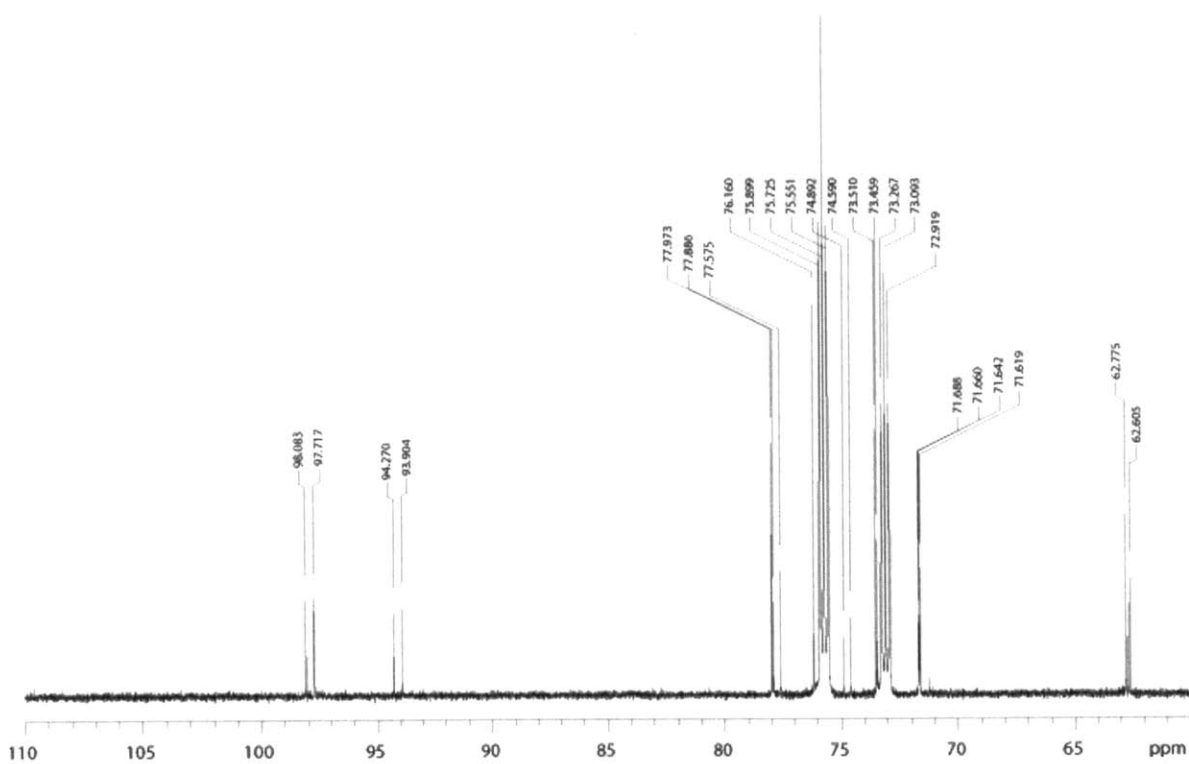


Figure S54. [2-¹³C;2-²H]glucose 4:1 sodium tetraborate with 100:1 Sn-Beta at 85°C for 2 h glucose fraction ¹³C spectra

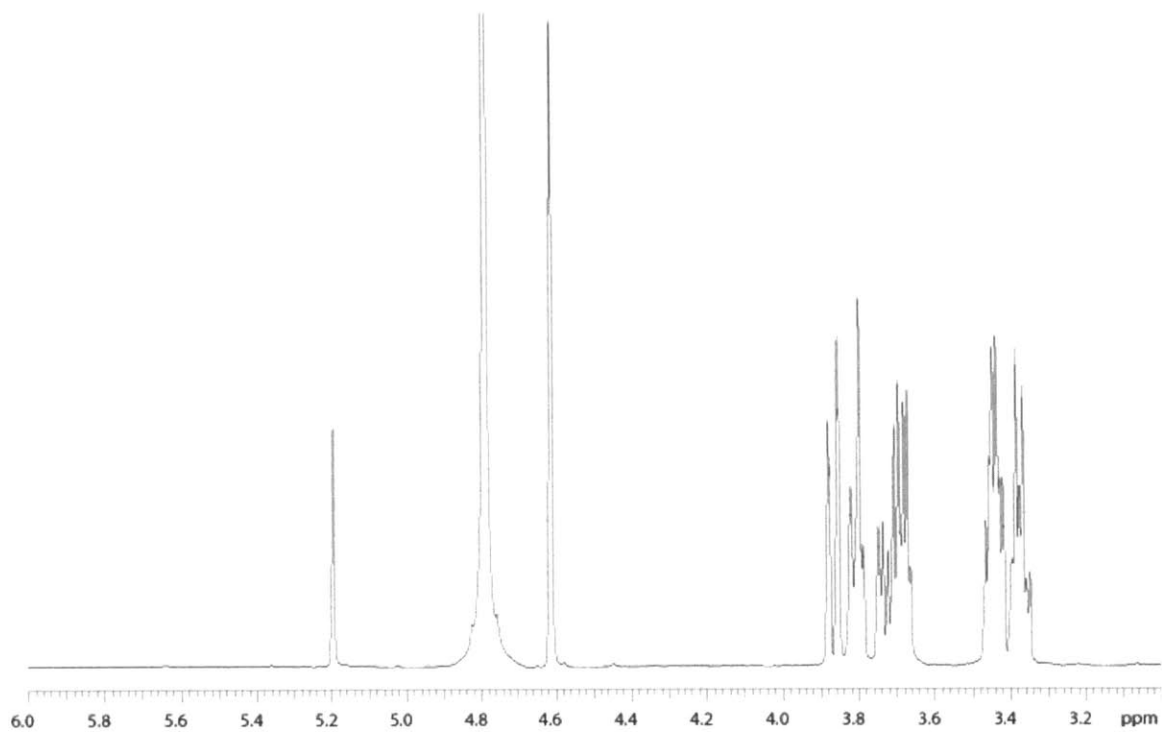


Figure S55. [2-¹³C;2-²H]glucose 4:1 sodium tetraborate with 100:1 Sn-Beta at 85°C for 2 h glucose fraction ¹H spectra

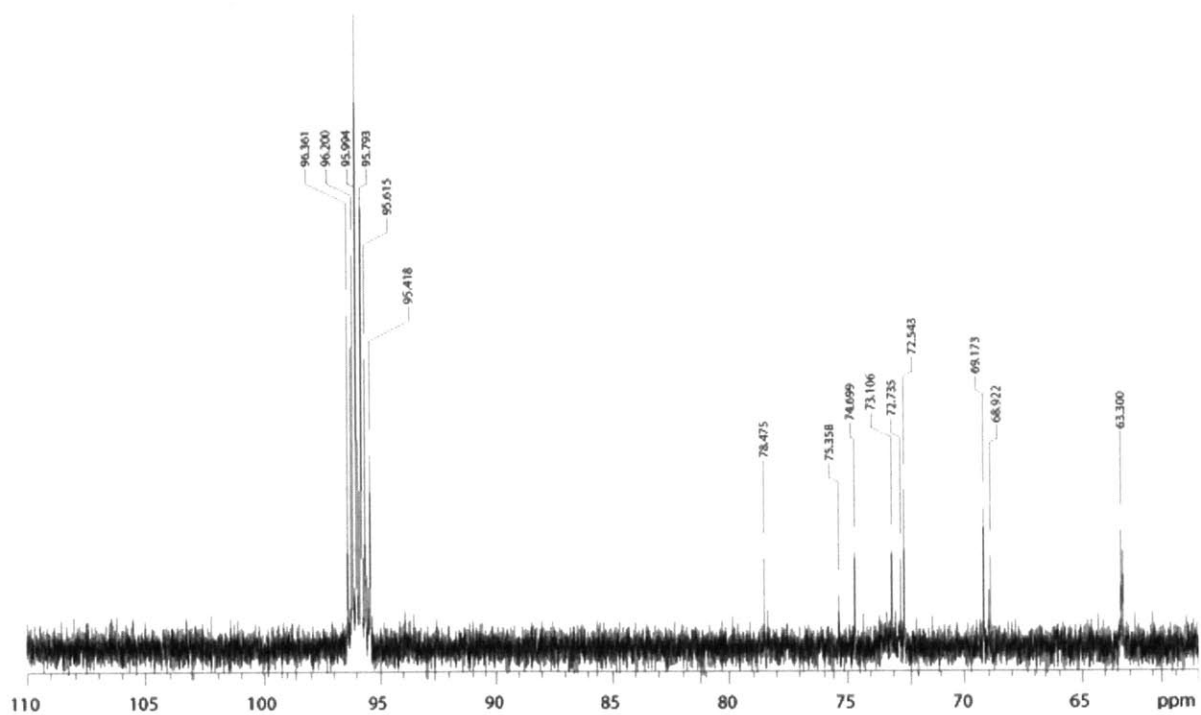


Figure S56. [2-¹³C;2-²H]glucose 4:1 sodium tetraborate with 100:1 Sn-Beta at 85°C for 2 h mannose fraction ¹³C spectra

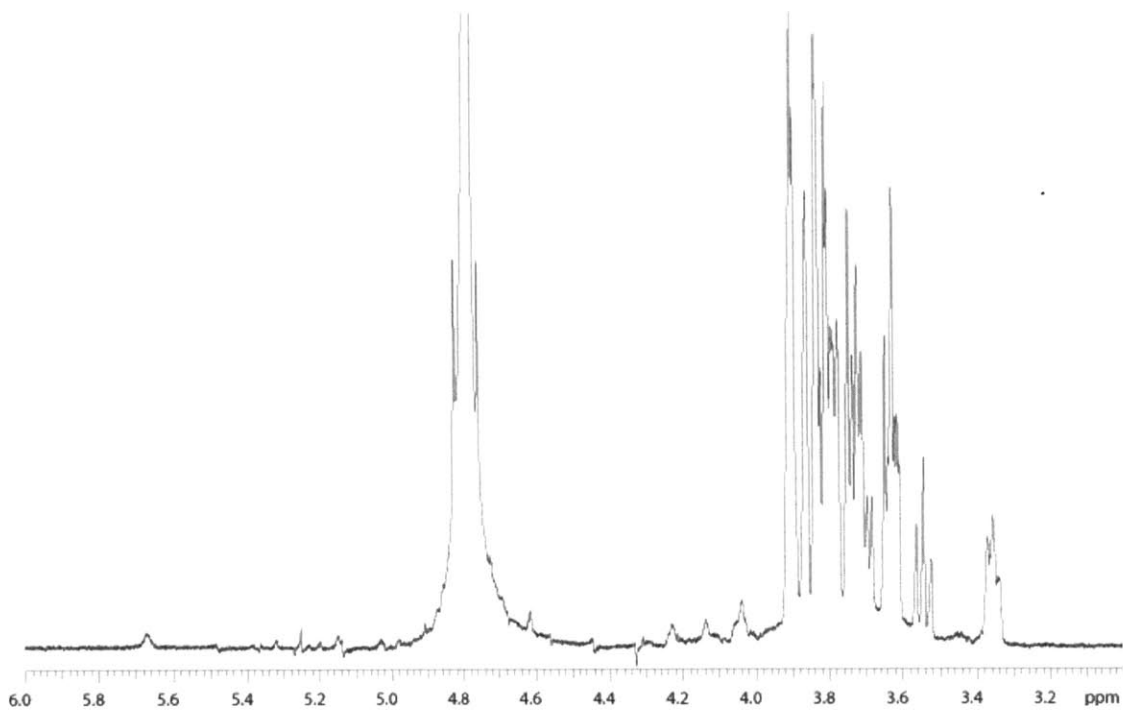


Figure S57. [2-¹³C;2-²H]glucose 4:1 sodium tetraborate with 100:1 Sn-Beta at 85°C for 2 h mannose fraction ¹H spectra

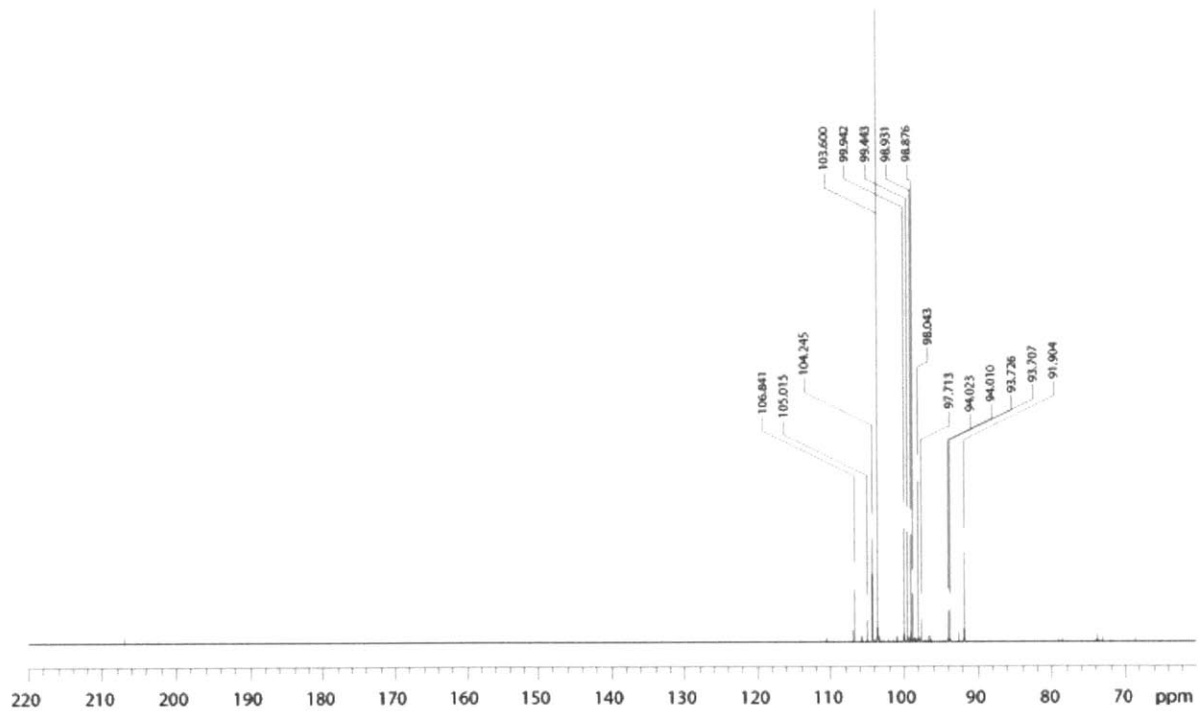


Figure S58. [1-¹³C]erythrose ¹³C spectra

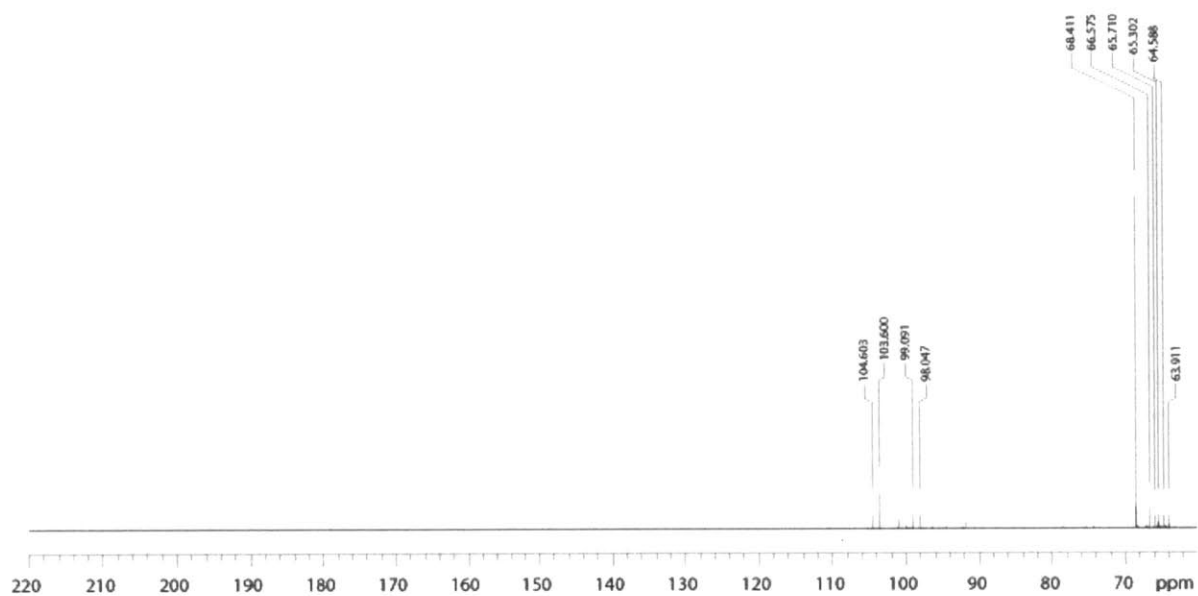


Figure S59. [1-¹³C]erythrose with 100:1 Sn-Beta at 50°C for 2 h ¹³C spectra

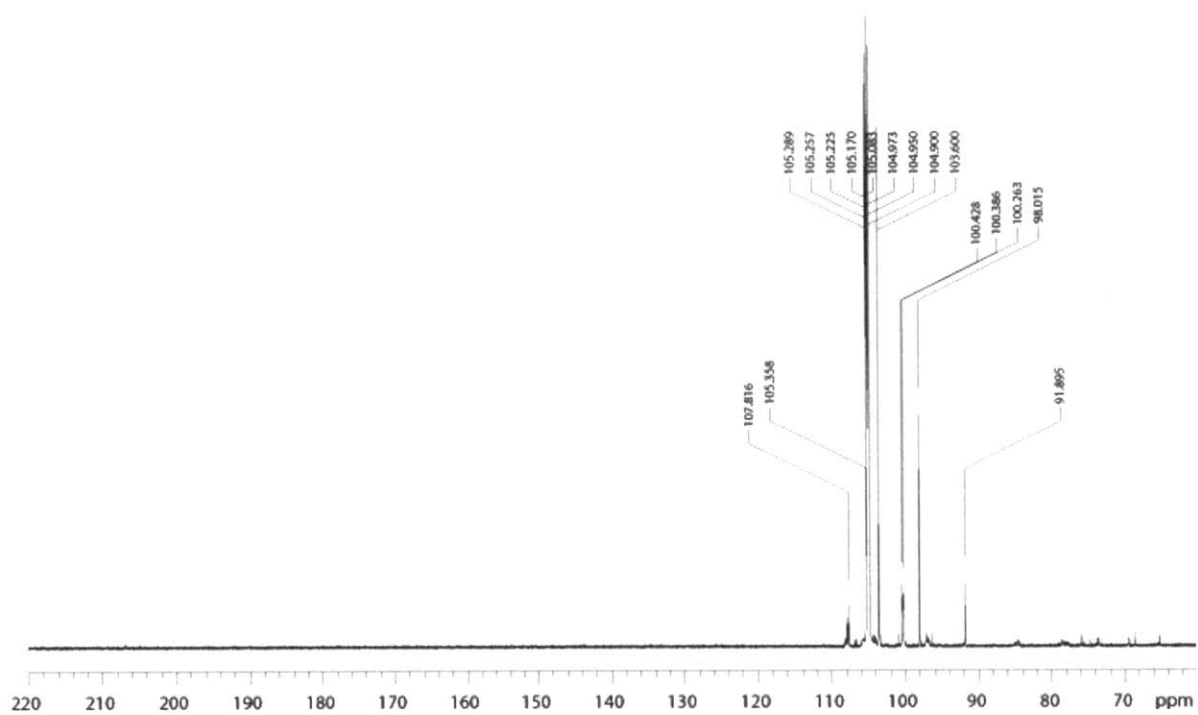


Figure S60. [1-¹³C]erythrose 4:1 sodium tetraborate ¹³C spectra

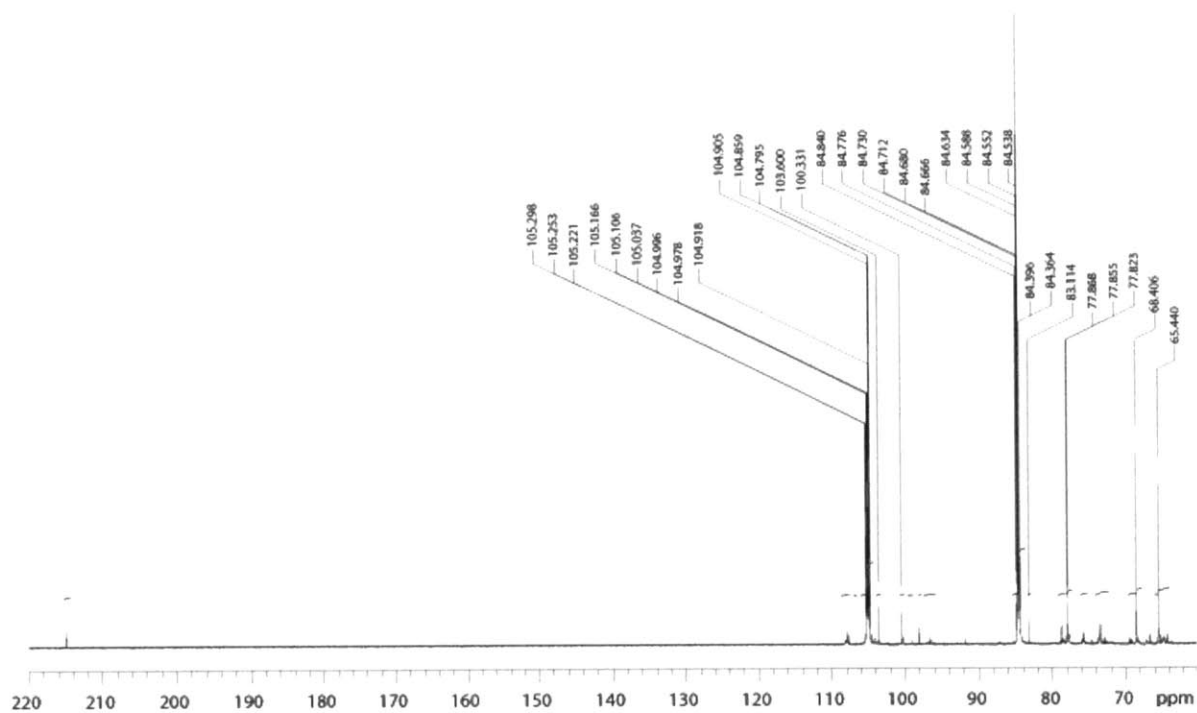


Figure S61. [1-¹³C]erythrose 4:1 sodium tetraborate with 100:1 Sn-Beta at 50°C for 2 h ¹³C spectra

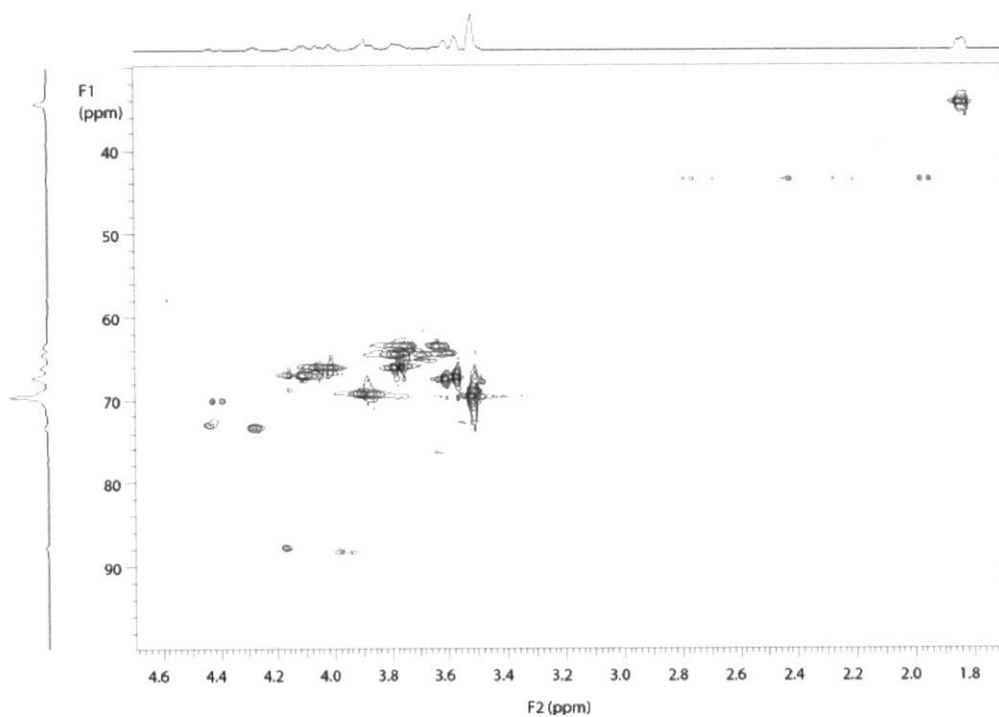


Figure S62. 3-deoxy-D-glucose 4:1 sodium tetraborate with 100:1 Sn-Beta at 85°C for 2 h mannose fraction HSQC spectra

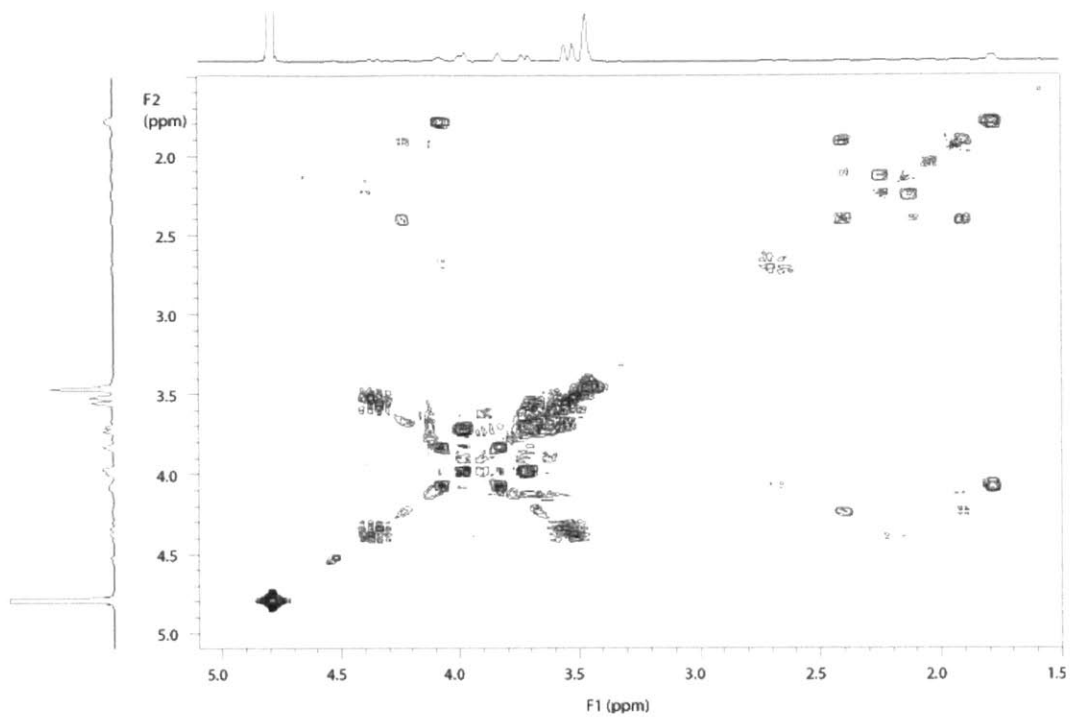


Figure S63. 3-deoxy-D-glucose 4:1 sodium tetraborate with 100:1 Sn-Beta at 85°C for 2 h mannose fraction gCOSY spectra

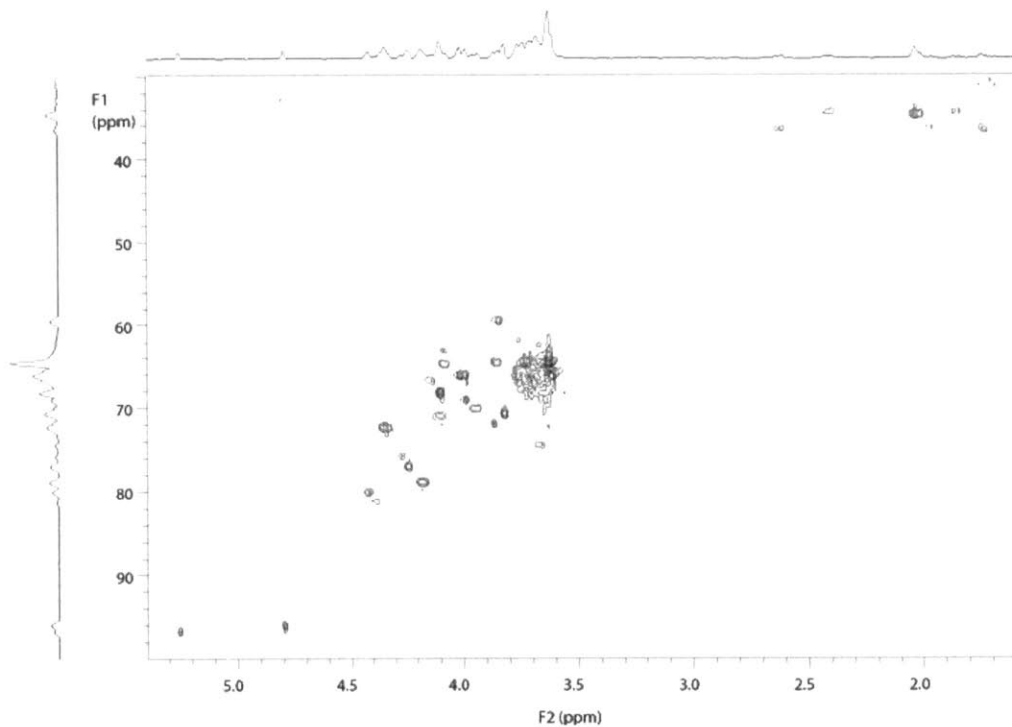


Figure S64. 4-deoxy-D-glucose 4:1 sodium tetraborate with 100:1 Sn-Beta at 85°C for 2 h mannose fraction HSQC spectra

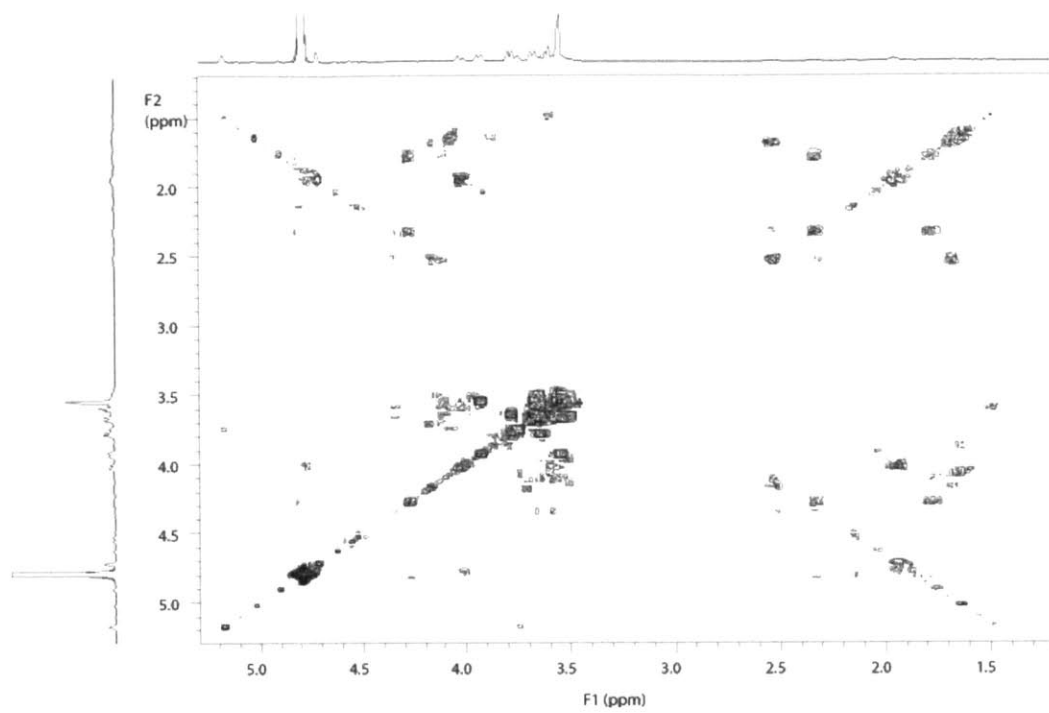


Figure S65. 4-deoxy-D-glucose 4:1 sodium tetraborate with 100:1 Sn-Beta at 85°C for 2 h mannose fraction gCOSY spectra